MICROCOPY RESOLUTION TEST CHART

NATIONAL BUREAU OF STANDARDS-1963-A

AD-A149 386

TWENTY-FIFTH YEAR

GEOPHYSICAL FLUID DYNAMICS

Great Seal

$H = X\beta\theta + \overline{WT}$

WHOI

DTIC
SELECTED
JAN 1 6 1985

A

COURSE LECTURES
ABSTRACTS OF SEMINARS
SYMPOSIUM
LECTURES OF THE FELLOWS

SUMMER STUDY PROGRAM
in
Geophysical Fluid Dynamics
Woods Hole Oceanographic Institution

DYNAMIC DIFFERENTIATION

by

Willem V. R. Malkus, Director
and
Florence K. Mellor, Editor

Woods Hole Oceanographic Institution
Woods Hole, Massachusetts 02543

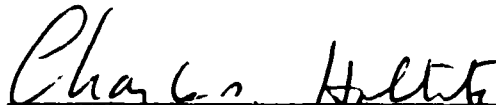November 1984

Technical Report

Approved for Distribution:

Charles D. Hollister
Dean of Graduate Studies

1984 SUMMER STUDY PROGRAM

in

GEOPHYSICAL FLUID DYNAMICS

at

THE WOODS HOLE OCEANOGRAPHIC INSTITUTION

DYNAMIC DIFFERENTIATION

GEOPHYSICAL FLUID DYNAMICS PROGRAM
June 25 - August 31, 1984

STAFF AND VISITORS

Aref, Hassan	Brown University
Busse, Frederick H.	University of California
Collins, William	University of Chicago
Dick, Henry, J. B.	Woods Hole Oceanographic Institution
Fearn, David	Cambridge University
Flierl, Glenn	Massachusetts Institute of Technology
Fowler, Andrew	Massachusetts Institute of Technology
Grimshaw, Roger	University of Melbourne
Hocking, Leslie	University College of London
Holyer, Judy	Bristol University
Howard, Louis, N.	Florida State University
Huppert, Herbert E.	University of Cambridge
Keller, Joseph B.	Stanford University
Krishnamurti, Ruby	Florida State University
Malkus, Willem V.R.	Massachusetts Institute of Technology
Pedlosky, Joseph	Woods Hole Oceanographic Institution
Pomeau, Yves	Schlumberger-Doll Research
Proctor, Michael	Cambridge University
Richter, Frank	University of Chicago
Rhines, Peter N.	Woods Hole Oceanographic Institution
Ruddick, Barry	Halifax University
Schmitt, Raymond W.	Woods Hole Oceanographic Institution
Sparks, R. Steven J.	University of Cambridge
Spiegel, Edward A.	Columbia University
Stern, Melvin E.	University of Rhode Island
Stommel, Henry M.	Woods Hole Oceanographic Institution
Veronis, George	Yale University
Welander, Pierre	University of Washington
Whitehead, John A.	Woods Hole Oceanographic Institution
Worster, M. Grae	Massachusetts Institute of Technology
Young, William R.	Scripps Institution of Oceanography
Zaleski, Stephane	University of Paris

CAMS SYMPOSIUM

Baker, Michael	Massachusetts Institute of Technology
Bryan, Wilfred B.	Woods Hole Oceanographic Institution
Dick, Henry, J. B.	Woods Hole Oceanographic Institution
Grove, Tim	Massachusetts Institute of Technology
Huppert, Herbert E.	University of Cambridge
Kerr, Ross	University of Cambridge
Loper, David	Florida State University
Reid, John	Hampshire College
Ribe, Neil M.	Yale University
Sigurdsson, Haraldur	University of Rhode Island
Sparks, R. Steven J.	University of Cambridge
Whitehead, John A.	Woods Hole Oceanographic Institution

FELLOWS

Bayly, Bruce J.	Massachusetts Institute of Technology
Gorius, André	Ecole Normale Superieure, Paris
Hayashi, Yoshi-Yuki	University of Tokyo
Kerr, Oliver, S.	Bristol University
Kerr, Ross C.	Cambridge University
Polvani, Lorenzo M.	Massachusetts Institute of Technology
Smith, Leonard A.	Columbia University
Taylor, John R.	Australian National University
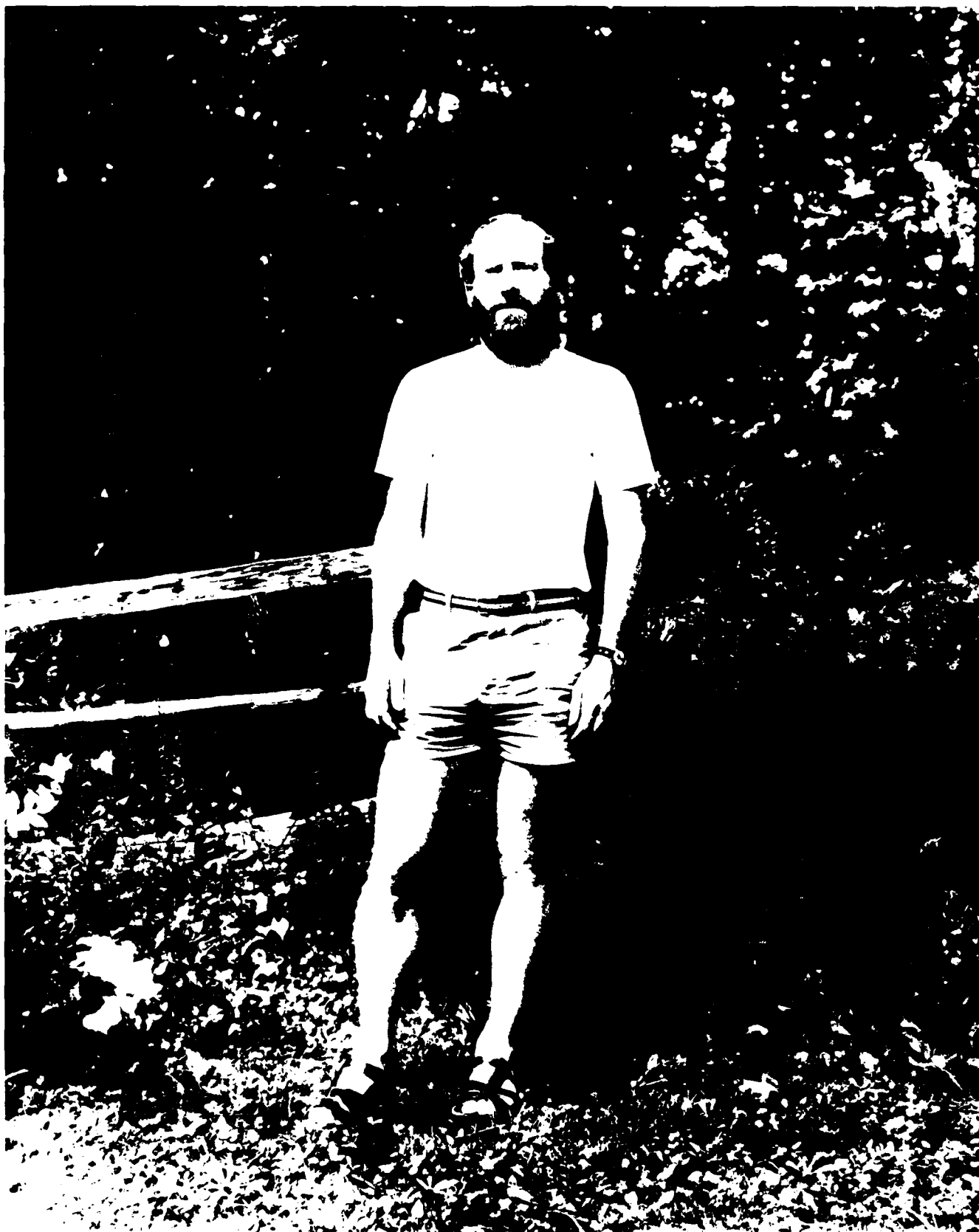
PRINCIPAL LECTURER - HERBERT E. HUPPERT

Back Row: Smith, Spiegel, Huppert, Holyer, Howard, Malkus, Grimshaw, Collins, Worster.

Middle Row: Flierl, Pomeau, Fowler, Keller, Veronis, Busse, Stern, Mellor, Young.

Front Row: Sparks, Zaleski, Gorius, Bayly, Hayashi, R. Kerr, Polvani, Taylor, O. Kerr.

Absentees: Aref, Dick, Fearn, Hocking, Krishnamurti, Pedlosky, Proctor, Richter, Rhines, Ruddick, Schmitt, Stommel, Welander, Whitehead.

PREFACE

Those attending G.F.D. 1984 were introduced to the novel topic of Geological Fluid Mechanics by our Principal Lecturer, Herbert Huppert. He presented his studies both as a discipline with recent fascinating successes, and as a challenge to his listeners to further isolate mathematically tractable examples of these multi-component flows. Geological Fluid Mechanics has been the responsible process for the formation and modification of most of the geological objects studied today. The dynamics of fluid mixtures in magma chambers, the changing fluid boundary conditions and composition during selective crystallization of parts of the melt, and the separation of fluid fractions of different density and viscosity all represent areas in which quantitative theories are currently being tested. However, equally many areas, including convection mechanisms in the Earth's core and quantitative predictions for upper mantle motion, resist simplistic modeling.

The following pages also contain abstracts of a symposium by geophysicists on observed fluid-like geological phenomena. It became clear that the most accessible phenomena would not be quantified soon by the models currently available. Equally clear was the prospect that the limits of validity of current quantitive theory soon would necessitate theories based on more detailed properties of the materials.

The Fellowship lectures reflect the interests of the Principal Lecturer more than at any time in the recent past. Five of these involve double-diffusive processes in one way or another. Members of the staff also explored this phenomenum. The manuscript by L. N. Howard (aided by G. Veronis) clarifies an important new aspect of double-diffusion. These reports are to be treated as unpublished manuscripts. Readers desiring to quote from the material should seek the permission of the author. As in past years, these reports are often reworked for publication or are incorporated into doctoral theses.

We are indebted to the Office of Naval Research and to four branches of the National Science Foundation for financial support of the program. The initial editing and final assembly of this report are due to the firm and skillful hand of Florence Mellor. We are also grateful to A. L. Peirson for his thoughtful administration of our program.

Willem V. R. Malkus

The death of Mary Cobb Thayer on August 27, 1984 at age ninety-two, is reported with sorrow. Mary will be remembered by previous Fellows as the spirited coordinator of our G.F.D. program during its first twenty years.

TABLE OF CONTENTS

GEOLOGICAL FLUID MECHANICS

HERBERT E. HUPPERT   Page

ABSTRACTS OF SEMINARS

LECTURES OF FELLOWS

GEOLOGICAL FLUID MECHANICS

Herbert E. Huppert

LECTURE 1

I. INTRODUCTION

In this lecture we will introduce the subject of Geological Fluid Mechanics and describe the material to be covered in the lectures. Adopting a musical metaphor, the sequence will be:

Program Notes: What is Geological Fluid Dynamics?

Overture: Description of the course.

Divertimento: Physical properties of molten rock, and the idealizations thereof that we shall use in our analysis.

What is Geological Fluid Mechanics?

It is difficult to sharply delineate what constitutes the new subject of Geological Fluid Mechanics. It overlaps branches of geology, applied mathematics, and geophysical fluid mechanics -- and is without doubt another part of science. The subject matter can be partly determined by example.

A) The Route of Magma from the Mantle to the Surface

Geological fluid dynamical processes can be considered to begin with the melting of rock at grain boundaries in the upper mantle. Blobs of liquid

surface

magma chamber

deep mantle
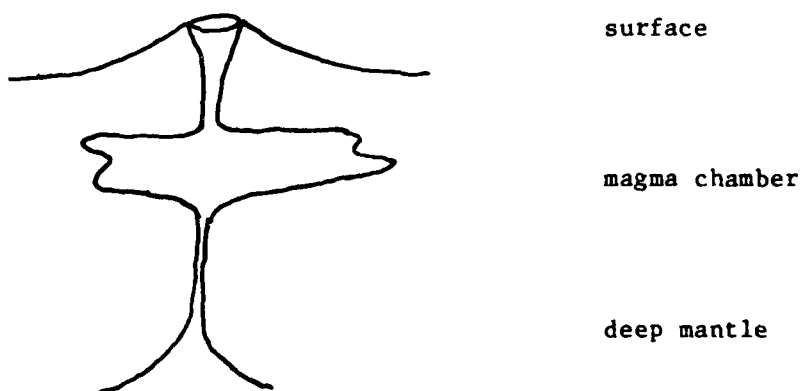
coagulate and, because they are lighter than the surrounding 'solid' rock, tend to rise. The rising of light, liquid magma through a conduit in heavier, solid rock, is a fluid mechanical phenomenon of considerable interest. The pipe terminates at a magma chamber, which acts as a large storage reservoir. Chambers can be up to 10 km in horizontal dimensions, and a few kms in vertical dimensions. The magma may remain for a considerable time in these

chambers. Within the chamber, the magma flows, convects, crystallizes, and may even solidify. There are plenty of interesting fluid mechanical problems here. The magma chamber that has been most extensively observed is the one under Kilauea in Hawaii, which has a very convoluted structure. There is an extinct magma chamber on the island of Rhum (off the northwest coast of Scotland) from which the surrounding rock has been eroded away, so that its internal structure is easily observed.

B) Mid-Ocean Ridge Spreading

Below the ridge that exists at the separation point between two diverging oceanic plates, there is an upwelling of hot material from the mantle to form the rear of the plates. The dynamics of mid-ocean ridge spreading are not understood at present, particularly in a predictive sense. Magma chambers are predominately located in the spreading zone.
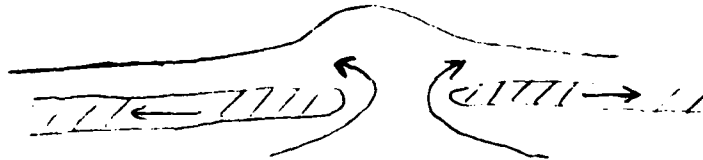
C) Eruptions

From a magma chamber, a conduit may lead to the surface where it becomes the source for a volcano. Sequence of shots of Ngaurahoe shows the

Schematic Picture of Ngaurahoe Sequence

first few seconds of the eruption, which is described as the following order of events. First, a sudden overpressure of three atmospheres developed inside the volcano, and a rush of ash-laden gas moving at $\sim$ 400 m/sec (supersonically) was ejected into the atmosphere. The hot ash at the edge of the cloud,

in contact with the outside air, caused the latter to expand rapidly. Thus the outer layers of the ash cloud became buoyant and rose, while the inner regions of the ash cloud remained heavier than the surroundings and fell down the mountain, developing into a hot gravity current travelling at $\sim$ 45 miles/hour. The dynamics of these hot ash flows contain many unsolved problems. (It was suggested by a member of the audience that there may be some similarity between ash flows and fluidized bed dynamics; this suggestion was strenously debated.)

D) <u>Geological Fluid Dynamics</u> also includes such diverse topics as mud flows, sand transport by waves, rock mechanics (rheology), geothermal systems, plate tectonics, and the dynamics of flows in the core. Most of these topics will not be discussed in these lectures.

Description of the Lectures

<u>Lecture 2</u> Review of thermal convection, double-diffusive convection and and applications (e./g. iceberg melting), convection from point sources (e.g. black smokers).

<u>Lecture 3</u> Crystallization in cooled saturated solutions of different constitutions.

<u>Lecture 4</u>
and   <u>5</u>   The internal dynamics of replenished magma chambers. This will be discussed from a fluid-dynamical perspective, with reference to the blue, green, red, brown, and yellow experiment, each of which display unique fluid mechanical phenomena.

<u>Lecture 6</u> Cooling of a magma chamber from the side: crystallization and the formation of layers. Also, the effects of replenishing chamber with hot, light magma.

<u>Lecture 7</u> Steve Sparks will talk about the physics of eruptive columns and starting plumes from eruptions like Mt. St. Helens.

<u>Lecture 8</u> We will dramatically switch Reynolds numbers, and look at viscous gravity currents -- on level surfaces, with viscous application to lava domes, and on slopes, which may model 5 lava flows.

<u>Lecture 9</u> What happens when hot fluid flows down a surface which it can erode (e.g. hot water flowing down a wax bed)? The stream beds thus created look remarkably similar to certain channels observed in the nickel-sulphide fields of Kambalda.

Physical Properties of Molten Rock

<u>Rheology</u>: Well beyond the liquidus (crystallization) point, laboratory investigations indicate that liquid rock is approximately Newtonian,
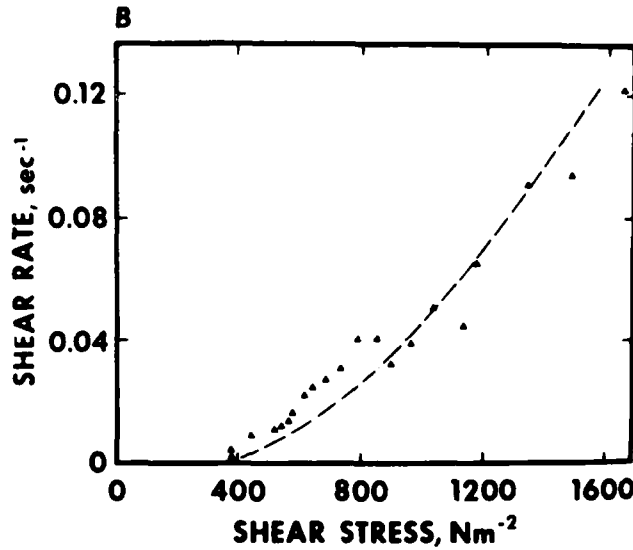
Figure 1: Stress/strain-rate curve for simple shear

Field evidence shows that magma (plus crystals) on the liquidus has a yeild
strength, i.e.for shear stress less than a critical value, the material
appears to resist like a solid. Above this value the relationship between
stress and rate of strain is quite closely linear. In the discussions to
follow the shear stress is typically well above the critical value and we
shall assume that the fluid can be considerd to be Newtonian.
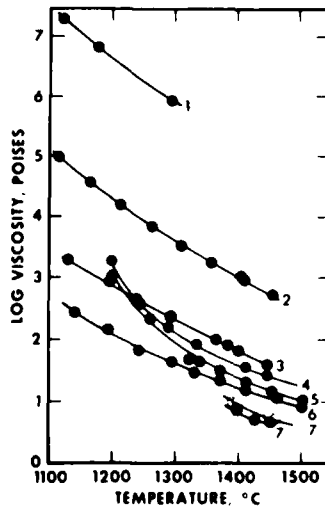
5.2 1 The viscosity of some common igneous rock melts
as a function of temperature (Murase and McBirney,
1973) (1) rhyolite (2) andesite (Mount Hood), (3) Columbia
River basalts (4) Skaergaard liquid at 35 crystalliza
tion, (5) Skaergaard liquid at 76 crystallization (6) oliv
ine basalt (Galapagos), (7) synthetic lunar basalt in air,
(7) synthetic lunar basalt in argon

Figure 2: Temperature dependence of magma viscosity.

The fluid viscosity varies considerably with temperature and with
silicate contents as shown in Fig. 3 . While there may be some phenomena
associated with the variation of viscosity with temperature, they have not yet
been considered in the situations discussed in these lectures. There are,
however, some interesting effects due to the mixing of magmas of greatly
differing viscosities, which will be considered a number of times during the
lectures. One aspect which is of relevance to oceanographic situations but
generally geological situations because of the different time scales is the
distinction between stirring and mixing.
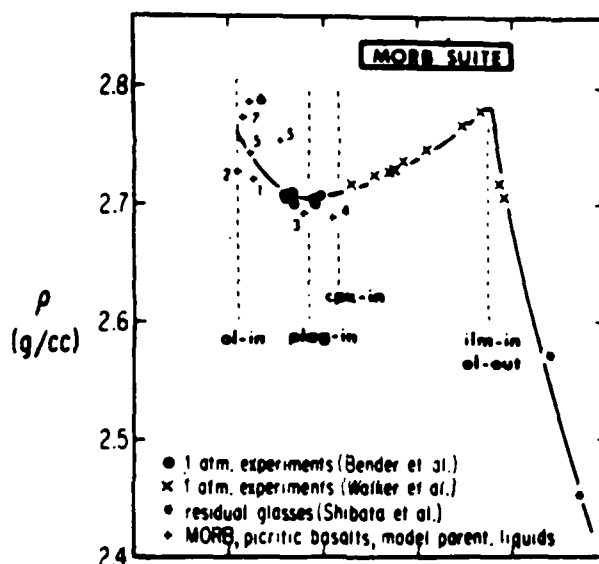
Figure 3: Temperature Dependence of Magma Density.

Having eliminated some inessential complications, we now consider an
essential feature of the magmatic fluid -- the temperature-dependence of its
density. At temperatures on the liquidus, the density of the magma is
determined mainly by its content of various dissolved minerals. As the
temperature is lowered and crystallization takes place, first a mineral
crystallizes out, to be followed at lower temperatures by possibly another and
then another. Thus the temperature-density curve may have quite a wiggly
shape. The Prandtl number for molten rock is usually very large, so we shall
suppose it is infinite in calculation.

NOTES SUBMITTED BY
Bruce Bayly and
Andre Gorius

LECTURE 2

REVIEW OF THERMAL CONVECTION AND DOUBLE-DIFFUSIVE CONVECTION

Herbert E. Huppert

In this lecture we present a brief survey at some of the results for thermal, and then double diffusive, convection.

1. Thermal Convection

Consider the idealized case of convection between two infinite, horizontal perfectly conducting flat plates with the upper plate held at temperature 0 and the lower plate at ΔT. There exists a solution to the governing equations with a linear temperature gradient and the fluid between the plates stationary.

If a small parcel of fluid is raised then it will find itself in a region of cooler, denser fluid and will continue to rise if it can overcome the effects of viscosity and not dissipate its heat too quickly. Any motion will be driven by the relative density difference between the upper and lower boundaries given by

$$\frac{\Delta \rho}{\rho_o} = - \alpha \Delta T$$

The only quantities that affect the motions are $g\frac{\Delta \rho}{\rho}$, ν (kinematic viscosity), K (thermal diffusivity), H (fluid depth). These give two independent nondimensional parameters by which the whole system can be described.

The Rayleigh number $\qquad Ra = \frac{g \Delta \rho H^3}{\rho K \nu}$

The Prandtl number $\qquad \sigma = \frac{\nu}{K}$

The linear stability of the conduction solution can be investigated by linearizing the equations and finding the marginally stable solutions. This occurs for steady motions ($\partial_t = 0$) and leads to

$$\mathcal{L} \phi \equiv \nabla^6 \phi + R_a \nabla_H^2 \phi = 0$$

with six boundary conditions.

This equation is independent of the Prandtl number and from it the minimum value of the critical Rayleigh number for convection to occur can be found.

The values of the Rayleigh number for the onset of convection are

$$Ra = \frac{27\,\pi^4}{4} \qquad \text{for the stress free boundaries}$$

$$Ra = 1708 \qquad \text{for rigid boundaries.}$$

In the stress-free case this corresponds to a horizontal wave number for the first unstable mode of $\sqrt{2}\,\pi$. However, linear theory does not tell us about the planform that is expected, to find this we have to resort to non-linear theory(see, for example, Busse 1978).

When a flow is strongly nonlinear the observed motions can be summarized in the diagram below (Krishnamurti, 1973).
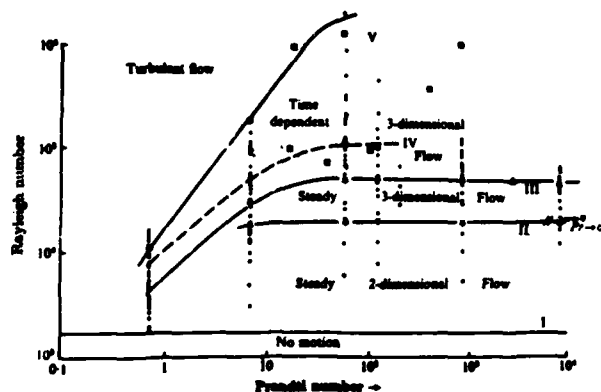
The nondimensional heat transfer is given by the Nusselt number

$$Nu = \frac{\bar{F}_H}{\rho\,C\,\kappa\,\Delta\bar{T}/H} = f(Ra, \sigma)$$

This is the ratio of the true heat flux F_H to the expected conductive heat flux. This will be a function of the parameters of the system, Ra and σ.

When the fluid is heated strongly (i.e. for large Ra), it is found that

$$Nu \approx C\,Ra^{1/3}$$

This result can be described by noting that at high Ra the fluid in between the plates will be strongly turbulent and that the heat flux F_H will be dependent on conditions at the boundaries only and not on the depth of the layer. This requires the $Ra^{1/3}$ dependence.

2. Double-Diffusive Convection (Huppert and Turner, 1981)

The conditions for double-diffusive convection are that there are two or more components to the fluid, of different molecular diffusivities, that contribute in opposing senses to the vertical density gradient. Some examples of this are heat and salt, two different salts, or heat and helium. Here we will adopt the terminology of heat and salt with diffusivities $K_T > K_S$. We will also assume a linear density relation

$$\rho = \rho_0 (1 - \alpha T + \beta S)$$

There are two cases of particular interest,

Case A

$$\frac{\partial \rho_T}{\partial z} < 0 \qquad \frac{\partial \rho_S}{\partial z} > 0 \qquad \frac{\partial \bar\rho}{\partial z} < 0$$
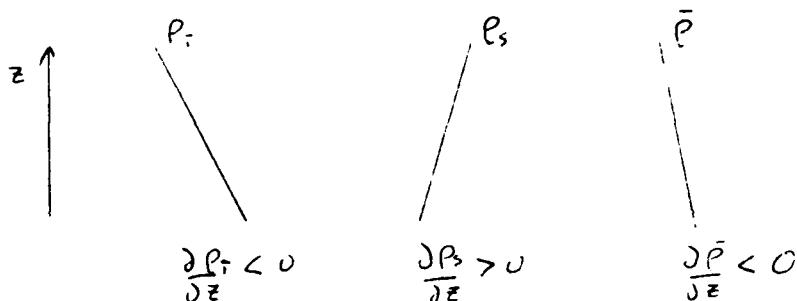
The contribution of heat to the vertical density gradient is stabalizing and that of salt destabalizing, while the total density gradient is stable.

Case B

$$\frac{\partial \rho_T}{\partial z} > 0 \qquad \frac{\partial \rho_S}{\partial z} < 0 \qquad \frac{\partial \bar\rho}{\partial z} < 0$$
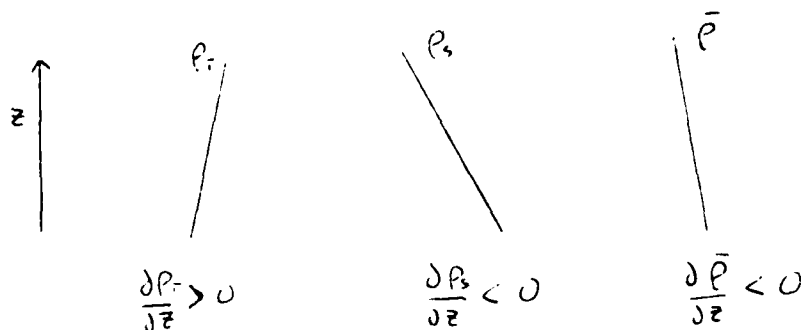
The contribution of heat to the density gradient is destabalizing and that of salt stabalizing, while the total density gradient is stable.

In Case A, if a small parcel of fluid was displaced downwards, it would find itself in a colder, fresher environment. Since heat diffuses much more rapidly than salt the parcel of fluid will lose its heat quickly to the surrounding fluid while remaining saltier. The parcel of fluid will then find itself denser than its surroundings and so will continue to fall. This case is called salt fingering because the fluid tends to form tall, thin vertical convective cells. Away from the case of marginal stability it is found that the horizontal wave number a of the fastest growing mode is given by

$$\pi a = \left(\frac{g \, \frac{\partial \rho}{\partial z}}{\rho \, \nu \kappa} \right)^{1/4}$$

Similar motions can also occur between layers of fluids of very different viscosities. An example of this would be when a layer of a salt dissolved in water lies over a layer of glycerine and water.

The relative diffusivity of a substance A into B is given by the relation

$$K_{A \to B} \propto \frac{1}{a_A \, \nu_B}$$

The diffusion rate is inversely proportional to the product of the molecular size of substance A and the kinematic viscosity of fluid B.

In the case of glycerine and sugar dissolved in water, the molecules do not differ very much in size compared to the very large difference in viscosity between glycerine and water. Since glycerine is much more viscous than water, glycerine will diffuse much more quickly into the water than either the water or the sugar will dissolve into the glycerine.

If a small parcel of the sugary water is displaced downwards into the glycerine, the glycerine will diffuse into it making the parcel denser. However, a mixture of water and glycerine is less dense than pure glycerine and so the fluid parcel will only continue downwards if there is a sufficiently large sugar content to make it denser.

The physical argument for the heat-salt case is symmetrical so fingers grow upwards and downwards in a symmetrical fashion, but for sugary water and glycerine this is no longer true and so the motions seen are asymmetric.

The diagram below gives the results of some experiments looking at the formation of fingers between a layer of sugar and water over a layer of glycerine and water. It is interesting that the transition from nothing happening to fingering seems to depend only on the density of the upper layer and not on the ratio of glycerine and water in the lower layer. The reason for this is not understood.
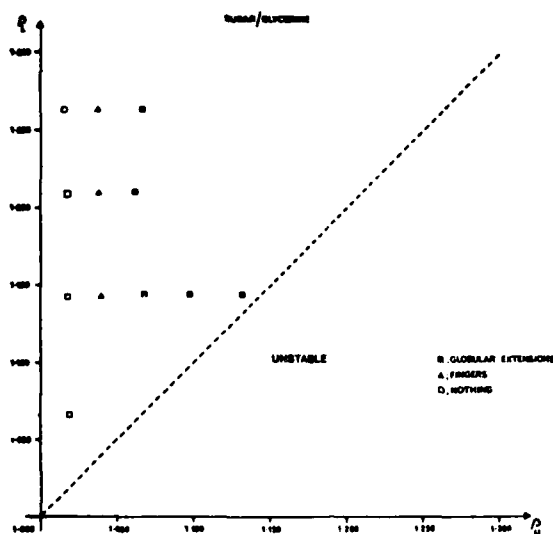
In Case B we had a stabalizing salt gradient and a destabalizing temperature gradient. If a small parcel of fluid is displaced downwards then it will gain heat from its surroundings while only gaining a little salt. It will then be less dense than its surroundings and so will return to its initial position. Due to the phase lay between the displacement and the temperature fields it will be warmer and less dense than the neighboring water and tend to continue rising, overshooting its initial position. This process may be repeated leading to an overstable oscillatory growth of the initial disturbance.

As with the purely thermal convection, we can perform a linear analysis to find the cases of marginal stability for a fluid between two infinite horizontal perfectly conducting stress-free boundaries.
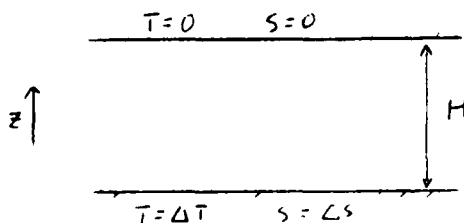
This time there will be a Rayleigh number associated with the salt gradient as well as the temperature gradient. The nondimensional numbers that characterize the motion are

Thermal Rayleigh number $\qquad R_T = \dfrac{g \alpha \Delta T\, H^3}{\kappa_T \nu}$

Solutal Rayleigh number $\qquad R_S = \dfrac{g \beta \Delta S\, H^3}{\kappa_T \nu}$

Prandtl number $\qquad \sigma = \dfrac{\nu}{\kappa_T} \qquad 0 < \sigma < \infty$

Salt/heat diffusivity ratio $\qquad \tau = \dfrac{\kappa_S}{\kappa_T} \qquad 0 < \tau < 1$

The case of marginal stability for the nonoscillatory instability is found by setting $\partial_t = 0$ and for the oscillatory instability by setting $\partial_t = i\omega$. The results are summarized in the following diagram.

Nonlinear analysis shows that the fingers have the same region of instability as for the linear case. For the oscillatory case there are nonlinear monotonic instabilities that occur for values of R_T less than that given by the linear analysis and that these may exist down to $R_T = \frac{27\pi^4}{4}$ in the limit of very small τ.

1st Application - Heating a salinity gradient from below
             (Huppert and Linden, 1979)

If a stable salinity gradient, which is initially at a uniform temperature, is heated from below it will cause the fluid next to the boundary to rise. This fluid cannot rise indefinitely since, because of the vertical salt gradient, it would find itself in less dense fluid. The heated fluid then

forms a well mixed layer at the bottom with a diffusive temperature profile above it. Eventually the region above the mixed layer will also become unstable and another distinct mixed layer will form on top of the original layer. This process is repeated, forming a series of distinct mixed layers. Eventually the lower layers breakdown and merge. The evolution of these layers is shown in the results of an experiment below.
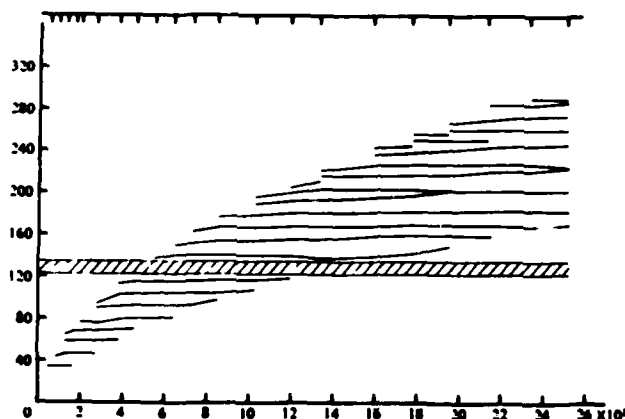
This motion will depend on the nondimensional numbers

$$Q = K_T \, S^*/H^* \; , \; \sigma \; , \; \tau$$

where the buoyancy flux $H^* = \dfrac{\alpha g \, F_H}{\rho \, c}$ and $S^* = -1/2 g \beta \dfrac{ds}{dZ}$.

It is found that the top layer forms at a height Z_f given by

$$Z_f = (4Kt)^{1/2}$$

where

$$K = 0.72 \, Q^{-1} K_T$$

It is also found that the depths of the convective layers formed are independent of the height at which they are formed (and so independent of the heat flux) and have a depth $\bar{h}$ given approximately by

$$\bar{h} = 51 \, (K_T/N)^{1/2}$$

where N is the buoyancy frequency.

These layers have been recorded below an ice island; this case is the analagous situation of cooling a stable salinity gradient from above.

2nd Application - Heating a salinity gradient from the side. (Huppert and
                    Turner, 1980)
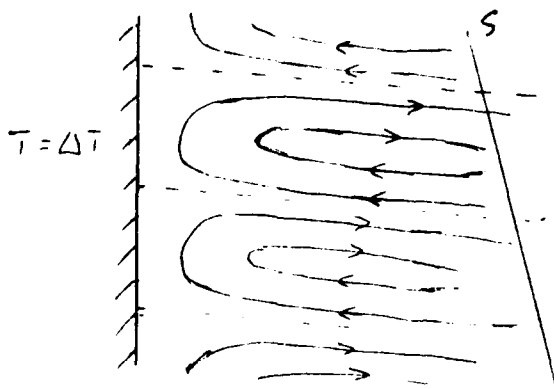
If a stable salinity gradient is heated from the side then the fluid in
the layer next to the wall will rise. As before it does not rise indefinitely
and so moves out forming almost horizontal layers. The thickness of these
layers is found by experiment to have a depth h given approximately by

$$h = 0.65 \; \Delta_h \rho \Big/ \frac{\partial \rho}{\partial z}$$

where $\Delta_h \rho$ is the horizontal density difference due to the temperature
difference.

These layers are also seen when a vertical ice wall melts into a stable
salinity gradient. This injects cold fresh water into the boundary layer
which (if density of the salty water is high enough) tends to rise, absorbing
salt on its way. But the thermal anomaly, due to the horizontal temperature
difference, dominates and forms horizontal convective layers just as with side
wall heating. The thickness of the layers scales as the above formula.

Both of these applications show how horizontal layers can be formed in
double diffusive situations. Layering seems to be a feature in all double
diffusive phenomena. The visual similarity between double-diffusive layers
observed in rocks first suggested that double-diffusive layering may have
important geological consequences.

REFERENCES

Busse, F.H., 1978. Non-linear properties of thermal convection. _Rep. Prog. Phys._ 41, 1929-1967.

Huppert, H.E. and P.F. Linden, 1979. On heating a stable salinity gradient from below. _J. Fluid Mech._ 95, 431-464.

Huppert, H.E. and J.S. Turner, 1980. Ice blocks melting into a salinity gradient. _J. Fluid Mech._ 100, 367-384.

Huppert, H.E. and J.S. Turner, 1981. Double-diffusive convection. _J. Fluid Mech._ 106, 299-329.

Krishnamurti, R., 1973. Some further studies on the transition to turbulent convection. _J. Fluid Mech._ 60, 285-303.

NOTES SUBMITTED BY
Oliver Kerr and
Yoshi-Yuki Hayashi

LECTURE 3

THE COOLING AND CRYSTALLIZATION FROM ABOVE OR BELOW
OF A FLUID WITH A SIMPLE PHASE DIAGRAM

Herbert E. Huppert

Consider a typical phase diagram at constant pressure for a binary system composed of two chemical components A and B (Fig. 1). It shows which phases exist for various temperatures and concentrations, under thermodynamic equilibrium.
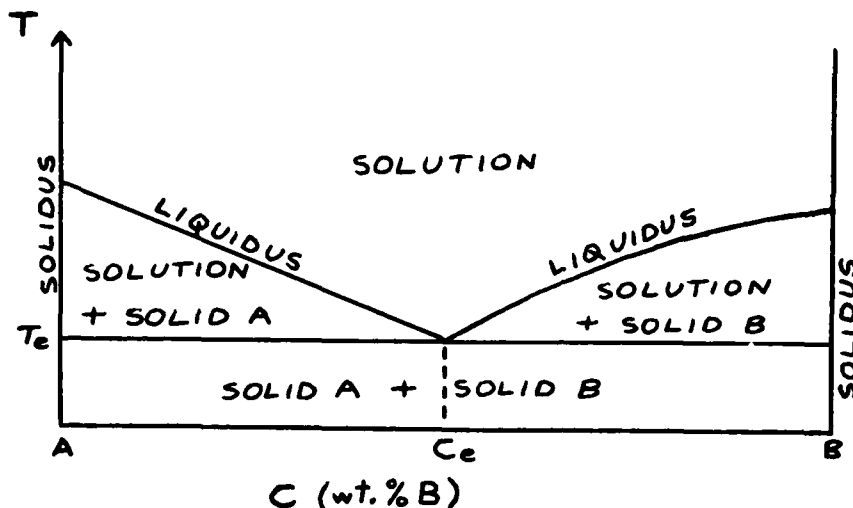
FIGURE 1

Solution temperature T is plotted on the vertical axis while the horizontal axis represents its concentration C, given by weight percent of component B.

Above the liquidus the two components exist in solution; at the liquidus crystallization occurs producing solid A if the concentration of the solution is less than the eutectic concentration ($C < C_e$), solid B if $C > C_e$ and solid of composition C_e if $C = C_e$.

In Figure 1 the solidus lines, which determine the concentration of the solid in equilibrium with the solution, are vertical.

Below the eutectic temperature T_e the system is completely solid. The components A and B may be H_2O and $NaCl$ (in the ocean), Sn and Pb (in metallurgy) or $FeSiO_3$ and Fe (in the earth's core). In each case component B is chosen so that the density of the solution increases with increasing weight percent B. As a specific example we show the phase diagram (Fig. 2) of the water-sodium carbonate system. On this diagram contours of constant solution density are drawn. These contours are almost vertical, illustrating that composition plays a much larger role than temperature in determining the density of the solution. Given that the (initially homogeneous) solution can

be cooled from above or below, and the solution concentration may be less than, equal to or greater than the eutectic concentration, six cases are possible:

COOLING FROM

	ABOVE	BELOW
C C$_e$	T unstable	T stable
	C stable	C unstable
C = C$_e$	T unstable	T stable
	C uniform	C uniform
C C$_e$	T unstable	T stable
	C unstable	C stable

The stabiity of the temperature and concentration profiles of the solution is given above for each case. For example, when a solution of concentration C $>$ C$_e$ is cooled from above the temperature profile is unstable and the concentration profile is stable.

Case 1   Cooling a eutectic solution from below

This situation has been considered by Carslaw and Jaeger (1959) in a chapter entitled "Changes of State". The temperature profile is shown below:
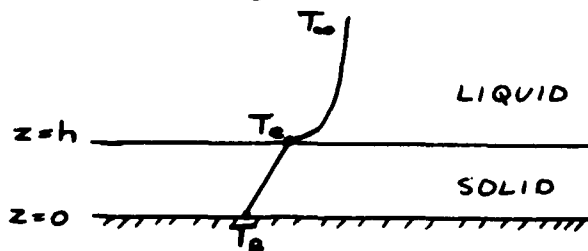
where T is the initial solution temperature, T$_e$ is the eutectic temperature at which solidification occurs and T$_B$ is the imposed temperature at the base of the solution. In the solid and solution, the equations of thermal diffusion are

$$T_t = K_s T_{zz} \tag{1}$$

and

$$T_t = K_m T_{zz} \tag{2}$$

where K$_s$ and K$_m$ are the thermal diffusivities in the solid and solution, respectively.

The interfacial condition is

$$\rho L h_t = k_s T_z \Big|_{z=h-} - k_m T_z \Big|_{z=h+} \tag{3}$$

where h is the (assumed uniform) height of the crystal block, and k$_s$ and k$_m$ are the thermal conductivities of the solid and the melt.

The solution to equations (1) - (3) can be written in the form

$$h = 2 \; \lambda_T \; \sqrt{K_s t} \; , \tag{4}$$

where the thermal eigenvalue λ_T is found from an equation of the type

$$\mathcal{E}_1 (\lambda_T) = 0 \tag{5}$$

In this problem for typical parameter values the rate of crystal growth is controlled by heat diffusion through the solid as indicated in equation (4). The solid interface is stable because there are no compositional effects and no convection here. The theoretical calculations are in very good agreement with the results of several experiments using aqueous $NaNO_3$ which were performed to test the theory.

Case 2   Cooling from below a solution whose concentration is less than the eutectic concentration

In this situation, described in more detail in Worster (1983), solidification produces stable profiles of both temperature and concentration. These profiles are shown below:
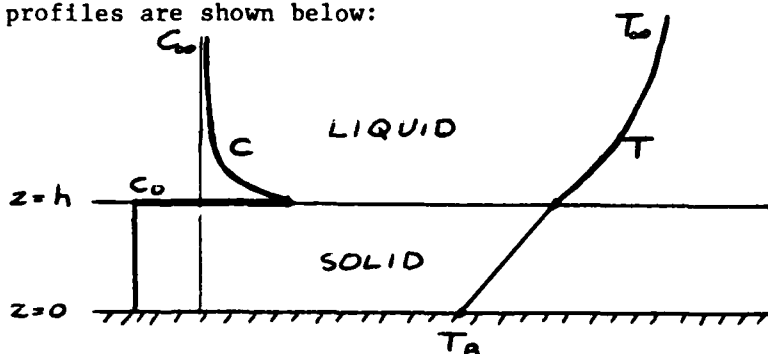
In addition to thermal diffusion equations (1) and (2) in the solid and the solution, we also have the equation for compositional diffusion in the solution:

$$C_t = D \; C_{zz}. \tag{6}$$

Compositional diffusion in the solid is neglected. The interfacial conditions are equation (3) and the additional equations

$$(C + C_0 - C_\infty) \; h_t = -D \; C_z \Big|_{z=h+} \tag{7}$$

and

$$T = - mC + \text{constant}. \tag{8}$$

Equation (7) specifies conservation of mass (assuming the melt and solid densities are equal), and equation (8) specifies thermal equilibrium at the growing interface. The linearization in equation (8) is assumed because it enables a similarity solution of the equations to be found.

The solution can be written in the form

$$h = 2 \; \lambda_c \sqrt{D t} \equiv \gamma_c \, t^{1/2}, \tag{9}$$

where the compositional eigenvalue λ_c is found from an equation of the type

$$\mathcal{E}_2 \left(\lambda_c \right) = 0 \cdot \tag{10}$$

If T_B is sufficiently large, the crystal growth is controlled by compositional diffusion. This solution is morphologically stable if, at the interface,

$$\frac{dC}{dT} > -m \cdot \tag{11}$$

a situation which will occur for T_B sufficiently small for given T_∞ . For example, Figure 3 illustrates the region of morphologically stability in the H_2O - $NaNO_3$ system, for $T_\infty = 15^\circ C$ and $T_\infty = 30^\circ C$. The region of stable growth is seen to be quite narrow. Note that as $C \to 0$, we approach the morphologically stable Case 1, and the range of T_B for which stable crystal growth occurs is rapidly increased.

A series of experiments was performed to determine the growth rate of the dendritic crystal mush produced when T_B was well below the morphologically stable value. The results for one experiment are shown in Figure 4, indicating that the thickness is proportional to $t^{1/2}$, but the growth rate is considerably greater than that predicted for the flat interface controlled by compositional diffusion. The ratio of these growth rates as a function of the initial solution composition C_∞ is plotted in Figure 5.

The reason for the enhanced growth rate is due to the morphological instability, which removes the constraint that the crystal growth is controlled by compositional diffusion. Experimental measurements at undercoolings greatly (about $15^\circ C$) below the morphological stability limit indicate that the dendrites grow with interfacial thermal and compositional values not very different from those in the far-field. In solidifying, the dendrites reject heavy, compositionally enriched fluid which descends into the spaces between the dendrites, where the temperature is lower. Further crystallization can take place in these spaces, which also releases heavy fluid. The overall process suggests that the dendrite growth can be modelled by assuming it is controlled by thermal diffusion only and by using the purely thermal theory outlined in Case 1. Such a procedure leads to results in good agreement with the experimentally determined ones (Fig. 6). Worster (1983) has developed a more complete theoretical model of the process, an abstract of which appears in this volume (page 98).

REFERENCES

Carslaw, H. S. and J. C. Jaeger, 1959. Conduction of heat in solids. Oxford University Press.

Worster, M. G., 1983. Some convective flow problems in geological fluid mechanics. Ph.D. Thesis, University of Cambridge.

NOTES SUBMITTED BY
Ross Kerr and
Lorenzo Polvani
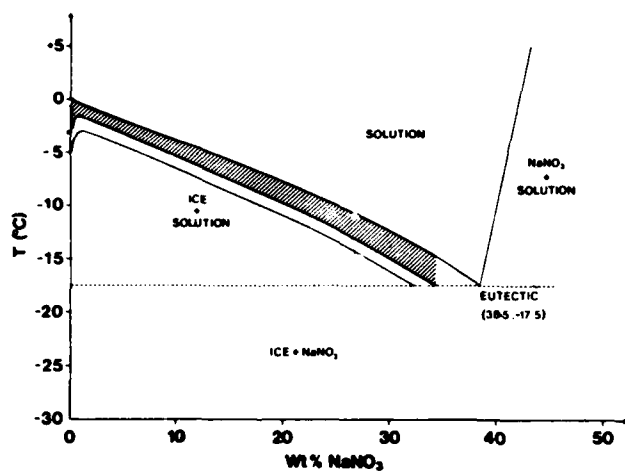
FIGURE 3
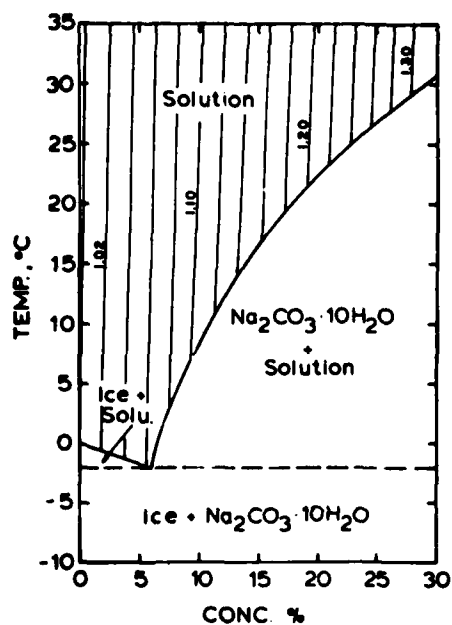
FIGURE 4
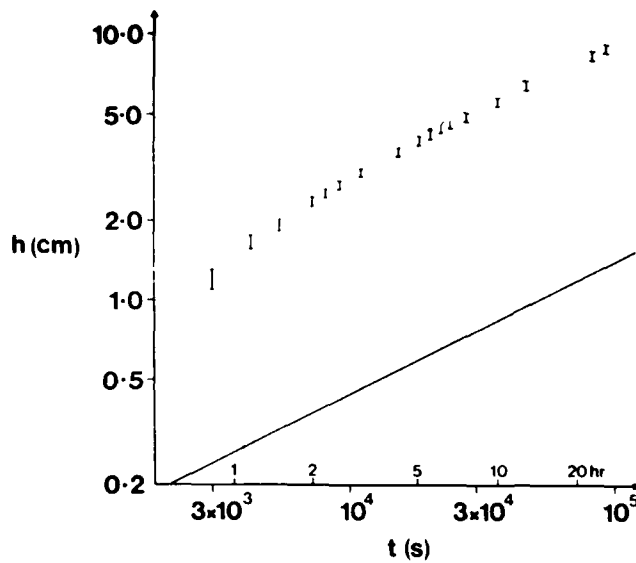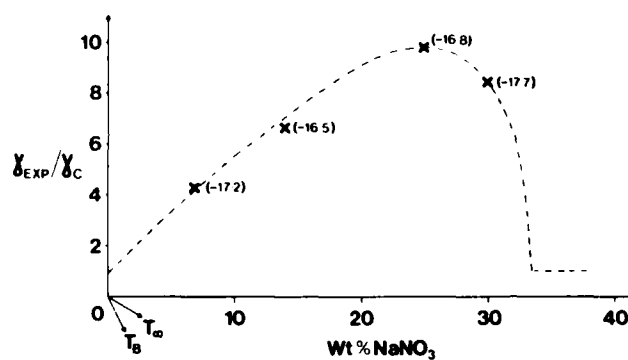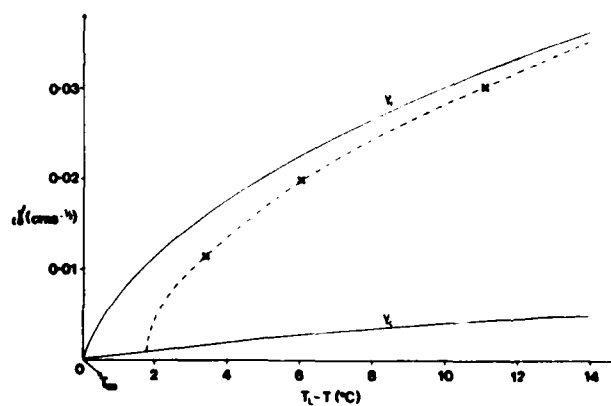
FIGURE 2

FIGURE 5

FIGURE 6

LECTURE 4

REPLENISHED MAGMA CHAMBERS

Herbert E. Huppert

Let us motivate the geological study by a chemical investigation of what happens when we have a layer of hot, heavy, KNO3 below a layer of light, cool NaNO3?

A. The Blue Experiment (Huppert and Turner, 1981)

The hot heavy input of KNO3 is rapidly introduced under the colder and lighter layer of NaNO3 in a perspex tank measuring 40 cm x 20 cm x 40 cm high. The initial KNO3 solution is undersaturated to avoid crystallization in the filling tubes. Note that if the fluids were simply mixed together, the temperature would reach a weighted mean and there would be no crystallization because the solution would be undersaturated in both salts. The diffusivities of the two salts are almost equal.
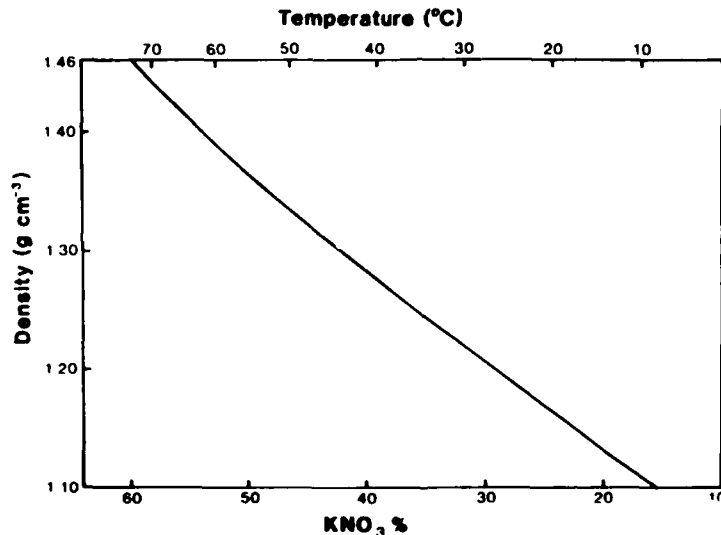
After the initial input phase there is a strong transfer of heat across the interface which drives convection in both the upper and lower layers. Because of the small diffusivity of chemical species, there is very little transport of mass across the interface. Crystallization begins in the lower layer and its density changes, approaching that of the upper layer. The crystals form mainly on the sides and bottom of the box. After a time the densities become equal and the layers overturn, mixing the fluids. On a time scale of days to weeks the crystals gradually dissolve because the mixed solution is undersaturated.

B. __Theory__
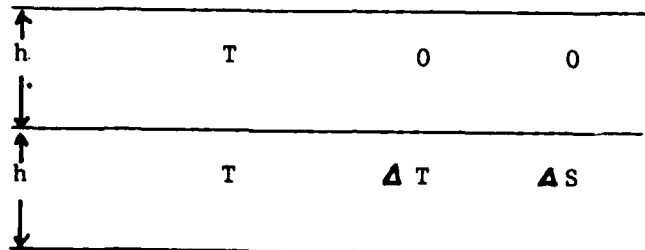
From thermal convection theory we have

$$Nu = c \, Ra^{4/3}$$

$$F_H \propto \Delta T^{4/3}$$

In the double diffusive extension of this argument

$$F_H \propto S\left(\frac{\beta \Delta S}{\alpha \Delta T}, \sigma, \gamma\right) \Delta T^{4/3}$$

where $\dfrac{\beta \Delta S}{\alpha \Delta T}$ is the density ratio across the surface,

σ is the Prandtl number,

and γ is the ratio of the diffusivities.

The salt flux is nondimensionalized by the heat flux and expressed as a bouyancy flux ratio. It should be a function of the same quantities:

$$\frac{\beta \, F_s}{\alpha \, F_T} = g\left(\frac{\beta \, \Delta s}{\alpha \, \Delta T}, \sigma, \gamma\right)$$

While there is no verification of this relation from first principles, an empirical form suggested by Huppert (1971) has been widely accepted

$$f = .32 \left(\frac{\beta \Delta s}{\alpha \Delta T}\right)^{-2}$$

For purely diffusive transport through the interface

$$g = \gamma^{1/2} \qquad \text{for} \qquad \frac{\beta \Delta s}{\alpha \Delta T} > 2$$

The heat and salinity flux fits have been verified on a large scale in Lake Vanda (Huppert and Turner, 1972).

The equation for the temperature of the lower and upper layers are:

$$h_L \dot{T}_L = -A(T_L - T_U)^{10/3}$$

$$h_U \dot{T}_U = +A(T_L - T_U)^{10/3}$$

Latent heat effects are neglected. These equations may be solved to give T_U and T_L as a function of time, physical properties, and initial conditions. The time behavior of temperature is well predicted as shown below.
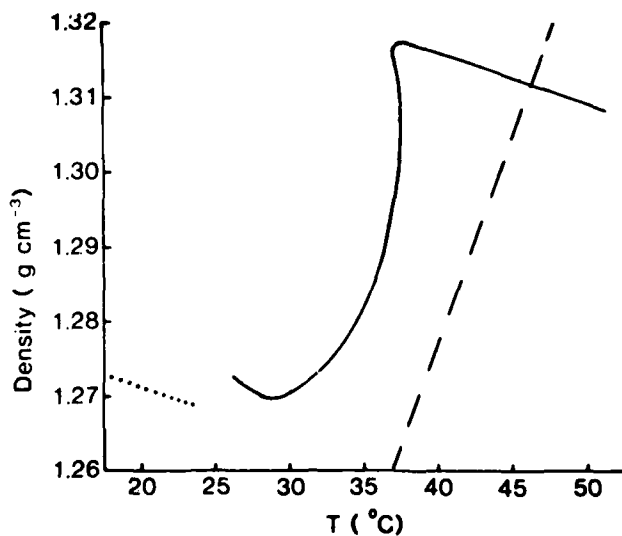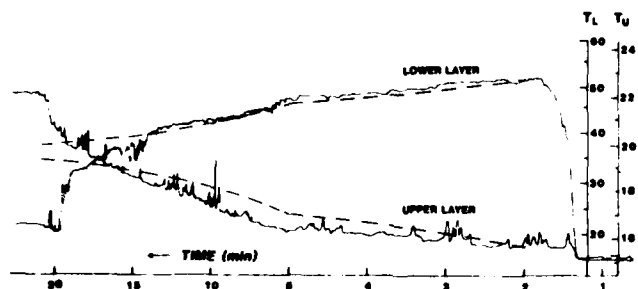
It is not possible to predict the composition or density because in any experiment the degree of supersaturation the system achieves cannot be predicted.

Geological Applications

Consider what happens when there is an influx of magma containing 18% MgO at a temperature of 1400°C into a magma chamber typically at 1200°C. The influx is of order 1% by volume. The change in volume is accomplished either by the expansion of the country rock or by magma forcing its way into fissures (dykes). The hotter, compositionally heavier magma ponds at the chamber base, 2 to 3 km below the volcano.
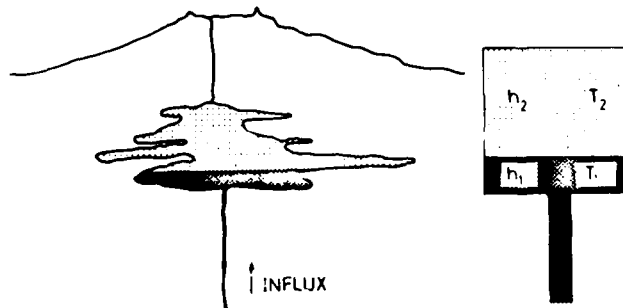
By assuming the idealized geometry on the right, some effects due to geometry may be lost (e.g. rapid sedimentation can occur at sloping wall, the "Boycott Effect"). It will be assumed that the system is always on the liquidus.
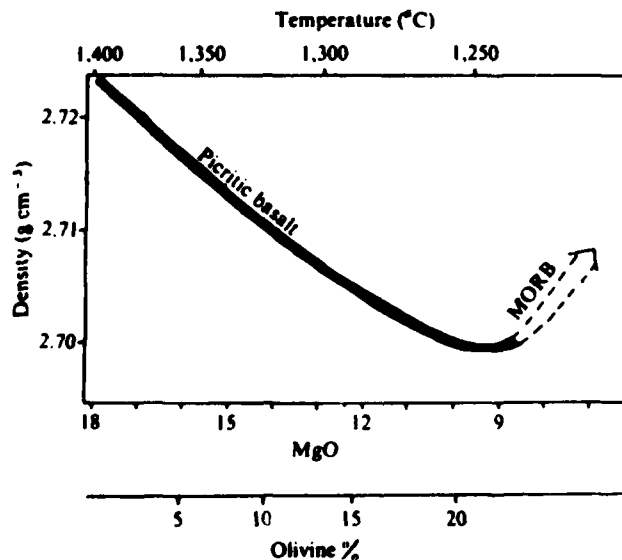
This was a big dispute in the geological community: How was it possible to have an input of 18% MgO and an output of only 9% MgO. The model of Huppert and Sparks (1980a,b), which I will describe, shows how fluid mechanics acts as a buffer between this high input and low output.

In the model there is an input at A which will spread across as a gravity current quite quickly and form two layers. The input will follow the same time history as the experiment, so the same basic calculations can be used. We assume supersaturation and pressure effects are minimal. We do not know how to scale the flux laws, hence we use the same flux laws. It is admittedly a large extrapolation from heated salt to magma, but you either do that or you do nothing and the lecturer said that he gets bored doing nothing.

The salt equations work for magma, but we must now allow for latent heat effects in crystal formation which are much greater in the magma case. Recall that the system is saturated all the way -- it is on the liquidus all the time: if you know the temperature then you know the crystal content. You know all about the system if you know the temperature.

$$h_L \dot{T}_L = -A (T_L - T_u)^{10/3} + \frac{h_L L}{c_\rho} S'(T_L) \dot{T}_L$$

$$h_u \dot{T}_u = A (T_L - T_u)^{10/3}$$

The value of A changes with different magmas.

The additional term in the T_L equation varies in a nonlinear manner. Good applied mathematical tradition would suggest replacing this term by its mean value. Once this function, $(1 - \frac{h_L L}{c_\rho} f'(T_L))$, is approximated by its mean value the thermal evolution equations may be solved analytically to obtain a time/temperature history (a cooling curve). The solution agrees quite well with the numerical solution of the original nonlinear problem.

Dimensional analysis would give you a time scale that would be almost sufficient. This is partly because geologists previously thought magma chambers cooled almost entirely by conduction which would lead to a very long cooling time for a chamber of order Km cubed in volume.
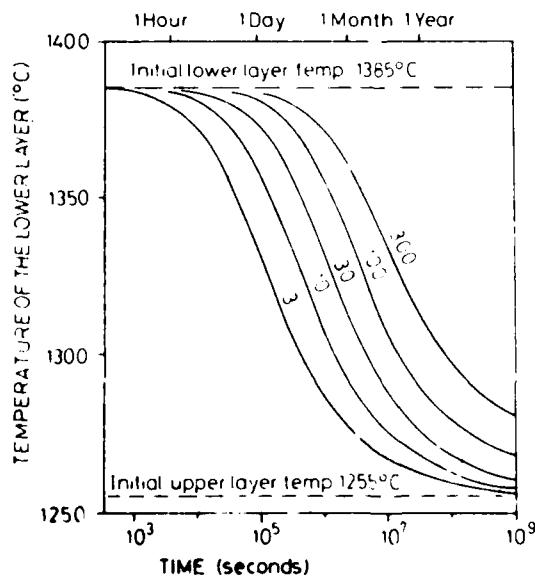
C. Crystal Settling vs Suspension
(Or: A Little Side Step and a yes or no Question)

This is a proper question, no tricks, gravity is there, it is a real fluid, small does not mean not negligible, just small. Imagine you have a steady two-dimensional flow - if you like a series of convective rolls - in a real, incompressible fluid and let us say it is between horizontal boundaries. Place some small spherical particles into this uniform, steady 2-D flow. The particles are heavier than the fluid, they do not interact. There is no brownian motion. They are sufficiently small so they sink like low Reynolds number particles with terminal velocity less than the maximum fluid velocity. If they hit the boundary they stick and effectively disappear. After a sufficiently long time, do they all settle out on the bottom: yes or no?

Vote: Rather evenly divided.

Incorrect Argument for Fallout:

If you calculate the horizontal average of the velocity, the mean vertical fluid velocity is zero, hence the particles, with their positive downward velocity through any horizontal plane, should be able to fall through.

Argument for Suspension:

The correct answer is that some may remain in suspension (Stommel, 1949).

Consider the velocity of the fluid in terms of the stream function $\psi_f(x,z)$

$$q_s = F\left(\frac{\partial \psi_f}{\partial z}\right) - \frac{\partial \psi_f}{\partial x}\right) \qquad \text{with} \quad |\psi_{max}| = 1$$

The particle velocity is clearly equal to that of the fluid in the horizontal and is just the fluid motion plus terminal velocity in the vertical. Thus

$$q_p = \left(F\frac{\partial \psi_f}{\partial z}, -F\frac{\partial \psi_f}{\partial x} - v\right)$$

or

$$\psi_p = F\left(\psi_f + sx\right)$$

where

$$s = \frac{v}{F}$$

This shows that the important and only parameter of the problem is some indication of the terminal velocity of the fluid. The argument goes that $\nabla \psi_f = 0$ because there is a stagnation point in the fluid flow and, for sufficiently small s, $\nabla \psi_p = 0$ and there will be a stagnation point for the particle motion as well. Then, by continuity in x and z, if there is a stagnation point, there must be closed streamlines for the particle trajectories.

What will happen in a container with very large unsteady motion (i.e. turbulent convection)? The equivalent value for s is v /w where v is the Stokes velocity for particles with low Reynolds number, and w is a measure of the rms turbulent velocity of the fluid. If $s \ll 1$ then the particles will remain in suspension while if $s \gg 1$ they will fall out.

There are two things to talk about. First, what happens in the inter-mediate range where s is not so much less than one, and second how does one calculate w?

1) The Intermediate Range of s

For small s all the particles stay up, for large s they all fall down. We are talking in a mean sense about largely unsteady flow. What we have in mind, and what experiments indicate, is that some concentration C = f(z) is produced. In steady state one may use the following eddy diffusivity argument.

The downward flux of particles (= vC) is balanced by an upward flux due to the concentration gradient. Thus

$$v C = - \varepsilon \frac{dc}{dz}$$

where the proportionality constant ε is identified with eddy diffusion and is given by the rms velocity measure times the height of the container.

$$\varepsilon = w h$$

Thus

$$\frac{dc}{dz} = - \frac{v C}{w h}$$

with solution

$$C(z) = C_0 \quad EXP \left\{ - \frac{v}{wh} z \right\}$$

and, by conservation of mass

$$\int_0^h C \, dz = C_{init} \, h$$

Thus if $\frac{v}{wh}$ is very small the concentration profile is flat, while if it is large there is a sharp concentration gradient. Measurements agree well with this kind of argument. In a magma chamber the important result is that during most of the time the crystals are growing and the two layers are stable $s \ll 1$. Thus, the crystals grow in suspension. This can make a difference in crystal composition and size.
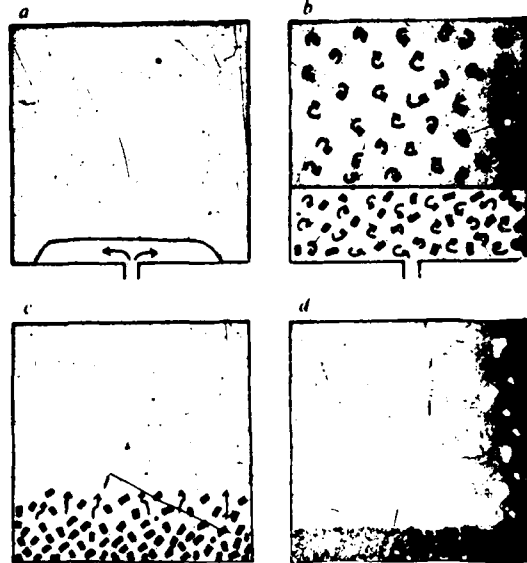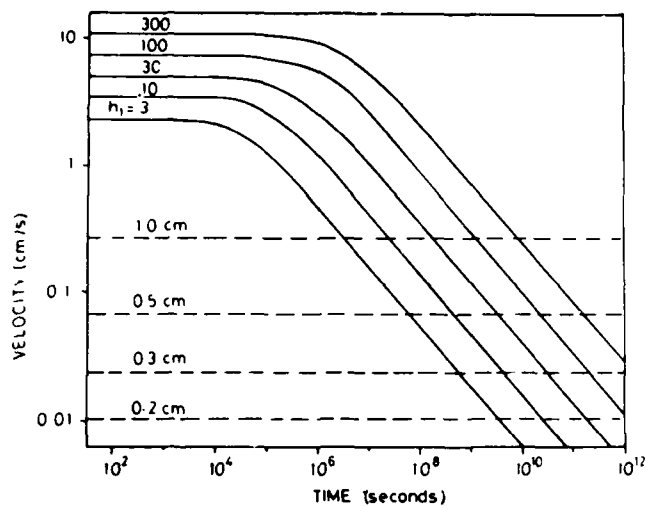
Important Idea:

In the above cartoon we see the olivine crystals forming in turbulent motion. They grow in suspension in equilibrium which makes a large difference in the nickel content (which is only a trace element). Geologists can go out and measure Ni content. The measurements that have been made (and there are only preliminary measurements) are consistent with this idea.

Geological Examples

This situation described can be applied to a number of different geological areas.

1) The above models what happens at midocean ridges.

2) Island of Rhum. The hill of Hallival represents a 90 million year old magma chamber beneath a volcano which has been eroded. Pulses of MgO rich liquid entered the chamber and cooled rapidly forming layers of olivine, the remainder cooled conductively and formed layers as observed.

3) Ophiolites are magma chambers which were part of the sea floor and have come up above land (it is not understood why they did so -- they should have been subducted).

REFERENCES

Huppert, H. E. On the stability of a series of double-diffusive layers.
    Deep-Sea Res. 18, 1005-21.

Huppert, H.E. and R.S.J. Sparks, 1980a. Restrictions on the composition of
    mid-ocean ridge basalts: a fluid dynamical investigation, Nature 286,
    46-48.

Huppert, H.E. and R.S.J. Sparks, 1980b. The fluid dynamics of a basaltic magma
    chamber replenished by influx of hot, dense ultrabasic magma.
    Contributions to Min. and Petrol. 75, 279-289.

Huppert, H.E. and J.S.T. Turner, 1972. J. Phys. Ocean. 2, 456-461.

Huppert, H. E. and J. S. Turner, 1981. A laboratory model of a replenished
    magma chamber. Earth and Planet. Sci. Lett. 54, 144-152.

Stommel, Henry S., 1949. J. of Marine Research 8, 324.

NOTES SUBMITTED BY
Leonard Smith and
John Taylor

LECTURE 5

REPLENISHMENT OF MAGMA CHAMBERS

Herbert E. Huppert

1. <u>The "Green" Experiment</u> (Huppert, Turner and Sparks, 1982)

Let us consider the following extension of the "blue" experiment of Lecture 4. The initial conditions are:

$$
\rho = \begin{array}{l} 28.4 \text{ to } 26.7 \text{ wt } \% \text{ } K_2CO_3 \\ 1.25 \text{ to } 1.28 \text{ g/cm}^3 \text{ (linear gradient)} \\ T = 11.0^oC \end{array}
$$

$$
\rho = \begin{array}{l} 43 \text{ wt } \% \text{ } KNO_3 \\ 1.31 \text{ g/cm}^3 \qquad \text{(slight green dye)} \\ T = 64.6^oC \end{array}
$$

The lower layer cools and crystallizes exactly as in the blue experiment. Associated with the cooling of the lower layer, there is a heat flux passing through the density gradient in the upper layer, and so layers are produced, as explained in Lecture 2. This stable stratification inhibits the rise of the overturning green fluid which occurs only in the lower part of the container.

(green) convective motion (thermal and compositonal)

crystals (KNO_3)
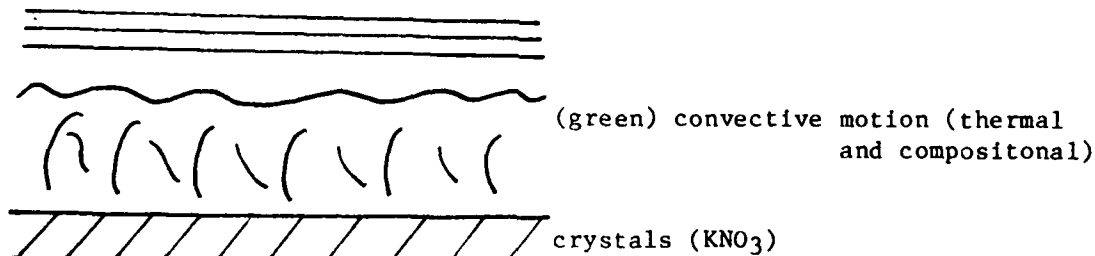
The upper (regular) stratification arises from the horizontal thermal gradient between the container (11^oC) and the room (20^oC).

2. <u>The "Red" Experiment</u>

   a) <u>The Experiment</u>

As another extension of the "blue" experiment, the "red" experiment consists in introducting slowly (0.86 cm^3/s) hot, heavy fluid (KNO_3) at the base of a uniform lighter and colder $NaNO_3$ solution. Explicit initial conditions are:

$$
\begin{array}{l} 38 \quad \text{wt } \% \quad NaNO_3 \\ T = 8.5^oC \\ \rho = 1.31 \text{ g/cm}^3 \end{array}
$$

$$
\begin{array}{l} \text{input } (0.86 \text{ cm}^3/s) \\ \text{of } 46 \text{ wt } \% \text{ } KNO_3 \\ T = 65^oC \\ \rho = 1.36 \text{ g/cm}^3 \end{array}
$$

One observes quenching of hot fluid and immediate crystallization, which deposits crystals in a heap on the container bottom, and releases light fluid (colored in red) which mixes with the upper fluid, in a quasi-steady way. After a few minutes, the system looks like:

crystals (porous medium)
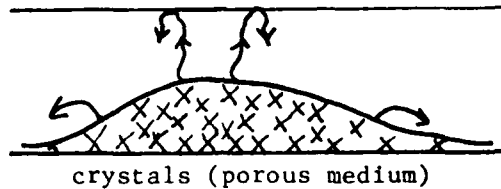
After a longer time, to the side of the heap a horizontal regular layer of crystals and red liquid has been formed. On those parts of the container the conditions are the same as in the blue experiment (heavy and hot under cold and light fluid), and so the same processes are involved.

b) Black Smokers

An interesting investigation is to change the motivation of the experiment and to simulate some aspects of "black smokers". These form at mid-ocean ridges, where hot water ($\sim 350^{\circ}$C) is emitted from the seafloor. This outflow deposits crystals and forms chimneys, whose growth rate can be as large as 40 cm per day. Their growth stops as the site moves away from the ridges. It has been possible to simulate this growth in the "red" experiment. The growing of a crystal tower like a black smoker appeared to be initiated by the withdrawal of a small amount of fluid from the top of the tank.

fluid rising

tower

heap

red (hot heavy KNO_3)

input
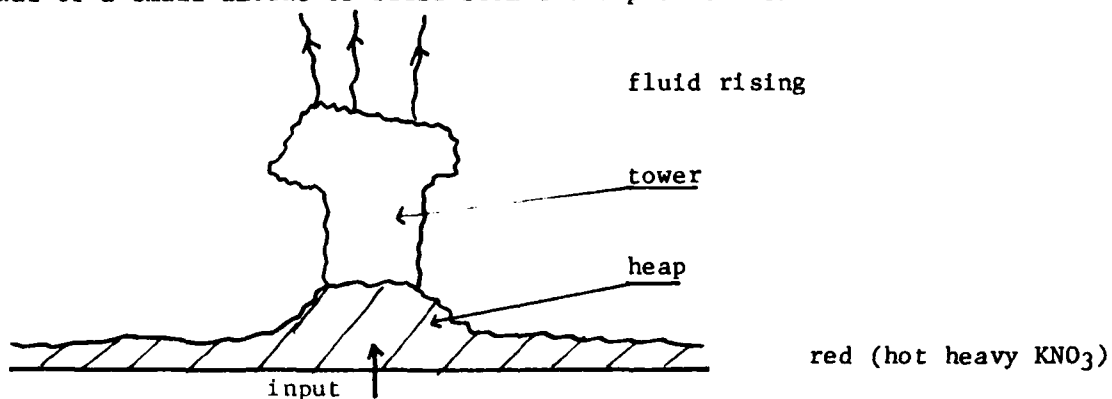
The question of how the growth of this "black smoker" is initiated by the withdrawal of fluid from above has not yet been satisfactorily answered.

3. Magma Chambers near Subduction (Huppert, Sparks and Turner, 1982)

The "blue" experiment supposedly modelled the mid-ocean ridge magma chambers. Let us now consider magma chambers near subduction (for example in Japanese volcanoes).
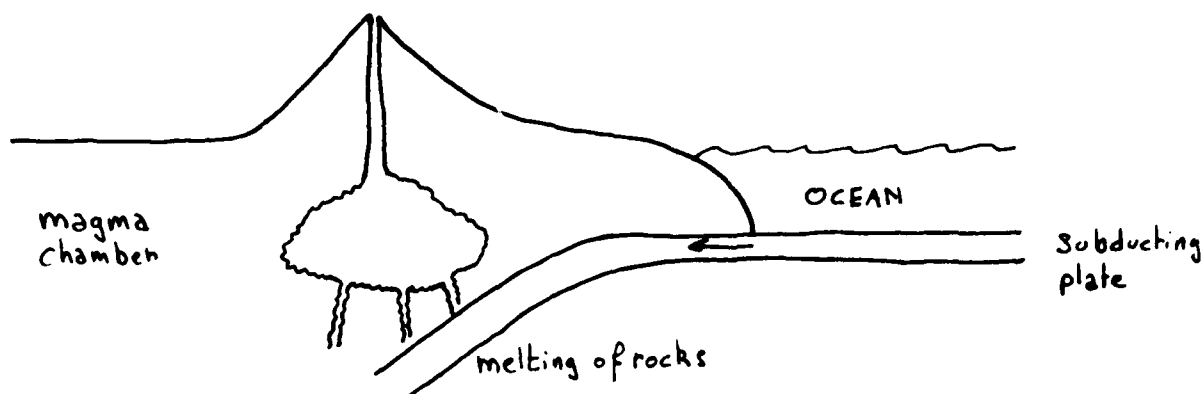
The magma that enters these chambers has water dissolved in it. Consider the magma family known as the calcalkaline association:

<div>

Heavy ($\sim 2.7 \text{g/cm}^3$)   BASALT
Mafic ($SiO_2 \sim 45\%$)
Low Viscosity ($\sim$ 10 $\text{cm}^2\text{sec}^{-1}$)

gradual variation through

                                     ANDESITE

                                     DACITE

Light ($\sim$ 2.3 g/cm^3)

Silicic ($SiO_2 \sim 75\%$)   RHYOLITE

Viscous ($\sim 10^6$ cm^2s^{-1})

</div>

Some samples, erutpted from these volcanoes surprisingly appear to contain different magmas intimately mixed. Furthermore, some thin sections of such samples showed that there is very little diffusion between such substances, although they were in very intimate contact. The idea for explaining such a situation is to suppose that the intrusion of heavy inviscid fluid contains dissolved water (0 to 5% in weight)

magma chamber
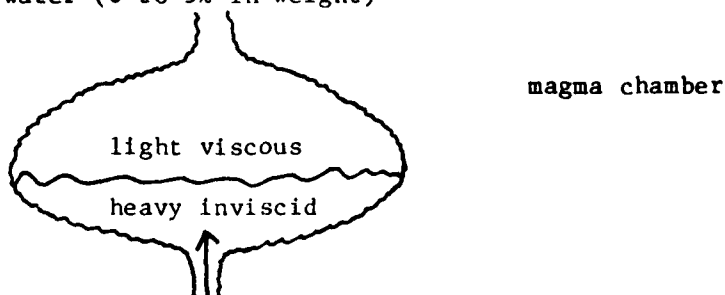
Consider a parcel of fluid containing some water. As the melt cools it crystallizes, and the crystals formed are anhydrous. Thus the water concentration in the remaining fluid increases and eventually saturates. At the relevant temperature and pressure, it comes out as water vapor, which is very light, and so the bulk density can be reduced by an enormous amount.

Quantitatively, let N be the total weight fraction of water in the system, let n be the saturated fraction of dissolved water. Considering water vapor as a perfect gas,

$$\frac{1}{\rho_{bulk}} = (N-n)\,\frac{RT}{P} + \frac{1 - (N-n)}{\rho_{melt\ +\ crystals\ +\ dissolved\ water}} \qquad (0 \leqslant n \leqslant N)$$

for N = n, this involves

$$\rho_{bulk} = \rho_{melt\ +\ crystals\ +\ dissolved\ water}$$

n is a known function of P and T, well fitted analytically by

$$n = S(1-X)P^{1/2}$$ where X is the weight fraction of the crystals. X = X(T) is well fitted by:

$$T = (1100 - 200\,X) + 273$$

and S is a constant. So, one gets the density curves at P = 5 kbar.

a
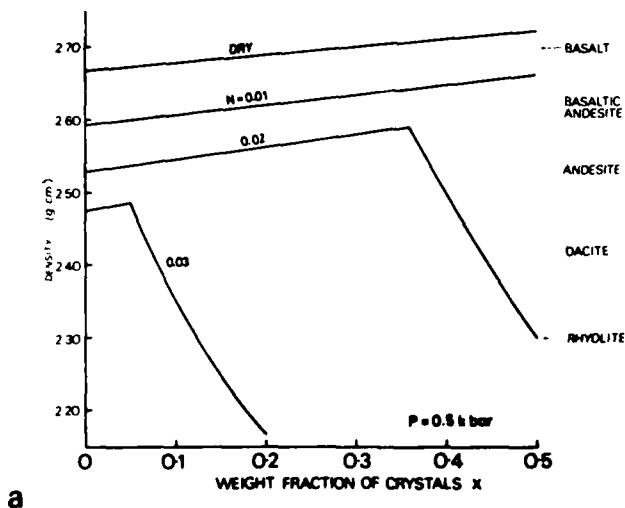
This is applicable even when some crystals remain in turbulent suspension. So, one gets the sequence:

    - influx at the base

1)   - cooling and crystallization (crystals remains in suspension)
2)   - water saturates and comes out of the solution (probably nucleating on
      crystals), decreasing the density of the lower fluid.
3)   - sudden and violent overturning of the lower layer, with a massive
      release of gas.
4)   - eruption when the internal pressure build-up drives the outflow from
      the vent.

A modelization of these processes has been made using a chemical reaction
between $NaCO_3$ or K_2CO_3 with HNO_3 to release small bubbles of CO_2
(Turner, Huppert, Sparks, 1983). A film of an experiment was shown.

    The initial conditions were:

$$NaNO_3 + Na_2CO_3 \text{ aqueous solution}$$
$$= 1.268$$
$$T = 11^oC$$

_____

$$4.8\,\ell. \text{ KNO}_3 \text{ aqueous solution}$$
$$= 1.299$$
$$T = 55^oC$$
$$300 \text{ ml of } 70\% \text{ HNO}_3$$

    Cooling and crystallization took place in the lower layer, producing
strong thermal convection in both layers (as in the "blue" experiment).

    As the density in this layer approached that of the upper layer, the
interface rapidly broke down, the lower fluid rose and bubbles of CO_2 were
produced by reaction of HNO_3 with Na_2CO_3. This gas facilitated the
convection and the mixing of the fluids. The eruption was modelled by closing
the top of the tank by a domed lid, having a small vent at its top. As CO_2
was released, the pressure increase in the tank forced the fluid-gas mixture
through the vent, producing a very nice eruption.

4. The "Yellow" Experiment (Huppert, Sparks and Turner, 1983)

    A last extension is to consider the layers of fluid to have very
different viscosity. The experimental situation was the following:

Viscous fluid (glycerine)
(Yellow)
_____
KNO_3 solution
(blue)

Here, the released blue fluid is taken up into the yellow one immediately, and
is drawn out into long streaks. Then one again gets cooling and crystalliza-
tion within the carried-up streaks.

    The mixing of the two fluids is very small compared to that in the blue
experiment, where the two viscosities were of the same order of magnitude. At
the interface, only convection is seen (no diffusion of blue into yellow
fluid).

- 34 -

Laminar plumes go up to the top of the container, and then one has aqueous KNO_3 over glycerine, and so one can observe salt-glycerine fingers descending from the upper layer (after 45 minutes). After a long time, there remain large unsteady motions in the container. So, this experiment shows that the difference in the viscosities of the two fluids plays a significant role in the processes that take place.

In particular, if $\nu_U \ll \nu_L$, one has to wait before lower fluid rises, and if $\nu_U \gg \nu_L$, lower fluid rises immediately. This can be understood as follows:

If $\nu_U \ll \nu_L$, the lower fluid sees a "stress-free boundary" at the interface and so horizontal movements are allowed and mix the fluid within the layer. If $\nu_U \gg \nu_L$, the lower fluid sees a "rigid boundary" and cannot move horizontally. If lighter, it can then rise.

REFERENCES

Huppert, H.E., R.S.J. Sparks, J.S. Turner, 1982. Nature 279, 554-557.

Huppert, H.E., J.S. Turner, R.S.J. Sparks, 1982. Earth Planet. Sci. Let. 57, 345-357.

Huppert, H.E., R.S.J. Sparks, J.S. Turner, 1983. Earth Planet. Sci. Let. 65, 377-381.

Turner, J.S., H.E. Huppert, R.S.J. Sparks, 1983. J. Volcanol. and Geotherm. Res., 16, 263-277.

NOTES SUBMITTED BY
Bruce Bayly and
André Gorius

LECTURE 6

COOLING AND CRYSTALLIZING FROM A SIDE WALL

Herbert E. Huppert

In Lectures 3, 4 and 5 we were mainly concerned with the one-dimensional features of multi-component convection. Basically the gradients of the fields are vertical and physical quantities are essentially functions of only time and the vertical coordinate z. In the first half of this lecture we will deal with cooling and crystallizing from a side wall, where the situation is inevitably two dimensional.

Flow with a Gradient of One Component

As an introduction to the subject, let us consider the case of cooling (heating) alone (Fig. 1). The temperature is

Figure 1   Figure 2
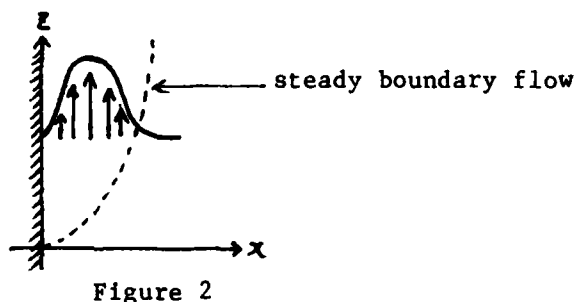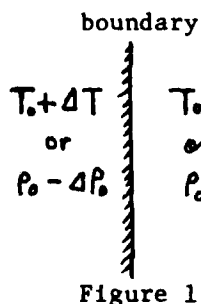
given at the boundary of a semi-infinite reservoir. The equations governing a steady state flow are as follows:

$$\psi_z \, \psi_{xx} - \psi_x \, \psi_{xz} = -g'\phi - \nu \, \psi_{xxx},$$

$$-\psi_z \, \phi_x + \psi_x \, \phi_z = D\phi_{xx},$$

where ψ is the stream function, ϕ is a density deviation normalized by $\delta\rho$ (i.e. $\phi = \dfrac{\rho_o - \rho}{\delta\rho}$), g' is the reduced gravity ($= g\dfrac{\delta\rho}{\rho_o}$), ν is the viscosity and D is the diffusivity. As we are concerned with a boundary layer, the z derivatives of friction and diffusion terms were dropped. The boundary conditions are

$$\psi = \psi_z = 0 \quad at \quad x = 0,$$

$$\psi_x, \phi \rightarrow 0 \quad as \quad x \rightarrow \infty.$$

These equations can be solved in terms of a similarity solution

$$\eta = 2^{-1/2}(ScG)^{1/4} (x/L) (z/L)^{-1/4},$$

$$\Psi = 2^{3/2}D(ScG)^{1/4}(z/L)^{3/4} f(\eta),$$

$$\phi = g(\eta),$$

where $Sc = \nu/D$,   Schmitt number

$G = g'L^3/\nu^2$,   Grashof number

L = some length scale

This gives equations for f and g:

$$g" + 3fg' = 0$$

$$Sc(f'''+ g) + 3ff" - 2f'^2 = 0$$

$$f = f' = 0 \text{ and } g = 1 \text{ at } \eta = 0$$

$$g, f' \longrightarrow 0 \text{ as } \eta \longrightarrow \infty$$

The Grashof number is the important parameter which is the measure of the forcing. It is similar to the Rayleigh number $Ra = g'L^3/D\nu$ but D is replaced by ν. In the case of vertical convection thermal diffusion reduces the buoyancy forcings while in the side wall heating case thermal diffusion plays a more positive role. The Schmitt number is identical to the Pandtl number σ. A constant η line (which is also a constant density line) is shown as a dashed line in Fig. 2.

Typical numerical solutions for various values of Sc are shown in Figs. 3a and 3b. One of the notable points is that the profiles of scaled velocity $u^* = u \, L/\nu \left(\dfrac{Sc}{G} \; \dfrac{L}{4z} \right)^{\frac{1}{2}}$ vary significantly with Sc, while the profiles of density
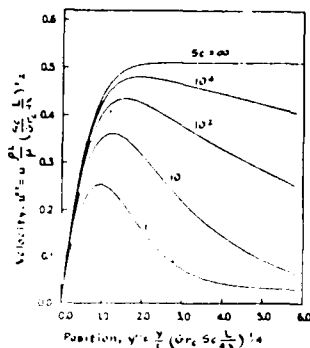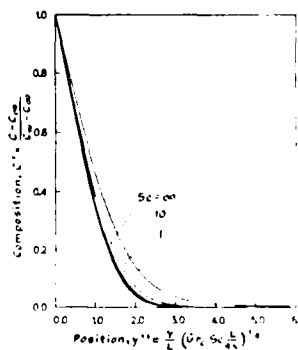
Figure 3a   Figure 3b

(or of temperature) do not. High Sc (or large value of ν) causes penetration of upward motion into the outer region due to the larger viscous effect. The ratio of the scale of the velocity variation and density variation is given by $\sqrt{Sc}$.

In a magma chamber, ν is a highly dependent variable of temperature so that significant modification of the above features is expected. The order of the viscosity variation may be by a factor $10^4 - 10^5$ between the wall of the chamber and the interior in either direction. The following temperature dependency of viscosity was used by A. McBirney and his coworkers to calculate the effect of viscosity variation.

$$\mu = \mu_\infty \exp \{-\ln (\mu_\infty/\mu_w)\phi\},$$

Here μ_∞ and μ_w are the viscosities far from the wall and at the wall respectively.

The Schmitt number and Grashof number are scaled using the ad hoc viscosity measure

$$\mu = (\mu \text{ smaller})^{4/5} (\mu \text{ larger})^{1/5}$$

where $\mu_{smaller}$ is the smaller of μ_∞ and μ_w and μ_{larger} the larger.
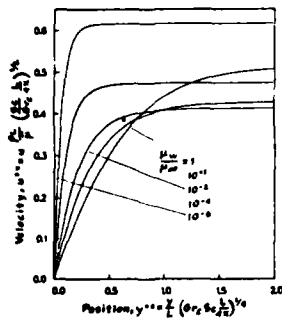
Figure 4a
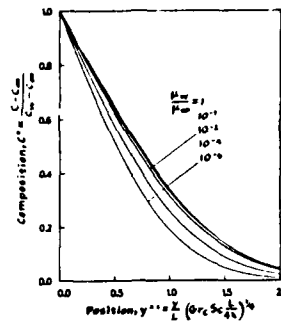
Figure 4b
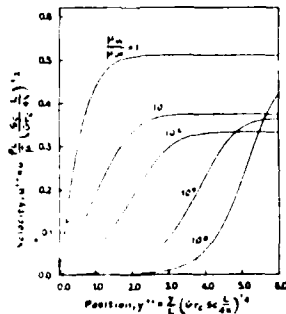
Figure 4c
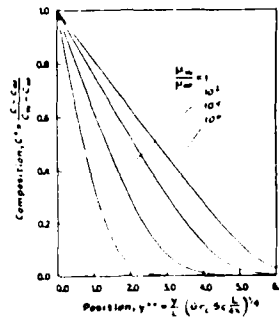
Figure 4d

The corresponding similarity solutions are summarized above. Figs. 4a and 4b show the case where the viscosity at the wall is smaller than the viscosity at infinity, while Figs. 4c and 4d show the opposite case. In all these cases the Schmitt number is very large. When the viscosity at the wall is small compared to the interior the compositional profile (or temperature profile) is not affected significantly by the viscosity variation. On the other hand, as shown in Fig. 4d, the highly viscous layer at the wall pushes out not only the velocity profile but also the compositional profile.

So far we have only considered steady flows, but as the flow comes up the boundary layer it becomes unstable because of the increase in local Grashof number which is roughly similar to the square of the Reynolds number (Fig. 5).

The critical value of G is $O(10^6)$ that means $Re = O(10^3)$. Experiments with constant viscosity show that the wave caused by the instability grows with height and eventually becomes "turbulent" when

$$G = O(10^9) \qquad \text{for } \sigma = O(1)$$

and

$$G \sim 10^{8\,2} \qquad \text{for } \sigma \gg 1$$

$$L \rightarrow G \equiv \frac{g' L^3}{\nu^2}$$
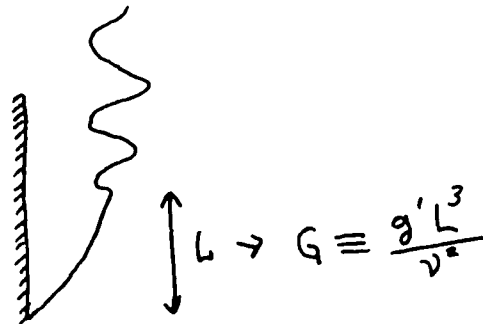
Figure 5

(the validity of this last relationship is not on such a sound base). When considering the turbulent regime McBirney used an eddy viscosity whose form has been found by experiments to be as follows:

$$\frac{\nu \text{ effective}}{\nu \text{ molecular}} = 1 + 0.4 x_T \left(1 - e^{-\gamma x_T}\right)$$

where

$$\gamma = 0.0017$$

$$x_T = \frac{x}{\nu_{\text{molecular}}} \left(\frac{\tau_w(z)}{\rho}\right)^{\frac{1}{2}},$$

τ_w is the wall stress.

This formula is consistent with mixing length theory, since ν effective is proportional to x (distance from the wall) when x is large. For the case of viscosity with temperature dependence the effect of turbulence can be estimated by using the above empirical formula. The results are shown in Fig. 6 for a large value of Sc and a viscosity which has a large value near

the wall ($\mu_w = 10^4 \mu_\infty$). Here x is the vertical distance along the wall.
A larger value of x/L means more intensive turbulent mixing. Turbulence
does not play any significant role near the wall, while it affects the profile
of the inner region. This separation occurs when $Sc > G^{1/3}$.
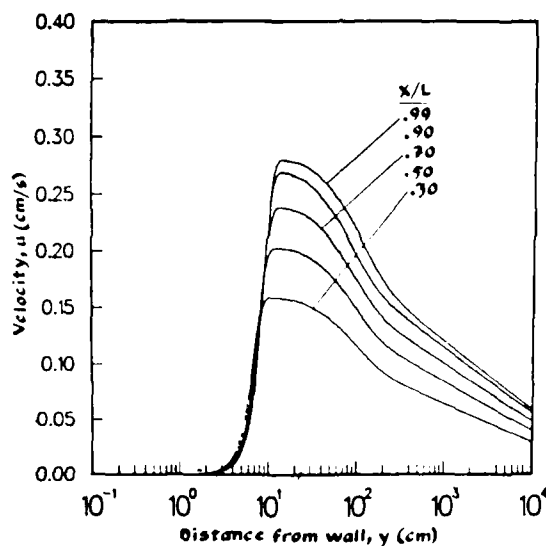
Figure 6

Flow with Both Temperature and Component Gradients

When the density is changed by the effects of more than one component the
structure of the flow is determined by their competition. Since the thermal
diffusivity τ is generally much larger than the compositional diffusivity
D, the flow will be upward near the wall and downward in the interior for
cooling and crystallizing from the side. This can be visualized in laboratory
experiments (Fig. 7).
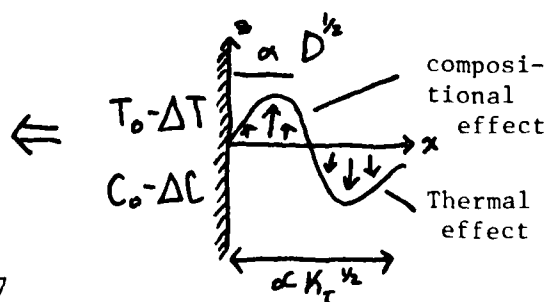
Figure 7

The simple similarity solution discussed for one component convection is not now applicable because of the different effects. When the compositional effect is dominant, the flow will be totally upward (region (A) of Fig. 8). When the thermal effect is dominant the flow will be totally downwards (region (C)). There is also an intermediate parameter region (region (B) or Fig. 7, right) where both effects are comparable. The hatched region in the diagram indicates the ranges of parameters found in magma chambers and showing that both effects are important. Even if varying viscosity is taken into account, the geological importance of competing effects is still unaffected.
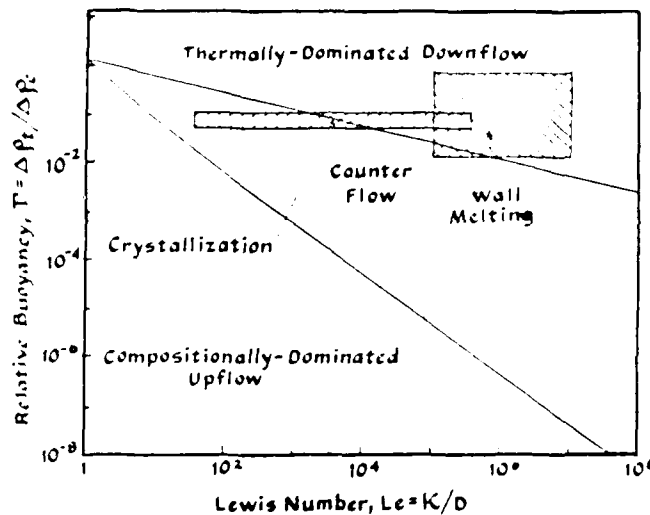
Figure 8

Although no uniformly effective similarity solution can be found for region (B) when $D \ll K \ll \nu$ then the regions dominated by temperature, solute and viscosity are distinct and solutions in each can be matched. Some examples of solutions are shown in Fig. 9 in which the effects of variable viscosity are also included. It indicates that compositional upflow is basically independent of turbulence while the thermal downflow is noticeably affected. As a magma chamber is a finite box it is expected to
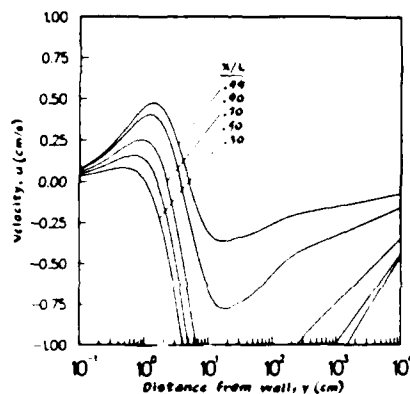
Figure 9

cause another effect, vertical stratification. This effect has been visualized in experiments. The upward flux of relatively fresh water caused by crystallization reaches the top of the tank and moves outwards so that a vertical compositional gradient is set up. In a stratified fluid the convection forms a layered structure (see Lecture 2, p. 8).

Convection from a Point Source

In the previous lectures the driving forces were mainly uniform horizontally. In this section we will consider, paraphrasing the approach of Turner (1979), the fluid dynamical phenomena due to replenishment by a hot light magma, where convection is driven by a point source. We will deal mainly with the motion of buoyant plumes which do not have initial momentum, but the case of buoyant jets will be briefly mentioned.

When Re $\gg$ 1 the fluid motion of the plumes becomes independent of molecular properties (i.e., K_T, ν) which permits extrapolation of experimental data into various ranges of parameters.

The important quantities which characterize plumes are:

1) Specific buoyancy flux $F = \int wg'dA \Big|_{source} = L^4 T^{-3}$

   where $g' = g \dfrac{\Delta \rho}{\rho} = g \dfrac{\rho_\infty - \rho}{\rho_\infty}$

2) Specific mass flux $Q = \int wdA \Big|_{source} = L^3 T^{-1}$

3) Specific momentum flux $M = \int w^2 dA \Big|_{source} \equiv L^4 T^{-2}$

Although w (vertical velocity), b (radius of plume) and $\Delta \rho$ (density difference) are highly time dependent variables, it is possible to regard them as functions of z and r by the use of temporal averaging (Fig. 10). Typically, experiments show that the averaged velocity has the form

$$w = w(z)\, e^{-r^2/b^2}$$

$$b = b'z$$
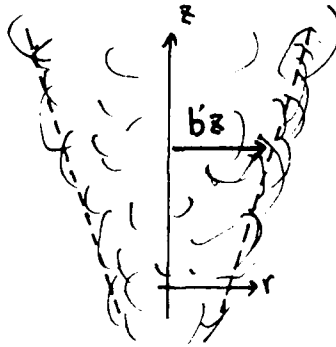
Figure 10

Usually a top hat profile is assumed for w when performing any anlaysis. The plume is also found to be approximately conical, so b is assumed to be a linear function of z. The evolution of the plume is caused by turbulent entrainment of the environmental fluid at a rate which can be assumed to be proportional to the mean upward velocity (entrainment rate = α). These assumptions were first explored by Batchelor (1954).

The equations for the plume evolution are as follows:

Conservation of mass

$$\frac{d}{dz}(b^2\bar{w}) = 2\alpha b\bar{w},$$

Conservation of momentum

$$\frac{d}{dz}(b^2\bar{w^2}) = b^2 g',$$

Buoyancy

$$\frac{d}{dz}(b^2\bar{w}g') = -b^2\bar{w}N^2,$$

where

$$\bar{w}b^2 = \int_0^\infty w r\, dr,$$

$$\bar{w^2}b^2 = \int_0^\infty w^2 r\, dr,$$

$$N^2(z) = -\frac{g}{\rho}\frac{d\rho}{dz}.$$

If there is no stratification ($N^2 = 0$) the buoyancy flux F is constant with height, and the solution is:

$$b = \frac{6}{5}\alpha z$$

$$\bar{w} = \left(\frac{5}{6}\alpha\right)(0.9\alpha F)^{\frac{1}{3}} z^{-\frac{1}{3}}$$

$$g' = \frac{5}{6\alpha} F(0.9\alpha F)^{-\frac{1}{3}} z^{-\frac{5}{3}}$$

The rate of spreading of the plume depends on the buoyancy and momentum flux at the source and on stratification

$$\frac{db}{dz} = 2\alpha - \frac{1}{2}bg'/\bar{w^3}$$

$$= 2\alpha \text{ when } g' = 0 : \text{ nonbuoyant jet}$$

$$= \frac{6}{5}\alpha \text{ when } N = 0 : \text{ no stratification}$$

A number of experiments indicate the value of α as

$$\alpha = 0.1 + 0.02$$

This is valid for Re $\gg$ 1. α = 0.1 is the most used while α = 0.08 seems to be the "best". As Re decreases α does have some variation.

When the ambient fluid is stratified a buoyant jet will entrain heavier fluid and will eventually reach a level where it spreads out. Because of entrainment the density of this level is much greater than the initial jet.

It can be shown that:

the height where there is no buoyancy ($g' = 0$) is $z = 1.04 \, \alpha^{-1/2} L_{FN}$,

the height where the plume stops rising ($w = 0$) is $z = 1.37 \, \alpha^{-1/2} L_{FN}$,

where $L_{FN} = F^{1/4} \, N^{3/4}$. It has been determined experimentally that the height of the spreading out of the plume is 3.47 L_{FN} which is lower than the height of $w' = 0$. These results are applicable over a large range of scales as shown in Fig. 11.
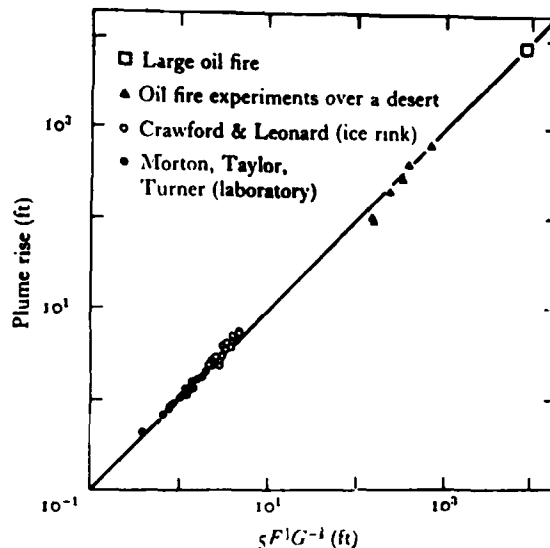
Figure 11

Finally, if momentum is added at the source to the buoyant jet, the plume can rise to a lower height. This is because the extra momentum spreads the plume and it entraps more fluid. Thus the plume becomes denser more quickly and spreads out at a lower level.

REFERENCES

Batchelor, G.K., 1954. Heat convection and buoyancy effects in fluids, Quart. J. Roy. Met. Soc. 80, 339-358.

Turner, G.K., 1979. Buoyancy Effects in Fluids. Cambridge University Press.

NOTES SUBMITTED BY
Yoshi-Yuki Hayashi
and Oliver Kerr

LECTURE 7

PHYSICS OF ERUPITVE COLUMNS

R. Steven J. Sparks

Figure 1 illustrates the fundamental fluid mechanical processes which occur during an explosive volcanic eruption. Such an eruption begins at depth in a magma chamber in the earth's crust. The magma can contain several weight percent dissolved volatiles (mostly CO_2 and H_2O) under pressure. However, at some height (called the exsolution height), the pressure will be insufficient to keep these volatiles dissolved, and they will exsolve to form small bubbles of vapour gas in the magma.

The initial rise of magma from the magma chamber to the volcano is viscous (low Reynolds number) flow. Eventually, however, the magma reaches the fragmentation level where the pressure is sufficiently low that the bubbles burst, resulting in the transition to high Re flow. This flow is entrains solids, formed either by fragmentation of the magma (and crystals) or torn from the walls of the vent (xenoliths). The exit velocity of this mixture of volatiles, and solids, as it leaves the vent of the volcano, is typically several hundred metres per second. This mixture is usually denser than the atmosphere. The rise of the volcanic cloud is initially dominated by its momentum. In this gas thrust region, the cloud entrains surrounding air and decelerates rapidly. The magma in the cloud is quenched to form ash particles and pumice. After the cloud has risen a short distance (typically 1 km), it has lost most of its momentum. However, heating of the entrained air by the hot ash particles rapidly makes the cloud less dense than the atmosphere, enabling it to rise buoyantly for many kilometers as a turbulent plume (see LECTURE 6). It eventually overshoots its height of neutral buoyancy (H_N) due to its momentum and continues to rise until its momentum is zero (H_M). At this point, it is negatively buoyant and it falls before spreading out at an intermediate height H_F.

Wilson et.al. (1978) have modified the work of Morton, Turner and Taylor (1956) to obtain the formula

$$H_M = 5.77(1+n)^{-3/8} \left[QS(\theta_E - \theta_a) \right]^{1/4} \tag{1}$$

where n is the ratio of the environmental to adiabatic lapse rate, Q is the volume flux, S is the specific heat and θ_E and θ_a are the eruption and atmospheric temperatures. This agrees with all measured volcanic eruptions to date (Figure 2; where S79 and MSH indicate the eruptions at Soufriere on April 26, 1979 and the Mount St. Helens on May 18, 1980).

Detailed calculations of the Soufriere eruption can be made for comparison with a movie taken of the eruption. If u_c is the cloud velocity, h is the height of the plume, and K is the entrainment constant (≈ 0.092), the ratio of the plume and atmospheric densities (q) at each height is given by the equation (Sparks and Wilson, 1982):

$$(1 - q) = \frac{u_c^2}{\lambda_q} \left(\frac{1}{c} \frac{dc}{dh} + \frac{1}{u_c} \frac{du_c}{dh} + \frac{11.7K}{h} \right) \tag{2}$$

Umbrella Region
and dispersed
cloud
$(10^2-10^6 \ km^2)$

Convection Plume
(100 - 1000 m)

Gas Thrust Region
(100 - 1000 m)

Vent (3-300 m)
Exit Velocity
(100-600 m/sec)

High Re
Pipe Flow (10^{10})

Fragmentation Level
(depth, 0-3 km;
pressure, 10-250 bars;
flow rates, $10^2 - 10^8 \ m^3/sec$)

Exsolution level

Viscous Low
Re Flow
(≈ 1)
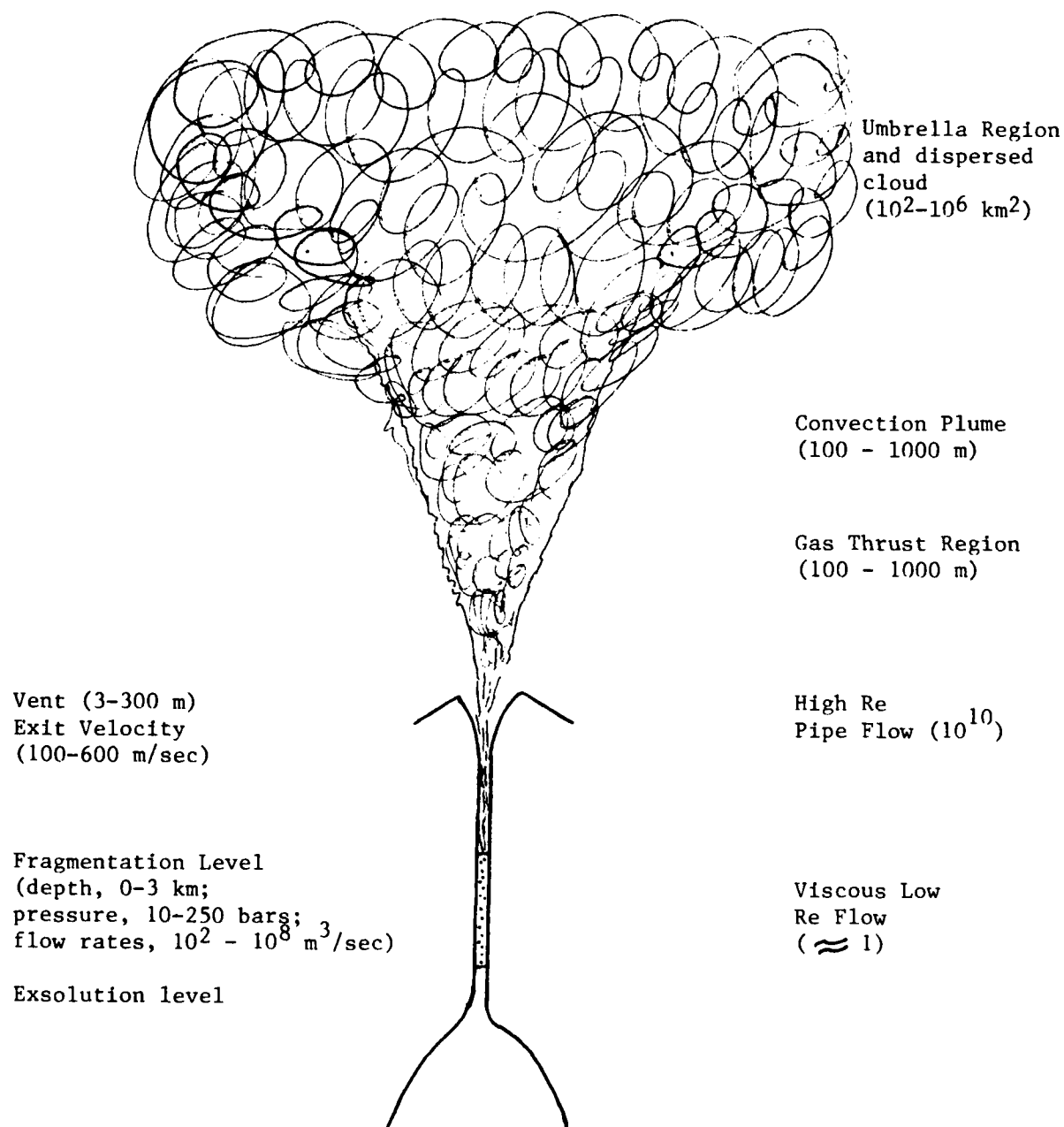
Figure 1

If $\frac{dq}{dh} = 0$ (an assumption which is found to be valid a posteriori), observations of $\frac{du}{dh}, u$ and h enable estimates of q for Soufriere (from film taken on April 22, 1979):

h(km)	β_c (m/sec)	q
3.0	82	0.938
3.7	77	0.964
5.2	59	0.999
6.5	49	1.012

The bulk density β_c is made up of hot air of density α and mass fraction (1 - Nc) and solid particles of density ρc and mass fraction N_c):

$$\frac{1}{\beta_c} = \frac{(1 - n_c)}{\alpha} + \frac{n_c}{\rho_c} \tag{3}$$

The plume temperature is θ_c, and thus the air density in the plume can be found by making a heat balance calculation:

$$\theta_c = (1 - n_c)\left(\frac{\theta_{ac} + \theta}{2}\right) - (1 - n_c)\left(\frac{\gamma - 1}{\gamma}\right)\frac{h}{H}\frac{\theta_{ac}}{2} + n_c \theta_c \tag{4}$$

where θ_c is the eruption temperature (1000K), H is the scale height of the atmosphere (8 km), and θ_{ac} and θ are the air temperatures at heights 0 and h. Equations (3) and (4) give an estimate of $N_c = 0.04$ at h = 3 kms. The mass flux rate of solids is found from

$$M = \pi u_i b^2 \beta_c n_c \tag{5}$$

where b is the radius of the plume (see Sparks and Wilson, 1982 for details). For Soufriere, calculations of M correspond to Q $\sim$ 12,000 m^3/sec. Using this estimate of Q, equation (1) can be used to predict the maximum height of this eruption as 19.8 kms, which is very close to the observed height of 18.7 kms.

The stability of the gas thrust region in Figure 1 is critical to understanding some important volcanic phenomena. In the analysis of this lower region the velocity is calculated as a function of height by a modified version of Prandtl Jet Theory is used, in which the effect of the presence of gas and solids on the total buoyancy is taken into account. The velocity can be obtained by integrating

$$u\frac{du}{dh} = \frac{-u2}{8b} - g(1 - \alpha/\beta) \tag{6}$$

where α is the density of air, is the bulk density, and b is the radius of the vent. Equation (6) is numerically integrated, taking into account heat sharing between air, gas, and solid (Wilson, 1976). This equation is only

valid for the momentum dominated part of the column. Solutions of this equation (Wilson, 1976; Sparks et al., 1978) lead to understanding of two fundamentally different kinds of column behavior. In one the jet region entrains enough air to smoothly change into a buoyant plume. In the other kind of behavior the column collapses at a low height to form a gravity current (pyroclastic flow). For a small enough vent radius the eruption will form a buoyant plume and will rise, but if the vent radius exceeds some critical value then the eruptive column will collapse and form a gravity current flowing down the side of the volcano.

The two parameters which determine whether or not the column will collapse are the vent radius b and the weight percent gas content n (the exit velocity is almost linearly related to the gas content n and is therefore not an independent parameter).

The figure below shows in which regions of the (b,n) plane one gets convecting plumes or collapsing columns.
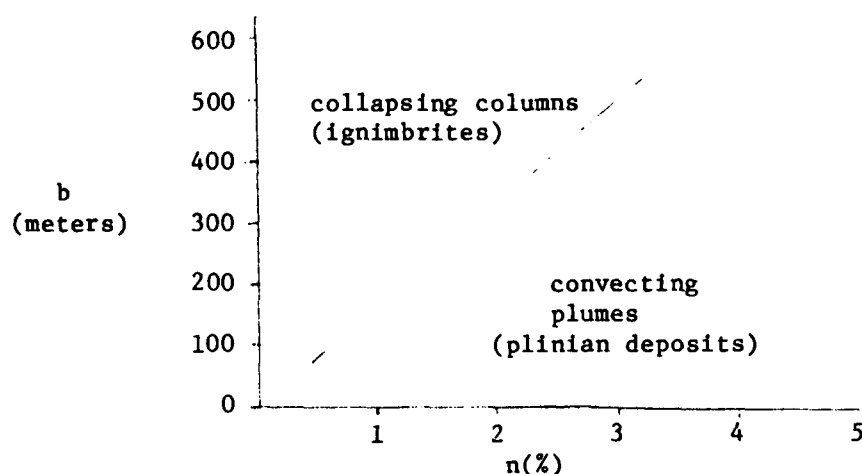
Before proceeding to the next topic it is probably useful to make a few comments about the assumptions made in calculating the above results. The weakest one is that the plume is assumed to be homogeneous horizontally. Also, the important radius for determining the vent size may not be the physical size of the vent, but the radius when the jet has expanded to 1-atmosphere exitpressure. Finally one might have to take into account the fact that the vent size is probably not constant during the eruption, but is widened by erosion.

The last quantity one wants to be able to predict is the height H_B at which the plume starts to spread out. If one uses the theory of Morton, Taylor and Turner (which was previously found to give considerably accurate results for the maximum height of the column H_T) to calculate H_B, one obtains results which consistently exceed the observed values.

REFERENCES

Morton, B.R., G. Taylor, and J.S. Turner, 1956. Turbulent gravitational convection from maintained and instantaneous sources. Phil. Trans. Roy. Soc. 234, 1-22.

Sparks, R.S.J., L. Wilson, and G. Hulme, 1978. Theoretical modeling of the generation, movement and emplacement of pyroclastic flaws by column collapse, J. Geophys. Res. 83, 1727 - 1739.

Sparks, R.S.J. and L. Wilson, 1982. Explosive volcanic eruptions V. Observations of plume dynamics during the 1979 Soufriere eruption, St. Vincent. Geophys. J. Roy. Astro. Soc. 69, 551-570.

Wilson, L., 1976. Explosive volcanic eruptions III. Plinian Eruption Columns. Geophys. J. Roy. Astro. Soc. 45, 543-556.

Wilson, L., R.S.J. Sparks, T.C. Huang and N.D. Watkins, 1978. The control of eruption column h eights by eruption energetics and dynamics. J. Geophys. Res. 83, 1829-1836.

Wilson, L., R.S.J. Sparks and G.P.L. Walker, 1982. Explosive volcanic eruptions IV - The control of magma properties and conduit geometry on eruption column behavior, Geophys. J. Roy. Soc. 63, 117-148.

NOTES SUBMITTED BY
Lorenzo Polvani and
Ross Kerr

LECTURE 8

VISCOUS GRAVITY CURRENTS

Herbert E. Huppert

A gravity current occurs whenever fluid of one density flows under (over) fluid of a smaller (larger) density. Typical geophysical examples are the afternoon sea breeze front and the spreading of oil on water. Most studies of gravity currents, both experimental and theoretical, have concentrated on high Reynolds number currents which propagate under a balance of inertia and buoyancy forces. Dissipation at the breaking nose plays a controlling role and the important dimensionless parameter is the internal Froude number at the nose $Fr = u/(g'h)^{1/2}$, where u is the nose velocity, g' the reduced gravitational acceleration and h the height of the current at the nose.

At low Reynolds number the current will propagate under a balance of viscous and buoyancy forces. Currents of this type will be studied in this lecture with applications to the formation and spreading of lava domes in mind.

Several geometries will be considered: 2-d current on a plane horizontal surface; 2-d current confined between vertical walls; axisymmetric gravity current and 2-d current on a slope. Other interesting geometries could include wavy walls and a V-shaped valley. A general power law volume flux will be considered $V = qt^{\alpha}$, which includes the cases $\alpha = 0$, constant volume release, $\alpha = 1$ steady input.

(1) Two Dimensional Bottom Current
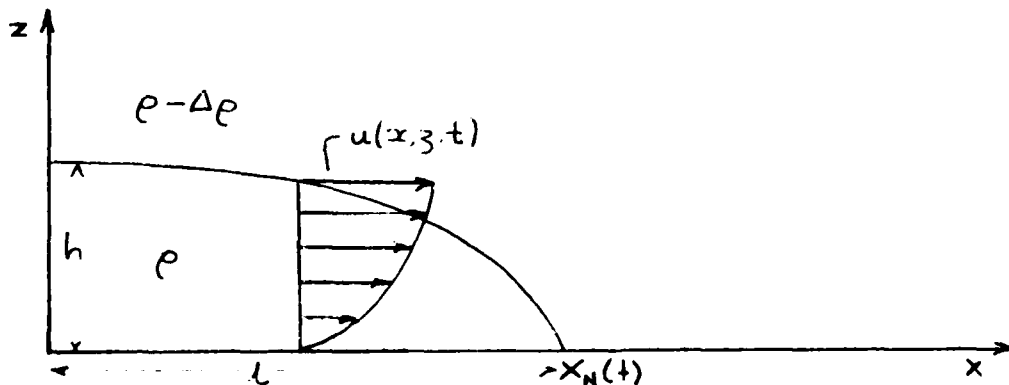
Figure 1. Sketch of the flow field and coordinate system

The theory of two-dimensional viscous bottom gravity currents has been investigated by Huppert (1982). Scaling arguments show that the flow regimes where viscosity dominates over inertia are:

$$\alpha < 7/4 \quad t \gg t_1 \qquad \text{where } t_1 = (\nu^3 g'^2/q^4 = J)^{1/(4\alpha - 7)}$$

$$\alpha > 7/4 \quad t \ll t_1$$

With a rapidly varying outflow viscosity will be important initially then inertia will become dominant. $\alpha = 7/4$ is a critical case where both inertial and viscous forces increase with time at the same rate.

Fluid is input through an ideal point source with negligible initial momentum. Consider the case where $\Delta\rho = \rho$, i.e. there is no fluid above the current. It can be shown for a deep environment the fluid above the current has no role in the dynamics apart from reducing the gravitational acceleration to g' $=\Delta\rho/\rho$.

The current is assumed to have a large aspect ratio, $h \ll l$, so the vertical pressure distribution is close to hydrostatic. The horizontal momentum equation reduces to:

$$\frac{1}{\rho}\frac{\partial p}{\partial x} = g\frac{\partial h}{\partial x} = \nu\frac{\partial^2 u}{\partial z^2} \quad . \tag{1}$$

This equation may be integrated twice with respect to z using the boundary conditions $\frac{\partial u}{\partial z} = 0$ at z = h and u = 0 at the lower boundary to give the velocity profile

$$u = -\frac{1}{2}\left(g/\nu\right)z(2h-z)h_x \quad . \tag{2}$$

The neglect of surface tension (T) in this analysis will be valid provided the Bond number $(\rho g l^2 / T)$ is much greater than 1.

The vertically integrated form of the continuity equation is:

$$h_t + \left(\int_0^h u\,dz\right)_x = 0 \quad . \tag{3}$$

Substituting (2) into (3) gives the governing nonlinear differential equation for the current:

$$h_t - \frac{1}{3}g/\nu\left(h^3 h_x\right)_x = 0 \quad . \tag{4}$$

Conservation of volume of the current also gives a global continuity equation

$$\int_0^{x_N(t)} h(x,t)\,dx = q\,t^\alpha \quad . \tag{5}$$

Rather than solve these equations exactly using numerical integration from initial values it is possible to find a similarity solution in terms of the variable

$$\eta = \tfrac{1}{3}\left(gq^3/\nu\right)^{-\frac{1}{5}} x\, t^{-(3\alpha+1)/5}.$$

The height of the current h is: $h = \eta_N^{4/3}\left(3q^2\nu/g\right)^{\frac{1}{3}} t^{(2\alpha-1)/5}\, \phi(\eta/\eta_N)$

where $\eta_N = \eta$ at $x = x_N(t)$ i.e. the value at the nose. Using these definitions, (4) and (5) lead to the governing equation for the similarity function $\phi(\eta/\eta_N)$

$$\left(\phi^3\phi'\right)' + \tfrac{1}{5}\left(3\alpha+1\right)y\phi' - \tfrac{1}{5}\left(2\alpha-1\right)\phi = 0 \qquad (6)$$

where $y = \eta/\eta_N$ and $\eta_N = \left(\int_0^1 \phi\, dy\right)^{-3/5}.$

This solution will not be valid at the origin because of the unrealistic condition that all fluid be input there, nor will it be accurate at the nose where the lubrication theory approximations must be wrong and surface tension will be important in determining the angle the nose makes with the boundary.

The function ϕ may be evaluated by integrating (6) from the nose using the conditions $\phi(1) = 0$, and as $y \to 1$:

$$\phi(y) = \left[\tfrac{3}{5}\left(3\alpha+1\right)\right]^{1/3}\left(1-y\right)^{1/3}\left[1 - \frac{(3\alpha-4)(1-y)}{24(3\alpha+1)} + O(1-y)^2\right]$$

as starting conditions. For $\alpha = 0$ the equation has an exact solution so it is possible to check the numerical solution for this value of α (fig. 2 and 3).
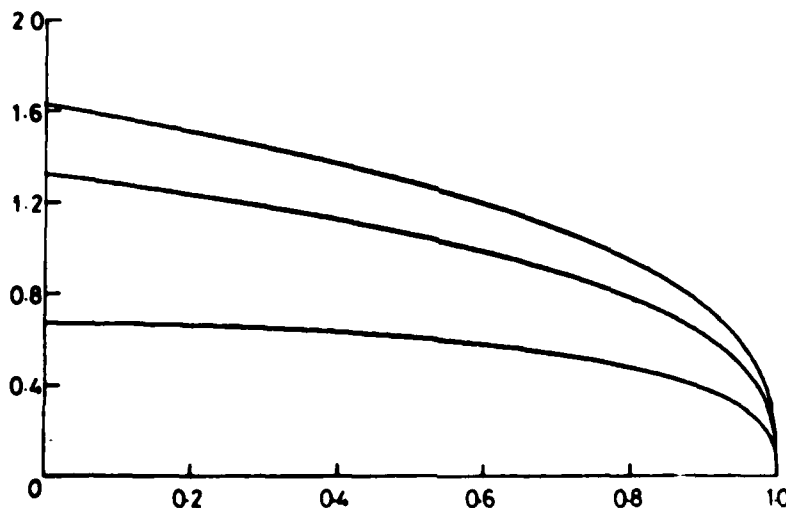
Figure 2. The shape of a two dimensional viscous gravity current for $\alpha = 0$, 1 and 2.

The solution for the current length as a function of time is:

$$l = x_N(t) = \eta_N \left(\tfrac{1}{3} g' q^3 / \nu \right)^{1/5} t^{(3\alpha+1)/5} \tag{7}$$

The presence of an upper layer is unimportant (except in reducing g to g') because the condition:

$$\delta = (\nu t)^{1/2} \gg h$$

(fig 4) is satisfied. This condition states that the vertical scale of motion induced in the upper layer by the gravity current is much greater than the thickness of the current. If the viscosity of the upper layer is comparable with the lower layer viscosity the condition is satisfied for all t for which the viscous buoyancy balance is valid and it follows that the boundary condition is satisfied at the interface.
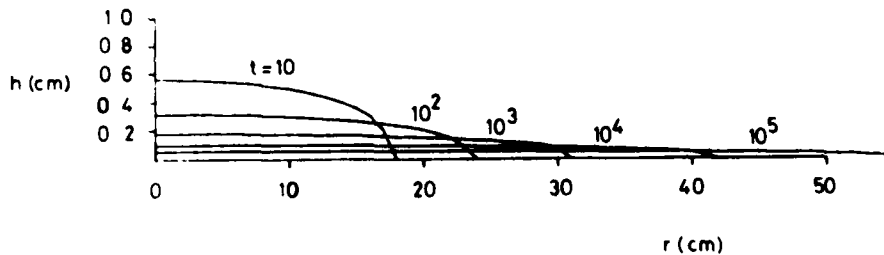
Figure 3. The shape of a radially spreading flow for
$V = 400$ cm^3 $\nu = 10$ cm^{2}s^{-1}
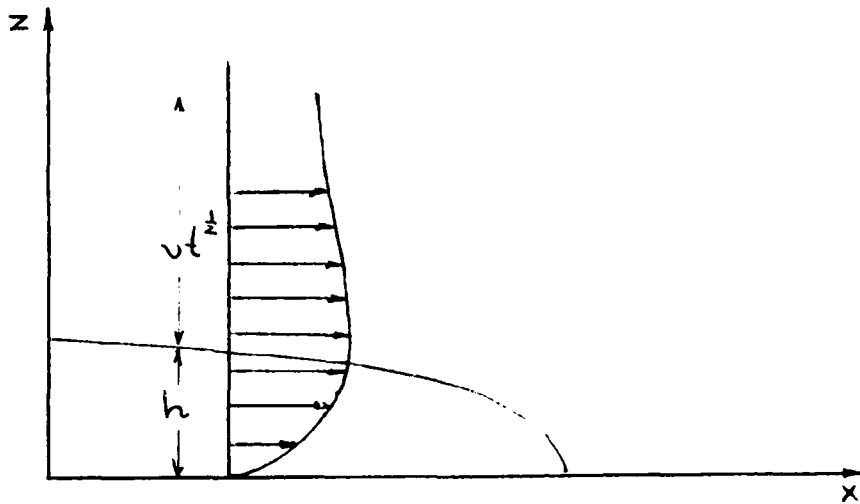
Figure 4. Sketch of the flow in the upper layer

(2) Viscous Gravity Currents between Parallel Walls

For a current confined between two vertical walls viscous drag at the sidewalls may be as important as drag at the lower boundary. If the wall spacing is L the horizontal momentum equation is:

$$gh_x = \nu (u_{yy} + u_{zz})$$

with the boundary conditions:

$$u = 0 \text{ at } y = 0, \ L \text{ and } z = 0$$

$$u_z = 0 \text{ at } z = h$$

Integrating this equation twice leads to the solution for the velocity profile:

$$u = \frac{4gL^2}{\pi^3 \nu} h_x \sum_{n_{odd}} n^{-3} \left[\cosh \frac{n\pi z}{L} - 1 - \tanh \frac{n\pi h}{L} \sinh \frac{n\pi z}{L} \right] \sin \frac{n\pi x}{L} .$$

Substituting this relation into the continuity equation gives the governing equation:

$$h_t + \frac{8gL^2}{\pi^4 \nu} \left[h_x \sum_{n_{odd}} n^{-4} \left(\frac{L}{n\pi} \tanh \frac{n\pi h}{L} - h \right) \right]_x = 0$$

There are two limiting cases. If $L \gg h$ the equations reduce to those given in section 1 for a 2-d current. If $L \ll h$ then dissipation at the sidewalls dominates bottom friction and the governing equation is:

$$h_t - (gL^2/12\nu)(hh_x)_x = 0$$

which gives a solution for the nose position as a function of time

$$x_N = \eta_N \left(\tfrac{1}{12} g L^2 q / \nu \right)^{1/3} t^{(\alpha+1)/3} \tag{8}$$

The profile of the gravity current is exactly linear for $\alpha = 2$ (fig. 5). Maxworthy has performed experiments for the case $\alpha = 0$ which show that the shape of the current is similar to the theoretical prediction.
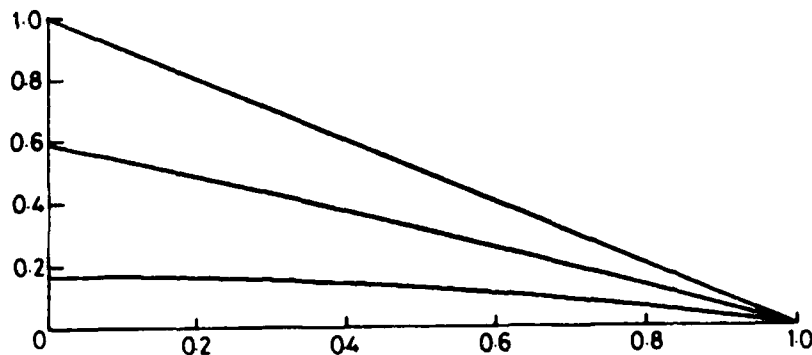
Figure 5. The shape of a viscous gravity current confined between vertical parallel walls with $L \ll h$ for $\alpha = 0$, 1 and 2.
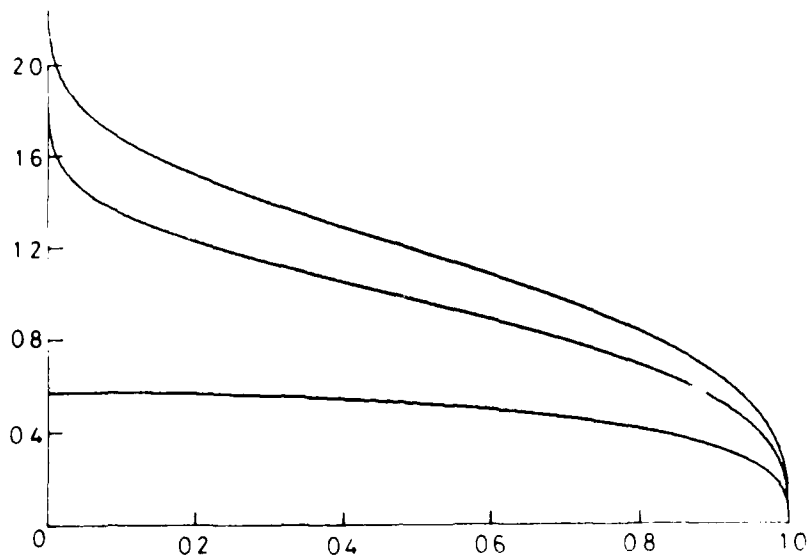
Figure 6. The shape of an axisymmetric viscous
gravity current for $\alpha = 0$, 1 and 2.

(3) Axisymmetric Gravity Current

Solutions for the shape of an axisymmetric viscous current may be
obtained in a similar manner to those for a 2-d current (fig. 6). The nose
position is given as a function of time as:

$$r_N(t) = \eta_N \left(\tfrac{1}{3} g q^3 / \nu \right)^{1/5} t^{(3\alpha+1)/5} \tag{9}$$

The similarity solution goes to ∞ at the origin for $\alpha \neq 0$ because a
finite volume flux is being imposed at one point.

Summary

In these currents the viscous stress at horizontal or vertical boundaries
is the most important force balancing buoyancy. This force balance is very
different to the high Re case where the current is hydraulically controlled at
the nose. If the nose was also dominant in the low Re limit as well, surface
tension effects would be important; the theory, however, predicts that the
nose shape is unimportant, in fact the theoretical predictions are completely
wrong at the nose. Some experiments were considered necessary to convince the
skeptics of the usefulness of the theory.

(4) Experiments

A known volume of viscous fluid was released onto a large perspex sheet. Measurements of the mean radius of the spreading current and its height at the origin were taken. The experiment was initiated either by simply pouring the fluid onto the sheet or by confining the fluid within a cylinder on the surface then lifting the cylinder. In either case the fluid front was very stable and the mode of initiation seemed unimportant. In some experiments a constant volume flow rate was supplied by dripping fluid from a burette with the head maintained at a constant level.

In the constant volume experiments the height of the fluid at the origin was measured by lowering a probe until it just touched the fluid surface. The probe caused a perturbation to the fluid surface, probably due to an electrostatic effect, in the form of concentric ripples on the free surface. This problem meant that the height measurements were somewhat scattered.

For the constant volume release ($\alpha = 0$) q was varied from 220 to 933 cm^3 and experiments were carried out at two viscosities $\nu = 13.2$ and 1,110 cm^2s^{-1}. The theoretical prediction of radius was

$$r_N = 0.894 \left(q \tilde{Q}^3 / 3\nu \right)^{1/8} t^{0.125}$$

and the experimental results (fig. 7) gave co-efficients of 0.887 ($\pm$.002) and 0.122 ($\pm$.002). The predicted height at the origin was:

$$h(0,t) = c \left(3\nu Q / 4\pi q \right)^{1/4} t^{-0.25}$$

with c predicted to be 1. The experimentally determined c was 0.94 $\pm$ 0.04 (fig. 8).

In the constant flux case q was varied between 0.223 and 0.0493 cm^3s^{-1} and fluid of viscosity 13.2 cm^2s^{-1} was used. The predicted radius was:

$$r_N = 0.715 \left(q \tilde{Q}^3 / 3\nu \right)^{1/8} t^{0.50}$$

and measured values (fig. 9) were 0.694 $\pm$ .004 and 0.499 $\pm$ .001.

No experiments were carried out for the two dimensional case, although experiments by Didden and Maxworthy (1982) using salt solutions flowing under water verified the expected power law for constant flux and constant volume releases, although the multiplying coefficients differed slightly from the theoretical predictions in a way consistent with the effect of sidewall friction.

The results of the experiments validated the theory and showed that a solution which is completely wrong at the nose is a good description of the flow simply because the nose shape is not important to the dynamics in the regime of interest.
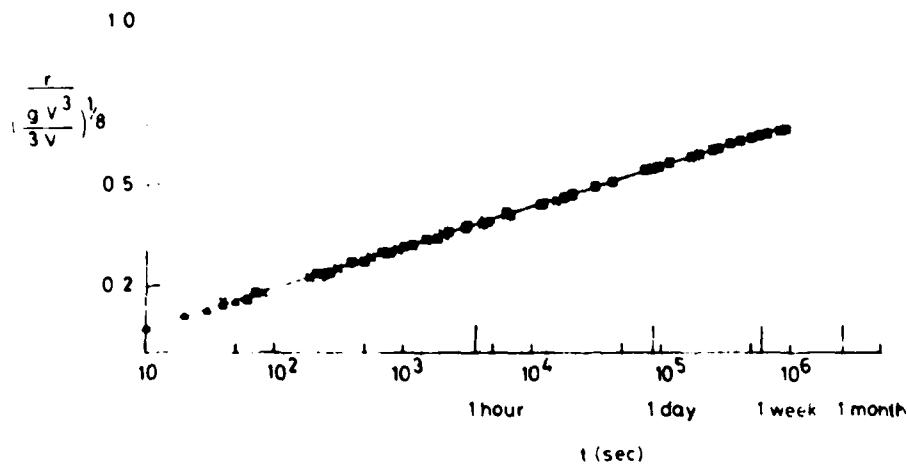
Figure 7. Experimental values of nondimensionalized current radius as a
function of time for the axisymmetric spreading of constant volumes
of silicone oils into air. Straight line is the best-fit power law.
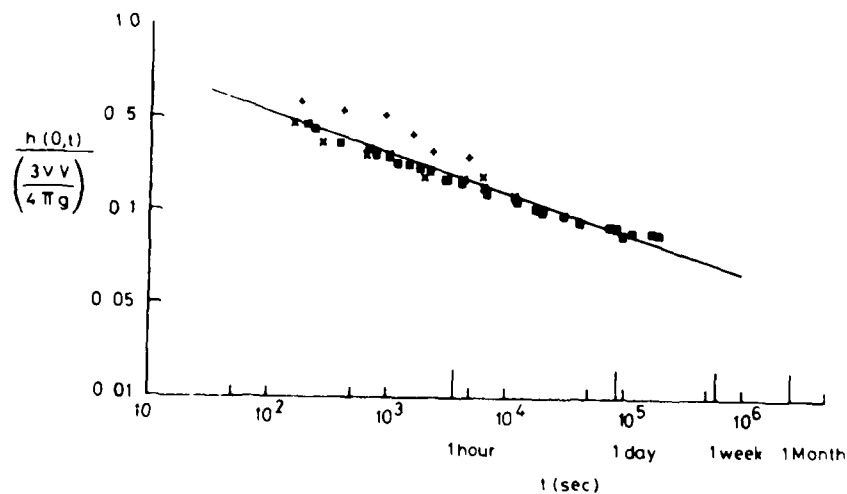
Figure 8. Experimental values of current height as a function of
time for the axisymmetric spreading of constant volumes
of silicone oils into air.
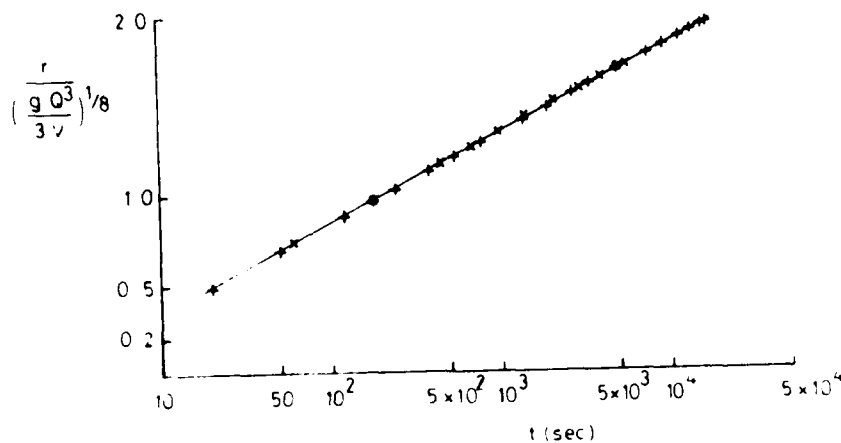
Figure 9. Experimental values of the nondimensionalized current radius for
the axisymmetric spreading of silicone oils into air at constant efflux rate.

An interesting physical question to consider is how the gravity current
approaches the similarity solution from its initial shape when released from
the container. Is there some "waiting time" during which the current redis-
tributes itself to the shape predicted by theory, then moves off or is there a
gradual approach to the correct shape? Experiment did not reveal the answer.

(5) Application to the Spreading of a Lava Dome

After the 1979 eruption of Mount Soufrière a flat crater floor of diameter
1.6 km was formed. Over a 120 day period a lava dome was extruded onto the
crater floor. Measurements of the dome were made and its volume, maximum
diameter and height determined.

Fitting the volume as a function of time to a power law (fig. 10) gave

$$V = 273t^{0.74} \ m^3$$
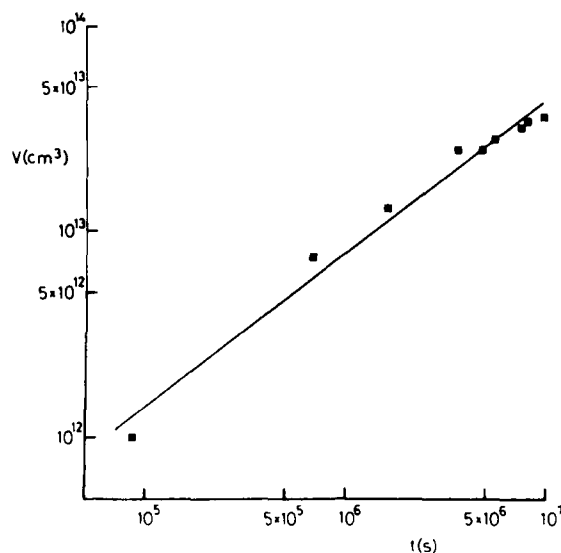
Figure 10. The volume of the 1979 lava dome as a function of time. The straight line is the best fit power law including all experimental points.

The maximum diameter could be fitted to the power law

$$r_N = 225t^{0.33}m.$$

Thus $V(t)$, $r_N(t)$ and constants g, q were known so the known solution for r_N (equation 9) could be used to determine ν. The process was not very sensitive since $r_N \propto \nu^{-1/8}$. A large variation in the viscosity had only a small effect on r_N.

For $\alpha = 0.74$ with $x_N \sim t^{(3\alpha +1)/8}$ gives an exponent of 0.40 to compare with 0.33 determined from the fit to the observations. If the first point (fig. 10) was neglected then $\alpha = 0.66$ and the calculated exponent was 0.36, a reasonable comparison with the field observations. Although this first point was deleted on purely arbitrary grounds it was later discovered that it had been evaluated from an aerial photograph rather than ground measurements like the other points. Using the theoretically determined solution this suggests a magma viscosity of 10^{12} poise.

Is it justified to apply this model to a lava dome which has a solidified shell over liquid lava? There are possible effects due to cooling and solidi-fication and the resultant latent heat release. In fact the thermal boundary layer is dominated by latent heat release and there is an increase in tempera-ture at both upper and lower boundaries, although after 90 days a calculation of the cooling shows that the thickness of the crust will be typically 5m which is negligible compared to the 133m depth of the dome. Since the skin

thickness is so small and it is not rigid it should not be important to the
dynamics, especially since the theory shows that what is happening at the
upper boundary is not important.

Another possible objection is that a Newtonian rheology is being applied
to a viscous lava flow. Experimental studies of flow of molten rocks show
that at the shear stress levels found in the lava flow the liquid's behaviour
will be closely Newtonian.

(6) Viscous Gravity Currents on a Sloping Boundary

Experimentally it was found that gravity currents on a plane perpendicular
to the gravity vector had very stable fronts. A different result is found if
the experiment is performed on a sloping boundary.

A fixed volume of viscous fluid was released from behind a dam on a
sloping perspex sheet (fig. 11). After the current had travelled 25 cm down-
slope it was only .2 cm deep at the nose and the front was quite straight
except for some curvature at the walls due to the viscous boundary layer.
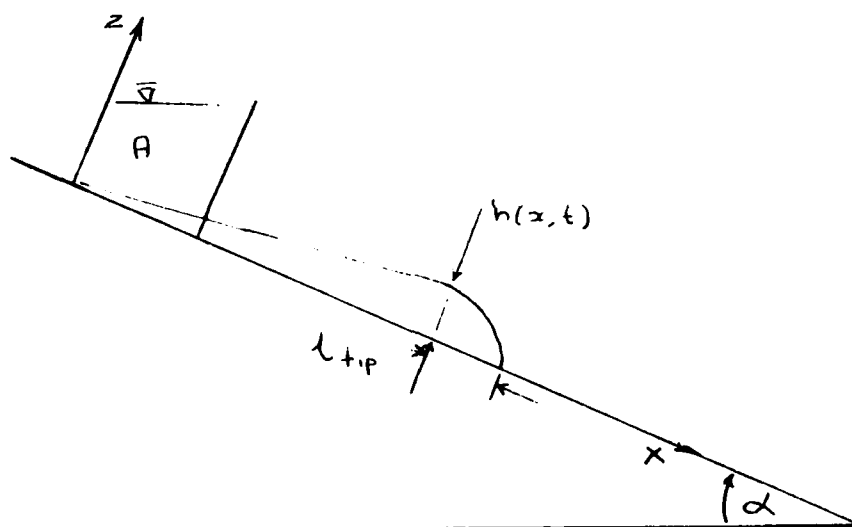
Figure 11. A sketch of the flow field and coordinate system.

After about 55 cm, when the current had been travelling for approximately 100s
instability at the front developed very rapidly (O(s)). The instability was
periodic with a wavelength, λ , of about 5 cm.

The long term form of the instability (fig. 12) was quite different for
silicone oil and glycerine even though they had very similar viscosities. A
feature of both instabilities at large amplitude was the very straight boun-
dary. The instability started uniformly across the front; if it had been
generated at the boundaries and diffused inwards it would have developed very
slowly.

downslope
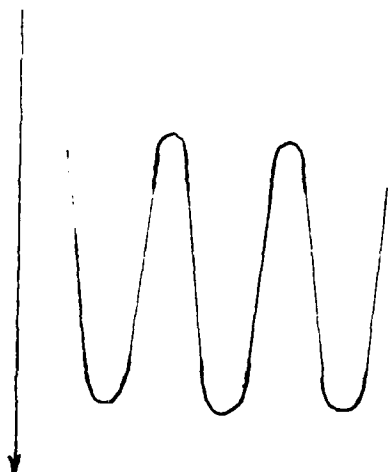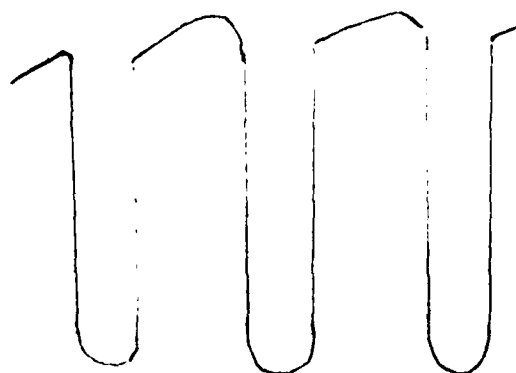
silicone oil   glycerine

Figure 12. A sketch of the long term form of the instability of a gravity
current down a sloping bed for two experimental fluids.

(7) Theory: Flow of a 2-d Viscous Gravity Current down a Slope

The controlling force balance will be between the downslope component of
the gravitational acceleration and the viscous stress (fig. 11).

$$g\sin\alpha + \nu u_{zz} = 0 \tag{10}$$

This equation is valid provided $\tan\alpha \gg h_x$. There would be an
interesting transition region between this flow and the flow on a flat bed
previously studied where this condition did not hold. Using the usual boun-
dary conditions (10) is integrated twice to give the z-velocity profile which
may be substituted into the local continuity equation to give the governing
equation:

$$h_t + \frac{g\sin\alpha}{J\nu} h^2 h_x = 0 \tag{11}$$

(11) may be solved using the global continuity equation by either a
similarity solution or using the method of characteristics. The height as a
function of (x,t) is:

$$h = \left(\nu/g\sin\alpha\right)^{1/2} x^{1/2} t^{-1/2} \tag{12}$$

At a fixed time $h \propto x^{1/2}$ and no nose is formed. The nose position is found by stopping the solution when the current volume/unit width is conserved.

$$x_N = \left(\frac{q}{4} A^2 \frac{g \sin \alpha}{\nu} \right)^{1/3} t^{1/2} \tag{13}$$

A is the initial area of the current. The height of the current at the nose is

$$h = h_N(t) = 1.5A/x_N$$

The agreement between theory and experiment was very good (fig. 13) in the region where the front was stable, showing again that the nose has no effect on the dynamics in this region. The nose profile may, however, be smoothed by considering the effect of surface tension on the flow.
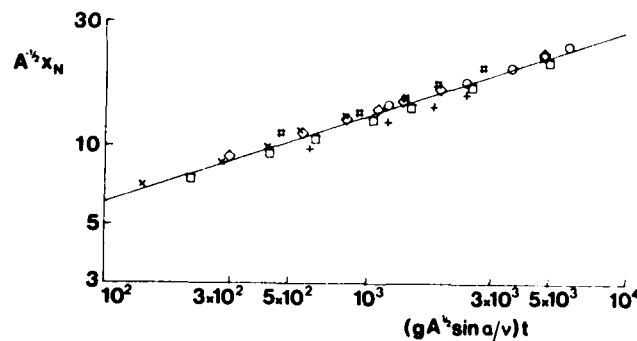
Figure 13. Experimental values of the nondimensionalized current length as a function of time.

Stability of the Front

The experiments suggested that the instability could not be explained by viscosity but suggested other factors were important. The evidence was:

(i) Two silicone oils with viscosities differing by an order of magnitude but with almost equal surface tensions had equal wavelengths of instability, λ , at the front.

(ii) Experiments using fluids with similar viscosities but different surface tensions showed that λ was a function of T.

(iii) With similar fluids but with initial volumes differing by a factor of 10 the wavelength was found to be weakly dependent on A.

Including terms due to surface tension and the surface slope across and along the current leads to the equation:

$$h_t + \frac{g\sin\alpha}{3\nu} h^2 h_x - \frac{g\cos\alpha}{3\nu}(h^3 h_x)_x - \frac{T}{3\rho}(h^3 \nabla^2 h_x)_x$$
$$- \frac{g\cos\alpha}{3\nu}(h^3 h_y)_y - \frac{T}{3\rho}(h^3 \nabla^2 h_y)_y = 0 .$$

In the tip region the dominant balance is between the second and fourth terms, rather than the first and second. The cross slope variations (5th and 6th terms) should be small. The solution may be written as:

$$h = h_N(t)H(\xi) \quad \text{where } \xi = (\rho g\sin\alpha/Th_N)^{1/3}(x_N - x)$$

and $H(\xi)$ satisfies the equation

$$H^3 H''' + H^3 = 1.$$

The boundary conditions on this equation will be $H \to (16/15)^{1/4}\xi^{3/4}$ as $\xi \to 0$, $H \to 1$ $\xi \to \infty$. The tip lengthscale is $\ell_{tip} = (Th_N/\rho g\sin\alpha)^{1/3}$. Experiment suggested that the instability occurred at a critical length

$$x_N^{crit} \propto A^{1/2}.$$

It is plausible that λ should be scaled by the tip length ℓ evaluated at the critical length, hence:

$$\ell_{tip}^{crit} \propto (A^{1/2} T/\rho g\sin\alpha)^{1/3} \propto \lambda .$$

Thus λ should be independent of ν , as observed experimentally (fig. 14).

A reasonable representation of the experimental results was

$$\lambda = 7.5 \left(A^{1/2} T / \rho g \sin \alpha \right)^{1/3}$$
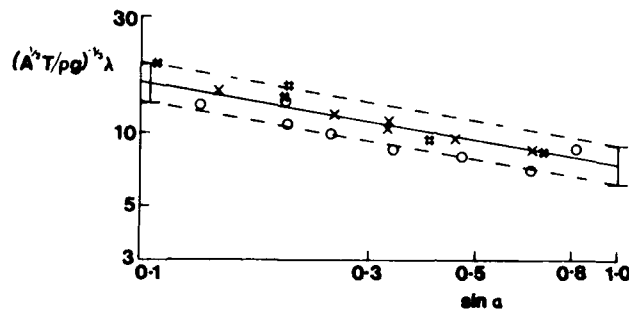
Figure 14. Experimental results for the wavelength of the frontal instability as a function of the slope angle. The solid line is the line of best fit with slope 1/3. The dotted lines are plus and minus one standard deviation from this line.

Several related questions were:

(i)   Why does the instability have such straight downslope edges?

(ii)   For a constant flow rate $V = qt$ the height of the current is constant. Is the flow unstable in this case? If q is sufficiently slow might the current be unstable from initiation?

(iii) Downslope lava flows seem to be stable until they hit the sea then become irregular. What are possible instability mechanisms for these flows?

REFERENCES

N. Didden and T. Maxworthy, 1982, The Viscous Spreading of Two-dimensional and Axisymmetric Gravity Currents, Fluid Mech. 121, 27-42.

Huppert, H.E., 1982, The propagation of two-dimensional and axisymmetric viscous gravity currents over a rigid horizontal surface, J. Fluid Mech. 121, 43-58.

ADDITIONAL REFERENCES

Huppert, H.E., 1982, Flow and instability of a viscous current down a slope, Nature 300, 427-429.

Huppert, H.E., J.B. Shepherd, H. Sigurdsson and R.S.J. Sparks, 1982, On lava dome growth, with application to the 1979 lava extrusion of the Soufrière of St. Vincent, J. Volcanol. and Geotherm. Res. 14, 199-222.

NOTES SUBMITTED BY
Leonard Smith and
John Taylor

LECTURE 9

THE MOTION OF A HOT, HIGH REYNOLDS NUMBER
GRAVITY CURRENT OVER AN ERODABLE BED.
THE FLUID DYNAMICS OF (KOMATIITE) LAVA FLOWS
THREE BILLION YEARS AGO

Herbert E. Huppert

The lava released in recent eruptions of oceanic basalt is typically silicic. It has a SiO_2 content of about 50%, with an MgO content that is below 20%. At its eruption temperature of 1200°C, such magma has a viscosity on the order of 200 cm^2sec^{-1}, which is relatively high. Because of the high viscosity, the lava flow is generally laminar (moderate or low Reynolds number) and heat is transported predominantly by conduction.

In contrast, there is evidence of lava flows from the Archaean age of the earth - called komatiite flows - in which the viscosity was low, and heat was transported much more efficiently by turbulent convection. Compared to recent lava, komatiite has a slightly lower SiO_2 content ($\sim$45%) , a substantially higher MgO content ($\sim$20% to $\sim$ 35%), and much smaller viscosity of 0.3 to 3.0 cm^2sec^{-1} at the extrusion temperature of 1600°C. Komatiite flows have been extensively studied because of the information they convey about the early history of the earth, and also because of the commercial importance of the nickel sulfide ore deposits frequently found in komatiite beds. The following is an account of the eruption and emplacement of a typical komatiite flow (see Huppert et al. in Nature(v309 no5963), 1984, and Huppert and Sparks "Komatiites I: Eruption and Flow", to appear in J. Petrol., 1985).

Komatiite Flow in a Two-Dimensional Fissure
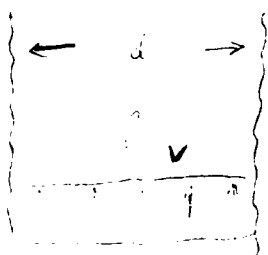
$$\nu = \text{komatiite viscosity}$$

$$Q = \nu d$$

$$R = Q/\nu \gtrsim R_{crit} \text{ for turbulence}$$

Consider a fissure of width d containing komatiite magma of density ρ within heavier country rock of density $\rho + \Delta \rho$. The effective pressure gradient in the liquid is then $g \Delta \rho$ in the upward direction. Because of the low viscosity of the komatiite, the channel flow is expected to be fully turbulent, in which case the volume flux Q up the fissure is roughly related to the width d by

$$u = \left(\frac{g}{k} \frac{\Delta \rho}{\rho} \right)^{1/2} d^{1/2}$$

where $k \simeq .03$ is an empirically determined parameter.

Some representative values are

$\rho = 2.8$ g cm^{-3} $\quad\quad \Delta\rho = 0.1$ g cm^{-3} $\quad\quad \gamma = 1.0$ cm^2 s^{-1}

d (m)	Q (m^2 s^{-1})	v (m s^{-1})	Re
0.3	0.56	1.9	$5.2*10^3$
1.0	3.4	3.4	$3.2*10^4$
3.0	17.8	5.9	$1.6*10^5$
10.0	108.0	10.8	$1.0*10^6$

Re$_{crit}$ = 2000, confirming that the flows are turbulent.

When the flow reaches the earth's surface, beneath the ocean, it flows out as an essentially two-dimensional gravity current.
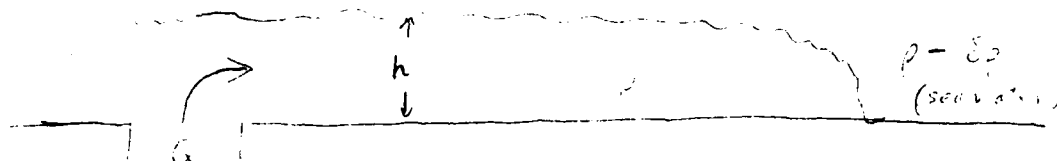
In such a current, the depth h of the advancing current and the volume flux are related by

$$h = \left(\tfrac{1}{2} a^2 \rho \,/\, g\,\Delta\rho \right)^{1/3}$$

$\rho = 2.8$ g cm^{-3} $\quad\quad \delta\rho = 1.8$ g cm^{-3} $\quad\quad \gamma = 1.0$ cm^2 s^{-1}

Q (m^2 s^{-1})	h (m)	u (m s^{-1})	Re
1.0	0.4	2.3	$9.3*10^3$
10.0	2.0	5.0	$9.3*10^4$
100.0	9.3	10.8	$9.3*10^5$

Re$_{crit}$ = 500

Flow Over an Erodable Bed

When a komatiite current of 1600°C flows over the ocean floor (which is assumed to be a basalt with melting temperature of $1200°c$) the bed is slowly melted and assimilated by the komatiite. It is expected that in this situation the horizontal scales of variation will be much greater than the depth of the current, so that the heat transfer processes can be treated locally as if they were homogeneous in the horizontal plane.

- 68 -
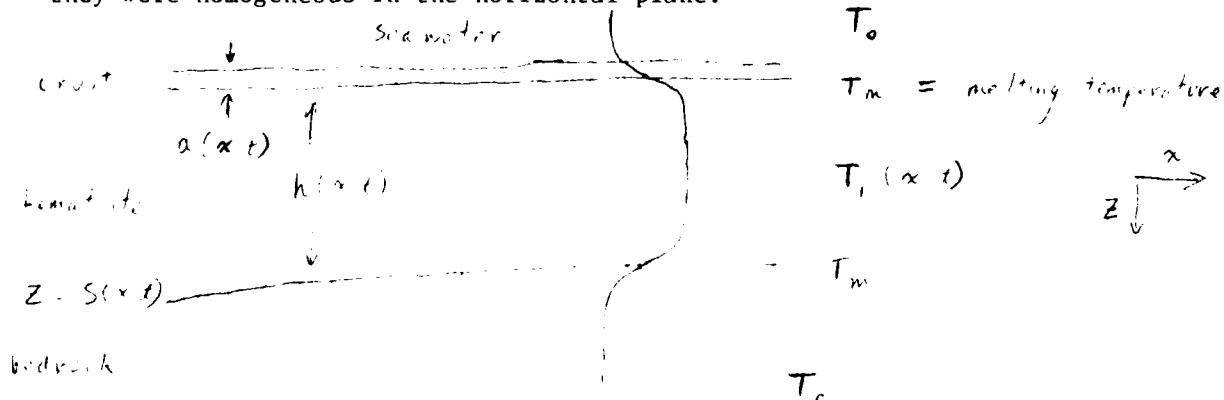
In the bedrock $T_t = k_s T_{zz}$ $z > S(x,t)$

with $T = T_m$ at $z = S$, $T \to T_c$

(k_s = thermal diffusivity in solid)

which has the solution

$$T = T_c + (T_m - T_o) e^{-(\frac{ds}{dt})(z - S)/k_s}$$

The heat transfer into the fluid at the lower interface is

$$H_L = -(\rho_s c_p k_s) \frac{\partial T}{\partial z} + \rho L (\frac{ds}{dt})$$

and so, for a steady current

$$\frac{ds}{dt} = H_L / \rho_s \left[L + c_p (T_m - T_o) \right]$$

The heat transfer at the lower interface is also related to the liquid temperature by

$$H_L = h_T (T_1 (x,t) - T_m)$$

where the transfer coefficient h_T is approximately given by the empirical formula

$$h_T = 0.015 (\frac{\rho_c c_p k_c}{h}) \mathcal{P}_r^{0.4} \mathcal{R}_e^{0.8}$$

At the upper surface of the current, a thin solid crust will form. The heat transfer through the crust is given by

$$H_U = (\rho_s c_p k_s)(T_m - T_c)/d(x,t) = h_T (T_1 - T_m)$$

therefore

$$d(x,t) = (\rho_s c_p k_s)(T_m - T_c) / h_T (T_1 - T_m)$$

Finally, the problem of determining the time-dependence of the temperature field is closed by constructing the global thermal energy balance:

$$\rho_L c_p h \left[1 - \frac{L \, X'(T)}{c_P} \right] \frac{dT}{dt} = \left[-2 h_T - \rho_L c_F \frac{dS}{dt} \right] (T - T_m)$$

$X(T)$ is the mass fraction of crystals in the liquid in equilibrium at temperature T, and its inclusion in the energy equation reflects the release of latent heat as the crystals form.
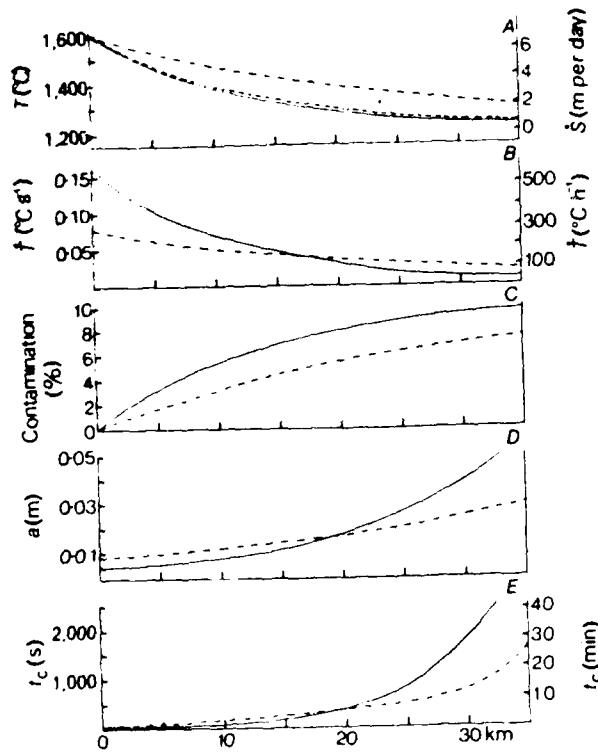
Fig. 2   A. The temperature of the lava, T, and the erosion rate of the ground, S. ——, With melting; - - -, without melting. B, The cooling rate; C, the percentage of contamination; D, the crustal thickness, a; and E, the time scale for the crust to form; all as a function of distance from the source. In A–E the dot–dash (– · –) line incorporates the latent heat release due to crystal formation, while the solid line omits this effect ($L = 0$).

(from Huppert et al (1984)

Experiments were done with a stream of $70°C$ water flowing over a bed of poly-ethylene glycol (PEG), which melts at $5c°c$ and is soluble in water. The stream carves channels in the PEG, which develops a characteristic profile rather like the boundary of a jigsaw-puzzle piece. Cross sections of ancient komatiite channels at the Kambalda nickel-sulfide mine exhibit very similar profiles on the scale of tens of meters.
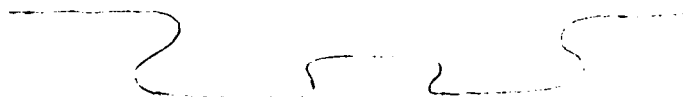
Aftermath of a Komatiite Flow

When the source of the current ceases, the komatiite on the surface will drain into whatever depressions and channels are available, where it continues to cool and crystallize. The cooling is expected to be dominated by conduction through the upper crust, because of the rapid removal heat by turbulent convec-tion in the overlying seawater. We shall look at some simple examples of the cooling and crystallizing of a binary mixture from above.

Cooling a Eutectic Solution from Above

$$T_A$$

$$z \downarrow$$

$$T = T_A + (T_e - T_A)\, z / h$$

$$\rho L \, \dot{h} = \kappa_s (T_e - T_A)/h \; - A\,(\theta - T_e)^{4/3}$$

$$T = \theta(t)$$

$$zero \ heat \ flux$$
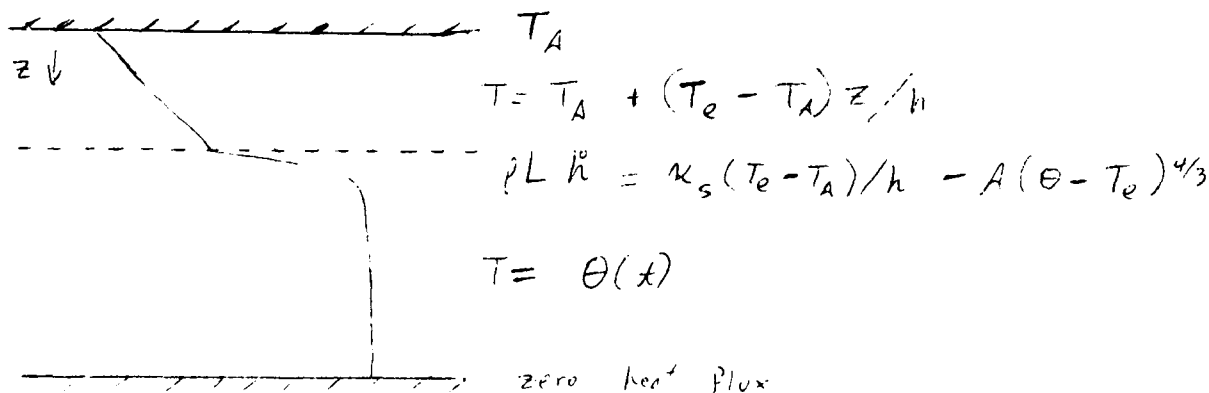
Assuming that the turbulence keeps the lower liquid well mixed, we can construct coupled ordinary differential equations for suitably nondimension-alized versions y, z of $h(t)$ and $\theta(t)$, that depend on the parameters β and γ, which measure respectively the importance of the latent heat release and the convective heat flux.

$$\theta = \theta_{ref}\, z \qquad\qquad z : 1 \downarrow$$

$$h = h_{ref}\, y \qquad\qquad y : 0 \to 1$$

$$t = t_{ref}\, \tau \qquad\qquad \tau : 0 \to \tau_s$$

$$\frac{1}{y} = \beta^2 \frac{dy}{d\tau} + \gamma z^{4/3}$$

$$(1-y)\frac{dz}{d\tau} = -3 z^{4/3}$$

$$y = 0, \quad z = 1 \quad at \quad \tau = 0$$

Typical solutions are shown below
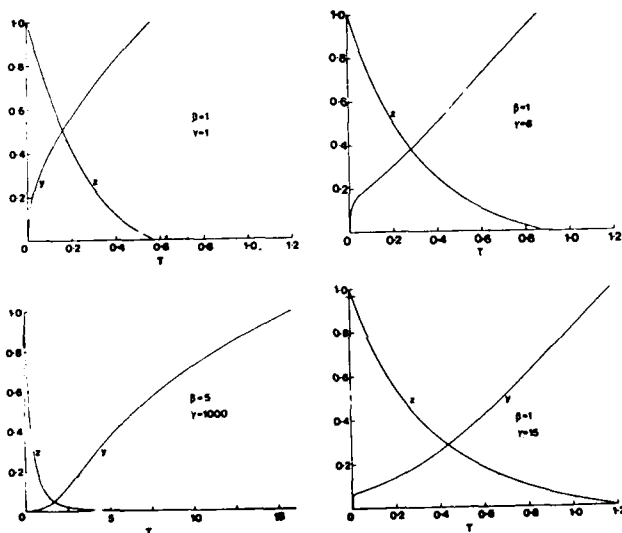
A more realistic problem, from a geological perspective, is the cooling from above of a solution whose composition is above the eutectic, so that light liquid is released when crystals form. Experiments on this system reveal a multi-layer structure. At the top of the experiment there is a quenched solid layer, immediately above a solid layer of eutectic composition. Below the solid, there is a region of dendrites and solute-depleted liquid, which has a large vertical extent; and below the dendritic region, there is a vigorously convecting region, just as in the eutectic theory. Eventually, the dendrites grow to occupy the entire region available to them. The resulting structure consists of long, thin needle-like filaments criss-crossing in a disorderly way. The similarity of these structures to the "spinifex textures" character-istic of the millimeter scales in komatiite rocks strongly supports the idea that the spinifex structure had its origin in just such a process.

NOTES SUBMITTED BY
Bruce Bayly and
André Gorius

ABSTRACTS OF SEMINARS

A LABORATORY EXCURSION

John A. Whitehead

Two experiments were demonstrated in the hydrodynamics laboratory. In the first experiment, a horizontal tubular line of water whose density is 1 gm/cc and kinematic viscosity is 0.01 cm/s was produced by injecting the water into a long rectangular tank of corn syrup whose density is 1.442 and whose kinematic viscosity is $1.2 \times 1.0^3 cm^2/sec$. The tube of water, owing to it's low density gradually rose through the syrup. It soon developed a gravitational instability which was relatively uniformly spaced along the axis. This is in spite of the fact that the injection was not completely uniform. It is a modified Rayleigh-Taylor instability and is characterized by a long unstable wavelength comparable to the diameter of the tube. The possibility of this instability occurring in island arcs to produce pockets of magma under island arc volcanism is suggested by Marsh (1979). We (Whitehead, Dick and Schouten, 1984, in press) have recently suggested that it occurs within a strip of partially melted mantle under spreading centers and is responsible for the enhanced volcanism between transform faults.

A second experiment was demonstrated on the two-meter turntable. Following Flierl, Stern, and Whitehead (1983) a small but turbulent jet of water was squirted into a homogeneous uniformly rotating fluid. In contrast to Flierl et al. the bottom of the tank was sloping so a topographic beta effect was present. Like the above study, an eddy pair (modon) emerged from the disorganized turbulent jet and meandered away from the source. It was explained that the formation of coherent structures from disorganized sources is one of the ongoing research projects in our laboratory.

REERENCES

Flierl, Glenn, Melvin Stern and John Whitehead, 1983. The physical significance of modons: Laboratory experiments and general integral constraints. Dynamics of Atmos. & Oceans, 7, 233-263.

Marsh, B. D., 1979. Island arc development: some observations, experiments and speculation. J. Geol. 87, 687-713.

Whitehead, John, Henry Dick and Hans Schouten, 1984. A mechanism for magmatic accretion under spreading centers. NATURE (in press).

MANTLE AND MAGMA DYNAMICS

Andrew Fowler

Convection occurs in the mantles of terrestrial planets due to solid-state creep processes in silicate rocks. On the earth, this is manifested by the active motion of the lithospheric plates. However, such active plate tectonics is not known to occur on other planets.

Turcotte and Oxburgh (1967) analyzed the structure of constant viscosity convection with free-slip boundaries at infinite Prandtl number, in the asymptotic limit $Ra \to \infty$ (large Rayleigh number). The flow has an isothermal interior and thermal boundary layers at the walls. In particular, they identified the top cold boundary layer with the active oceanic lithosphere, and deduced the well-known square root of age dependence of surface heat flux.

The direct application of this study to the earth is hindered by the fact that all experimental studies indicate that the viscosity of the earth's mantle is a strong function of temperature (and probably also pressure):

$$\eta = \frac{A}{\tau^{n-1}} \exp\left[\frac{E^* + pV^*}{RT}\right] \tag{1}$$

(Kirby, 1983). A typical value of the dimensionless exponent E^*/RT is ~ 40, when $T \sim 1500$ K.

The boundary layer analysis of variable viscosity convection, with a purely temperature dependent viscosity of the form

$$\eta = \eta_0 e^{-\gamma T}, \quad \gamma \Delta T \gg 1, \tag{2}$$

has recently been studied by the present author, and independently by S. Morris at Berkeley. The analysis involves two parameters, $\varepsilon = 1/\gamma \Delta T \ll 1$ (where ΔT is the applied temperature difference) and the Rayleigh number, computed with the basal viscosity, η_0. Results of interest are the heat flux:

$$Nu \sim 2\varepsilon Ra^{1/5}, \tag{3}$$

where Nu is the Nusselt number. The mean surface velocity is

$$\bar{V}_s \sim \frac{0.02\, a^{3/5} Ra^{4/5} e^{-1/\varepsilon}}{\varepsilon^2} \cdot \frac{\kappa}{d}, \tag{4}$$

where a is the aspect ratio, κ the thermal diffusivity, d the layer depth. A measure of the surface stress is the deviatoric longitudinal stress at the (downwelling) end of the top surface:

$$|\bar{\tau}_1| \sim \frac{0.16\, a^{-2/5} Ra^{4/5}}{\varepsilon^2} \cdot \left(\frac{\eta_0 \kappa}{d^2}\right). \tag{5}$$

These results are manifestations of the fact that with such a rheology, the cold (i.e. sticky) parts of the fluid do not want to move, whereas the warmer parts are more easily deformable. Thus one finds that when Ra $\gg$ 1, $\varepsilon \ll$ 1, the system adopts a structure of a vigorous (quasi-isothermal) convecting region overlain by a cold, thick stagnant lid. In particular, $\bar{V}_s$ (given by (4)) is much $\underline{less}$ than the conductive velocity κ/d. For earth-like values Ra $\sim \overline{10^8}$, $\varepsilon \sim 1/30$, we find $\bar{V}_s \sim 10^{-6}$ (κ/d), which is essentially zero.

On the other hand, the baroclinicity of the thick, cold lid generates large stresses within the lid, compared to those in the convecting flow. With the same values of Ra and ε, (5) gives $|\bar{\tau}_l| \sim 4 \times 10^8 . (\eta_o \kappa/d^2)$. With $\kappa \sim 10^{-2}$ cm^{2}s^{-1}, d $\sim$ 3000 km, $\eta_o \sim 10^{22}$ Poise, this is $|\bar{\tau}_l| \sim 400$ kilobars. This is well in excess of the plastic yield strength of rock.

The point of this study is to show that the fundamental physical nature of convection in the earth's mantle is not understood, notwithstanding Turcotte and Oxburgh's results. The process of subduction urgently needs a qualitative understanding. The variable viscosity calculation offers a clue to a possible mechanism, since for the earth-like values above, one should realistically adopt some kind of visco-plastic rheology. One might then expect that if the plastic region was as thick as the lid, the whole lid would be weakened, and could therefore subduct. If one makes a simple calculation based on the thickness of a plastic yielding zone required to support the baroclinically induced slab stress, one finds that this zone is of comparable thickness to the lid if the yield stress τ_y satisfies

$$\tau_y \lesssim \varepsilon \tau_{lid} , \tag{6}$$

where τ_{lid} is some measure of lid stress in the absence of plasticity. This might make some sense for the earth.

· ——— ·

Magma is generated within the earth's mantle, primarily at oceanic ridges, hot spots, and subduction zones. Particularly in the the first two cases, the melting occurs by pressure release: that is, the solidus temperature decreases with pressure more rapidly than the adiabat, so that as hot mantle rock ascends, it intersects the solidus, and so begins to partially melt. An understanding of the subsequent process of magma migration to the earth's surface is $\underline{vital}$ in order to make any sensible statements about the relation of surface $\underline{rocks}$ to geochemistry (for instance). Various other motivating phenomena are the occurrence of volcanism, the emplacement of magma chambers, and the initiation of lithospheric fracture.

This last topic concerns the problem of how hot magma gets through cold lithosphere. The idea of diapiric uprise has little to support it, and the principal mechanism is via fracture from the deep lithosphere. There is then the problem of initiation of such fracture. Weertman (1971) appealed to a tensile stress, but it seems unlikely that large enough tensile stresses can exist in the asthenosphere. Alternatively, excess pore pressure in the liquid ($\gtrsim$ 200 bars) can initiate fracture, virtually independently of the local deviatoric stress.

To examine this question, the model of Turcotte and Ahern (1978) has been generalized to allow explicitly for different liquid (p_ℓ) and solid (p_s) pressures within the partial melt zone. Turcotte and Ahern assumed that the melt (which is first formed on grain boundaries) forms an interconnected porous network, and that the matrix of solid grains would deform viscously sufficiently rapidly to allow any pressure difference to relax. After various approximations are made, our model can be written in the following form:

$$\underline{\nabla} \cdot (\chi \underline{v}) = S ,$$

$$\underline{v} = - \kappa \chi \underline{\nabla} [p_\ell + \rho_\ell g z] ,$$

$$\rho L S + \rho c_p \Gamma [\tfrac{\partial}{\partial t} + \underline{u} \cdot \underline{\nabla}] p_\ell = k \Gamma \nabla^2 p_\ell , \qquad (7)$$

$$\chi (p_\ell - p_s)/\eta_G + \operatorname{div} (\chi \underline{v}) = 0 .$$

Here $\underline{v}$ is the melt velocity, χ is the melt fraction, $\underline{u}$ is the matrix velocity, and p_ℓ is the liquid pressure. The assumptions involved are that $|\underline{u}| \ll |\underline{v}|$, $\chi \ll 1$, and that various terms (e.g. viscous heating) are small, as is indeed the case for pressure release melting. The equations are respectively mass conservation (note the source term S, which expresses the average volumetric source term due to melting), Darcy's law, energy conservation, where the temperature T is the solidus temperature given by $T = T_0 + \Gamma p_\ell$; the last equation is that of pore closure, and is based on a microscopic description of grain deformation. In this form, it is precisely analogous to prescribing a bulk viscosity ($= \eta_G/\chi$) for the medium, since p_ℓ is the thermodynamic (equilibrium) pressure, and p_s is approximately the dynamic pressure. The Turcotte limit $p_\ell \approx p_s$ corresponds to η_G being "small".

Other models including matrix deformation (via a bulk viscosity) are currently being studied by Scott and Stevenson at Cal Tech, McKenzie at Cambridge, and Richter (this volume, page 102). The purposes for which these models are being studied are very different, and it is not possible to seriously compare them.

For our model, we can approximately solve the equations, if a one-dimensional steady state is assumed. One finds that, in a dimensionless sense, η_G is not "small" for normal values of mantle viscosity ($\sim 10^{20}$P). One could argue that, when the grains are differentially stressed, the actual viscosity would be much lower. Then η_G would be "small". However, one finds that $p_\ell - p_s$ (which is > 0) actually <u>increases</u> as η_G decreases. For lower η_G, the pores open more rapidly (for given $p_\ell - p_s$). In a steady state, this is counterbalanced by increased flow of melt <u>downwards</u>, which requires an increase of pressure upwards. The arriving melt <u>refreezes</u> (to balance pore opening) and the latent heat released is advected away by the matrix.

Provided the analysis of the model is correct, the conclusion is that fracture of the asthenosphere is inevitable, and consequently there is no problem initiating cracks to migrate through the lithosphere. To make a specific statement about the earth, one now needs to adapt the model to cope with the permeability relevant to a fractured permeable medium. The next step is to then connect this fractured asthenosphere to a fractured lithosphere. Any meaningful statement about surface geochemistry lies about four papers away.

REFERENCES

Kirby, S.H., 1983. Rheology of the lithosphere. Revs. Geophys. Space Phys., 21, 1458-1687.

Turcotte, D.L. and J.L. Ahern, 1978. A porous flow model for magma migration in the asthenosphere. J. Geophys. Res., 83, 767-772.

Turcotte, D.L. and E.R. Oxburgh, 1967. Finite amplitude convective cells and continental drift. J. Fluid Mech., 28, 29-42.

Weertman, J., 1971. Theory of water-filled crevasses in glaciers applied to vertical magma transport beneath oceanic ridges. J. Geophys. Res., 76, 1171-1183.

STIRRING AND MIXING

William R. Young

The distinction between stirring and mixing is illustrated by considering a simple experiment: the release of a spot of dynamically passive dye into a moving fluid.

At small times the spot is teased into increasingly fine tendrils and filaments by the motion of the fluid. Thus the gradients of tracer concentration are <u>increased</u>. This cascade towards high wavenumbers is eventually quelled by the action of molecular diffusivity. Thus at large times the gradients of tracer concentration <u>decrease</u>.

Oceanographers refer to the first process as "stirring" and the second as "mixing". The distinction can be made more precise by the solution of a simple advection-diffusion equation. The idea is to locally analyse the action of fluid straining by moving in a translating and rotating frame of reference which reduces the velocity to a pure strain. Thus the concentration, θ, of the passive scalar satisfies.

$$\theta_t - ax\theta_x - by\theta_y - cz\theta_z = k\nabla^2\theta \qquad (1)$$

$$a + b + c = 0$$

$$\theta(x, y, z, 0) = \sin(k_0 x + l_0 y + m_0 z)$$

The solution of this is discussed by Batchelor (1959), but for our present purposes it suffices to note that the mean square gradient is given by

$$\tfrac{1}{2}\overline{\nabla\theta\cdot\nabla\theta} = \tfrac{1}{2}\exp\left[-\frac{\kappa k_0^2}{a}e^{2at}\right]k_0^2 e^{2at} \qquad (2)$$

where $a > b > c$. This function is sketched in figure 1.
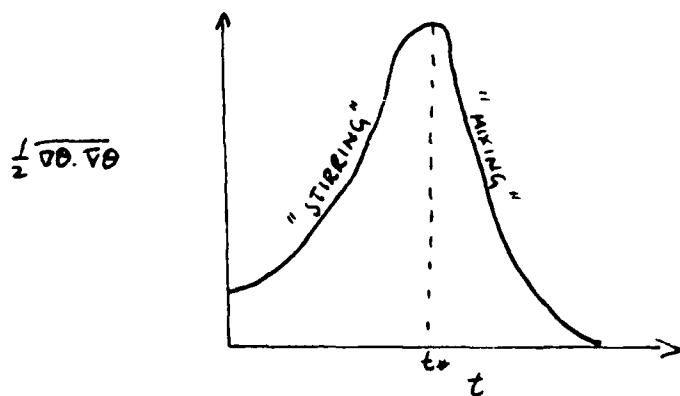
Figure 1. The mean square gradient of θ as a function of time. Initially the gradient increases exponentially (stirring) but eventually there is a precipitious decline (mixing).

Initially the gradients increase because the velocity field increases the wavenumber exponentially. At a time:

$$t* \quad (1/2a) \ \ln(a/\kappa k_o^2) \tag{3}$$

the gradients are a maximum and the wavenumber is

$$k_\kappa = \sqrt{a/\kappa} \tag{4}$$

At larger times the diffusivity takes hold and the gradients of tracer variance vanish rapidly. The transition between stirring and mixing is abrupt and is produced by the reduction of the scalar length scale to $\sqrt{\kappa/a}$. In many geological problems solidification occurs well before the transition scale is reached.

REFERENCES

Batchelor, G.K., 1959. Small scale variations of convected quantities like temperature in a turbulent fluid. Part I. General discussion and the case of small conductivity. J. Fluid Mech. 5, 113-133.

DYNAMICS OF VORTICITY FRONTS
Melvin E. Stern

A uniform vorticity layer rests on a rigid boundary and is separated from an overlying irrotational fluid by a free interface. This vorticity front intersects the rigid boundary at the "nose" of the front, and the evolution of the latter is determined using inviscid and two dimensional theory. The method of contour dynamics is used to eliminate one of the spatial dimensions and the resulting integro-differential equation is solved numerically. The results are partially interpreted by earlier approximate theories (Stern and Paldor, 1983); Stern and Voropaev, 1984) and some new asymptotic approxima- tions. We find that an initially gently sloping front steepens with time until it forms a robust blunt nose, which intrusion propagates into the irrotational fluid at a determined new speed. The irrotation fluid displaced up and over the nose eventually leads to wave breaking on the rear side of the latter. Later on irrotational fluid is engulfed (entrained) in the rear of the nose by the breaking wave. This process is regarded as an aspect of transition to turbulence, and therefore the wavebreaking process has been isolated for further study in a simple piecewise uniform vorticity model that contains no nose.

REFERENCES

Stern, M. E. and Nathan Paldor, 1983. Phys. Fluids 26, 906.

Stern, M. E. and S. I. Voropaev, 1984. Phys. Fluids 27, 848.

TIMESCALES FOR RELAXATION OF NONCONFORMITIES
IN CONTAINED STRATIFIED FLUID

Leslie Hocking

Consider a container full of stably stratified fluid which is abruptly moved to a new location. A translation has no effect on the position of the fluid relative to the container but a rotation alters the constant-density surfaces. For a container with elliptic cross-section, the density surfaces remain planar after the rotation is completed but they are tilted from the horizontal. The angle of tilt can be calculated as a function of the ellipticity and of the angle of rotation. A special case is where the container has parallel side walls. When moved so that these are vertical, the density surfaces are tilted and a sloshing motion is induced. This motion is damped by viscosity and density diffusion also acts to produce horizontal density surfaces. The two parameters governing these diffusions are

$$\lambda = \nu / a^2 (g\beta)^{1/2} \quad , \quad \mu = k / a^2 (g\beta)^{1/2}$$

where ν, k are the two diffusivities, a is a length scale, g gravity. β is the relative density gradient and $\lambda \gg \mu$. Analysis shows that the imescale (relative to the period of the sloshing motion) of the damping of the motion by viscosity is λ^{-1} but the density surfaces become horizontal in a time (λ/μ)$^{1/2}$. Hence the motion ceases before the density is equilibrated when $\lambda^3 \gg \mu$, but if $\lambda^3 \ll \mu$ there is still some motion present after the density surfaces have become horizontal.

LIESEGANG RINGS AND RECURRENT PRECIPITATION

Joseph B. Keller

In 1896 the chemist Liesegang accidentally discovered colored rings of silver chromate in a layer of gel upon which he had placed a crystal of silver nitrate. The rings were formed by silver ions from the crystal which had diffused into the gel and reacted with chromate ions that were present there in the form of potassium dichromate. The remarkable feature of the phenomenon was that the silver chromate had not formed in a continuous zone surrounding the crystal, but that it formed in separate rings with clear spaces between them.

In 1897 Ostwald proposed the explanation that the reaction product, silver chromate, did not precipitate out in the form of visible particles until its concentration exceeded the saturation concentration. He then argued qualitatively that the depletion of the chromate ions by the reaction would result in the observed ring structure.

The same phenomenon has been observed in other chemically reacting systems. It has been proposed as an explanation of the colored rings that occur in rocks and minerals. Therefore many experimental investigations have been made of this phenomenon. They are usually performed in a straight capillary tube, with one reagent A supplied at one end of the tube and the other reagent B initially distributed throughout the tube. As A diffuses into the tube it reacts with B to form a product C. The product C then precipitates out in the form of solid particles D in bands with clear spaces between them.

Measurements have been made of the time t_n at which the n-th band begins to appear, and of its distance x_n from the end at which A is supplied. These values are found to be related by the equation

$$x_n = \alpha\, t_n^{1/2} \tag{1}$$

This is the kind of relation which occurs in phenomena governed by diffusion. In addition the t_n, except for the first one which is zero, satisfy the equation

$$t_{n+1} = \beta \tag{2}$$

Theoretical Investigations

Mathematical formulations of Ostwald's explanation have been presented by Wagner (1950), Barenblatt, Zeldovitch and Sagalnick (1964), Prager (1964) and Keller and Rubinow (1981). The first three sets of authors analyzed the diffusion of the reactants A and B, and assumed that a band formed where and when the product of their concentrations reached a critical value. They were able to derive the relations (1) and (2). However they could not determine the absolute space or time scales, nor could they show why or when any band stopped growing. Keller and Rubinow (1981) supplemented the previous analyses by taking account explicitly of the chemical reaction rate r and of the precipitation rate p. By doing so they were able to determine the absolute scales and to show when a band stopped growing.

The equations they used to determine the concentration $a(x,t)$ of A, $b(x,t)$ of B, $c(x,t)$ of C and $d(x,t)$ of D are:

$$a_t = D_A a_{xx} - \nu_A r, \tag{3}$$

$$b_t = D_B b_{xx} - \nu_B r, \tag{4}$$

$$c_t = D_C c_{xx} + \nu_C r - p, \tag{5}$$

$$d_t = p. \tag{6}$$

These equations are assumed to hold in the tube $x > 0$ for $t > 0$. The initial and boundary conditions are:

$$a = 0, \quad b = b_o, \quad c = d = 0 \qquad \text{at } t = 0, \ x > 0, \tag{7}$$

$$a = a_o, \quad b_x = c_x = 0 \qquad \text{at } x = 0, \ t > 0. \tag{8}$$

The reaction rate, r, and precipitation rate, p, are given by:

$$r(\_,b,c) = k_+ a^{\nu_A} b^{\nu_B} - k_- c^{\nu_C} \tag{9}$$

$$p(c,d) = q(c - c_s)_+ \qquad \text{if } c \geq c^* > c_s \text{ or } d > 0,$$

$$= 0 \qquad \text{if } c < c^* \text{ and } d = 0. \tag{10}$$

Here ν_A, ν_B and ν_C are the numbers of molecules of each type involved in the elementary reaction

$$\nu_A A + \nu_B B \underset{k_-}{\overset{k_+}{\rightleftarrows}} \nu_C C, \tag{11}$$

while k_+ and k_- are the rate constants for the forward and reverse reactions. In (10) q is a constant while c^* is a fixed concentration exceeding the saturation value c_s, and $(c - c_s)_+ = c - c_s$ if $c - c_s \geq 0$ but $(c - c_s)_+ = 0$ if $c - c_s < 0$. Thus precipitation starts only when c exceeds c^*, and continues as long as c exceeds c_s provided that $d > 0$.

These reaction-diffusion-precipitation equations were simplified by assuming that reaction is fast compared to diffusion, and that $a_o \gg b_o$. Then (3) – (5) are replaced by two equations for the conservation of A and B molecules, plus the equilibrium condition $r(a,b,c) = 0$. This simplification is justified by an asymptotic analysis based upon b_o/a_o being small. Results for the width of the first band as a function of time were obtained. Then the method of the earlier authors was used to find the times and positions for initiation of the subsequent bands.

Later Experiments and Theories

Ross (1982) and his colleagues have performed experiments in which the reactants A and B were premixed, but in which bands still formed. Since the reactants do not diffuse toward one another, the Ostwald mechanism cannot explain this occurrence. Furthermore they observed that small precipitate

particles formed everywhere at first. Then later they disappeared from some regions, leaving clear spaces, while larger particles formed in other places, producing visible bands.

The initial formation of small particles everywhere is understandable since C is produced everywhere in sufficient concentration to produce a precipitate. The subsequent pattern formation is probably a consequence of the instability of the uniform state. This is due to the fact that particles smaller than average will shrink and disappear while particles larger than average will grow. An analysis of this mechanism, based upon the usual diffusion equation, shows that it does indeed produce an instability, but the most unstable wavelength is zero. Therefore another analysis of it, based upon the Cahn-Hilliard diffusion equation, has been performed by Falkowitz and Keller (1984). That analysis yields a finite wavelength of maximum instability, and leads to a steady state with equally spaced bands.

References to the earlier literature can be found in the following:

Falkowitz, M. and J.B. Keller, 1984. Precipitation Pattern Formation, preprint, Department of Mathematics, Stanford University.

Keller, J.B. and S.I. Rubinow, 1981. J. Chem. Phys., 5000.

Ross, J., S.C. Miller and S. Kaig, 1982. J. Chem. Phys., 76, 1392-1406.

Ross, J. and G. Venzel, 1982. Dept. of Chemistry, Stanford University, preprint.
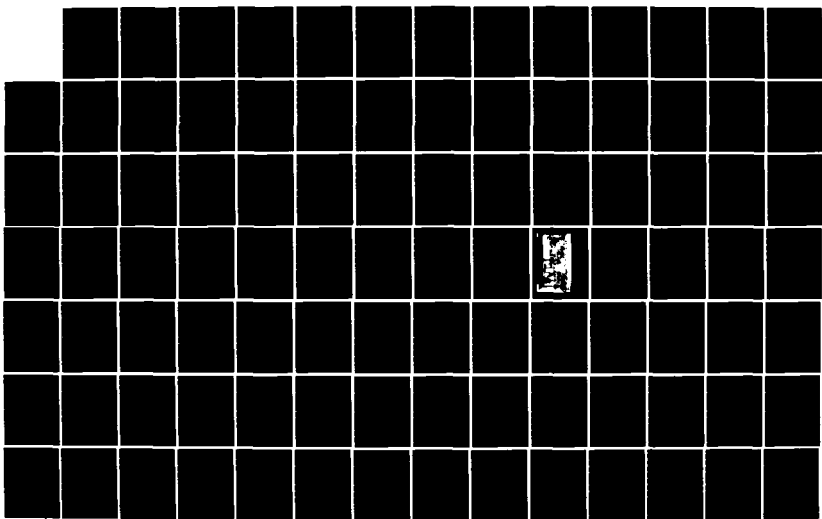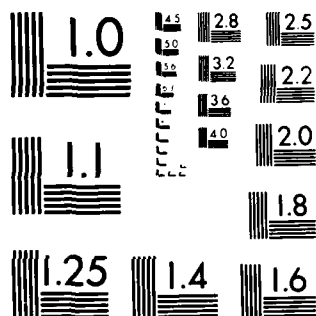
MICROCOPY RESOLUTION TEST CHART

NATIONAL BUREAU OF STANDARDS 1963 A

PATTERNS OF INSTABILITY

Edward A. Spiegel

When several bands of unstable modes can go unstable at once, one gets a set of nonlinear p.d.e.'s that govern the competition of the various structures. A scheme for deriving the general form of such amplitude-evolution equations has been worked out with P. H. Coullet. The work was supported by the CNRS and the NSF.

METALLIC RAIN

Edward. A. Spiegel

In many A-type stars one detects remarkable overabundances of certain elements (e.g. Hg, Mn) relative to stars of normal composition (Wolff, 1983). The most widely accepted explanation, given by Michaud (see Wolff, 1983), is that the overabundance is superficial and is the result of outward diffusion of certain elements on account of radiative forces. It is not yet so clear why these elements are not driven out of the star.

The overabundant species in question are trace elements and make negligible contribution to the density of the gas. Yet they do affect the buoyancy since the photobuoyancy is a significant part of the force on a fluid element. John Lin and I have computed the static state of the atmosphere seeded by an element with a strong resonance line. When the line is optically thick, the static state is unstable and an unusual sort of meteorology occurs.

The National Science Foundation supported the work.

REFERENCE

Wolff, S., 1983. The A-Stars. NASA.

THE SALT FINGER ZONE

Louis N. Howard

In double-diffusive convection with the less diffusible substance destabilizing and the more diffusible one stabilizing - e.g. hot and salty above, cold and fresher below - one generally obtains a series of layers of nearly homogeneous fluid, separated by zones occupied by salt fingers. A model for such developed finger zones was given by Melvin Stern, based on a solution of the equations which is periodic in the horizontal (x) and independent of the vertical (z), except for "background" uniform gradients of salt and temperature. The relevant equations are:

$$w_t + p_z - g(\alpha T - \beta S) = \nu w_{xx} \tag{1a}$$

$$T_t + w T_z = \kappa_T T_{xx} \tag{1b}$$

$$S_t + w S_z = \kappa_S S_{xx} \tag{1c}$$

Here T_z and S_z are constants, and T and S represent z-independent deviations from these background constant gradients. The vertical velocity w is also independent of z, and the horizontal velocity components are zero. These equations have solutions in which $p = 0$ and the other variables are multiples (denoted by the same letters) of $\sin(kx) \exp(\lambda t)$; these multiples satisfy the equations:

$$\lambda w - g(\alpha T - \beta S) = -k^2 \nu w$$

$$\lambda T + w T_z = -k^2 \kappa_T T$$

$$\lambda S + w S_z = -k^2 \kappa_S S$$

which may be regarded as determining λ (through the condition of existence of a nonzero solution), or as fixing a relation among the other parameters if λ is given.

If we introduce the parameters $\sigma = \nu/\kappa_T$ and $\tau = \kappa_S/\kappa_T$, nondimensionalize the variables by

$$T = T_z \theta/k \qquad S = S_z s/k \qquad w = k \kappa_T W,$$

and set

$$\lambda = \kappa_T k^2 \Lambda, \quad R_T = \alpha g T_z/(k^4 \nu \kappa_T), \quad R_S = \beta g S_z/(k^4 \nu \kappa_T),$$

the condition for existence of a nonzero solution is

$$(\Lambda + 1)(\Lambda + \tau)(\Lambda/\sigma + 1) - (\Lambda + 1)R_S + (\Lambda + \tau)R_T = 0.$$

In particular there is a steady solution ($\Lambda = 0$) if

$$R_S = \tau(R_T + 1).$$

This condition may be used to calculate k if the gradients are given, and actually gives a reasonable estimate of the horizontal size of salt fingers. It should be noted that although these calculations involve only very simple linear equations, this is not a linearized model but an exact nonlinear solution of the Boussinesq equations. However, it has the somewhat disturbing feature that if k is smaller than the value for a steady solution just mentioned then there is also an exact solution, and it grows exponentially in time. Various, not altogether conclusive, discussions referring to stability considerations etc. have been put forward to try to relate this attractive and simple solution more closely to real salt finger zones. Here we wish to discuss a somewhat different idealized model which has perhaps some advantages as a basis for understanding these zones.

Real salt finger zones cannot increase the speed of flow up and down in the fingers in the manner of Stern's model because they do not have the infinitely extended destabilizing salt gradient which in a sense is the "physical" basis of the exponential growth. Rather, they are supplied from above and below by "reservoirs" – the homogeneous regions. They are "driven" by salt and temperature differences rather than gradients; the model uses gradients because this is the way to get a z–independent solution and make the problem tractable. It is also true that the fingers really are much longer than they are wide, making the idealization plausible, and the horizontal mean temperature is usually quite close to a uniform gradient connecting the reservoir values. However, particularly when τ is small, the mean salt distribution is more nearly a constant half way between the reservoir values – the salinity is not much changed from that of the upper reservoir in the descending fingers nor from that of the lower in the ascending ones. For this reason, the "zero-order" form of the model to be discussed here is based on a salt difference and a temperature gradient. It is also going to be independent of z, and to make such a model consistent we must avoid the fact that a mere salt <u>difference</u> will eventually be completely "shorted out" by horizontal diffusion – thus the zero-order model will have $\tau = 0$.

Any model in which $u = v = 0$, $w = w(x,t)$, salinity $= S_0 + zS_z + S(x,t)$, temperature $= T_0 + zT_z + T(x,t)$ and pressure $= p(x,t) +$ (hydrostatic part balancing the x-independent density field) is described by the same equations (1) used above. In the present case we have $\kappa_S = 0$ and $S = $ const. (but a different constant in up than in down fingers), so (1c) is trivially satisfied, and S in (1a) is taken to be $\Delta S/2$ in descending fingers, $-\Delta S/2$ in ascending ones. We introduce dimensionless variables as above, except that now we set $R_S = g\,\beta\,\Delta S/(\,\nu\kappa_T k^3)$, and the equations become:

(as before $p = 0$)

$$W_t/\sigma - R_T\,\theta + R_S\,s = W_{xx} \qquad (2a)$$

$$\theta_t + W = \theta \qquad (2b)$$

in which x stands for the former kx and t for $\kappa_T k^2 t$, and $s = -1/2$ for $0 < x < \pi$ and is otherwise an odd periodic function of x with period 2π . It is easy to show that all solutions of these equations tend to the steady solution as $t \rightarrow \infty$; there is here no question of exponentially growing solutions, and the steady solution is stable to all perturbations which respect the periodicity and z-independence. The time-independent forms of these equations are analogous to those of the Ekman layer – they are in fact those of the "buoyancy

layer", forced by the s term which represents the weight of the salinity deviation. The two steady equations can be combined in the single complex equation

$$(W + iR_T^{\frac{1}{2}}\theta)_{xx} - iR_T^{\frac{1}{2}}(W + iR_T^{\frac{1}{2}}\theta) = R_S s \tag{3}$$

The solution to this equation which is a continuous and continuously differentiable (odd) periodic function is then readily determined; on $0 < x < \pi$ it is given by the formulas:

$$W = \frac{R_S}{2R_T^{-\frac{1}{2}}} \frac{\sin b(\pi - x)\sinh bx + \sin bx \sinh b(\pi - x)}{\cos b\pi + \cosh b\pi}$$

$$\theta = \frac{R_S}{2R_T}\left(\frac{\cos b(x - \pi)\cosh bx + \cos bx \cosh b(x - \pi)}{\cos b\pi + \cosh b\pi} - 1\right)$$

in which $b^4 = R_T/4$. If R_T is large, which may be thought of as small k, i.e. wide fingers, this structure becomes a row of antisymmetric buoyancy boundary layers on the interfaces between rising and descending regions. There is thus a natural horizontal scale in this problem, which in dimensional form is

$$L = 1/(kb) = (\alpha g T_z/\nu\kappa_T)^{-1/4},$$

the thickness of the buoyancy boundary layer. If the fingers are narrow compared to L the flow becomes essentially a row of Poiseuille flows, alternately up and down. Of course this model (so far) does not actually select any particular value of b as the one to use in comparing this idealization to measured quantities.

The interpretation I should like to give to this model solution is that it can be expected to give a reasonable description of the flow in a finger zone connecting two reservoirs when the actual finite thickness of the zone is large compared to the width of the fingers but not so large that horizontal diffusion of salt upsets the hypothesis of constant salinity in each finger. It is naturally to be expected that horizontal salt diffusion will develop some kind of a boundary layer along the interfaces between the rising and descending fingers, but assuming they are not too long this boundary layer (for small τ) should still be thin compared to the buoyancy layer. At the interface between adjacent fingers, the vertical velocity varies linearly with x. After appropriate rescaling (which we omit), the salinity boundary layer equation becomes

$$xS_z = S_{xx} \tag{4}$$

This equation is to be considered on $0 < z < 1$ and $-\infty < x < \infty$, with the conditions that $S = 1/2$ for $x < 0$ at $z = 1$ and $S = -1/2$ for $x > 0$ at $z = 0$, with S approaching $1/2$ and $-1/2$ as x goes to $-\infty$ and $+\infty$. These somewhat unusual conditions are seen to be appropriate both by consideration of the physics of the salinity boundary layer, and by noticing the mathematical structure: the characteristics of the parabolic equation (4) are directed upward for $x > 0$, but downward for $x < 0$.

To solve this problem, we consider first a simpler version of it: the same equation (4) but in $x > 0$, $z > 0$, with $S = 0$ on $z = 0$ and $S = f(z)$ on $x = 0$. Invariance of the equation under a scaling transformation leaving x^3/z fixed

suggests the existence of similarity solutions depending on this variable (or its cube root); the latter are readily found and one of them satisfies the condition $S = 0$ on $z = 0$ for $x > 0$, namely:

$$S_0(x,z) = \int_{x/z^{1/3}}^{\infty} \exp(-u^3/9)\, du$$

The value of this function on $x = 0$ for $z > 0$ is a constant, which can be shown to be $\Gamma(1/3)/3^{1/3}$; thus S_0, or a multiple of it, solves the problem in the special case of a constant for $f(z)$. The case of a general $f(z)$ can be treated by taking the Laplace transform in z, and using the above special solution to help in evaluation of the inverse transform. The result is

$$S(x,z) = (3^{1/3}/\Gamma(1/3)) \int_{x/z^{1/3}}^{\infty} \exp(-u^3/9)\, f(z - x^3/u^3)\, du$$

which can readily be checked directly.

By similar methods, the same problem with $S = f(z)$ replaced with $S_x = g(z)$ can be solved; from this the relation between an f and g which corresponds to the same solution S can be determined. It is

$$f(z) = -(\Gamma(1/3)/3^{1/3}\,\Gamma(2/3))\, I^{1/3}(g) \tag{5}$$

where I^n denotes the Riemann–Liouville fractional integral

$$I^n(f) = (1/\Gamma(n))\int (z - \zeta)^{n-1}\, f(\zeta)\, d\zeta$$

We now return to our original salinity boundary layer problem. Let $f(z) = S(0,z)$, and $g(z) = S_x(0,z)$, $0 < z < 1$. Both of these are at present unknown, but they must be approached from both positive and negative x. The function $S + 1/2$ is zero on $z = 0$ and $f(z) + 1/2$ on $x = 0$ (and satisfies (4)), so it can be related to $g(z)$ by the above formula (5). Similarly $S(-x, 1-z) - 1/2$ is zero on $z = 0$ and $f(1-z) + -1/2$ on $x = 0$, and has x-derivative $-g(1-z)$ on $x = 0$. A second use of (5) provides another relation between f and g, and elimination of f between these two finally gives the following integral equation for $g(z)$:

$$\int_0^1 |z-\zeta|^{-2/3}\, g(\zeta)\, d\zeta = -3^{1/3}\,\Gamma(2/3)$$

Making a slight rescaling, we now consider the integral equation

$$\int_0^1 |z - \zeta|^{-2/3}\, G(\zeta)\, d\zeta = 1 \tag{6}$$

The solution to this equation is

$$G(z) = (z(1 - z))^{-1/6}/(2\pi) \tag{7}$$

This fact does not seem to be immediately obvious, but I have found a proof of it (which is unfortunately somewhat too lengthy to fit into this so-called abstract). The conjecture that (7) solves (6) was originally obtained by guessing, on the basis of a partial analytical understanding combined with an approximate numerical solution of (6). From (7) and the formulas given above the whole structure of the salinity boundary layer can be determined.

Further investigations of the physical and mathematical aspects of this problem are in progress in collaboration with George Veronis, with whom I have had many interesting discussions on these topics this summer, and who has contributed a great deal to the ideas discussed here.

FINGER, BUBBLE, TENDRIL, SPIKE

Hassan Aref

An attempt was made to survey instances of interfacial dynamics in fluid flows, focussing on the structural features that interfaces develop and on the evolution and interaction of such structures. The limit of completely passive advection of a line of particles was briefly mentioned, and the possibility of "chaotic advection" was noted. Homoclinic oscillations, called "tendrils" by Berry and collaborators, are an important feature of passively advecting curves and lead to dramatic interfacial stretching.

Most attention was paid to examples in stratified flow where a sharp interface has at any instant a representation as a vortex sheet. Examples where this property has led to a useful numerical scheme for following the evolution include the "fingering" seen in stratified flow of immiscible fluids in a Hele Shaw cell, and the two-dimensional "bubble and spike" of the Rayleigh-Taylor problem (for incompressible, inviscid, immiscible fluids). Results for both these cases were discussed.

Most of the author's own work mentioned in this survey appears in the following publications:

Aref, H., 1984. Stirring by chaotic advection. J. Fluid Mech., 143, 1-21.

Tryggvason, G. and H. Aref, 1983. Numerical experiments on Hele Shaw flow with a sharp interface. J. Fluid Mech., 136, 1-30.

Tryggvason, G. and H. Aref, 1984. Finger interaction mechanisms in stratified Hele Shaw flows. J. Fluid Mech. (Submitted).

OBTAINING VELOCITIES FROM TRACER DISTRIBUTIONS

George Veronis

The justification for gathering an increasing amount of chemical tracer data on oceanographic cruises is often asserted to be its potential contribution to determining circulation patterns. Such a use requires an inverse calculation based on some form of the advective-diffusive equation. The purpose of the work reported in this seminar is to determine the feasibility of such an inverse study.

The approach is (the direct problem) to calculate tracer distributions consistent with a known velocity field and given boundary values for a finite basin and then (the inverse problem) to use the derived tracer distributions to determine a consistent velocity field for a portion of the basin. This calculated velocity is compared with the original (known) velocity in the same portion of the basin in order to assess the validity of the procedure. The inverse problem is intended to simulate the type of study that one makes when gathering tracer data to determine the implied velocity field in a limited portion (the sampling region) of the ocean.

Our "ocean" is a channel with uniform horizontal inflow at the left and outflow at the right. Our "sampling region" is a small (5 gridpoint x 5 gridpoint = 16 gridcell) box with the concentration at the center of each gridcell. For a 2D system the streamfunction (ψ) is evaluated at the gridpoints so for a single tracer the inverse problem leads to 25 unknown values of ψ connected by 16 equations (one for each gridcell). Since ψ needs to be determined only to within an arbitrary constant, there are really only 24 unknown values of ψ.

The linear algebraic system based on a single tracer is underdetermined (16 equations and 24 unknowns). All inverse calculations based on an underdetermined system led to a velocity field that bore no resemblance to the known field. When two tracers were used and the same grid network was used for the direct and inverse problems (i.e., no truncation error was present), the known velocity was reproduced exactly. When the tracer data was taken from alternate grid points (truncation error introduced), the derived velocity from the overdetermined system (32 equations and 24 unknowns) was a good approximation to the known flow.

Experiments were made with a single tracer and qualitative velocity information. For example, suppressing the vertical velocity is consistent with the original flow but it allows a shear in the horizontal flow. The inverse analysis of this overdetermined system with truncation error gave good results. When the auxiliary velocity information was downweighted to 10^{-3} of the normal weight, the derived flow was still a good approximation to the known flow. When the qualitative information was inconsistent with the known flow (e.g., suppressing horizontal velocity), the derived velocity did not resemble the known velocity. When this qualitatively incorrect information was downweighted, the system rejected it (in contrast to what it did with correct qualitative information).

FINGER PUZZLES

Raymond W. Schmitt

Results of theoretical and laboratory work on the heat/salt flux ratio in salt fingers were reviewed. The early laboratory work of Turner (1967) on heat-salt fingers gave a density flux ratio which was about 0.56 and independent of $R\rho$ ($=\alpha Tz/\beta Sz$). In contrast, the data from the sugar-salt system indicated that the flux ratio was about 0.9 (Lambert and Demenkow, 1972). Both of these results can be explained by assuming that the fastest growing finger either dominates the finger interface throughout the experiment or simply sets the scale for later equilibrium states of the system. This is shown in Schmitt (1979a). More recent experiments (Griffiths and Ruddick, 1980) continue to agree with the theory in the sugar-salt case, but discrepancies have appeared in the heat-salt experiments. Both Schmitt (1979b) and McDougall and Taylor (1984) have found that the flux ratio falls below the curve for the fastest growing finger as $R\rho$ increases. However, it remains above the relation for a simple equilibrium finger in the interface, and does approach the value of 0.25 given in the theory of Stern (1976) as $R\rho$ gets above 4.0. For $R\rho$ close to one, the data agree with the relation given by the growth rate maximization criteria. One possible explanation for this is that growth rate maximization is not strongly selective, since the instability is fairly broad-banded, and the fingers can select a mode which is still growing fairly rapidly, but has a lower flux ratio in order to maximize buoyancy flux (Stern, 1976).

Observations of salt fingers in the ocean by Magnell (1976) and Gargett and Schmitt (1982) clearly show that the fastest growing finger dominates the horizontal wavenumber spectrum. However, there is considerable bandwidth to the observed spectra which is consistent with the Schmitt (1979a) model, but hard to rationalize with the rather narrow peak of the Huppert and Linden (1976) spectral model. This poses something of a problem for any attempts to construct a steady salt finger interface model, for only one size finger can be in equilibrium once the average T and S gradients have been specified. This is finger puzzle number one for the GFD group of 1984.

Since geological fluid mechanics is the topic this year, the extension of the Schmitt (1979a) model to other Prandtl and Lewis number systems was reviewed. This has been presented in Schmitt (1983). For magmas, the theory predicts slow growth rates (like sugar-salt) but lower flux ratios (like heat-salt). The liquid metal systems appear to be especially interesting with high growth rates, large bandwidths and very low flux ratios. Some experimental data from such systems would be very valuable.

Finally, a distinct tendency for the ocean to "avoid" having $R\rho$ close to one was noted. Regions with $R\rho$ close to unity are found to be rich in fine- and microstructure and appear to be actively mixing. Histograms of the distributions of $R\rho$ have a bimodal structure, with a peak on the finger side ($R\rho > 1$) near 1.9, and a peak on the diffusive side ($0 < R\rho < 1$) near 0.7. This is what would be expected for the unequal mixing rates of T and S for the two processes; that is, fingers transport more salt than heat and increase $R\rho$, diffusive interfaces transport more heat than salt and decrease $R\rho$. For the fingers this peak corresponds to the density ratio at which the finger e-folding time is just equal to one local buoyancy period. Thus, a picture emerges of finger dominance of the mixing processes at density ratios close to

one. If the process is to be studied in analogous systems, such as sugar-salt, then care must be taken to work at $R\rho$ close enough to one ($R\rho = 1.02$), so that the fingers are growing sufficiently fast. Schmitt (1983) gives the appropriate value of $R\rho$ in a number of double diffusive systems.

REFERENCES

Gargett, A. E. and R. W. Schmitt, 1982. Observations of salt fingers in the central waters of the eastern North Pacific. J. Geophys. Res. 87, (C10), 8017-8029.

Griffiths, R. W. and B. R. Ruddick, 1980. Accurate fluxes across a salt-sugar finger interface deduced from direct density measurements. J. Fluid Mech. 99, (1) 85-95.

Huppert, H. E. and P. F. Linden, 1976. The spectral signature of salt fingers. Deep-Sea Res. 23, 909-914.

Lambert, R. B. and J. W. Demenkow, 1972. On the vertical transport due to fingers in double diffusive convection. J. Fluid Mech. 54, 627-640.

Magnell, B., 1976. Salt fingers observed in the Mediterranean outflow region (34 N, 11 W) using a towed sensor. J. Phys. Oceanogr. 6, 511-523.

McDougall, T. J. and J. R. Taylor, 1984. Flux measurements across a finger interface at low values of the stability ratio. J. Mar. Res. 42, 1-14.

Schmitt, R. W., 1979a. The growth rate of super critical salt fingers. Deep-Sea Res. 26, 23-40.

_____, 1979b. Flux measurements on salt fingers at an interface. J. Mar. Res. 37, 419-436.

_____, 1983. The characteristics of salt fingers in a variety of fluid systems; including stellar interiors, liquid metals, oceans, and magmas. Physics of Fluids 6, (9), 2373-2377.

Stern, M. E., 1976. Maximum buoyancy flux across a salt finger interface. J. Mar. Res. 34, 95-110.

Turner, J. S., 1967. Salt fingers across a density interface. Deep-Sea Res. 14, 599-611.

PETROLOGIC STUDIES OF THE RESIDUES OF MANTLE MELTING

Henry J.G. Dick

The proportion and composition of minerals from some 273 peridotites from 43 dredge stations in the Atlantic, Caribbean, and Indian Oceans have been compared to each other and to data from alpine-type peridotites to draw a picture of the conditions at the end of mantle melting along mid-ocean ridges and beneath island arcs and their adjacent basins. The principal conclusions to be drawn are that there are systematic differences in the degree of melting along mid-ocean ridges which correlate to proximity to mantle plumes, and that the conditions of melting in the mantle beneath the island arc and intra-arc environments represented by alpine peridotites differ greatly from that beneath ocean ridges.

Abyssal peridotites dredged from the ocean ridges range from diopside poor peridotites (harzburgite) to diopside rich peridotites (lherzolite) representing a continuous variation in the proportions of the principal constituents. The average composition contains 76.9% olivine, 19.2% enstatite, 3.34% diopside, and 0.53% spinel. Slightly less than a third of all abyssal peridotites contain small amounts of plagioclase ($<$ 1%) which has crystallized from trapped melt. Only rarely do dredged peridotites contain more plagioclase (up to 17%). Based on certain incompatible elements which are greatly enriched in the liquid during melting (e.g. Na_2O and TiO_2) abyssal peridotites contain virtually no basaltic component ($<$ 1%). Since estimates of the degree of melting of the mantle required to generate abyssal basalt range from 10 to 30%, it is evident that little, if any, melt is retained in the residual mantle at the end of melting as a general case. This would also suggest that little melt is actually held with the residue during melting, but must rapidly pass upwards towards the crust as it forms mixing with new melt forming in the rocks through which it flows.

Abyssal peridotites dredged in the vicinity of "mantle plumes" or "hot spots", such as the Azores or Bouvet Island, have the most depleted compositions, while peridotites dredged at locations removed from such regions are systematically less depleted. The modal data correlate well with mineral compositions, with the peridotites most depleted in enstatite and diopside also having the most refractory mineral compositions. This demonstrates that they are the probable residues of variable degrees of mantle melting. Further, there is a good correlation between the modal compositions of the peridotites and the major element composition of spatially associated basalts. This demonstrates that the two must be related as is frequently postulated. The high degree of depletion of the peridotites in basaltic components in the vicinity of "mantle plumes" reacquires additional heat providing direct evidence for a thermal anomaly in such regions - justifying their frequent designation as "hot spots". The high incompatible element concentrations in these plume basalts, however, are contrary to what is expected for such high degrees of melting, and thus require selective contributions from locally abundant enriched veins at the beginning of melting or contamination by another magma from depth.

Although many abyssal peridotites are poor in diopside, with some containing virtually none, enstatite from these same peridotites is always saturated with respect to diopside. This is a critical point, as it means that melting of the abyssal mantle is constrained by the thermal barrier represented by the pseudo-invariant point: olivine + enstatite + diopside + spinel. This is clearly not the case for mantle peridotites found in alpine-type peridotite complexes.

Alpine-type peridotites overlap the range of compositions found for abyssal peridotites, but extend to far more depleted and enriched compositions. A number of alpine-type peridotites are known to be far less depleted than abyssal peridotites. Typical of these are the Balmuccia, Baldissero, and Finero bodies in the Alps of Europe which are believed to represent sub-continental basement. Many alpine-type peridotites, however, contain enstatite undersaturated with respect to diopside. These same complexes also contain highly magnesian Al-poor and Cr-rich minerals lying outside the range for abyssal peridotites. Melting of such peridotites, then, has occurred well into the three phase field where only olivine, enstatite and spinel are left in the residue. This requires substantially different melting conditions t⁺ are present beneath mid-ocean ridges. It is unlikely that the thermal str ture of the mantle beneath back arc basins and island arcs permits higher temperatures at a given depth than beneath a mid-ocean ridge. This means th t the melting point of the mantle must be depressed in the arc and intra-arc environment, most likely due to the introduction of volatiles from a sub-duction zone. Supporting evidence for this hypothesis is found in the composition of late magmatic and pegmatitic veins in alpine-type peridotites. These suggest that there was incongruent melting of enstatite to olivine plus melt, leaving behind monomineralic dunites, and conversely a reaction-relation between melt and olivine to produce enstatite during crystallization, producing monomineralic orthopyroxenite pegmatites by reaction of melt with wall rock in dikes at the end of melting. The introduction of water into peridotite is known experimentally to both greatly depress the melting point and to induce incongruent melting of pyroxene at pressures consistent with mantle melting.

MULTIPLE CONDUCTIVE STATES FOR TWO-FLUID SYSTEMS

Pierre Welander

Consider a system of two immiscible fluids, between two horizontal boundaries, kept at temperatures $T = 0$ (lower) and $T = \Delta T$ (upper). The conductive, statically steady state has a temperature T_i at the interface, determined by the relations $K \dfrac{T_i}{h} = K' \dfrac{\Delta T - T_i}{h'}$ (continuity of heat flux), where h, h', K, K' are the layer thicknesses and thermal conductivities of the lower and upper layer fluids; we find $T_i = \gamma \Delta T$, $\gamma = \left(1 + \dfrac{K}{K'} \dfrac{h'}{h}\right)^{-1}$ (Fig. 1). If we interchange the two layers and let the system come to its conductive steady state, we have the new interface temperature $T_i^* = \gamma^* \Delta T$, $\gamma^* = \left(1 + \dfrac{K'}{K} \dfrac{h}{h'}\right)^{-1}$ (Fig. 2). Assume linear equations of state $\rho = \rho_o(1 - \alpha T)$, $\rho' = \rho_o'(1 - \alpha' T)$; then both above cases are statically stable provided

$$\frac{1 - \gamma^* \alpha \Delta T}{1 - \gamma^* \alpha' \Delta T} \leq \frac{\rho_o'}{\rho_o} \leq \frac{1 - \gamma \alpha \Delta T}{1 - \gamma \alpha' \Delta T} \tag{1}$$

This condition arises from the requirements that the original density step at the interface, $\rho - \rho'$, as well as the new step, $\rho' - \rho$, is nonnegative, at the temperatures T_i and T_i^*, respectively. If, for example, $\alpha' > \alpha$, $h' \ll h$, and $\rho_o' \approx \rho_o$, we can satisfy these relations and thus have two statically stable steady states, as exemplified in Figs. 1-2. The more "expansive", thin layer can stay either at the top as a light layer, or at the bottom as a heavy layer. We can actually have an infinity of steady conductive solutions, all statically stable, with part of the original thin layer at the top and part at the bottom (Fig. 3). It is, however, not possible to have more than three separate layers. Transitions between different statically stable states can take place by help of an open conduct-int tube, a "fountain" (Fig. 4). The fountain can only go in one direction, and only the more "expansive" fluid can run in the tube. It is assumed that the surrounding fluid adjusts conductively; if the tube flow gives a quick adjustment, and the interior stays adiabatic during this time, more complex solutions involving "overshooting" may occur. Finite amplitude instabilities may provide natural transitions between different steady states. The transitions may appear as "plumes" or "blobs" breaking off from the more "expansive layer. The perturbations may spread laterally from a local area of perturbation (see Fig. 6). Preliminary laboratory experiments, made with pthalic acid and salt water, suggest that a natural "fountain" can be sustained, even without a tube, if aided by interfacial tension (Fig. 5). The phenomenon discussed has similarities with "salt fingers" as well as with collective cumulus convection. The stability theory needs to be developed. The system is found to be stable for infinitesimal perturbations, but one should be able to find theoretical examples of growth for suitable finite amplitude perturbations. Work on this problem, along a line proposed by W. Young, is proceeding.
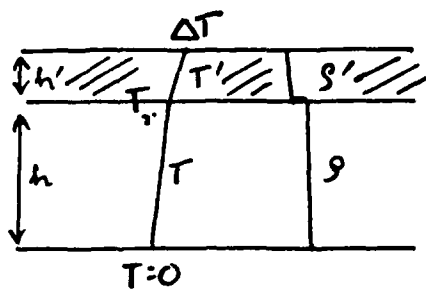
Figure 1: Original two-layer system, stably stratified. In all cases the temperature is T = 0 at the bottom, T = ΔT at the top. There may be a density step at the interface.
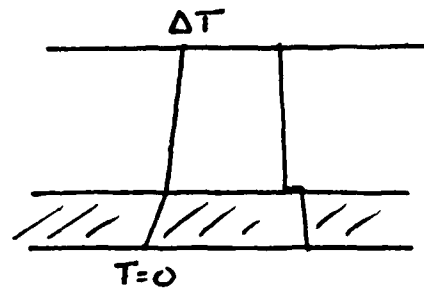
Figure 2: The switched state, in conductive balance. If the criteria (1) is satisfied, the fluid is still statically stable.
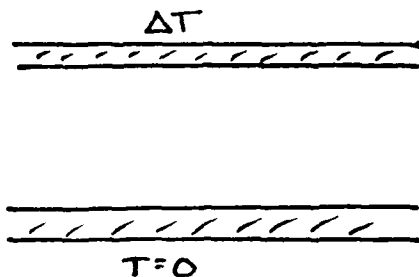
Figure 3: Partial switching, giving three layers.
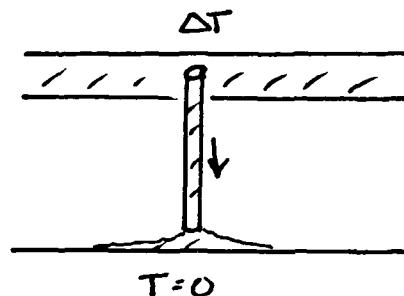
Figure 4: Switching by tube convection. The tube flow can only go in one direction, contrary to the "salt fountain".
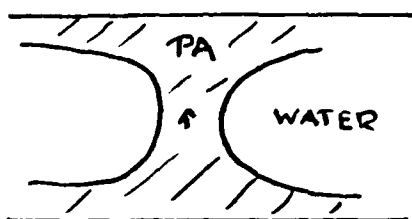
Figure 5: A natural "fountain", as seen in a preliminary experiment using pthalic acid (PA) and water (1% salt dissolved). Vertical dimension is about 5 cm. Weak creeping motions occur, the "tube" is kept together by surface tension.
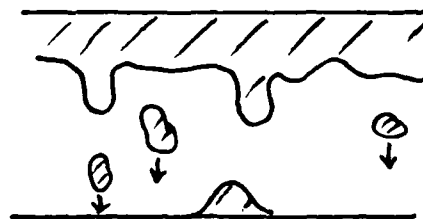
Figure 6: Hypothetical instability which spreads laterally. The problem has similarities with cumulus convection.

MOMENTUM TRANSPORT IN THERMOHALINE STAIRCASES

Barry Ruddick

Given the buoyancy flux in an actively convecting, sheared thermohaline staircase, what is the momentum flux? A simple constant stress model for such a system shows that the appropriate average viscosity $\langle A \rangle$, is the harmonic mean (Keller, 1977):

$$\langle A \rangle = \langle 1/A(Z) \rangle^{-1}.$$

This implies that the average viscosity is controlled by the regions of small eddy viscosity, where the shear and dissipation are high. If the staircase is idealized as a sequence of interfaces, of thickness H_2, eddy viscosity A_2, and layers of thickness H_1, and large eddy viscosity A_1 ($\gg A_2$), then

$$\langle A \rangle \approx A_2 (1 + H_1/H_2)$$

Thus the average viscosity is proportional to, but much larger than, that at the interface. Two mechanisms for interfacial momentum transport were considered; direct salt-finger Reynolds stresses and interfacial internal waves generated by the motion of convective elements. Because salt fingers effect downward salt transport by means of lateral heat transport, the effects of molecular viscosity are at least as important. In a shear, the viscous stresses annihilate the horizontal velocity difference between up- and downgoing fingers, so that the Reynolds stresses are small. A model of a sheared finger interface limits these stresses to less than the molecular viscosity stress.

A rough dimensional/mechanistic argument for momentum transport by convectively generated interface undulations was presented. It proposed that the stress is proportional to the buoyancy flux and the velocity difference. Both the audience and the speaker noted that these arguments left much room for future improvement. The results of laboratory experiments were shown which roughly supported the results for interfacial momentum transport, and gave an empirical value for an unknown constant in the theory. The final results imply

$$\langle A \rangle \approx 40 \text{ (Buoyancy flux)}/N^2,$$

which corresponds to a turbulent Prandtl number of -40. The predictions are consistent with dissipation measurements in the Bahamas by Larson and Gregg (1983), and imply eddy viscosities of about $10^{-3} \text{ m}^2\text{s}^{-1}$.

REFERENCES

Keller, J. B., 1977. Effective parameters of heterogeneous media. In _Statistical Methods and Statistical Models in Physics_. Uri Landman, ed.

Larson, N. G. and M. C. Gregg, 1983. Turbulent dissipation and shear in thermohaline intrusions. _Nature_ 306, 26-32.

SOLIDIFICATION OF A BINARY ALLOY

M. Grae Worster

The solidification of melts which are mixtures of more than one substance is a process of industrial importance in an age when the casting of alloys is commonplace, and of geological interest in present discussions of the evolution of magmas.

The solution of the classical Stefan problem of unidirectional solidification of a single-component (pure) melt has long been known (Carslaw and Jaeger, 1959). I have recently extended this to the case of a two-component (binary) melt with a simple phase-diagram such as that on page 15 . The central results of this analysis are: determination of the growth of the interface $b = 2\lambda_b\sqrt{Dt}$, where D is the solute diffusivity, t is time and λ_b is a constant for given external conditions; and determination of the conditions under which constitutional supercooling of the melt will occur. The undercooling at which constitutional supercooling first occurs for the $NaNO_3$ - H_2O system is shown on page 16.

When supercooling occurs the flat interface becomes unstable to the growth of dendrites. The region of mixed phase (dendrites plus melt) is often called a mushy layer and has been the subject of much recent research. I here present a model of a mushy region in which transport of heat and solute is purely diffusive. The differential equations governing the mush and the flux conditions at the interfaces separating solid from mush (x = a) and mush from melt (x = b) are

$$T_t = \kappa T_{xx} + \frac{L}{c_p}\varphi_t, \tag{1}$$

$$(1-\varphi)C_t = D\left[(1-\varphi)C_x\right]_x + C\varphi_t, \tag{2}$$

$$T = -mC, \tag{3}$$

$$\rho L(1-\varphi_a)\dot{a} = -k\left[T_x\right]_{a-}^{a+}$$

$$C_a\dot{a} = -DC_x\big|^{a+}$$

$$\rho L\varphi_b\dot{b} = -k\left[T_x\right]_{b-}^{b+}$$

$$C_b\varphi_b\dot{b} = -D\left[(1-\varphi)C_x\right]_{b-}^{b+}$$

where T is temperature, C is concentration of solute in the melt and φ is the volume fraction of the solid phase. The physical parameters are the thermal conductivity and diffusivity k and κ , the specific and latent heats C_p and L, and the density ρ . Equation (3) expresses the assumption that the melt within the mushy region is everywhere at the local liquidus temperature.

In addition it is assumed that the melt outside of the mush is "marginally stable" in the sense that it is just saturated near the interface with the mush. This is expressed by requiring

$$T_x \big|^{b+} = -m C_x \big|^{b+}$$

and it can be shown that (in the present system) this is equivalent to setting $\phi_b = 0$.

This system is accessible to the same kind of similarity solution as before though now the equations are nonlinear and must be solved numerically. The growth rates of the two interfaces are shown as a function of the undercooling T_1 in figure 1.
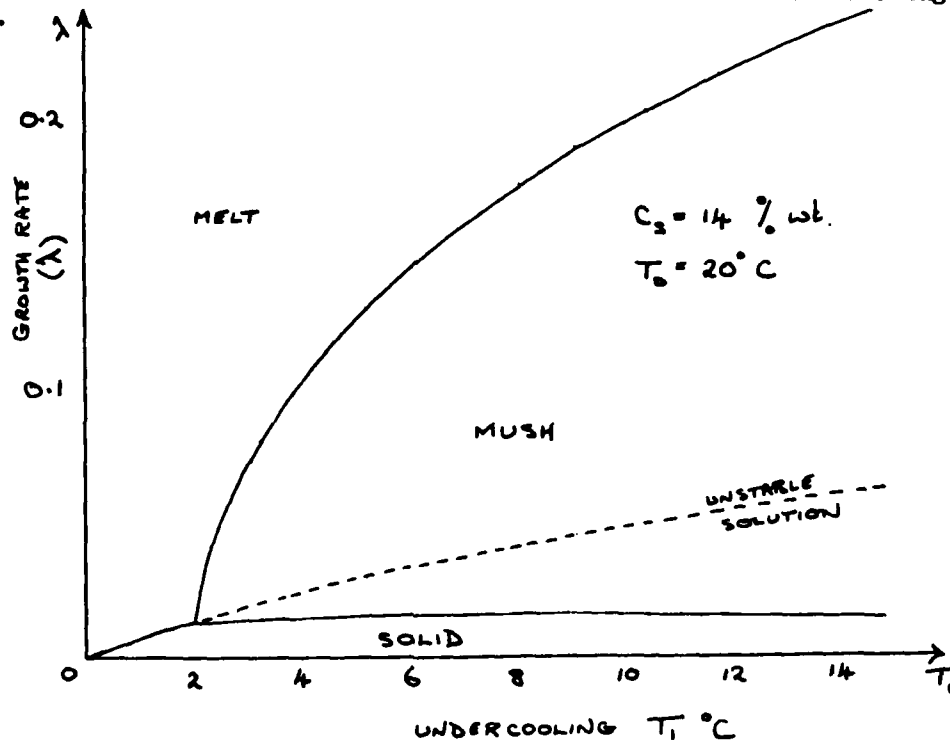
These results ignore the effects of gravity but it should be noted that in many practical situations convective transport may be important even when the bulk density field of the interstitial fluid is stable. This is because compositional boundary layers on the dendrites can provide a "counter-gradient" flux of both solute and heat. Nevertheless the present model provides a sound foundation for the analytical study of mushy regions.

REFERENCE

Carslaw, H. S. and J. C. Jaeger, 1959. Conduction of heat in solids. Oxford Univ. Press.

PATTERN SELECTION IN CELLULAR STRUCTURES
A ONE DIMENSIONAL EXAMPLE

Stephane Zaleski

Pattern selection in cellular structures has arisen a renewed interest since the discovery of a mechanism of wavenumber selection through lateral boundaries (Cross, Daniels, Hohenberg and Siggia, 1983), (Pomeau and Zaleski, 1981) Consider, for instance, the almost parallel-roll structure in the thermo-convective Rayleigh-Benard instability in large aspect ratio. The linear analysis predicts a band of stable wavenumbers of width $\mathcal{O}(\varepsilon^{1/2})$, where ε is the small relative distance to threshold. More refined nonlinear analysis of the stability of rolls themselves still allow for a broad $\mathcal{O}(\varepsilon^{1/2})$ band of stable rolls. (One should except, however, the somewhat particular case of Benard convection between stress free boundaries).

In the following, we present the basic steps of the derivation of the selected wavenumber. We take the simple case of an Hele-Shaw cell. This constrains the structure to be one dimensional, thus avoiding the exciting mysteries of the full two dimensional problem.

We consider a rectangular, thin box of size d x h x 1 with $d \ll h \ll L$. As d, the thickness of the cell is small, the flow has a parabolic profile in the corresponding direction y. The mean velocity is conveniently described by equations involving only the x and z directions. In the Boussinesq approximation, they read, in nondimensionalized form:

$$-p_x - u = 0 \tag{1}$$

$$-p_z - w + R^{1/2}\theta = 0 \tag{2}$$

$$\theta_t + u\theta_x + w\theta_z + R^{1/2}w = \Delta\theta \tag{3}$$

$$u_x + w_z = 0 \tag{4}$$

where
$$R = \frac{\Delta T\, g\, \alpha\, d^3 h}{12\, \nu\, \kappa}$$
with obvious notations.

Equations (1) and (2) express the linear Darcy Law for the seepage velocity in a porous media. To (1) - (4) we add the boundary conditions

$$\theta = w = 0 \quad \text{at} \quad z = 0, 1 \tag{5}$$

$$\theta = u = 0 \quad \text{at} \quad x = 0, \frac{L}{h} \tag{6}$$

(6) is realized in practice when the end walls are good heat conductors.

We make the usual Newell, Whitehead, Segel (Newell, Whitehead, 1969), (Segel, 1969) amplitude expansion. There

$$\theta = \theta^{(1)} + \theta^{(2)} + \dots$$

where $\qquad \theta^{(1)} = O(\varepsilon^{1/2}) \quad , \quad \theta^{(2)} = O(\varepsilon) \quad , \dots$

and $\qquad \theta^{(1)} = A(x,t) \sin \pi z \, \exp(i\pi x) \quad + \; c.c.$

where $A(x,t)$ is a small, slowly varying complex amplitude. Inserting (7) into (1), (4), one gets $u^{(1)}$, $w^{(1)}$, and then, at higher order in $\varepsilon^{1/2}$, $\theta^{(2)}, \theta^{(1)}$ etc. The solvability conditions applied on this expansion give conditions for A. At order ε^2 they can be written as a 1-d PDE of second order (Pomeau, Zaleski, Manneville, 1983):

$$2 A_t = \varepsilon A + 4 A_{xx} - \frac{\pi^2}{4} |A|^2 A - \frac{i\varepsilon}{\pi} A_x +$$
$$+ \frac{7 i \pi^3}{8} |A|^2 A_x - \frac{3 i \pi^3}{8} A^2 A_x^* \tag{8}$$

The boundary conditions at the relevant order are to be deduced using the expansion for θ, u, and (6). We get

$$A = 0 + 0(\varepsilon^{3/2}) \quad \text{at } x = 0, L/h \tag{9}$$

To construct a solution of (8) and (9), we match approximately periodic solutions in the bulk with boundary layers of order $\varepsilon^{-1/2}$ near the ends. This requires $L/h \gg \varepsilon^{-1/2}$. The stationary periodic solutions read

$$A = (\varepsilon - 4 S^2)^{1/2} \frac{2}{\pi^2} \exp(i S x + \varphi_i) \tag{10}$$

They correspond to a wavenumber $\pi + S$ for the rapid modulation $\theta(x,z)$. Solutions of the above form are subject to the Eckhaus instability outside the range $S \le \varepsilon^{1/2}/2\sqrt{3}$. This leaves a broad band of stable solutions, of order $\varepsilon^{1/2}$. If we now include the b.c. (9), we can analyze the matching of (10) with (9) by using a method of integration of (8) described in Zaleski, 1984. We find that the only wavenumbers for which (10) can be distorted to meet (9) have exactly

$$S = 0 + O(\varepsilon^{1/2}) \tag{11}$$

In the general case of a 1-d structure with A small at the boundaries (Cross, Daniels, Hohenberg, Siggia, 1983), (Pomeau, Zaleski, 1981), (Zaleski, 1984)

predicted

$$a_- \varepsilon + O(\varepsilon^{3/2}) < \delta < a_+ \varepsilon + O(\varepsilon^{3/2})$$ (12)

where a_-, a_+ are some constants for a given problem. The particular form of (11) is thus remarkable, and should allow for an easier experimental verification than in the cases already investigated in real life experiments (Wesfreid, Zaleski, 1984).

REFERENCES

Newell, A.C. and J.A. Whitehead, 1969. J. Fluid Mech., 38, 279.

Segel, L.A., 1969, J. Fluid Mech., 38, 203.

Pomeau, Y. and S. Zaleski, 1981. J. Phys., Paris, 42, 515.

Cross, M.C., P.G. Daniels, P.C. Hohenberg, and E.D. Siggia, 1983. J. Fluid Mech., 127, 155.

Pomeau Y., S. Zaleski, and P. Manneville, 1983. Phys. Rev., A27, 2710.

Zaleski, S., 1984. "Cellular Patterns with boundary forcing", to appear in J. Fluid Mech.

Wesfreid, J.E., S. Zaleski, 1984. An account of the experimental situation can be found in "Cellular Structures in Instabilities", Springer, New York (to appear).

DYNAMICAL MODELS FOR MELT SEGREGATION
FROM A DEFORMABLE MATRIX

Frank M. Richter

A mathematical formulation for the buoyancy driven segregation of a light fluid from a deformable matrix is applied to a geometrically simply system to illustrate its dynamical and chemical evolution. A layer with initially uniform fluid content contained above and below by impermeable boundaries, if sufficiently deep, displays three regimes: a compacting layer at its base, a noncompacting interior regime, and a growing pure fluid layer at the top. Various other initial conditions are discussed, including cases with linearly decreasing fluid content and with locally large (in relative terms) fluid content. The chemical evolution of the segregating fluid is also described. Having illustrated some of the properties of fluid segregation by matrix compaction, we use it as a framework for discussing the secular changes in $^{143}Nd/^{144}Nd$ and Sm/Nd of Hawaiian basalts.

STOCHASTICITY WITH MANY DEGREES OF FREEDOM IN CHAOTIC
PARTIAL DIFFERENTIAL EQUATIONS

Yves Pomeau

The analytic description of turbulent flows is still a poorly understood problem. This is in sharp contrast with the case of equilibrium and near equilibrium theories. It is interesting to understand the origin of the differences between the two situations. In usual continuum theory as describing – say a steady laminar flow, there is a clean scale separation between the fluctuation degrees of freedom (or molecular motion) and the macroscopic ones. Furthermore, the thermal fluctuations satisfy a very special property of time reversal invariance: no statistical study of these fluctuation allows us to know the arrow of time. The turbulent fluctuations of flows differ from the thermal noise first because there is no separation between the macroscopic and the fluctuating scales. Further, there is no chance that the turbulent fluctuations have the time reversal symmetry, except perhaps for the biggest space scales, where presumably the description is not very efficient. Owing to their extreme complexity, the Navier-Stokes equations have not yet been studied from a statistical point of view in computer simulations. So we have studied the statistical properties of the turbulent solutions of an equation looking more or less as the fluid equations, the Kuramoto-Sivashinsky equation

$$\phi_t + \phi\phi_x + \phi_{xx} + \phi_{xxxx} = 0 \tag{1}$$

It has a sustained turbulent behavior if the x-support of ϕ (or length L) is big enough and with the Dirichlet + Neuman boundary conditions ($\phi = \phi_x = 0/\partial$), a thorough integration over very long times by Paul Manneville indicates that, for periodic b.c., the evolution ends at a nonuniform steady state. For random initial condition, the solution of (1) defines – through time averages – a statistical ensemble for $\phi(.,.)$ that is both space and time invariant, at least for translations over distances much less than L. We have more specifically studied two points. The number of degrees of freedom may be defined as the number of positive Lyapunov numbers and grows linearly as L. The energy transfer from the unstable (long wavelength) to the stable (short wavelength) modes does not occur through an Onsager-Kolmogoroff cascade. This is shown in two different ways. The time fluctuations of the space power spectrum do not show any tendency to be peaked at more and more distant times as the wavenumbers become more and more widely separated. By looking at the mean structure of the eigenspace associated to the positive Lyapunov numbers, one sees no tendency of this space to split into independent fluctuations peaked at different wavenumbers.

This reports a joint work done with Alain Pumir and Pierre Pelce, and to be published in J. of Stat. Phys. Paul Manneville has also very much participated in the elaboration of the ideas and results presented here.

THE EMERGENCE OF DIPOLES FROM INSTABILITIES
ON THE f AND β PLANE

Glenn R. Flierl

The initial growth and large amplitude evolution of perturbations upon various flow fields have been studied in collaboration with Paola Rizzoli and Norman Zabusky. Preliminary results indicated that the vorticity often clumps into relatively strong, discrete eddies and that the evolution of the flow is often dominated by interactions between these vortices. In some cases, the interactions occur as pairing events and these dipoles transport fluid rapidly away from the initial region of instability. The beta effect can greatly modify the vortex structures formed.

I. Breakup of Circular Vortices

Previous studies of the instability of circular vortices have been concerned dominantly with flows having single-signed vorticity (e.g. Howard and Gupta, Michalke and Timme); however, for application to oceanic flows such as Gulf Stream rings, the case of zero integrated vorticity appears more relevant. We have studied the barotropic instability of a vortex with a circle of vorticity 1 and radius 1 surrounded by an annulus of vorticity q and outer radius b. Figure 1 shows the parameter relationships which permit instability for various azimuthal mode numbers m. The dashed curve indicates the relationship between q and b which gives no net integrated vorticity. (This is, of course, equivalent to zero basic state flow outside radius b.) For the relevant case of negative vorticity in the annulus around the central positive region, the instability first occurs for the m = 2 mode (elliptical deformations), in striking contrast to the single-signed case where the higher modes enter first (fixed b, increasing $|q|$). The patterns of instability are shown in figure 2, along with numerical computations of the fully nonlinear evolution. The linear phase of the instability draws the interior vorticity out in an elliptical shape and causes the exterior vorticity to clump into two pools oriented at about 30° to the major axis. At this point, the vortex pair forces between the external clumps and the ends of the interior ellipse become dominant, pulling the structure apart into two dipoles.

A mode 1 (neutral) disturbance apparently generates sufficient mode 2 through the nonlinear terms to initiate the instability; the subsequent evolution is identical. In contrast, when an equivalent barotropic model is used, the instability may grow to an equilibrated state of a rotating elliptical vortex; the parameter relations which lead to such a state have not yet been determined.

If we begin with an axisymmetric vortex and turn on a weak beta effect, we can find two distinct behaviors. When the initial profile is unstable, β forces an m = 1 perturbation which (apparently) in turn excites an m = 2 instability. However, the resulting pattern remains quite asymmetric (figure 3). On the other hand, a stable profile simply begins to move and slowly disperse. Arguments based on small β suggest that a westward propagating state exists (it has the form of a modon + a rider, Flierl, 1984), but that it may not be the final state for arbitrary initial profiles.

Baroclinic vortices constructed like the Rankine vortex with only a single cylindrical region of at nonzero potential vorticity can be unstable by baroclinic instability for large enough eddies. Barotropic components can enhance or suppress the instability, depending upon their sign and magnitudes.

II. Jet Flows

We have also considered the evolution of instabilities of a jet flow for perturbations of various wavenumbers and with or without β. The regimes found are indicated on a linear stability diagram (Fig. 4). For short wave perturbations, the vorticity clumps into a vortex street, representing an equilibrated wave. (This is probably long lived but never the less transient; the street becomes unstable to merger events.) With β, similar things happen but the final state appears (1) to have a different propagation rate because of β and (2) to have vortex centers significantly less separated meridionally. Patches of vorticity are thrown off the sides and apparently propagate westward.

For longer wave varicose instabilties, the jet evolves by forming dipoles centered at the jet axis. This seems to occur by north-south extrusion of vorticity and then a backward breaking and roll-up. Weak β effects only decrease the final propagation rate.

For long sinuous perturbations, on the other hand, the evolution is completely different. As the initial wave grows, it puts energy into sub-harmonics which are themselves able to extract energy from the mean and the wave develops kinks. The vorticity becomes distributed into a much more complex pattern and a modon forms. Rapid spread occurs by outwardly-directed dipoles (Fig. 5).

With β, the long wave is stabilized; now nonlinearity feeds some energy into short waves and these grow at the expense of the mean. Thus a high wavenumber perturbation appears instead of a long wave.

If many scales are excited simultaneously, the long, slowly growing modes are not unimportant compared to the rapidly growing short modes (perhaps because the long modes do not equilbrate). Rather they cause rapid merger events and cascade of energy back to larger scales. Temporary dipoles can be seen during this process, again carrying fluid far outward from the jet. Similar events occur with β; indeed merger is visible in the evolution of the single long (neutral) wave described in the previous paragraph. While the lateral growth of a turbulent jet has often been ascribed to merger events, our calculations indicated the dipole formation can also lead to rapid outward spreading and we suggest that both may play an important role. The beta effect appears to modify both of these processes and leads to a more meridionally confined flow.

REFERENCES

Flierl, G. R., 1984. Rossby Wave Radiation from a Strongly Nonlinear Warm Eddy. Jour. Phys. Oceanogr. 14, 47-58.

Howard, L. N. and A. S. Gupta, 1962. On the Hydrodynamic and Hydromagnetic Stability of Swirling Flows. Jour. Fluid Mech. 14, 463-476.

A. Michalke and A. Timme, 1967. On the inviscid instability of certain two-dimensional vortex-type flows. Jour. Fluid Mech. 29, 647-666.

STABILITY DIAGRAM FOR ANNULAR VORTEX
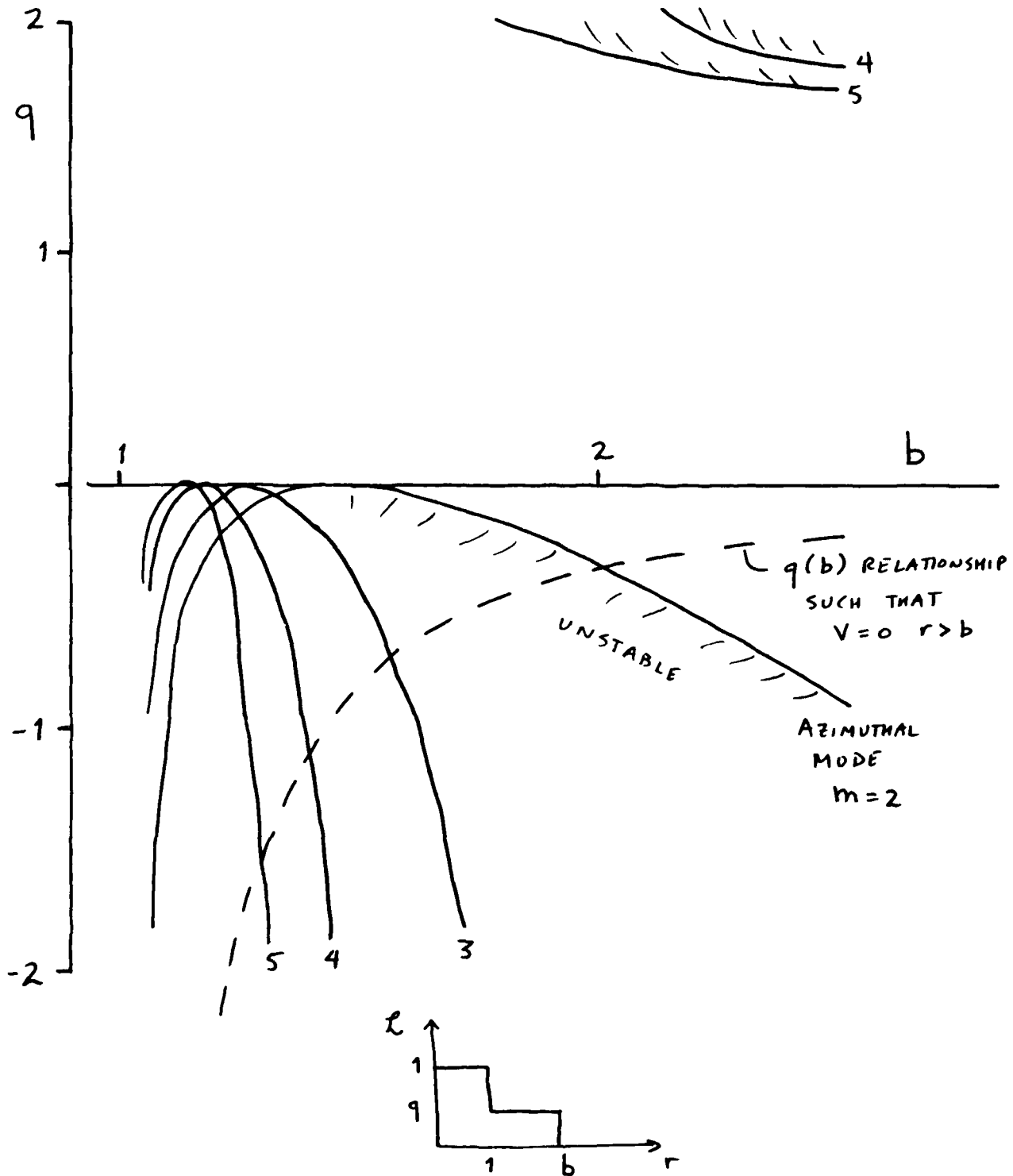
Figure 1

Instability of a circular vortex on the f plane.

Left four panels show the streamfunction and vorticity at various times in the
fully nonlinear numerical calculation. On the right is the linear perturbation
solution with an arbitrary amplitude assigned to the perturbation.
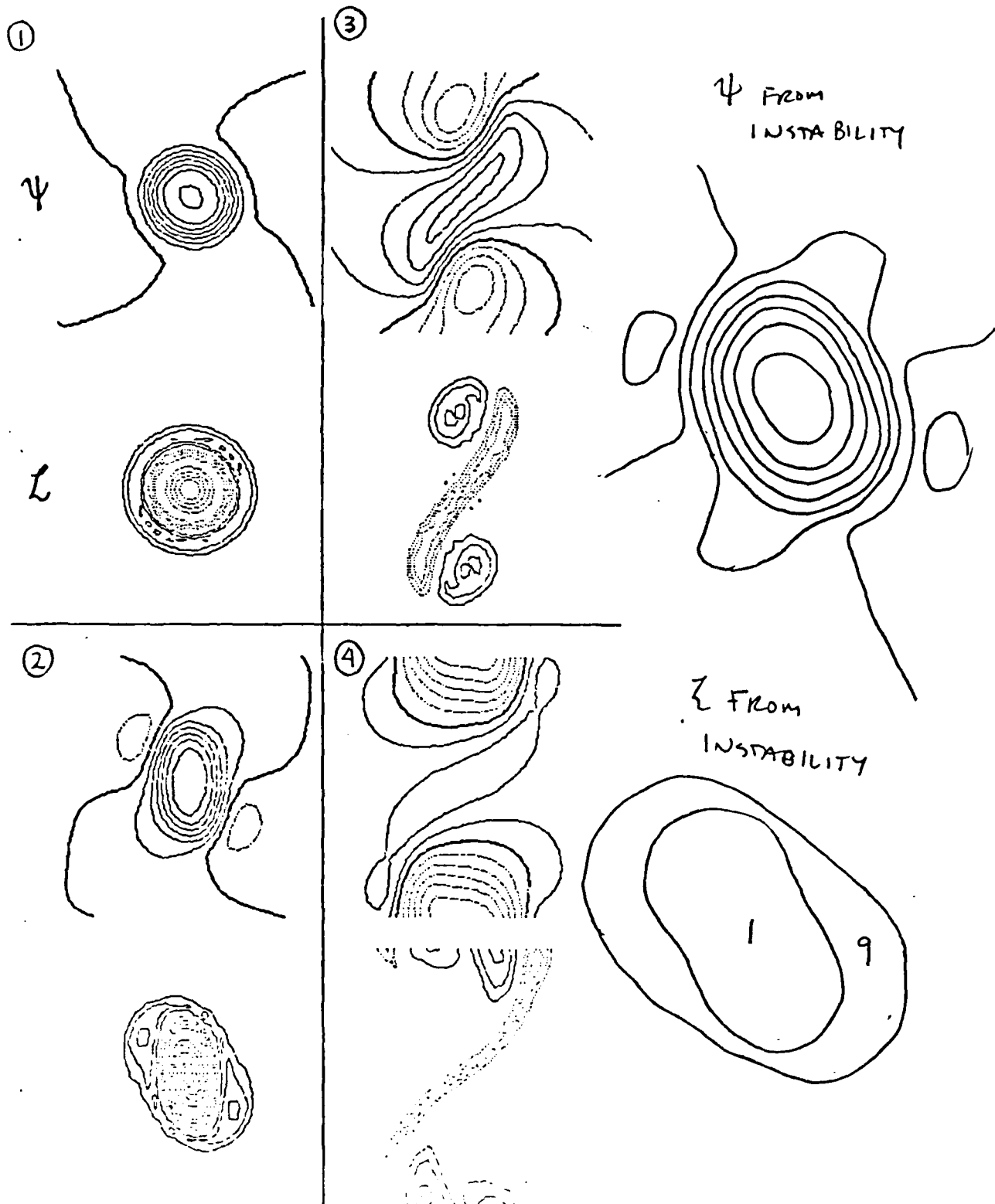
Figure 2

Instability of an unperturbed circular vortex on the β plane.
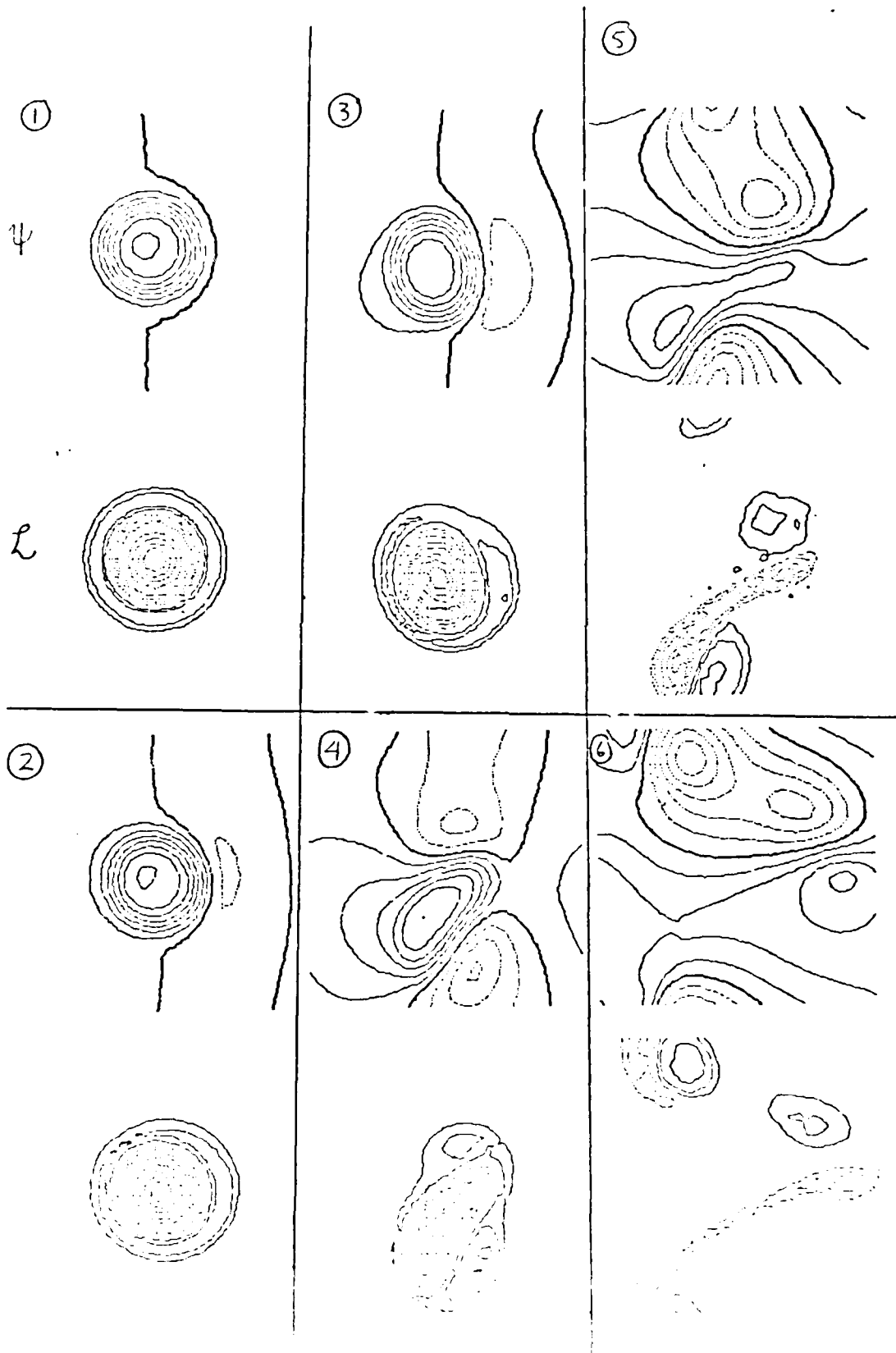
Figure 3

Growth rates for perturbations on a jet.

Small sketches show nonlinear evolution for various initial wavenumbers and perturbation symmetries.
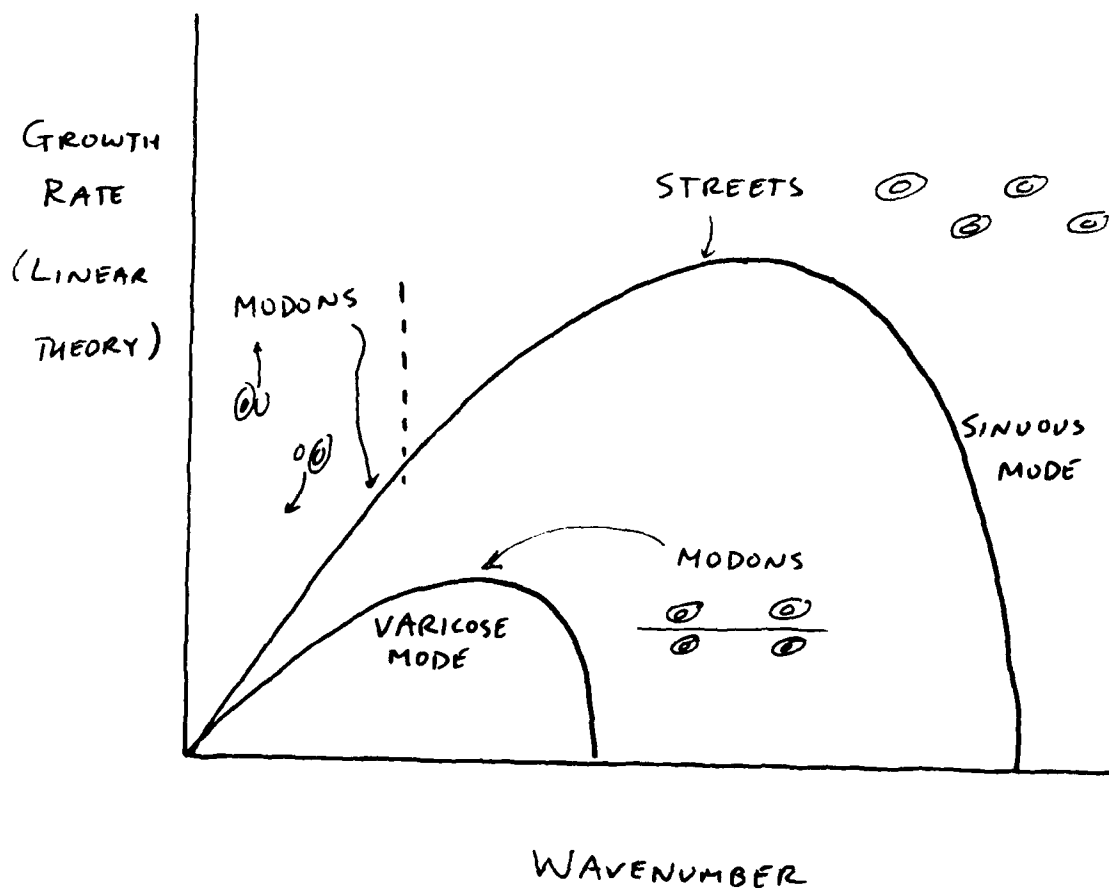
Figure 4

Long wave perturbations on a jet.

Panels show the evolution of the streamfunction and vorticity fields; note the breakup of the jet into patches of vorticity which pair to form dipoles moving away from the center.
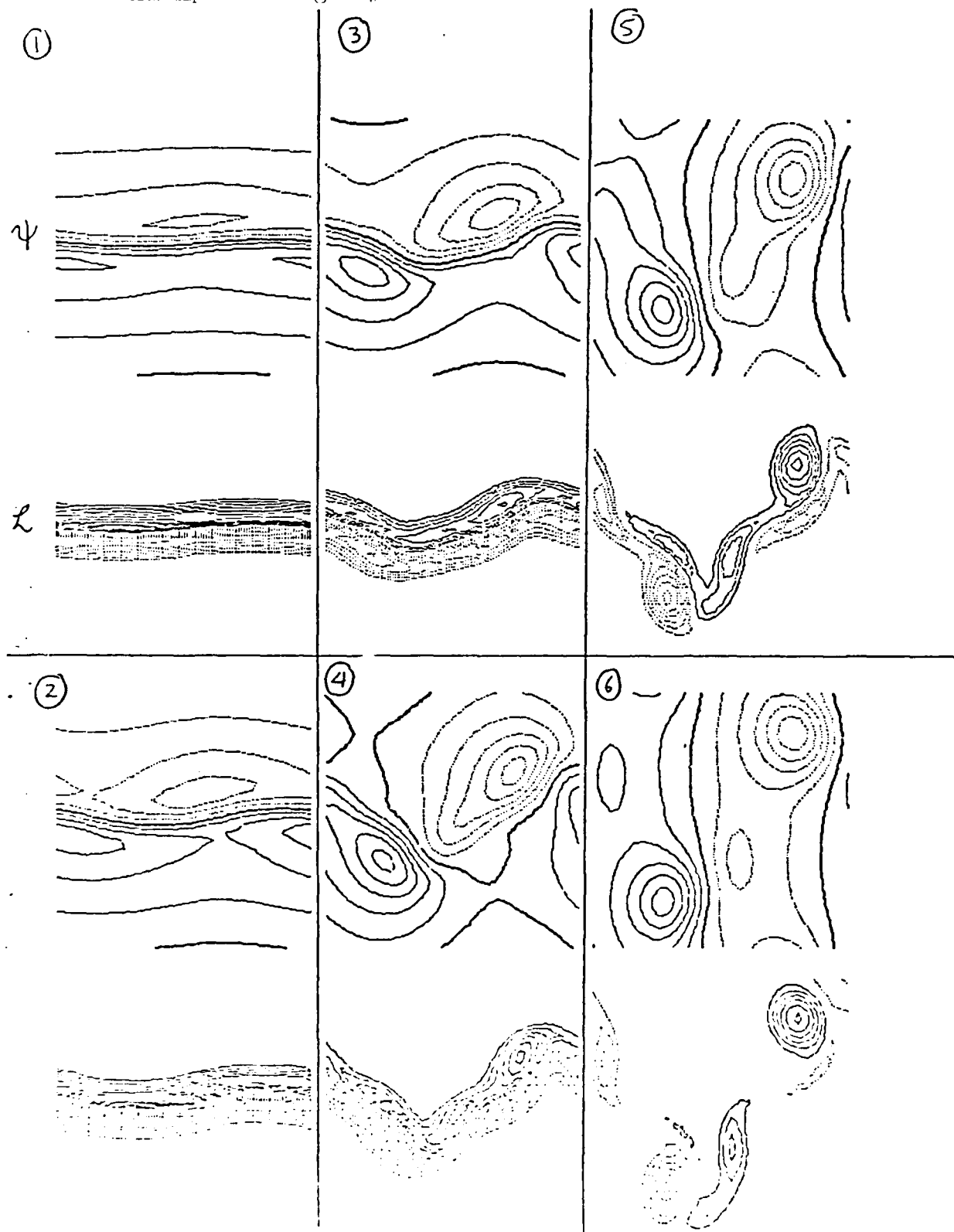
Figure 5

FRONT PROPAGATION WITH INTERFACIAL TENSION

Yves Pomeau

I consider two problems of front propagation where surface tension plays a role.

In the Saffman-Taylor instability (Saffman and Taylor, 1958; McLean and Saffman, 1981; and Vanden-Broeck, 1983), surface tension is important for removing the degeneracy of the Saffman-Taylor solution for a finger, as well as for suppressing the "generic" cusp singularities that have been shown to appear after a finite time (Shraiman and Bensimon, preprint) for smooth initial data.

By the general argument of Birkhoff for the Kelvin-Helmholtz instability, these singularities occur because the growth/rate of unstable fluctuations with the wave vector q is $\sigma(q) = qu$ at large q. Surface tension supresses these singularities, as it stabilizes the short scale fluctuations. Surface tension is important too for this Saffman-Taylor (S.T.) instability, because it removes (McLean and Saffman, 1981; Vanden-Broecke, 1983; and Pomeau, preprint) the degeneracy of the steady S.T. solution for the finger advancing in a long rectangular channel. Let k be a dimensionless measure of the strength of the surface tension $\left[k \sim \text{(capillary number)}^{-1} \right]$, the relative width λ of the finger in the channel expands as $\lambda \simeq 1 + bk^{-1/2} + \ldots$ near $k \to \infty$ (= large surface tension or small velocity). This finger tends to fill completely the channel in this limit, to lower the interfacial energy ($\lambda \to 1$). The computation of $b(<0)$ is a nontrivial numerical problem involving the solution of a similarity equation of a particularly complicated form (Pomeau, preprint).

Another example of front propagation, where surface tension is important is the dendritic growth (Langer, 1980; Clavin, Pelce and Pomeau, in prep.) If a solid grows at the expense of an undercooled melt, there is a critical undercooling ΔT_c such that, if $|\Delta T| < \Delta T_c$, no plane solution of the Stephan problem exists with a constant speed: if $|\Delta T| < \Delta T_c$ there is too much latent heat generated at the interface.

This critical undercooling ΔT_c (usually very difficult, if not impossible, to reach experimentally) is defined by the condition $C_p \, \Delta T_c = L$, C_p being the heat capacity of the melt and L the latent heat. For $|\Delta T| < \Delta T_c$, the displacement of a plane solidification front has a diffusion-like dependence $x(t) \sim t^{1/2}$. This front is unstable against the Mullins-Sekerka instability (Langer, 1980 and Clavin, Pelce and Pomeau, in prep.): if a bump of solid on the front reaches cooler region behind it this bump gets a larger velocity, by the Stephan condition, and grows. The ultimate evolution of this instability yields the so-called dendritic growth. A partial solution of the dendrite structure is given by the Ivantsov parabola (Langer, 1980 and Clavin, Pelce and Pomeau, in prep.): in two dimension, a parabola of solid of Cartesian equation $y = ax^2$ grows in the melt with a constant velocity parallel to the y-axis. If D is the heat diffusion coefficient in the melt and P_e the dimensionless ratio $\Delta T / \Delta T_c$, this Ivantsov solution implies a relation between P_e and ua^{-1}/D, that becomes in the $P_e \to 0$ limit:

$$ua^{-1} \sim P_e^2 D \tag{1}$$

A similar solution exists for a circular paraboloid, and the relation between μa^{-1} and P_e is now, for $P_e \to 0$:

$$\mu a^{-1} \sim P_e D / \ln P_e \qquad (2)$$

This Ivantsov solution is degenerate, because one can change at will the velocity μ, if one changes the geometrical parameter of the parabola (a) to keep the product μa^{-1} constant. This degeneracy is due to the fact that there is not enough dimensionalizing physical quantities in the physical data ($\Delta T / \Delta T_c$ and D). It is removed when one takes care of the Gibbs-Thomson (G.T.) condition: the temperature at the ℓ/S interface is no longer the thermodynamic melting temperature, but depends also on the main curvature of the interface. With this G.T. condition, there are enough physical parameters to make a velocity and a length. But the Ivantsov parabola (as well as the paraboloid) is no longer a solution for the equations of the problem. We have found (Pelce, Pomeau, preprint) similarity equation for the structure of the tip of the dendrite (both in 2d and 3d) with surface tension near $P_e \to 0_+$. These equations yield the following estimates for the velocity (μ) and the curvature (a) at the tip in this weak undercooling limit ($0 < \Delta T_c \ll \Delta T$):

in 2d:

$$\mu \sim \left(\frac{\Delta T}{\Delta T_c}\right)^4 \qquad , \quad a \sim \left(\frac{\Delta T}{\Delta T_c}\right)^2$$

in 3d

$$\mu \sim \left(\frac{\Delta T}{\Delta T_c}\right)^2 \ln^{-2}\left(\frac{\Delta T}{\Delta T_c}\right) \qquad , \quad a \sim \frac{\Delta T}{\Delta T_c} \ln^{-1}\left(\frac{\Delta T}{\Delta T_c}\right)$$

To get back quantities with a physical dimension, one has to multiply the dimensionless estimates by combination of thermodynamic parameters so that the absolute velocity scale is quite large (say of the order of the sound velocity) and the absolute length scale quite small (say an intermolecular distance). There is also a possibility of existence of hollow axissymmetric dendrite with a hole along theire axis.

REFERENCES

Clavin, P., P. Pelce and Y. Pomeau, in preparation. Physica D, Nonlinear Physics.

Langer J.S., 1980. Instabilities and pattern formation in crystal growth, Rev. of Mod. Physics 52, 1-28.

McLean, J.W. and P.G. Saffman, 1981. J. Fluid Mech. 102, 455-469.

Pelce, P. and Y. Pomeau, preprint.

Pomeau, Y. The Saffman-Taylor fingers in the limit of very large surface tension, SDR, preprint.

Saffman, P.G. and G.I. Taylor, 1958. Proc. Roy. Soc. of London A245 312-329.

Shraiman, B. and D. Bensimon. James Franck Institute (U. of Chicago), preprint.

Vanden-Broeck, J. M., 1981. Phys. of Fluids 26, 2033-2034.

NARROW-GAP EKMAN FLOW

Willem V.R. Malkus

Normal Ekman flow has steady supercritical shear wave solutions. The individual instabilities can be satisfactorily described by finite amplitude theory and the small amplitude interaction of the waves by coupled nonlinear Schrodinger equations. In contrast, the first disturbances in Poiseuille flow are subcritical and chaotic. The theory for narrow gap Ekman flow will be described which exhibits these two extremes of initial behavior as a consequence of varying the rotation rate. We determine numerically the parameteric boundary between single wave initial instabilities and initial instabilities on which secondary (3^d) modes also appear. This boundary is near the parameter value at which the first Lindstedt (Landau) constant of the non-linear theory vanishes. At somewhat small gap-spacing and higher Reynolds number the observed initial disturbances are no longer global. These simpler prototypes of the inhomogeneous, intense bursts of Poiseuille flow may be accessible by finite perturbation analysis. Amplitude equations for this region and their relation to recent experimental results will be discussed.

STRONG INTERACTIONS BETWEEN
INTERNAL SOLITARY WAVES

Roger Grimshaw

The interaction of weakly nonlinear long internal gravity waves is studied. Strong interactions occur when waves belonging to different modes have phase speeds that are nearly equal. It is shown that this interaction is described by a pair of coupled Korteweg-de Vries equations. These equations are integrated numerically and, depending on the parameters in the equation, various kinds of solutions are found. In particular, for parameters corresponding to a fluid model describing two inversion layers, phase-locked solitary waves are found. However, when the coupling between the equations is predominantly through the dispensive terms, leap-frogging solitary waves are found.

FINITE-AMPLITUDE INTERFACIAL GRAVITY WAVES:
WAVE PROFILES AND STABILITY

Roger Grimshaw

We consider finite-amplitude interfacial gravity waves in a two-layer fluid. Wave profiles and other wave properties are found analytically by a Stokes expansion for small wave amplitudes, and numerically for large wave amplitudes by solving a nonlinear integral equation. Results are obtained for a range of basic flow models, including some with velocity shear in the upper fluid. In some cases, wave profiles near the highest wave develop an S-shape. The stability of these waves is investigated analytically for small amplitudes by deriving a nonlinear Schrodinger equation coupled to a wave-induced mean flow equation to describe long wavelength modulation instability. All waves are found to be unstable and the instability configuration as a function of modulation wavenumber is determined as a function of the basic state parameters. For finite-amplitude waves the instability regions are calculated numerically and it is found that the modulation instability is part of a low-order resonance instability. Although higher order resonance instabilities exist we find that at small wave amplitudes the low-order resonance instability dominates, and at higher wave amplitudes a local Kelvin-Helmholtz instability sets in.

THE STABILITY OF SALT FINGERS

Judy Holyer

There have been many oceanic observations of salt fingers which typically show salt fingers confined to a region about 20 cm thick, separated by convecting regions several meters thick. This suggests that a field of long salt fingers is unstable and will break down into layers.

Stern (1969) investigated the stability of long, steady, two-dimensional salt-fingers to long wavelength, internal-wave perturbations. He showed that if the fluxes through the salt fingers are large enough then the fingers are unstable. This instability is known as the collective instability of salt fingers. Holyer (1981) studied this instability more rigorously and showed that two-dimensional, salt fingers are unstable to long-wavelength internal-wave perturbations if

$$\frac{\beta \overline{F_s} - \alpha F_T}{\nu(\alpha T_z - \beta S_z)} > \frac{1}{3} \quad ,$$

where F_T and F_S are the heat and salt fluxes of the fingers, ν is the kinematic viscosity, and T_z and S_z are the heat and salt gradients. I have now extended this work to include two-dimensional perturbations of all wavelengths, by applying Floquet theory to the basic, periodic, salt-finger state. As well as being able to find out how the growth rate for the collective instability varies with the wavelength of the perturbation, a new non-oscillatory instability is found. For a salt finger with maximum vertical velocity $\hat{W}$ the growth rate λ for this new instability is

$$\lambda = -\frac{\sigma m^2}{2} + \sqrt{\frac{\sigma^2 m^4}{4} + \frac{m^2 \hat{W}^2}{2}}$$

where σ is the Prandtl number, m is the vertical wavenumber of the perturbation and m is small. For heat-salt and salt-sugar systems this instability has a larger growth rate than the collective instability and it is possible that in some experiments it is this instability, rather than the collective instability, that is being observed.

In practice salt fingers are not two-dimensional. They have a square cross-section. I have therefore looked at the stability of square, salt-fingers to long, three-dimensional perturbations. There are no qualitative changes - the same instabilities appear as for the two-dimensional case, but there are quantitative changes. For square fingers the collective instability first occurs when

$$\frac{\beta \overline{F_s} - \alpha F_T}{\nu(\alpha T_z - \beta S_z)} > \frac{2}{3} \quad .$$

Thus this talk could have been entitled "$\frac{2}{3}$, not 1/3"!

REFERENCES

Holyer, J.Y., 1981. On the collective instability of salt fingers. _J. Fluid Mech._, 110, 195.

Holyer, J.Y., 1984. The stability of long, steady, two-dimensional salt fingers. _J. Fluid Mech._, (to appear).

Stern, M.E., 1969. Collective instability of salt fingers. _J. Fluid Mech._, 35 209.

HETONIC EXPLOSIONS

Henry Stommel

Nelson Hogg and I have discovered a simple interaction between discrete geostrophic vortices in a two layer uniformly rotating gravitationally stratified system that transports heat. This occurs when two nearly vortices are in different layers, with different sign, but equal algebraic strength. Such a pair, called a heton, can be either hot or cold.

Two hetons of opposite temperature attract each other and simple heat engines can be built for them. Hetons of like temperature repel each other, unless very close, and hence when assembled in large clouds form explosives. It is shown that such clouds form a pair of narrow streams around their rims, the sense of rotation differing by layer. Individual hetons in the rim are split so rapidly that they cannot escape by radial explosion, but clumps of them can. The size of these clumps is about 1.25 times the size of an internal Rossby circle. Hetons thus provide an alternate explanation of the baroclinic instability problem.

PATTERNS OF SOLUTIONS BIFURCATING FROM SPHERICALLY SYMMETRIC STATES WITH APPLICATIONS TO CONVECTION IN THE EARTH'S MANTLE AND TO THE ANISOTROPY OF THE UNIVERSE

Friedrich H. Busse

The problem of the patterns that are generated when a spherically symmetric state becomes unstable with respect to asymmetric disturbances can be considered without reference to the physical mechanism causing the instability. Only for the purpose of focussing the imagination it is convenient to discuss this problem within the framework of convection in a spherical fluid shell. Other problems that can be used as examples of the theory exposed here are the buckling of a spherical elastic shell and the Rayleigh-Taylor instability of a spherically symmetric implosion. These problems have in common that the eigenvalue R of the linear problem is characterized by a $2\ell + 1$ degeneracy where ℓ is the degree of the preferred spherical harmonics. The degeneracy is two-fold in character. First there is the orientational degeneracy caused by the property that a two-parametric manifold of solutions can be obtained by translations of a given solution on the spherical surface. For $\ell = 1$ there exists only the orientational degeneracy. All three independent eigensolutions of the linear problem depict the same pattern. The two degrees of freedom represented by the two independent eigensolutions, in addition to the first one, correspond to the two independent angles by which a pattern can be rotated on a sphere. But in the case $\ell = 2$ the problem of pattern degeneracy arises. According to the linear theory, an infinite manifold exists of solutions which cannot be transformed into each other by a rotation on the sphere. The solvability conditions, however, which arise when the nonlinear terms are taken into account as perturbations, restrict the manifold of solutions to a finite number. The physically preferred solution among this finite number can be determined by a stability analysis.

It is remarkable that the former problem can be solved independently of the physics of problem (radial structure of a convecting spherical shell, for example). The results about possible patterns of bifurcating solutions derived by Busse (1975) and by Busse and Riahi (1982) are thus general. Even the stability problem can be solved to a considerable extent with the result that the axisymmetric solution is preferred in the case $\ell = 2$, while solutions exhibiting the symmetrics of the Platonic bodies are preferred in the cases $\ell = 3$, 4 and 6.

The problem of convection in the Earth's mantle has been the major motivation for the study of convection in spherical shells. It has long been known that the Coriolis force is unimportant in this problem because of the high Prandtl number of the order 10^{23} of the mantle. Nevertheless an anisotropy of plate motions with respect to the axis of rotation can be noticed (mid-oceanic spreading ridges are mainly north-south). The cause of this correlation is the property that the $\ell = 2$ component of convection affects the moment of inertia tensor of the Earth. It turns out that for a Boussinesq fluid the stable position of the Earth's axis rotation must be orthogonal to the symmetry axis of the $\ell = 2$ mode of convection, i.e. the latter axis must lie in the equatorial plane of the Earth (Busse, 1983a).

Another application is concerned with the shape of the possible anisotropy of the universe. The problem of patterns of solutions bifurcating from a basic state which is isotropic with respect to a three-dimensional hyper-spherical surface is analogous to the problem of solutions bifurcating from a basic state which is isotropic with respect to a two-dimensional spherical surface which we discussed above. For details see the recent paper (Busse, 1983b).

The analysis of preferred patterns can be generalized by considering the case when the eigenvalues R and R* corresponding to two different degrees ℓ and $\ell*$ of spherical harmonics nearly coincide. Patterns of three cells, four cells, seven cells, etc. can be found in this case in addition to the two-cell, six-cell, and ten-cell patterns obtained in the case of a single degree of spherical harmonics. This work done in collaboration with Dr. N. Riahi is presently in progress.

REFERENCES

Busse, F.H., 1975. Patterns of convection in spherical shells. J. Fluid Mech. 72, 67-85.

Busse, F.H. and N. Riahi, 1982. Patterns of convection in spherical shells Part 2, J. Fluid Mech. 123, 283-301.

Busse, F.H., 1983a. Quadrupole convection in the lower mantle?, Geophys. Res. Letts. 10, 285-288.

Busse, F.H., 1983b. Preferred anisotropies of the universe, Phys. Rev. D28, 1248-1250.

INSTABILITIES OF CONVECTION ROLLS IN A FLUID LAYER WITH STRESS-FREE BOUNDARIES

Friedrich H. Busse

Convection in a layer heated from below has become a favored fluid system for the study of the evolution of turbulence. Experiments and theories on convection at low to moderate Rayleigh number can answer questions about the increasing number of degrees of freedom of motion that become occupied as the fluid approaches a turbulent state through several transitions as the Rayleigh number increases. Moreover, the degeneracy of the problem at the critical Rayleigh number permits the investigation of competition between different modes at low amplitudes of motion. In particular, the situation can occur that an infinite manifold of steady solutions exist, all of which are unstable, such that a complex time dependence arises as the realized state drifts through the phase space spanned by the steady solutions. This particular kind of weakly nonlinear turbulence is known as phase turbulence.

Stability theory is an important tool for the understanding of these aspects of the transition to turbulence. Since the different instabilities of convection rolls are nearly orthogonal to each other, the mechanisms of other instabilities change relatively little if a given instability produces a transition from rolls to a more complex three dimensional form of convection. Thus the results of the analysis of roll instabilities apply at least qualitatively at higher Rayleigh numbers when more complex forms of convection are realized. The case of convection with stress-free boundaries is of particular interest, because many of the instabilities that usually occur only at higher Rayleigh numbers come in already at the critical point (R_c, α_c) where α_c is the wave number for onset of convection. Analytical expressions can thus be derived for the onset of zig-zag-, cross-roll-, Eckhaus-, skewed-varicose-, and oscillatory skewed-varicose-instabilities. The first three of these instabilities were discussed in the papers by Schlüster et al. (1965) and Busse (1971). But it was not realized at that time that the zig-zag instability depends strongly the Prandtl number P in the case of stress-free boundaries because of the presence of a nearly undamped vertical vorticity mode. As Siggia and Zippelius (1981) have shown, a component of the disturbance flow of the form $\tilde{u} = \nabla \times \underline{k} \psi$ (x, y) is generated in connection with zig-zag instability and decreases its growth rate significantly. Here $\underline{k}$ is the vertical unit vector in the direction of the z-axis. In the case of rigid boundaries, the boundary condition do not permit a z-independent function ψ (x, y) and a weakly damped flow component of the above form cannot be realized. Zippelius and Siggia (1982) also found the skewed varicose instability but predicted the criterion $\alpha < \alpha_c$ for instability while the correct form of this criterion near the critical point (R_c, α_c) is given by

$$R - R_c > \alpha (\alpha - \alpha_c) \, 108 \, \pi^2 / 7 \tag{1}$$

This criterion and a similar criterion

$$R - R_c < \alpha (\alpha - \alpha_c) \, 36\pi^2 \left(1 + \frac{1}{P}\right)^2 \left\{ (3+P)\left(\frac{2+2P}{3P^2} + 1\right) + \left(5 + 6P + P^2\right)^{\frac{1}{2}} \right\}^{-1} \tag{2}$$

for the newly discovered oscillatory skewed varicose instability have been derived by Busse and Bolton (1984). According to criteria (1) and (2) all steady convection flows are unstable for Prandtl numbers P less than 0.543. This property presumably will lead to the phenomenon of weakly nonlinear phase turbulence that has been mentioned above.

The analytical work has been extended and checked by a numerical investigation of the stability of convection rolls. This numerical work exhibits one additional instability, the oscillatory instability which is well-known from earlier work (Busse, 1981) and which bounds the region of stable rolls in the (R, α)-space towards high Rayleigh numbers for $0.8 \leq P \leq 10$. For higher Prandtl numbers the zig-zag and skewed varicose boundaries cross and the maximum Rayleigh number at which stable rolls can exist is given approximately by

$$R_{max} \approx R_c(1 + 192/49P) \qquad (3)$$

It should be mentioned that the growth rate of the skewed varicose instability vanishes in the limit of infinite Prandtl number. The result (3) thus becomes irrelevant in that limit. Further details on the results of the numerical computations can be found in the paper of Bolton and Busse (1984, submitted to the Journal of Fluid Mechanics).

REFERENCES

Busse, F.H., 1971. Stability regions of cellular fluid flow, Instability of Continuous Systems (H. Leipholz, ed.), 41-47.

Busse, F.H., 1981. Transition to turbulence in Rayleigh-Benard convection, Hydrodynamic Instabilities and the Transition to Turbulence(H.L. Swinney and J.P. Gollub, eds.) 45, 97-137.

Busse, F.H., and E.W. Bolton, 1984. Instabilities of convection rolls with stress-free boundaries near threshold, J. Fluid Mech. 146, 115-125.

Schluter, A., D. Lortz and F. Busse, 1965. On the stability of steady finite amplitude convection, J. Fluid Mech. 23, 129-144.

Siggia, E.D., and A. Zippelius, 1981. Pattern selection in Rayleigh-Benard convection near threshold, Phys. Rev. Lett. 47, 835-838.

GENERATION OF MEAN FLOWS BY CONVECTION

Friedrich H. Busse

The generation of mean flows by convection is not found in horizontally isotropic layers heated from below which are the most studied examples of convection flow. However, physical conditions introducing small anisotropies can in principle lead to the new phenomenon of the generation if of mean flow owning to the Reynolds stresses of the convection velocity field. Many convecting systems observed in nature do indeed exhibit strong mean flows. The zonal jets of Jupiter and the solar differential solution are but the most spectacular examples.

The mechanisms of mean flow generation can be divided in three groups:

(i)   The generation of a mean flow is an intrinsic nonlinear property of the realized convection mode.

(ii)   The mode at onset of convection is not associated with a mean flow; but a more complex mode of convection setting in after an instability of the primary mode is associated with a mean flow.

(iii)   The instability itself of the primary mode of convection involves a mean flow. In this case the sign of the mean flow is arbitrary in contrast to the cases (i) and (ii) in which the sign is determined because of the quadratic nature of the Reynolds stress terms.

The generation of the zonal flows in the major planets in an example for case (i) (Busse, 1983a). Case (ii) can be realized in a rotating layer heated from below when the axis of rotation is inclined with respect to the vertical. Strong mean flows were first observed in this case in the numerical experiment of Hathaway and Somerville (1983). An analytical theory explaining this phenomenon on the basis of the transition to a time-dependent form of convection owing to the Kuppers-Lortz instability was given by Busse (1982). The third possibility was first noticed by Thompson (1970) in numerical model of the moving-flame phenomenon (Stern, 1959). But numerical difficulties prevented Thompson from exploring the mean flow instability. A simple semi-analytical model of the mean-flow instability has been described by Busse (1972).

The temperature dependence of the viscosity leads to nonlinear terms of similar nature as the Reynolds stresses. Thus it appears to be possible that mean flows can be generated by convection even in fluids of infinite Prandtl number, provided the viscosity depends on temperature. A simple model of forced convection which exhibits a mean flow generated by this mechanism is described in a recent review of the subject (Busse, 1983b).

REFERENCES

Busse, F.H., 1972. J. Atmos. Sci. 29, 1423-1429.

Busse, F.H., 1982. Zeitschrift.f. Naturferschung 37a, 753-758.

Busse, F.H., 1983a. Geophys. Astrophys. Fluid. Dyn. 23, 153-174.

Busse, F.H., 1983b. Physica 90, 287-299.

Hathaway, D.H., and R.C.J. Somerville, 1983. J. Fluid Mech. 126, 75-89.

Stern, M.E., 1959. TELLUS 11, 175-179.

Thompson, R., 1970. J. Atmo. Sci. 27, 1107-1116.

GROWTH OF THE EARTH'S INNER CORE

David R. Fearn

The core of the Earth is composed predominantly of iron together with a small mass fraction of some lighter elements. Likely candidates are sulphur and oxygen in the forms FeS and FeO respectively (Ahrens, 1980; McCammon et al., 1983). Whatever the identity of the light component it has two roles. First it must be present in sufficient quantities to give a mean core density which agrees with seismic observations (some 10% lighter than pure iron), and it must depress the melting temperature compared with that of pure iron. As the Earth cools, freezing first takes place at the center of the core since the liquidus temperature gradient is steeper than the adiabat (Stacey, 1977). The subsequent evolution of the core is strongly dependent on whether the mass fraction ξ of the lighter constituent is greater or less than the eutectic composition ξ_e . The simplest picture obtains when the core is iron-rich ($\xi < \xi_e$). Then the solid which freezes is nearly pure iron. This accumulates to form a dense solid inner core while the remaining fluid which is enriched in the light constituent is buoyant and drives convective motions in the outer core (see Loper and Roberts, 1983 for a review). The alternative (iron-poor) regime ($\xi > \xi_e$) was first considered by Braginsky (1963), and he discussed how a dense solid inner core might grow in this case. We pursue this idea here, given motivation from the recent work by McCammon, et al. (1983). They give arguments for oxygen being the light alloying element and they estimate that the mass fraction of FeO is greater than that present in an Fe-FeO eutectic mixture.

In an iron-poor core, the solid which first freezes is composed primarily of the light constituent (for example FeO). As this is lighter than the surrounding fluid it floats upward. In this manner the center of the core is depleted in the light constituent and a variable composition layer (VCL) forms in which the concentration of iron increases with depth. The VCL is thus stably compositionally stratified. As freezing continues, the composition at the center of the core moves towards the eutectic. If the eutectic is reached, there is the possibility of the growth of a solid inner core of eutectic composition. Two causes of freezing are considered: (a) slow cooling over the age of the Earth and (b) the relatively rapid increase in the central pressure which took place during the accretion of the Earth some 4.5×10^9 years ago. The conclusions of the analysis depend on some very poorly determined physical parameters but for both cases, there are good reasons to believe that the presence of the inner core in the Earth is not consistent with an iron-poor core. In case (a) we argue that because of the stable compositional gradient, convection is unlikely to be an effective means of removing the latent heat released by the freezing process and so the rate at which the heat can be conducted away is the factor limiting inner-core growth (Fearn and Loper, 1983). In case (b) the latent heat is not a problem since even if no heat is removed freezing can still take place if the liquidus temperature gradient $\partial T_L / \partial p$ is steeper than the wet adiabat. The principal problem is reaching the eutectic. From the available parameter estimates the rate $d\xi/dp$ at which the central composition decreases with increasing pressure is small so unless the initial composition is close to eutectic, the eutectic can never be reached. This situation is exacerbated by the response of the eutectic composition to pressure. For the Fe-FeS system $d\xi_e/dp < 0$ and it may well be that $d\xi_e/dp < d\xi/dp$. In that case, the eutectic can never be reached. Even if the eutectic <u>is</u> reached there are further impediments to the growth of an inner core.

In the Earth, an inner core is present, but this may not be true in the cores of other planets. It is therefore of interest to calculate the gravitational energy released in the formation of the VCL. The light solid which floats up out of the VCL will remelt when it finds itself once again above the liquidus. This acts as a source of buoyant fluid and so we expect compositionally driven convection in the region above the VCL. Thus, useful gravitational energy is released even in the case of an iron-poor core and the presence of an inner core is not a prerequisite for a gravitationally powered dynamo.

REFERENCES

Ahrens, T.J., 1980. Dynamic compression of Earth materials. Science 207, 1025-1041.

Braginsky, S.I., 1963. Structure of the F-layer and reasons for convection in the Earth's core. Doklady Akad. Nauk SSSR 149, 1311-1314, English translation 8-10.

Fearn, D.R. and D.E. Loper, 1983. The evolution of an iron-poor core. I. Constraints on the growth of the inner core, in Stellar and Planetary Magnetism (A.M. Soward, ed.), Gordon and Breach, London, 351-370.

Loper, D.E. and P.H. Roberts, 1983. Compositional convection and the gravitationally powered dynamo. In Stellar and Planetary Magnetism (A.M. Soward, ed.), Gordon and Breach, London, 297-327.

McCammon, C.A., A.E. Ringwood and I. Jackson, 1983. Thermodynamics of the system Fe-FeO-MgO at high temperature and pressure and a model for the formation of the Earth's core. Geophys. J.R. Astr. Soc. 72, 577-595.

Stacey, F.D., 1977. A thermal model of the Earth. Phys. Earth. Planet Inter. 15, 341-348.

MAGNETIC FIELD GENERATION BY CONVECTION I.
BACKGROUND: WAVES AND INSTABILITIES

David R. Fearn

Since convective motions are believed to be responsible for driving the geodynamo, it is important to understand the properties of convection in the environment of the Earth's core. The influences of rotation (with frequency Ω) and of a strong toroidal magnetic field B are certainly important and have been studied by many authors (see Eltayeb,1981 for a recent review). In models applicable to the core it is found that rotation inhibits convection because of the geostrophic constraint and the influence of the boundaries. The effect of a weak magnetic field is to relax the geostrophic constraint and the critical Rayleigh number R_c is inversely proportional to the Elsasser number $\Lambda = B^2/2\Omega\mu\varrho\eta$ where μ is the magnetic permeability, ϱ the density and η the magnetic diffusivity. The Elsasser number may be thought of as a measure of the strength of the Lorentz force compared with the Coriolis force. When Λ becomes $O(1)$, R_c reaches a minimum and for $\Lambda > O(1)$ the magnetic field adopts an inhibiting role with $R_c \propto \Lambda$. All this is well established, but the picture becomes more complicated when we move towards a more realistic model of the core and include the influence of differential rotation and allow for instabilities of the magnetic field.

There are several contributions to the differential rotation in the core (see for example Braginsky 1975), but for the purposes of an initial investigation, it is sufficient to arbitrarily prescribe a flow and study its influence on convection. A simple model consists of a rotating Benard layer with an applied magnetic field $\underline{B} = B s \hat{\phi}$ and flow $\underline{U} = U s \Omega(z) \hat{\phi}$ where (s, ϕ ,z) are cylindrical polar coordinates and B and U are constants. This problem illustrates the inhibiting role of differential rotation. The critical Rayleigh number increases with the magnetic Reynolds number $R_m = U\ell/\eta$ (where ℓ is a lengthscale) and the convection becomes concentrated in the narrow region in which diffusion can be effective in counteracting the shear. The region is a critical layer centered on the location where the phase speed of the instability equals the differential rotation speed. The details of the problem depend on the diffusivity ratio $q = \kappa/\eta$ where κ is the thermal diffusivity. The plane layer model is restricted to $q = 0$ and, in this case, only the temperature perturbation is concentrated [typically in a region of width $(R_m/q)^{-1/3}$ when $(R_m/q) \gg 1$] (Fearn and Proctor 1983b). Less detailed studies are available for nonzero q in a spherical geometry and these suggest that the perturbations to the magnetic and velocity fields become concentrated when $R_m \gg 1$. Since this is precisely the limit which is of interest for the nearly axisymmetric dynamo (see part II of this talk by Proctor), concentrated convection and hence concentrated generation of magnetic field are likely to be features of a convection driven dynamo, and may well cause resolution problems when a numerical solution is attempted.

Two mechanisms which act to oppose field growth have already been mentioned. The critical Rayleigh number increases both with the differential rotation and the field strength, while the toroidal field strength itself increases with R_m. Thus when $\Lambda > O(1)$, if the field grows, it acts to suppress the convection which ultimately generates it. There is a further mechanism which may be important in limiting the growth of the field; instability of the field itself. There are many types of instability.

Some require too high a field strength and others operate on too long a time-scale to be applicable to the geodynamo, but others may be important. One example is the field gradient instability. For a field $B = B(s)\hat{\phi}$, this is locally unstable where B increases with s faster than $s^{3}|^{2}$ (Acheson, 1983), and the field is strong enough to maintain the instability against diffusive losses. Numerical work (Fearn, 1983) has confirmed the presence of this instability and also displayed the presence of another (Fearn, 1983, 1984) which is resistive, and is found in the vicinity of a zero of B(s). These instabilities have been studied in detail in a cylindrical geometry. Little is yet known about their behavior in a more realistic spherical geometry nor about their nonlinear development so any application of these ideas to the core must remain very tentative. It seems probable, though, the instabilities deriving their energy from the strong toroidal field must play a role in determining the shape of the field and its maximum strength.

REFERENCES

Acheson, D.J., 1983. Local analysis of thermal and magnetic instabilities in a rapidly rotating fluid, Geophys. Astrophys. Fluid Dynam. 27, 123-136.

Braginsky, S.I., 1975. Nearly axially symmetric model of the hydromagnetic dynamo of the Earth I., Geomag. Aeron. 15, 122-128.

Eltayeb, I.A., 1981. Propagation and stability of wave motions in rotating magnetic systems, Phys. Earth Planet. Inter. 24, 259-271.

Fearn, D.R., 1983. Hydromagnetic waves in a differentially rotating annulus I. A test of local stability analysis, Geophys. Astrophys. Fluid Dynam. 27, 137-162.

Fearn, D.R., 1984. Hydromagnetic waves in a differentially rotating annulus II. Resistive instabilities, Geophys. Astrophys. Fluid Dynam., in press.

Fearn, D.R. and M.R.E. Proctor, 1983a. Hydromagnetic waves in a differentially rotating sphere, J. Fluid Mech. 128, 1-20.

Fearn, D.R. and M.R.E. Proctor, 1983b. The stabilizing role of differential rotation on hydromagnetic waves, J. Fluid Mech. 128, 21-36.

MAGNETIC FIELD GENERATION BY CONVECTION II
A SELF-CONSISTENT DYNAMO MODEL

Michael Proctor

Any attempt to construct a self consistent-dynamo model for the Earth must first address the question of the strength of the toroidal field. If the toroidal field $B \approx |(\underline{B}_p)|$, the poloidal field, then the Elsasser number

$$\Lambda \equiv \frac{B^2}{2\Omega\mu\rho\eta} \ll 1 \tag{1}$$

where Ω is the rotation rate, μ,ρ the permeability and density and η the magnetic diffusivity. In this case convection is constrained by the Coriolis force, and has a columnar nature (see Fearn, this volume, page 125). The separation of scales has recently been exploited by Busse to obtain a relatively simple set of equations describing the evolution of the fields and flows. We, however, prefer to concentrate on a model in which $B \gg |\beta_p|$, and $\Lambda = O(1)$. This corresponds to a zonal field strength which is most favorable for convection, and to concomitant zonal velocities which seem to be compatible with the westward drift of the nondipole geomagnetic field. However, the convection in this regime is of global scale and so a numerical treatment is necessary (Fearn and Proctor, 1983a,b). We construct the dynamo by finding the most unstable convective mode for a given axisymmetric toroidal field B (normalized to have maximum value unity). Then the mean electromotive force $\underline{\varepsilon} = \langle \underline{u} \times \underline{b} \rangle$ is calculated, where $\langle \cdot \rangle$ denotes a zonal average and $\underline{u}$ and $\underline{b}$ are the convective velocity and magnetic fields. Then the vector potential A for the axisymmetric poloidal field $[\underline{B}_P = \nabla \times (A\hat{\phi})]$ can be calculated from the relation

$$0 = \varepsilon_\phi + (\nabla^2 - \tfrac{1}{s^2})A - \tfrac{1}{s}\underline{u}_P \cdot \nabla(sA) \tag{2}$$

where s is the distance from the rotation axis and $\underline{u}_P$ the mean poloidal velocity. (2) is derived by taking the average of the induction equation, and considering its poloidal part. This determines A up to an arbitrary constant factor (since the magnitudes of $\underline{u}$, $\underline{b}$ are arbitrary at this stage). Then B is calculated from the ϕ component of the induction equation, namely

$$s\,\underline{u}_P \cdot \nabla(B/s) = s\,\underline{B}_P \cdot \nabla(U/s) + (\nabla^2 - \tfrac{1}{s^2})B \tag{3}$$

where the term $(\nabla \times \underline{\varepsilon})_\phi$ is neglected in accordance with the scaling $B \gg |\beta_P|$. The mean velocities $\tilde{U}\phi$ and $\underline{u}_P$ are not determined by the theory as yet, but will, we hope, emerge naturally in future extensions of this work. When the new B field is normalized (by adjusting the amplitudes of A, ε_ϕ and $\underline{u}$) it will in general differ from the original B. Then the procedure is repeated until successive values of B coincide. This program has been successfully used for a number of different forms of U and $\underline{u}_P$. (See Fearn and Proctor 1984 for a preliminary report.)

The first step towards a more complete theory is to understand the dynamics of the mean flow. In the magnetostrophic approximation relevant here viscous and inertial forces are ignored. Then the zonal velocity U is only determined

up to an arbitrary geostrophic flow $U_G(S)$, and a solution is possible if, and only if, the "Taylor condition"

$$T(S) \equiv \int_{C(S)} [\nabla_x(B\hat{\phi})_x \nabla_x(A\hat{\phi})]\cdot\hat{\phi}\, dz \equiv 0 \qquad (4)$$

is satisfied, where C(S) is the surface of a cylinder of radius S coaxial with the rotation axis and inscribed in the core. Since $U_G(S)$ appears in equation (3), one hopes that U_G is determined (up to a solid body rotation) by (4). It can be shown by example that there are certain rather special fields for which such a solution is impossible, but in general a compatible magnetostrophic state exists. We find solutions by solving (2) and (3) for fixed ℓ and μp (and so fixed A), setting $U = \hat{0}$ (S,Z) [prescribed] + $U_G(S)$ and attempting to satisfy (4). The technique employed is to minimize $\Sigma T^2(S_i)$ by varying $U_G(S_j)$, $j = 1\text{----}m$ [m < n] and fitting a smooth function to $U_G(S_j)$ using Chebyshev polynomials. This iterative process will be included in future models.

The procedure described above for finding B says nothing about the stability of the evolved state. A lumped parameter model has been developed to test this, which in its simplest form consists of the three ode's

$$\dot{E} = R(1-B^2)E - \frac{\mu_1}{R}E^2$$

$$\dot{B} = A - B \qquad (5)$$

$$\dot{A} = EB - \mu_2 A$$

where E is measure of the kinetic energy of the convection and R is the Rayleigh number. This equation can be shown to have stable steady solutions in a certain range of R, which goes some way towards justifying the method.

REFERENCES

Fearn, D.R. and M.R.E. Proctor, 1983a. J. Fluid Mech. 128, 1-20.

Fearn, D.R. and M.R.E. Proctor, 1983b. J. Fluid Mech. 128, 21-26.

Fearn, D.R. and M.R.E. Proctor, 1984. Phys. E. Plant. Int., (in press).

NONLINEAR OSCILLATIONS IN DOUBLE-DIFFUSIVE CONVECTION

Michael Proctor

Double diffusive convection effects can arise in a variety of ways. Apart from the conventional thermohaline problem of interest in oceanography there is the situation of convection in a rotating layer and convection in the presence of a magnetic field. In the last two cases the system would support waves (respectively inertial and Alfvén) in the absence of heating or diffusion, and waves of these types can be destabilized by an unstable temperature gradient provided that the thermal diffusivity is sufficiently great. We concentrate on the magnetoconvection problem here, and attempt to answer the question of the range of parameters in which oscillations can be expected to occur. A full description of most of the conclusions of this lecture appears in the review article of Proctor and Weiss (1982). We support the imposed magnetic flux to be vertical, and adopt the Boussinesq approximation.

The dynamics depends on the four dimensionless parameters

R	(Rayleigh No.)	proportional to temperature contrast
Q	(Chandrasekhar No.)	proportional to the square of the magnetic flux
σ	(Prandtl No.)	$\dfrac{\text{viscosity}}{\text{thermal diffusivity}}$
ζ		$\dfrac{\text{magnetic}}{\text{thermal diffusivity}}$

Oscillations can occur provided $\zeta < 1$ and Q exceeds a critical value that depends on ζ. If we focus on two-dimensional motion we can define scaled Rayleigh and Chandrasekhar numbers r, q by the relations

$$R = R_0 r \qquad R_0 = (\pi^2 + \alpha^2)^3/\alpha^2$$

$$Q = Q_0 q \qquad Q_0 = (\pi^2 + \alpha^2)/\pi^2 \tag{1}$$

where π and α represent the vertical and horizontal wave numbers of the disturbance field in linear theory. R_0 is the critical Rayleigh number for the onset of convection when $Q = 0$. Then if $\zeta < 1$ and $q > \dfrac{\zeta}{\sigma}\left(\dfrac{1+\sigma}{1-\zeta}\right)$ there is a simple bifurcation of the static state at

$$r = r^{(e)} = 1 + q \tag{2}$$

and a Hopf bifurcation at

$$r = r^{(o)} = (\sigma + \zeta)\left[\frac{1+\zeta}{\sigma} + \frac{\zeta q}{1+\sigma}\right] < r^{(e)} \tag{3}$$

weakly nonlinear perturbation theory then tells us that branches of steady and oscillatory solutions bifurcate at $r^{(e)}$ and $r^{(o)}$ respectively. The steady solution branch is always unstable at small amplitudes while the oscillatory branch is typically supercritical and stable locally. Essentially two distinct cases arise, as expressed in figure 1, showing sketches of amplitude squared against r.
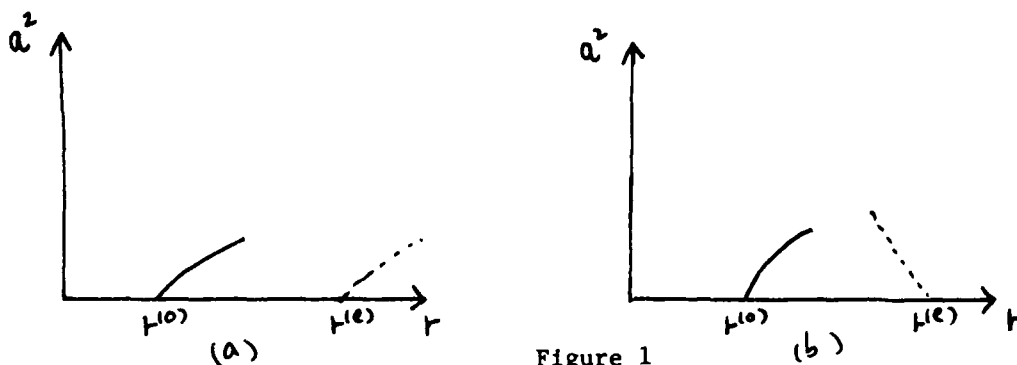
Figure 1

It should be noted that figure 1 shows only behavior for small a^2: at lower amplitudes the steady solution branch may turn back to reach a value lower than $\mu(0)$.

It turns out that the branch of oscillatory solutions always terminates on the steady solution branch. If, at the point of conjunction the gradient $d(a^2)/d\mu$ of the steady solution branch is negative, the termination is via a heteroclinic orbit of infinite period. If, on the other hand $d(a^2)/d\mu > 0$ the termination occurs via a Hopf bifurcation.[†] In the former case if the so called "Shilnikov" condition or the eigenvalues of the perturbation equations from the steady branch is satisfied, the oscillations may break down via a sequence of period doubling bifurcations (See Knobloch, Weiss and DaCosta, 1981). It turns out that in the limit $\zeta \ll 1$ almost all the interesting behavior may be described by the following third order system of equations

$$\dot{a} = \mu + \tilde{q}\, d\,((\varpi - 3)e - 1)$$

$$\dot{d} = -d + a(1-e)$$

$$\dot{e} = -(4 - \varpi)e + \varpi a d$$

where $\varpi = 4\pi^2/(\pi^2 + \nu^2)$ and a represents the velocity amplitude, and d and e the two most significant spatial components of the magnetic field. These equations are easily derived from a fifth order system described in Knobloch et al., 1981. Numerical integrations are not yet complete, but they do show the existence in some parameter ranges of two branches of oscillations. To find an even simpler description of this phenomena, we may further reduce the equations when $\varpi \approx 2$ (corresponding to square convection cells). By setting $\varpi = 2 - \epsilon^2$ and rescaling a, d, and e appropriately for small ϵ, we arrive at the canonical system

$$\ddot{a} - \dot{a}(\tilde{q} - 2a^2) - \gamma a + a^3 - a^5 = 0$$

(where $\tilde{q}$ is a measure of q and γ a measure of μ/q) which has been integrated numerically. The results are reproduced below (fig. 2). For small q, the oscillatory branch always ends at a Hopf bifurcation, and there is a region of stable vacillation near the bifurcation point. As q increases the oscillatory branch intersects the steady branch, leading to two heteroclinic orbits. The one marked A in the figure persists for layer q, while the other becomes confined to a smaller and smaller region, finally becoming vacillatory and vanishing when q = 1.

[†] See e.g. Knobloch & Proctor (1981).

$(i) = \text{smaller } \tilde{q}$

$(ii) = \text{larger } \tilde{q}$
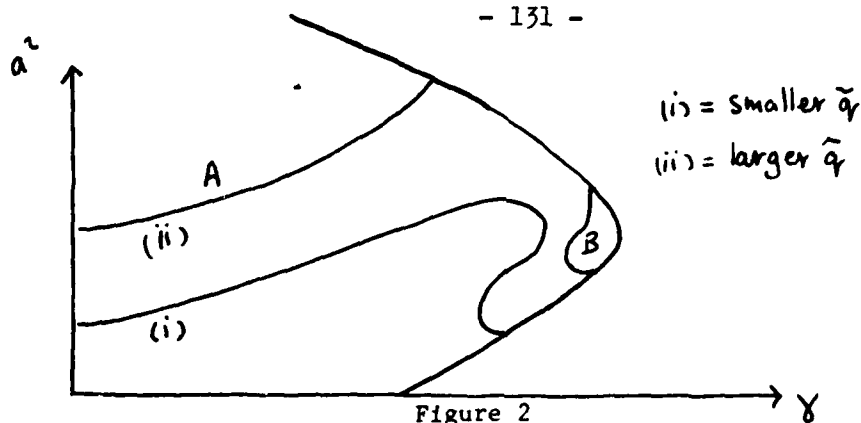
Figure 2

Thus the behavior of the oscillatory modes in this simple Boussinesq problem is now understood. The next task is to extend the theory to compressible convection and thus produce results that can be related directly to convection in the solar photosphere in the presence of strong magnetic fields.

REFERENCES

Knobloch, E., N.O. Weiss and L.N. DaCosta, 1.81. J. Fluid Mech. 113, 153-186.

Knobloch, E., and M.R.E. Proctor, 1981. J. Fluid Mech. 108, 291-316.

Proctor, M.R.E. and N.O. Weiss, 1982. Rep. Prog. Phys. 45, 1317.

Weiss, N.O., 1981a,b. J. Fluid Mech. 108, 247-272 and 273-288.

MINISYMPOSIUM ON GEOLOGICAL FLUID DYNAMICS

Jointly sponsored by GFD 1984 and

Center for Analysis of Marine Systems

CAMS MINISYMPOSIUM

Back Row: Lea, Graham, Carey, Sigurdsson, Sparks, Huppert, Hamaru, Baker, Hocking, Torrey, Reed, Malkus, Spiegel.

Middle Row: Loper, Grove, Taylor, Hayashi, Smith, Kerr, Ribe, Whitehead, Dick, Schouten, Chen, Bryan.

Bottom Row: Worster, Gorius, Feigl, Meyer, Bayley, Veronis, R. Kerr, Zaleski, Lesher.

PREFACE

The Minisymposium on Geological Fluid Dynamics

All geologists know that every spot on the face of the earth has moved, and is presently flowing - but so slowly that the present flow is immeasurable. If we could stand like the man in H. G. Wells' short story "The Time Machine" and watch the earth and mountains with a time compression of one second of our time equal to one hundred thousand years of earth time, and with a space compression so that what is to us ten centimeters is really ten kilometers, the earth would look like a vat of boiling pitch. Some important geological processes would occur too quickly. Thus erosion would resemble a giant sanding machine and volcanism would occur, at least on the surface, as instantaneous eruptions. There would be a new Hawaiian island every ten seconds and the suggested 20,000 year cycle of volcanic crust emplacement at spreading centers would occur at the rate of five per second.

But we do not need a miracle machine to see these upheavals. The fluid mechanics scaling laws laid out almost a century ago allow such compression to be realized in vats of sugar/salt solution, in tanks of syrup or in numerical experiments. Moreover, we can analyze simple problems to sharpen our focus and dive deep in the earth with no problem.

In our minisymposium on Geological Fluid Dynamics ideas were presented with full interaction between fluid dynamicists, petrologists, field geologists, and geophysicists. The studies centered around mixing processes by magmas and raised the issue of the consequences of large viscosity variation upon transport processes - a field of fluid dynamics which is virtually unexplored and indeed hardly even thought of until now. After three days of discussion we were refreshed by a field trip to a nearby site where two lavas of different viscosity merged, but did not mix a "short" time ago (forty to eighty million years ago).

DENSITY VARIATIONS IN MAGMAS:
FLUID DYNAMIC IMPLICATIONS

R. Steven J. Sparks

Both compositional and thermal effects on density influence convection within magma chambers. Consequently it is important to assess the relative contributions of composition and temperature to the density of magmas, particularly during crystallization and melting processes. Recent studies (Sparks and Huppert, 1984) have shown that during fractional crystallization of basaltic magmas the compositional changes during an increment of fractionation are generally much larger than associated thermal effects. Sparks and Huppert (1984) introduced a parameter called <u>fractionation density</u>, which is defined as the density of the fluid component being selectively removed by crystallization:

$$\rho_c = \frac{M_c}{V_c} \tag{1}$$

where M_c is the gram formula weight and V_c is the partial molar volume of the components being removed from the melt into the crystals. When ρ_c is greater than the melt density, the residual melt decreases in density. When ρ_c is less than the melt density, the residual melt increases in density. In the case of basaltic magmas olivine and pyroxenes have fractionation densities greater than the melt. However, plagioclase has a lower fractionation density. Consequently, density will initially decrease in basalt differentiation, but can often increase when plagioclase joins in as a crystallizing phase.

With a quantitative understanding of density variations and present knowledge of convection in crystallizing fluids, new insights into the evolution of igneous rocks can be obtained. Compositional stratification can be caused by repeated replenishment of magma chambers by dense primitive magma or by sidewall crystallization. Mixing in magma chambers can be caused by compositional convection and replenishment by low density magma. There is a wide range of geological applications of these ideas (Huppert and Sparks, 1984; Sparks et al., 1984).

REFERENCES

Huppert, H.E. and R.S.J. Sparks, 1984. Double-diffusive convection due to crystallization in magmas. <u>Ann. Rev. Earth Planet. Sci.</u>, <u>12</u>, 11-37.

Sparks, R.S.J. and H.E. Huppert, 1984. Density changes during the fractional crystallization of basaltic magmas: fluid dynamic implications, <u>Contrib. Mineral. Petrol.</u>

Sparks, R.S.J., H.E. Huppert and J.S. Turner, 1984. The fluid dynamics of evolving magma chambers. <u>Philos. Trans. Roy. Soc. London,</u>

THERMAL AND COMPOSITIONAL ZONING
IN THE FAMOUS AREA:
EVIDENCE FOR A ZONED MAGMA CHAMBER

Wilfred B. Bryan

Precisely located basalt samples from the floor of the median valley in the FAMOUS area, Mid-Atlantic Ridge, show a systematic pattern of compositional zonation, from the center to flanks of the valley, over a total width of about 4 km. Contours draw through compositional parameters also close across the valley, north and south of extrusive volcanic hills represented by Mt. Pluto and Mt. Venus, over a distance of about 10 km. Ages of the extrusive basalts are about equal, and range from a few hundred to about 10,000 years, based on calibrated measurements of manganese oxide coatings on rock samples. Thermal and density variations calculated from compositional data indicate a temperature of about 1250° C for the central lavas, and about 1200° C for flank lavas. Magma density ranges from about 2.70 in the valley center to about 2.80 on the flanks. Although many lavas are almost free of suspended crystals (phenocrysts), some basalts on the west side of the valley are distinctly enriched in plagioclase (density = 2.72) while some basalts just to the east of the valley axis are enriched in olivine (density = 3.4).

These relationships are interpreted as reflecting compositional and physical zonation in a shallow (1 - 2 km depth) magma chamber beneath the median valley. A tectonic event associated with spreading apparently opens fissures that inject hot, relatively light magma into the base of the chamber, and also causes cracking of the chamber roof and eruption of lava on the valley floor. Hot, relatively light magma rises as a plume through the center of the chamber and erupts in the center of the valley; colder, denser magma settles along the chamber walls and also is erupted from fissures along flanks of the valley. At least locally, the chamber may have the form of an inclined, asymetrical lens, allowing plagioclase to float to the high apex on the west, and olivine to accumulate by settling to the lower side of the lens on the east; disruption of these cumulate zones during eruption may create the mineralogical asymetry in some of the basalts.

Other geochemical complications include an excess enrichment of volatile components (H_2O, CO_2) and of certain incompatible trace elements. These are "in excess" in the sense that they are concentrated in two to three times the amount predicted by simple, single-stage crystallization of the observed central magma. One possibility is that the flank magma evolved from a previous batch f parental magma that was initially more enriched in volatiles and in the i..compatible elements. A second possibility is that these enrichments developed from the continual rejection of residual liquid from crystal networks accreting to the cooler walls of the chamber. Both the physical and geochemical constraints on these alternative models are being investigated.

CRYSTALLIZATION AND COMPOSITIONAL
CONVECTION IN POROUS MEDIA:
A MECHANISM FOR PRODUCING ADCUMULATE ROCKS

Ross C. Kerr

Huppert and Sparks (1980 a, b) have developed a fluid mechanical model of a replenished basaltic magma chamber. In order to test this model, Steve Tait and I have collected rocks from Unit 10 of the Eastern Layered Series of the Rhum Intrusion in North-West Scotland. This unit consists of 65 meters of an olivine cumulate rock called peridotite, overlain by 15 meters of gabbro. Tait's (1984) analysis of the olivine crystals has shown that they are virtually uniform in Mg/(Mg + Fe) ratio, Ni content and Sr^{87}/Sr^{86} ratio. These geochemical observations demonstrate that the olivine crystals nucleated and grew in suspension (as predicted in the Huppert and Sparks model), before they settled out to form a porous medium of crystals at the base of the chamber. If the magma in the porespace had been solidified without any further fluid mechanical processes occurring, the porespace of the observed rocks would have consisted of a variety of chemically zoned minerals (orthocumulate texture, Irvine 1980). The peridotites, however, contain large, unzoned, poikilitic porespace crystals of pyroxene and plagioclase (adcumulate texture), which together do not make up any plausible magmatic composition. A process is therefore required which can remove from the crystal pile porespace magma depleted in the chemical components necessary for the growth of these unzoned porespace minerals.

Kerr (1984) and Tait (1984) propose that the adcumulate textures of the Rhum peridotites is due to compositional convection in the unconsolidated pile of olivine crystals. Such compositional convection occurs whenever inter-cumulus crystallization decreases the density of the porespace magma, and will result in chemical exchange between the porespace and the overlying magma chamber.

We have modelled this process experimentally by cooling and crystallizing from below aqueous solutions of $CuSO_4$ and Na_2SO_4, partially contained in porous media consisting of glass spheres. Such cooling resulted in the nucleation and growth of $CuSO_4 \cdot 5H_2O$ and $Na_2SO_4 \cdot 10H_2O$ crystals, and the release of light depleted fluid. Convection takes the form of rising fingers of this depleted fluid in the porous medium. The experiments were performed with spheres of varying diameters, and hence varying permeability. They demonstrated that adcumulus growth occurs whenever the convective velocities in the porespace are significantly greater than the rate of solidification of the porous medium. Our scaling of these quantitative results to the Unit 10 peridotites shows that this process is consistent with the observed amount of adcumulus growth.

Experiments have also been performed in order to determine the rate of convective exchange between a magma contained in a cumulate pile and a large volume of heavier, possibly less viscous, overlying magma. Descending fingers of heavier magma descend into the porous medium with a velocity

$$v = 0.55 \, kg \, \Delta\rho / \mu_l^{0.6} \, \mu_u^{0.4} \, \epsilon \quad ,$$

where $\Delta\rho$ is the difference in the density of the two magmas, k is the permeability of the porous medium, g is the acceleration due to gravity, $\mathcal{E}$ is the porosity of the porous medium and μ_l and μ_u are the lower and upper layer viscosities. This velocity is sufficient to enable a layer of replenishing magma to exchange significantly with the underlying cumulate pile, profoundly changing its porespace chemistry.

REFERENCES

Huppert, H.E. and R.S.J. Sparks, 1980a. Restrictions on the compositions of mid-ocean ridge basalts: A fluid dynamical investigation. *Nature* 286, 46-48.

Huppert, H.E. and R.S.J. Sparks, 1980b. The fluid dynamics of a basaltic magma chamber replenished by influx of hot, dense ultrabasic magma. *Contributions to Min. and Petrology*, 75, 279-289.

Irvine, T.N., 1980. Terminology for Layered Intrusions. *Journal of Petrology* 23, 127-162.

Kerr, R.C., 1984. Crystallization and Compositional Convection in Geological Fluid Mechanics. *Ph.D. Thesis, University of Cambridge.*

Tait, S.R., 1984. Fluid Dynamical Processes in the Formation of Layered Igneous Rocks. *Ph.D.Thesis, University of Cambridge.*

FRACTIONAL CRYSTALLIZATION
ASSIMILATION AND MAGMA MIXING

Timothy L. Grove

Some of the factors that allow tholeiitic and calc-alkaline differentiation trends to be generated from a common basaltic parent melt are discussed and liquid lines of descent for the two divergent trends are calculated. Phase proportions and compositions measured in 1-atmosphere experiments on natural basalts are used as input to calculate the tholeiitic trend, and high pressure phase proportions, inferred from phase equilibrium studies on natural compositions, are used to calculate the calc-alkaline trend. An important control on the development of the contrasting tholeiitic vs. calc-alkaline trends is the proportions of olivine, plagioclase and pyroxene that crystallize from the basaltic parent melt. The tholeiitic trend is produced by fractional crystallization of a basalt magma at low pressures. The crystallization sequence is olivine, followed by plagioclase, followed by augite, and plagioclase dominates the assemblage. The calc-alkaline trend develops when olivine, calcic plagioclase and augite crystallize in nearly equal mass proportions. This phase assemblage precipitates under conditions of moderate pressure and water undersaturation in the middle to upper crust. Liquids derived by such a process can evolve to andesites and dacites by continued crystallization involving plagioclase, orthopyroxene, pigeonite, augite and magnetite. The assimilation of a crustal component by a fractionating basaltic melt and the mixing of basaltic liquids with siliceous residual liquids produced by either fractionation or fractionation aided by assimilation are additional process that assist in the production of the calc-alkaline trend.

A DISCUSSION OF THE DYNAMICS OF PARTIALLY
MOLTEN/SOLIDIFIED SYSTEMS

David E. Loper

There are a number of geophysical-fluid-dynamical systems which may be characterized as partially solidified. The phrase "partially solidified" means that the fluid is in contact with the corresponding solid phase and that change of phase can and does occur as the system evolves. Typically the fluid and solid are in intimate contact throughout a volume rather than at a surface. There are two configurations for this mixture of solid and liquid that occur quite often. The first is a "mushy zone" in which the solid crystals form a (nearly) rigid open network while the fluid fills the voids between the crystals. The second is a "slurry" in which the solid crystals are dispersed throughout the fluid. In this discussion, these two configurations will be described and Boussinesq-like equations governing their dynamical behavior will be presented. Much of the following is based upon three papers: Loper and Roberts (1978, 1980) and Hills, Loper and Roberts (1983).

Although most geophysical systems such as magma chambers are composed of many constituents, the essential features may be modeled by considering a simple system of two constituents. We will refer to the principal constituent as A and the minor or impurity constituent as B. The thermodynamic state of the system is characterized by three variables: pressure, p, temperature, T, and mass fraction of B, ξ. The system may be characterized as partially solidified if the state variables p, T and ξ lie below the liquidus and above the solidus or eutectic line; that is, within the hatched region of Figure 1.

p = constant

L = Liquidus
S = Solidus
E = Eutectic
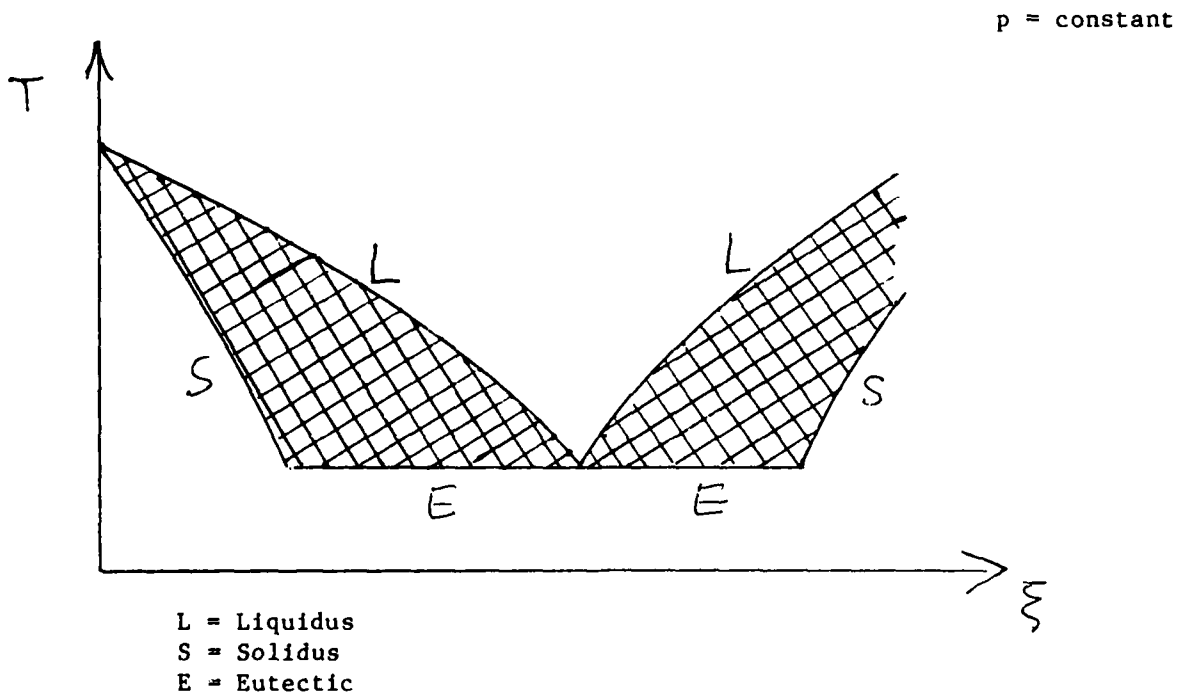
A Boussinesq-like set of equations for the flow of fluid in a mushy zone is:

$$\nabla \cdot \left[(1-\phi)\, \underline{w} \right] = 0 \tag{1}$$

$$D\,\xi^L / Dt = \nabla \cdot \left[\bar{D}\,(1-\phi)\,\nabla \xi^L \right] + (1-\lambda)\,D^S(\phi\,\xi^L)/Dt \tag{2}$$

$$\rho_0\,\nu\,\underline{w} / (1-\phi)\,\gamma \;=\; -\nabla p - \rho^L\,\underline{g} \tag{3}$$

$$\rho_c\,C_p\,DT/Dt - \alpha T_0\,Dp/Dt \;=\; \nabla \cdot (k\,\nabla T) + \rho_0 L\,D^S\phi/Dt \tag{4}$$

$$(1-\lambda)\,\bar{\mu}\,\xi_0^L\,(\xi^L - \xi_0^L) = \delta(p - p_0) - (L/T_0)(T - T_0) \tag{5}$$

$$\rho^L = \rho_0 \left[1 - \alpha(T - T_0) - \rho_0\,\tilde{\delta}\,(\xi^L - \xi_0^L) \right] \tag{6}$$

In this model the solid matrix is assumed to be rigid and its velocity $\underline{u}^S$ is known and prescribed. In this case the familiar continuity equation

$$\nabla \cdot \underline{u} = 0$$

leads directly to (1) when the barycentric velocity is expressed as

$$\underline{u} = \underline{u}^S + (1-\phi)\,\underline{w}$$

where $\underline{w} = \underline{u}^L - \underline{u}^S$ is the velocity of the liquid relative to the solid, and ϕ is the mass fraction of solid.

Equation (2) governs the conservation of constituent B in the liquid phase; ξ^L is the mass fraction of B in the liquid. The value of ξ^L within a parcel can change due to the familiar diffusion of B down the concentration gradient in the liquid (solid diffusion is ignored); this effect is represented by the first term on the right hand side of (2) with $\bar{D}$ being the material diffusivity. The second term on the right hand side of (2) represents the change of ξ^L due to melting and freezing. The parameter λ is the alloying fraction:

$$\lambda = \xi^S / \xi^L$$

where ξ^S is the mass fraction of B in the solid. Clearly $0 \le \lambda < 1$; we assume λ = constant. Note that

$$D/Dt = D^S/Dt + (1-\phi)\,\underline{w} \cdot \nabla \quad , \quad D^S/Dt = \partial/\partial t + \underline{u}^S \cdot \nabla$$

In the mush, conservation of mass reduces to D'Arcy's Law (3) where ρ_0 is a (constant) reference density, ν is the kinematic viscosity, γ is the permeability, ρ^L is the density of the liquid and $\underline{g}$ is the acceleration of gravity. The liquid density can vary with temperature or composition (6); isothermal compressibility is neglected. The permeability γ is a function of the mass fraction of solid ϕ; this is equivalent to the usual permeability - porosity relation. This is an important relation, being the macroscopic parameterization of the microscopic pore structure. The relation $\gamma(\phi)$ makes the set of equations strongly nonlinear and difficult to solve.

The energy equation (4) has a volumetric source term representing the latent heat released due to solidification, with L being the latent heat; the remaining terms are standard.

Equation (5) is a linearized version of the liquidus relation

$$f(p, T, \xi^L) = 0$$

with

$$\overline{\mathcal{M}} = \partial \mu^L / \partial \xi^L$$

being the variation of chemical potential with composition and

$$\delta = \frac{1}{\rho^L} - \frac{1}{\rho^S}$$

being the change of specific volume upon melting.

These equations include a number of important physical effects, with perhaps the most interesting being the formation of pipes and chimneys. Generally flow toward the source of cooling induces deposition of solid and flow away induces erosion. The process of erosion changes the permeability which, in turn, changes the structure of the flow. Often this results in pipes or chimneys in the mush, through which relatively vigorous flow occurs. On the other hand, there are several important effects not included. The most important of these is deformation of the solid which allows for compaction and expulsion of the liquid from the solid. Also not included are Taylor dispersion and the effects of surface tension (e.g., Ostwald ripening). Efforts are underway to incorporate these into model.

The set of equations (1) – (6) governs the flow of the fluid portion of the system in the case that the solid forms a rigid porous matrix. If the solid is in the form of discrete unconnected particles, i.e. a slurry, we must formulate equations for the system as a whole. These are

$$\underline{\nabla} \cdot \underline{u} = 0 \tag{7}$$

$$D\xi / Dt = \overline{D} \, \underline{\nabla} \cdot \left[\underline{\nabla} \xi + \xi \underline{\nabla} \phi \right] + \underline{\nabla} \cdot \left[\xi \left(\frac{1}{\rho_0} - \frac{1}{\rho^S} \right) b \underline{g} \right] \tag{8}$$

$$\rho_0 \, D\underline{u} / Dt = -\underline{\nabla} p + \rho \underline{g} + \rho_0 \nu \nabla^2 \underline{u} \tag{9}$$

$$\rho_0 C_p^* \, DT / Dt - \alpha^* T_c \, Dp / Dt = \underline{\nabla} \cdot (k^* \underline{\nabla} T) - \underline{\nabla} \left[a^* L \left(1 - \frac{\rho_c}{\rho^{\cdot \cdot}} \right) b \underline{g} \right] \tag{10}$$

$$\bar{\mu}\,\xi_0\left[\,\zeta - \xi_c(1-\phi)\right] = \delta(p - p_0) - (L/T_c)(T - T_0) \tag{11}$$

$$\rho = \rho_0\left[1 - \alpha^*(T - T_c) - \rho_0\,\bar{\delta}^*(\xi - \xi_0)\right] \tag{12}$$

In this model we have set the alloying fraction λ to zero to avoid the complications of history dependence. Now the total mass fraction of B is given by

$$\xi = (1-\phi)\,\xi^L$$

and, in the limit

$$\phi \ll 1$$

the material diffusion term takes the form given on the right-hand side of (8). The last term on the right-hand side of (8) represents the local change of composition due to sedimentation of solid particles of density ρ^s in a fluid of density ρ_c. The sedimentation coefficient is, in the limit $\phi \ll 1$, given by

$$b = \left(\rho^s \rho_c^2 \phi^5 \,/\, 162\pi^2 \, \nu^3 N^2\right)^{1/3}$$

where N is the number of solid particles permit volume.

One unusual feature of a slurry is that several of the familiar coefficients take on distinctly different values with solid particles present. Specifically

$$C_P^* = C_P + L^2/T_c\,\bar{\mu}\,\xi_c^2$$

$$\alpha^* = \alpha + \rho_0\,L\delta/T_0\,\bar{\mu}\,\xi_c^2$$

$$\bar{\delta}^* = \bar{\delta} + \delta/\xi^L$$

$$k^* = k + L^2\alpha^* b/T_c$$

where

$$a^* = \rho_0\,\bar{D}\,/(\rho_c\,\bar{D} + b\,\bar{\mu}\,\xi_c^2)$$

REFERENCES

Loper, D.E. and P.H. Roberts, 1978. On the motion of an iron-alloy core containing a slurry. I. General theory. Geophys. Astrophys. Fluid Dyn., 9, 289-321.

Loper, D.E. and P.H. Roberts, 1980. On the motion of an iron-alloy core containing a slurry. II. A simple model. Geophys. Astrophys. Fluid Dyn., 16, 83-127.

Hills, R.N., D.E. Loper and P.H. Roberts, 1983. A thermodynamically consistent model of a mushy zone. Q.J. Mech. Appl. Math., 36, 505-539.

BUOYANT MOTIONS WITH LARGE VISCOSITY DIFFERENCES
HAVE LARGE LATERAL MOTION

John A. Whitehead, Jr.

The low Reynolds number dynamics of a thin layer of fluid bounded below by a flat horizontal boundary above by a fluid of another viscosity and greater density is studied by means of model experiments and linear stability theory. Three distinct stages of growth were observed. The first stage is described by a linearized Rayleigh-Taylor instability, in which disturbances of one specific wave number grow most rapidly. If E is the ratio of the viscosities of the thin layer to the viscosity of the thick layer, fastest growth is for wavenumber $E^{1/3}$. In the second stage, distortion of the interface is large enough to invalidate the linearized analysis. It is found experimentally that the fluid moves upward as circular columns surrounded by relatively broad regions of descending material. In the third stage, fully matured structures are formed. If the upwelling material has greater viscosity than the surrounding material, the structure is a long vertical column; if the upwelling material has less viscosity than the surrounding material, the structure develops a rim syncline and a pronounced overhang and eventually ascends as a spherical pocket of fluid fed by a conduit.

Next, a laboratory and theoretical study of the stability of conduits is reviewed. In some experiments the upper fluid was sheared laterally so that the conduit gradually rotated to a more horizontal position. The diameter of the conduit increased with time due to a decreasing component of gravitational force along the axis of the conduit. When the conduit was tilted to more than 60° with the vertical, it began to go unstable by developing bumps which ultimately initiated a new spherical pocket which rose to a new spot. If the Reynolds number of the conduit was greater than approximately ten, an axisymmetric wavy instability appeared in the walls of the conduit and the conduit had to be tilted less before a new chamber was initiated.

We then discussed the possibilities of such instabilities under spreading centers. Typically, the formation, ascent and aggregation of magmas along the mid-ocean ridges is regarded two dimensionally, and modelled in a section through the crust and mantle across the strike of the ridges. We addressed the problem with a new three-dimensional model for which we provide supporting geologic evidence.

In this model we postulate that a linear region of high-melt content exists in the mantle below the ridge where melt aggregates from the rising asthenosphere. This region could be approximated as a cylindrical body with lower viscosity and density compared to the overlying mantle. Under such a circumstance, a fluid will develop a gravitational instability leading to regularly spaced vertical protrusions. We have conducted some simple experiments in which a water-glycerine mixture was quickly injected into glycerine along a horizontal line. Although this line will gradually rise because the water-glycerine mixture is less dense than the pure glycerine, an instability will always develop and lead to semi-spherical pockets. It is reasonable to expect that a linear region of partially molten mantle in the earth will behave in a similar manner and will lead to more or less regularly spaced intrusions from which the melt will ascend to form magma chambers at spreading ridges.

Effects of viscosity variation in magmatic mixing between conduits and surrounding fluid were then discussed. Steady state experiments with water injected below an ambient layer of glycerine indicate that the general mixing processes can be strongly influenced by the Reynolds number $R_{i,e} = (Q^3 g^*/\nu_{1,e}^5)^{1/4}$. Here Q is mass flux of the intruding fluid, g^* is reduced gravity and ν is viscosity of the intruding (ν_1) or external (ν_e) fluids. At small R_i there is a laminar conduit of buoyant material. As R_i is increased at small R_e, an axisymmetric wave grows (a varicose instability) and at further increase there is some glycerine stripped off the walls. If R_e is increased starting from the varicose state with Ri constant, there is a transition to a nonaxisymmetric meandering state. As both numbers are increased from any of these states, fine scale entrainment and detrainment get progressively more intense until at R_i and R_e of order 10^3 there is a fully turbulent plume.

THE GENERATION AND COMPOSITION OF PARTIAL MELTS
IN THE EARTH'S MANTLE

Neil M. Ribe

The generation and composition of partial melts in the mantle are examined using equations which describe the flow of two interpenetrating Newtonian fluids which exchange mass, momentum and energy. The equations are applied to a simple one-dimensional model in which mantle material rises at constant velocity U_o and undergoes pressure release melting. The liquid so produced (the "melt") then migrates upward relative to the more dense crystalline residue (the "matrix"). Solutions to the equations are obtained for two simple model problems chosen to illustrate the dynamics of partially molten systems. In the first model problem, mantle material rises at velocity U_o to a level $z = 0$, where a volume fraction ϕ_o of the material melts. Above $z = 0$, the melt migrates rapidly upward relative to the matrix, which undergoes a corresponding deformation or "compaction". Solution of the equations for conservation of mass and momentum shows that compaction of the matrix occurs only in a thin boundary layer whose thickness (the "reduced compaction length") is of the order of 10-100 meters in the earth's mantle. Over most of the earth's mantle, therefore, compaction can be ignored, and the migration of melt can be accurately described by Darcy's Law.

In the second model problem, the upwelling mantle material is assumed to comprise only two chemical components (Forsterite, Mg_2SiO_4, and Fayalite, Fe_2SiO_4). Melting begins at some level $z = z_o$ where the material reaches its solidus. Above $z = z_o$, melt and matrix coexist in chemical equilibrium. The continuity and energy equations, together with the phase equilibrium relations, are solved to determine the temperature and composition (weight percent forsterite) in the melt and the matrix as functions of height above $z = z_o$. An equation governing the conservation of a trace element is derived, and solved to give an expression for the concentration in the melt as a function of z. The solutions obtained are independent of the momentum equations, which implies that the temperature and composition of the melt are independent of the mechanics of melt migration.

LATE STAGE COMPOSITE DIKES IN THE
GRANITIC ROCKS OF THE SIERRA NEVADA:
### CLUES TO THE GENERATION OF THE BATHOLITH ITSELF

John B. Reid, Jr.

A combination of field observations, petrography and geochemical data suggests that mantle-derived basaltic magmas have played an important role in the generation of the Sierra Nevaua batholith. These melts, traversing upward through the overlying continental crust, provide the heat necessary to partially melt it; subsequent mafic melts contaminate these crustal melts in a complex series of mixing episodes to create the observed spectrum of granodioritic compositions. Injections of basaltic magma may also occur late in a pluton's cooling history, creating microcosms of crust-mantle interaction that hold valuable clues to the petrogenesis of the Sierra Nevada batholith itself.

Depending largely on the temperature (T_i) of the invaded granitoid, basaltic injections may create a wide variety of textures. For $T_i \ll T$ solidus, the essentially unaffected host quickly chills crack-filling basalt. When $T_i \backsimeq T$ liquidus, basaltic injections into large volumes of felsic magma chill into rounded pillows that are represented in the eventual plutonic rock as mafic inclusions. These inclusions may undergo subsequent dissolution in the felsic host, contaminating it to intermediate compositions. (In regions dominated by mafic melts, two-magma interactions lead to direct mixing without the intermediate chilling event.) If $T_i \backsimeq T$ solidus, the felsic host may be sufficiently crystallized to undergo brittle fracture, and yet may suffer subsequent partial melting when these fractures are invaded by mafic melts. Observations of closely related felsic and mafic materials in composite dikes in the central Sierra Nevada suggest that many late stage felsic magmas are created and in some cases contaminated by mantle-derived melts.

The central aim of this work is to understand the petrogenetic details of these late-stage, small-scale dike systems with the hope that they will shed light on the evolution of the much larger plutons whose long cooling times have largely blurred the textural record of their petrologic development. At Hell Hole Meadow along the periphery of the Mt. Givens granodiorite body is a system of aplite dikes whose centers were filled with dark finegrained high-Si andesitic magma prior to the complete solidification of the light colored melt. In some regions, andesitic melts have chilled as pillows in the felsic host; in others where less felsic melt was present, the andesite flushed the still molten aplite with it, creating hybrid compositions by direct mixing. Major and trace element (Sr, Zn, Zr, V) data for this dike system are strikingly rectilinear, and mimic trends created in the felsic part of the spectrum of rocks in the North America Wall of El Capitan, and in the felsic rocks of three larger plutons (Tuolumne, Mt. Givens and Eagle Peak). Petrographic textures within the mafic portions dike record its rapid solidification, and closely resemble the petrography of the common mafic inclusions of the larger plutons. The generation of the andesitic melts is not recorded at Hell Hole Meadow. They are compositionally similar to high-Si andesites from Medicine Lake Highland, California interpreted by Grove et al. to have evolved from high-Al basaltic magmas by a combination of fractional crystallization and crustal assimilation.

Although volumetrically insignificant on the scale of the batholith, the late-stage injections have recorded a series of processes of interaction between mantle-derived basaltic melts (and their associated andesites) and felsic melts created in the crust probably using heat contributed by the mafic magmas. The dikes appear to provide valuable information about the evolution of the very much larger plutons with which they share a wide range of texture and chemical similarities.

HELL HOLE MDW/EAGLE PEAK

HELL HOLE MDW/EAGLE PEAK
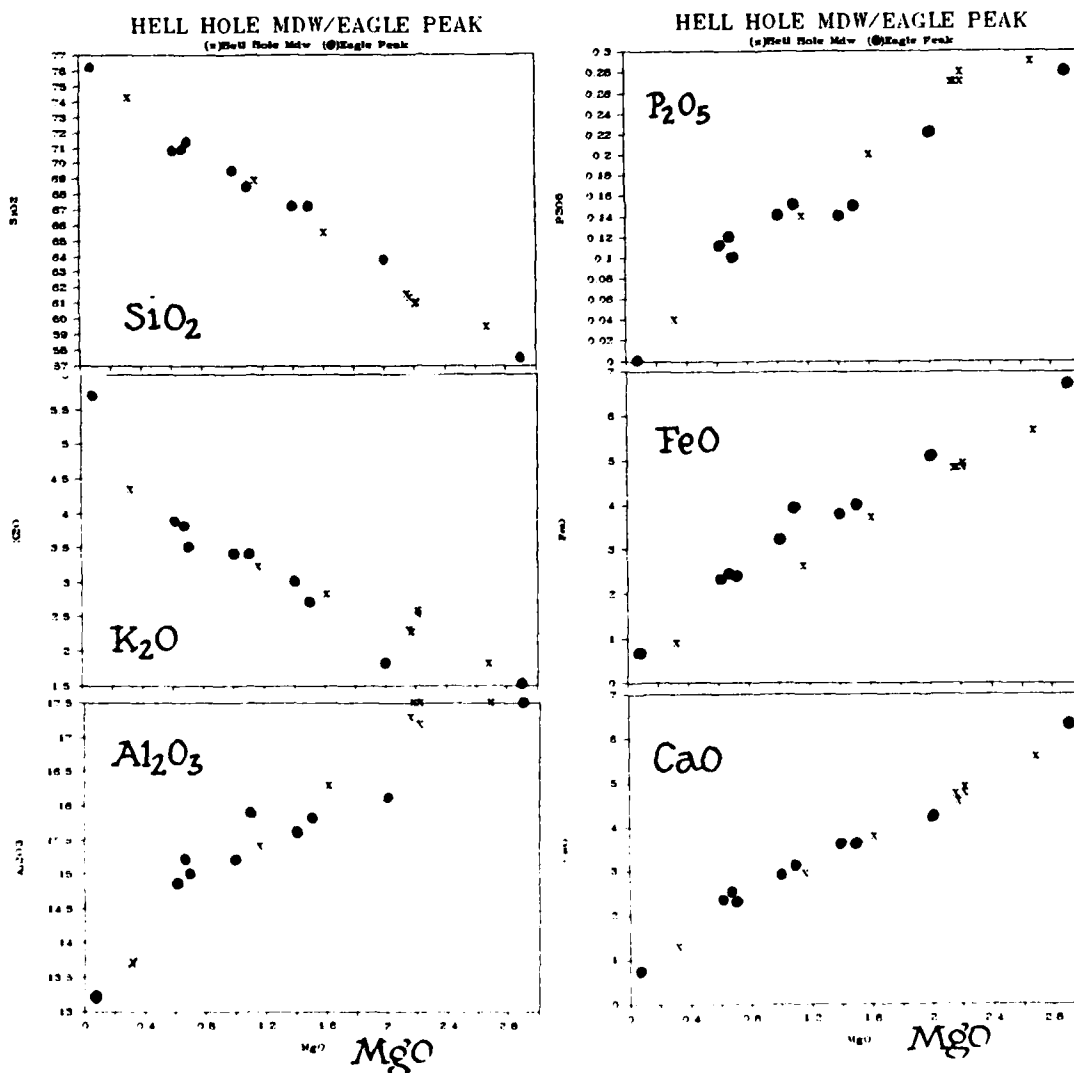
CONDITIONS IN THE MOUNT ST. HELENS MAGMATIC RESERVOIR
AND DYANMICS OF THE 18 MAY 1980 PLINIAN ERUPTION:
EXPERIMENTAL PETROLOGY AND PHYSICAL MODELING

Haraldur Sigurdsson and Steven Carey

Pre-eruption conditions in the MSH reservoir have been determined by combined studies of glass inclusions in plagioclase phenocrysts in the 18 May 1980 dacite pumice and hydrothermal melting and crystallization experiments at water-saturated and undersaturated (mixed volatiles) conditions from 0.1 MPa to 320 MPa total pressure. The glass inclusion analyses (Table 1) show a homogeneous rhyodacite liquid with major and minor oxide total of 95.4 wt. % in 57 analyses after correction for beam-induced Na-loss. The oxide difference is taken to reflect 4.6 wt.% volatile content in the inclusions and hence in the magma. Scandone and Malone (1984) independently estimated 4.6% water in the 18 May magma on basis of viscosity increase observed in the MSH plumbing system during 1980. When glass inclusion compositions and tephra matrix glass are recalculated to same total, the two are identical in composition within one standard deviation. Fractional crystallization of the inclusion liquid or the magma has therefore been insignificant after the inclusion trapping event. Petrologic evidence thus indicates a rhyodacite liquid with 4.6% water, coexisting with 40% crystals of PL-OPX-AMPH-MT-IL in the magma resevoir at 920-940°C and fO_2 = log -10. Temperature and oxygen fugacity are calculated from composition of iron-titanium oxides, formulated according to the technique of Stormer (1983).

Water-saturated melting experiments on the pumice where $P_{TOTAL} = P_{FLUID}$ do not reproduce the MSH phase assemblage or the glass and plagioclase composition at the observed temperature in the range 0.1 to 320 MPa. Under these conditions the experimental glass composition is invariably too primitive compared to the MSH liquid. Water-undersaturated experiments, on the other hand (Fig. 1), reproduce both glass and plagioclase composition and dissolved water content at the observed temperature, when $P_H O/P_{TOTAL}$ = 0.5 to 0.7. The experiments indicate that the MSH dacite evolved in a magma reservoir at 220 + 30 MPa or 7.2 + km depth. This agrees closely with the 7 to 9 km estimate of depth to the magma chamber (Fig. 2), based on seismic studies (Scandone and Malone, 1984). These results indicate that the 18 May MSH magma resided in the cupola of the reservoir. Progressively higher viscosity of magmas erupted later in 1980 indicate that the reservoir was zoned with respect to volatile content.

Dynamics of the 9-hour plinian phase of the 18 May eruption can be modeled on basis of these results and field evidence of 1.8 x 10^7 kg/s magma discharge rate. The water-undersaturated reservoir magma ascended in the conduit at approx. 1 m/s. Saturation occurred at 4560 m depth or 125 MPa and exsolution of gas continued as magma rises until 580 m (16 MPa) where the volume of gas relative to liquid is 75% and where magma fragmentation occurs. Mass eruption rate, magma viscosity and independent estimates of magma ascent velocity suggest a 94 meter diameter conduit linking the reservoir to the surface. Dispersal patterns of pyroclasts indicate a minimum exit velocity of roughly 200 m/s suring the plinian phase. An upper limit of 310 m/s is obtained from the total amount of exsolved volatiles. Model-derived vent diameters based on 0.1 MPa exit pressure, petrologically-inferred magma properties and known mass eruption rate, range from 98 to 122 meters with a flared vent configuration. The calculated vent diameter, mass eruption rate and exit velocity define conditions close to the transition between convective column rise and column

collapse based on the model of Sparks and Wilson (1976). These results are consistent with the sporadic generation of pyroclastic flows during a period characterized mainly by a sustained eruption column. Transitions from convecting to collapsing column were most likely triggered by slight variations in eruption parameters, such as mass eruption rate, as is evident from observed fluctuations in column height. In addition to the volatile content, the high crystal content (40%) of the dacitic magma was an important factor contributing to the style and dynamics of the May 18 eruption (Fig. 3).

TABLE 1. Composition of matrix glass inclusions and bulk composition of May 18, 1980 MSH pumice

	A	B	C	H
SiO	69.90 (.87)	73.00 (.72)	73.50	62.81
Al O	13.86 (.39)	14.60 (.28)	14.57	17.89
FeO*	1.93 (.31)	2.07 (.21)	2.03	3.91
MgO	0.56 (.11)	0.50 (.07)	0.59	1.70
CaO	1.92 (.20)	2.36 (.14)	2.02	5.29
Na_2O	4.77 (.29)	5.16 (.22)	5.02	4.88
K_2O	1.87 (.19)	2.18 (.11)	1.97	1.29
TiO_2	0.32 (.08)	0.36 (.04)	0.34	0.60
MnO	0.04 (.03)	0.09 (.03)	0.04	0.07
P O	0.13 (.05)	N.D.	0.13	N.D.
S	0.01 (.01)	N.D.	0.01	N.D.
Cl	0.10 (.03)	N.D.	0.10	N.D.
TOTAL	95.41	100.32	100.32	98.40
NO.	57	17		3

A. Average of 57 melt inclusions analyzed in 33 plagioclase phenocrysts from pumice SH-084.
B. Average matrix glass from SH-084 pumice.
C. Average melt inclusion (A) recalculated to SH-084 matrix glass total (B).
H. Bulk composition of SH-084.

* - Total iron as FeO.
 - One standard deviation.
1 - Sulphur, phosphorous and chlorine were determined as trace elements by microprobe analysis at 25 kv, 0.03 A beam current.

REFERENCES

Scandone, R. and S. D. Malone, 1984. Magma supply, magma discharge and readjustment of the feeding system of Mount St. Helens during 1980. J. Volcano. Geotherm. Res. (in press).

Sparks, R.S.J. and L. Wilson, 1976. A model for the formation of ignimbrite by gravitational column collapse. J. Geol. Soc. Lond. 132, 441-451.

Stormer, J. C., 1983. The effects of recalculation on estimates of temperature and oxygen fugacity from analyses of multi-component iron-tatanium oxides. Am. Mineral 68, 586-594.
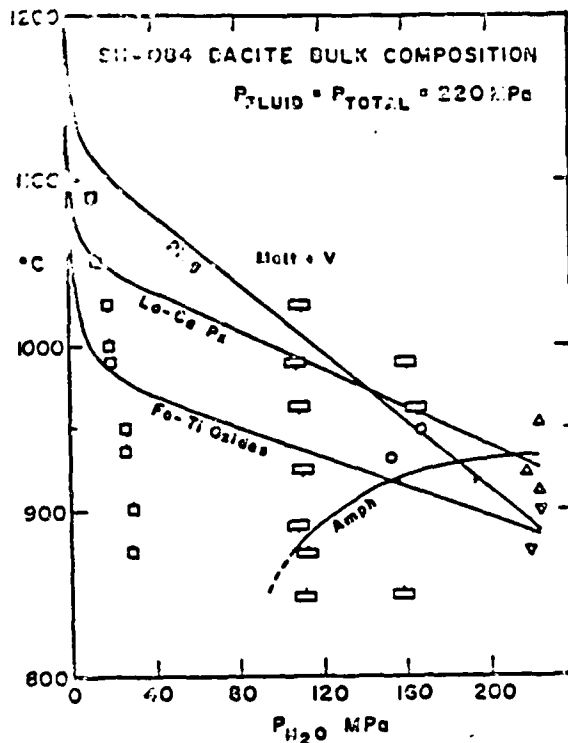
Fig. 1: Water-undersaturated melting experiments.
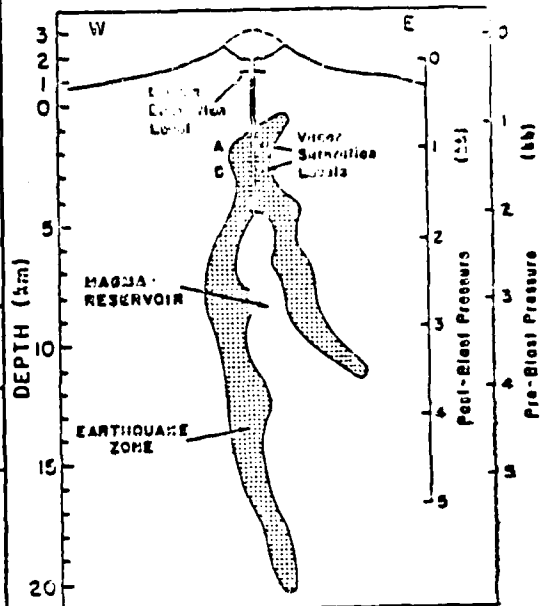
Fig. 2: MSH reservoir.
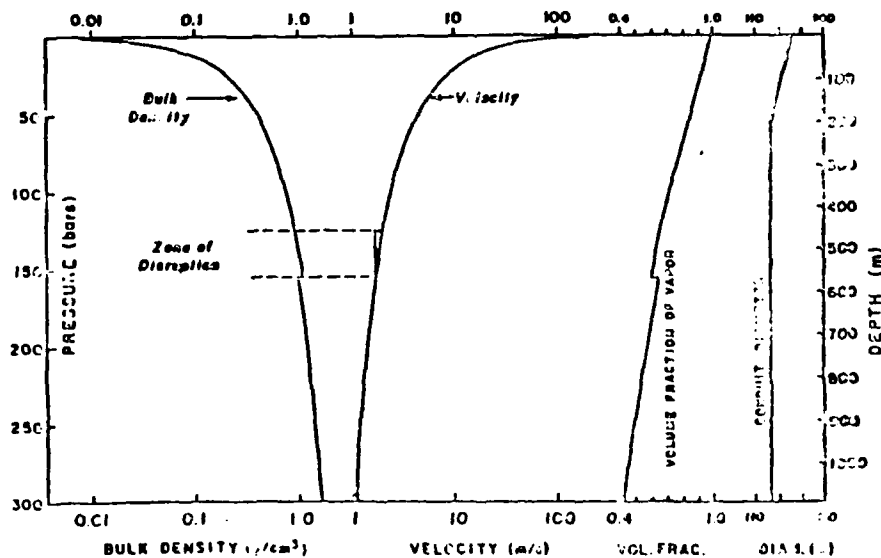
Fig. 3: Magma discharge model for plinian phase of 18 May 1930 MSH eruption.

MAGMA MIXING

R. Steven J. Sparks

There are many geological relationships in volcanic rocks and intrusive complexes, which have been interpreted as the consequence of mixing between magmas with large contrasts in viscosity and solidus temperature. A method has been developed in predicting the behavior of such mixing magmas. It is assumed that the mixing magmas come to thermal equilibrium in a time scale which is short compared to the time scale for complete mixing by stirring and chemical diffusion. The physical properties of the magmas thus only depend on the proportions of the magmas, and their liquidi and solidi. For any two magmas the hotter and more mafic magma will be in one of three physical states after mixing: a solid, a fluid with greater viscosity than the acid magma and a fluid with lower viscosity than the surrounding acid magma. A diagram of mixing ratio versus composition of the mafic magma can be divided into these three fields. When conditions are such that the mafic magma becomes a solid, true mixing cannot occur and mafic xenoliths form. Mixing can only occur when both magmas are fluid at the same temperature. These ideas provide an explanation for the selective mixing of magma types observed in the field.

LECTURES OF FELLOWS

REALISTIC DOUBLE-DIFFUSIVE CONVECTION BETWEEN POROUS MEDIA

André Gorius

Abstract: A linear analysis of a general double diffusive problem between porous slabs is carried out. General equations of thermohaline convection in porous media and a new set of boundary conditions are considered, which show significant differences with the ideal case of free-slip boundaries kept at fixed temperature and salinity.

Introduction

This summer, we heard a lot about double-diffusive convection. Huppert, e.g., presented us some nice modelizations of magma chambers, involving both thermally- and compositionally- driven convective motion in a container, the bottom of which was strewn with crystals (cf. the "Green" Experiment, Lecture 5, p. 29). Krishnamurti (no mms received) showed a first experimental investigation of double-diffusive convection in the presence of a stabilizing salt gradient, achieved by putting the experimental cell in contact with two reservoirs through a porous membrane.

The monotonic instability has been discussed by Stern (1960) for a horizontal layer of fluid where top and bottom boundaries were assumed to be stress-free and at fixed salinity and temperature. Lieber and Rintel (1963) considered the possibility of overstability for the same case, the only one admitting a complete analytic treatment. Nield (1969) investigated the influence of thermal and salinity boundary conditions for one free and one rigid boundary. The present work will be devoted to the investigation of the influence on the onset of steady convection of both thermal boundary conditions and porosity of the limiting slabs for two rigid boundaries. A linear analysis is carried out which shows that when the thermal boundary conditions are close to the so-called "fixed heat-flux" conditions, the marginal stability curve in the R_T-R_S plane is no longer a straight line, as in the ideal cases (fixed T and S), but a curve which is concave towards the origin. The analysis for porous limiting slabs shows that small porosity does not affect significantly the results of previous calculations, as long as no salt gradient is present. The presence of a destabilizing salt gradient then consists of a significant decrease of both critical Rayleigh and wave numbers, even for small porosities.

I) The Equations of the Problem.

Let us consider the following situation:
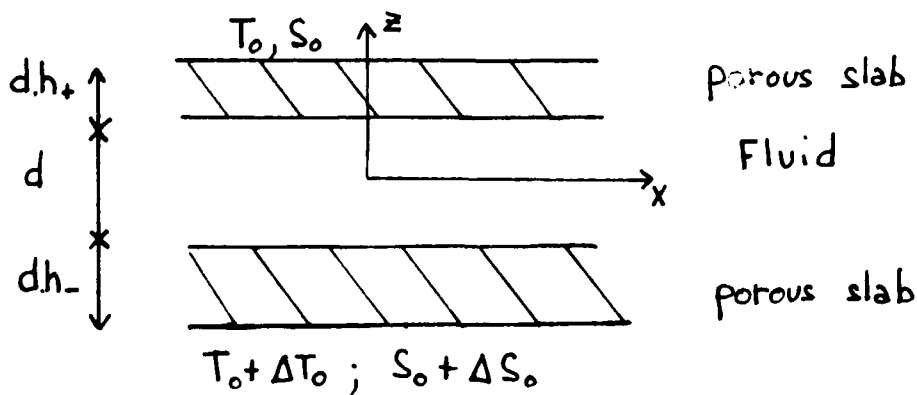
The planes $z = \pm (1/2 + h_{\pm})d$ are assumed to be held at fixed temperature and salinity. The porosity φ of the solid slabs is defined as the volume fraction of the pores present in those materials.

1) The equations

In the Oberbeck-Boussinesq approximation, the equations in the fluid $(-1/2 \leqslant z/d \leqslant + 1/2)$ are (Chandrasekhar, 1961; Yih, 1965):

$$\rho = \rho_o + \Delta\rho \quad ; \quad \Delta\rho = \rho_o \left[\beta(S-S_o) - \alpha(T-T_o) \right] \quad (1)$$

$$\vec{\nabla}.\vec{v} = 0 \quad (2)$$

$$\partial_t \vec{v} + \vec{v}.\vec{\nabla}\vec{v} = -\frac{1}{\rho_o} \vec{\nabla}p + \nu \nabla^2 \vec{v} - \frac{\Delta\rho}{\rho_o} g \vec{z} \quad (3)$$

$$\partial_t T + \vec{v}\vec{\nabla}T = \mathscr{x}_T^L \nabla^2 T \quad (4)$$

$$\partial_t S + \vec{v}\vec{\nabla}S = \mathscr{x}_S^L \nabla^2 S \quad (5)$$

The dependent variables are the velocity v = (u, v, w), density ρ, pressure p, temperature T and salinity S. $\mathscr{x}_T^L$ and $\mathscr{x}_S^L$ are, respectively, the coefficients of diffusion of heat and salt in the liquid. The equation of motion in the porous medium is obtained following Busse and Joseph (1972) by replacing in equation (3) the frictional force by a term proportional to $-\vec{V}$, where $\vec{V}$ = (U, V, W) is defined according to Darcy's law as an average over the microscale of the porous medium. Thus, the equation of motion writes:

$$\partial_t \vec{V} = -\frac{1}{\rho_o} \vec{\nabla}\pi - \frac{1}{\rho_o} \frac{1}{D} \vec{V} - \frac{\Delta\rho}{\rho_o} g \vec{z} \quad (6)$$

where $\rho = \rho_o + \Delta\rho$ is the density of the liquid filling the pores and thus is the same as in equation , π is the pressure field and D is Darcy's law coefficient, depending essentially on the dynamic viscosity μ of the liquid, the microscale δ of the medium and its porosity φ. There is no nonlinear term in $\vec{V}$ in this equation, according to Irmay (1958).

If Θ and Σ are the temperature and salinity fields respectively,

$$\Delta\rho = \rho_o \left[\beta(\Sigma - \Sigma_o) - \alpha(\Theta - \Theta_o) \right] \quad (7)$$

The derivation of the equation of heat is made via the assumption that there is no temperature difference between the solid itself and the fluid which it contains.

More precisely, the timescale of heat exchanges between the solid and the fluid in the pores is assumed to be much smaller than all other diffusion timescales.

We can then define $\ominus$ as the local temperature in the (solid + fluid) mixture. The equation of heat then becomes:

$$\partial_t \left[\varphi \rho^L C_p^L \ominus + (1-\varphi)\rho^S C_p^S \ominus \right] + \varphi \rho^L C_p^L \vec{V}.\vec{\nabla}\ominus = \overline{\hat{k}}(\varphi)\nabla^2\ominus \quad (8)$$

where the subscripts L and S represent, respectively, the fluid and the solid. $\hat{k}(\varphi)$ is defined to be the effective heat conductivity of the (solid + fluid) mixture.

Defining $\qquad \overline{\rho C_p} = \varphi \rho^L C_p^L + (1-\varphi)\rho^S C_p^S \; , \; n = \dfrac{\rho^L C_p^L}{\overline{\rho C_p}}$

and $\qquad \overline{\mathcal{X}}_T(\varphi) = \dfrac{\overline{\hat{k}}(\varphi)}{\overline{\rho C_p}} \qquad$ (effective heat diffusivity)

This equation takes the form

$$\partial_t \ominus + n\varphi \vec{V}\vec{\nabla}\ominus = \overline{\mathcal{X}}_T \nabla^2 \ominus \qquad (9)$$

The equation for the salinity Σ is derived in a similar way and leads to

$$\partial_t \Sigma + \varphi \vec{V}.\vec{\nabla}\Sigma = \overline{\mathcal{X}}_S \nabla^2 \Sigma \qquad (10)$$

where $\overline{\mathcal{X}}_S(\varphi)$ is the effective salt diffusivity of the (fluid + solid) mixture. Adding the continuity equation to the previous ones, we can write down the set of equations in the solids:

$$\rho = \rho_0 + \Delta\rho \quad ; \quad \Delta\rho = \rho_0 \left[\beta(\Sigma - \Sigma_0) - \alpha(\ominus - \ominus_0) \right] (11)$$

$$\vec{\nabla}\vec{V} = 0 \qquad (12)$$

$$\partial_t \vec{V} = -\frac{1}{\rho_0}\vec{\nabla}\pi - \frac{1}{\rho_0}\frac{1}{D}\vec{V} - \frac{\Delta\rho}{\rho_0}g\vec{z} \qquad (13)$$

$$\partial_t \ominus + n\varphi\vec{V}\vec{\nabla}\ominus = \overline{\mathcal{X}}_T \nabla^2\ominus \qquad (14)$$

$$\partial_t \Sigma + \varphi\vec{V}\vec{\nabla}\Sigma = \overline{\mathcal{X}}_S \nabla^2\Sigma \qquad (15)$$

2) The boundary conditions

Mechanical: We assume continuity of both vertical stress and vertical velocity at the solid-fluid interface, considered as a rigid boundary. Thus, for $z = \pm d/2$,

$$\omega = \varphi W \qquad (16)$$

$$u = \vartheta = 0 \qquad (17)$$

$$\rho_0 \nu \partial_z \omega + p = \pi \qquad (18)$$

Using the continuity equation (2), the relations (17) involve $\partial_z \omega = 0$, so that these conditions become, for $z = \pm d/2$

$$\omega = \varphi W$$

$$\partial_z \omega = 0$$

$$P = \Pi$$

In the planes $z = \pm (1/2 + h_+)d$, we shall assume impenetrability conditions, so that we have

at $z = \pm(1/2 + h_\pm)d$, $W = 0$

Thermal: We assume continuity of temperature fields and fluxes at the fluid-solid interface: at $z = \pm d/2$,

$$\Theta = T$$

$$\bar{k} \, \partial_z \Theta - \varphi \rho^L c_P^L \, W\Theta = k_L \, \partial_z T - \rho^L c_P^L \, \omega T$$

the condition (16) then allows us to rewrite the last equation as

$$\bar{k} \partial_z \Theta = k_L \partial_z T$$

At $z = \pm (1/2 + h_\pm)d$, we assume fixed temperatures, so that

at $z = +(1/2 + h_+)d$, $\Theta^+ = T_0$

at $z = -(1/2 + h_-)d$, $\Theta^- = T_0 + \Delta T_0$

Salinity: Similar conditions hold for S and Σ

at $z = \pm d/2$, $\Sigma = S$

and $$\bar{æ}_s \partial_z \Sigma - \varphi W \Sigma = æ_s^L \partial_z S - \omega S$$

so that $$\bar{æ}_s \partial_z \Sigma = æ_s^L \partial_z S$$

at $z = +(1/2 + h_+)d$, $\Sigma^+ = S_0$

at $z = -(1/2 + h_-)d$, $\Sigma^- = S_0 + \Delta S_0$

3) The steady state solution

The equations (1 - 15) together with the boundary conditions admit the steady state solution

$$\vec{\mathcal{J}} = \vec{V} = 0$$

$$T = T_0(z) = -\frac{\Delta T_L}{d} z + T_0 + \frac{1}{2} \Delta T_0 \frac{1 + 2 h_+ \chi_T}{1 + (h_+ + h_-) \chi_T} \qquad \text{in the fluid}$$

$$\Theta^+ = \Theta_0^+(z) = -\chi_T \frac{\Delta T_L}{d} z_+ + T_0 \qquad \text{in the upper solid}$$

$$\Theta^- = \Theta_0^-(z) = -\chi_T \frac{\Delta T_L}{d} z_- + T_0 + \Delta T_0 \qquad \text{in the lower solid}$$

where $Z_\pm = Z \mp \left(\frac{1}{2} + h_\pm\right) d$

$$\chi_T = k_L / \bar{k}(\varphi)$$

and ΔT_L is the effective temperature difference seen by the fluid

$$\Delta T_L = \frac{\Delta T_0}{1 + (h_+ + h_-) \chi_T}$$

The equations for salinity are formally the same, with $\chi_S = \mathscr{x}_S^L / \bar{\mathscr{x}}_S(\varphi)$
and $\Delta S_L = \dfrac{\Delta S_0}{1 + (h_+ + h_-)\chi_S}$ replacing respectively χ_T and ΔT_L.

4) The nondimensional equations

Let us scale the lengths with d, the pressure with $\rho_0 \nu \, \mathscr{x}_T^L / d^2$ and the velocities with $\mathscr{x}_T^L / d$. The temperature and salinity scales will be taken respectively as ΔT_L and ΔS_L. T, S, Θ, Σ will denote now the deviations from the linear profiles T_0, S_0, Θ_0, Σ_0 respectively, and all the terms which can be written as gradients will be included in the pressure terms $\vec{\nabla} P$ and $\vec{\nabla}\pi_\pm$.

The equations thus become

$$\vec{\nabla}\cdot\vec{\vartheta} = 0 \tag{19}$$

$$\frac{1}{\sigma}\left[\partial_t \vec{\vartheta} + \vec{\vartheta}\,\vec{\nabla}\vec{\vartheta}\right] = -\vec{\nabla}P + \nabla^2\vec{\vartheta} + (R_T T - R_S S)\vec{z} \tag{20}$$

$$\partial_t T + \vec{\vartheta}\,\vec{\nabla}T = \omega + \nabla^2 T \tag{21}$$

$$\partial_t S + \vec{\vartheta}\,\vec{\nabla}S = \omega + \zeta\nabla^2 S \tag{22}$$

$$\tag{23}$$

$$\vec{\nabla}\cdot\vec{V} = 0$$

$$\frac{1}{\sigma}\partial_t \vec{V} = -\vec{\nabla}\pi - \frac{\vec{V}}{K} + (R_T\Theta - R_S\Sigma)\vec{z} \tag{24}$$

$$\partial_t\Theta + n\varphi\vec{V}\vec{\nabla}\Theta = n\varphi\chi_T W + n/\chi_T\,\nabla^2\Theta \tag{25}$$

$$\partial_t\Sigma + \varphi\vec{V}\vec{\nabla}\Sigma = \varphi\chi_S W + \zeta/\chi_S\,\nabla^2\Sigma \tag{26}$$

In those equations $R_T = \dfrac{g\alpha\,d^3\,\Delta T_L}{\nu\,\mathscr{x}_T^L}$ and $R_S = \dfrac{g\beta\,d^3\,\Delta S_L}{\nu\,\mathscr{x}_T^L}$ are thermal and compositional Rayleigh numbers respectively. They represent the constraints applied to the system.

$\sigma = \nu/\mathscr{x}_T^L$ and $\zeta = \mathscr{x}_T^L/\mathscr{x}_S^L$ are the Prandtl and Lewis numbers and are intrinsic properties of the considered fluid. $K = \dfrac{\rho_0\nu}{d^2}\,D$ is the nondimensional Darcy coefficient.

In the new definitions of the pressures P and Π appear three integration constants, which can be chosen so that the continuity of the pressure field leads to the same equation as before:

$$\text{at } z = \pm 1/2 \qquad P = \Pi$$

so that the boundary conditions become, in dimensionless form

at $z = \pm(1/2 + h_\pm)$

$$W = \Theta = \Sigma = 0$$

at $z = \pm 1/2$

$$\omega = \varphi W ; \quad \partial_z \omega = 0 ; \quad P = \Pi_\pm$$

$$\Theta = T ; \quad \partial_z \Theta = \chi_T \partial_z T$$

$$\Sigma = S ; \quad \partial_z \Sigma = \chi_S \partial_z S$$

II) The Perturbation Analysis

Let $\vec{v} = (u, v, w)$, $\vec{V} = (U, V, W)$, T, S, Θ, Σ be infinitesimal perturbations of the steady state solution. Since we are interested in stationary convection, all these variables will be functions of space only.

We now make a normal mode analysis and write all these quantities $X(x, y, z)$ as $X = X(z) \exp i(q_x x + q_y y)$. $q = (q_x^2 + q_y^2)^{1/2}$ is the horizontal wavelength of the disturbances. Using Chandrasekhar's notation $D = d/dz$, the system $(19-26)$ becomes, at leading order in the perturbations and after elimination of horizontal velocities via the continuity equations:

$$(D^2 - q^2) D\omega = q^2 P \tag{I}$$

$$(D^2 - q^2) \omega + (R_T T - R_S S) = Dp \tag{II}$$

$$(D^2 - q^2) T + \omega = 0 \tag{III}$$

$$(D^2 - q^2) S + \frac{\omega}{6} = 0 \tag{IV}$$

$$DW = -K q^2 \Pi \tag{V}$$

$$W = -K D\Pi + K(R_T \Theta - R_S \Sigma) \tag{VI}$$

$$(D^2 - q^2) \Theta + \varphi \chi_T^2 W = 0 \tag{VII}$$

$$(D^2 - q^2) \Sigma + \varphi \chi_S^2 \frac{W}{6} = 0 \tag{VIII}$$

We are now going to solve these equations in both cases $\varphi \neq 0$ and $\varphi = 0$. This resolution will introduce several integration constants $\{C_n\}$. Replacing the solution into the boundary conditions equations will lead to a homogeneous system of linear equations in $\{C_n\}$ which determinant is denoted by Δ. The critical surfaces in the (R_S, R_T, q) space will then be defined by the condition of existence of a nonvanishing solution: $\Delta = 0$.

1) The case $\varphi = 0$

The equations in the liquid are (I – IV) and in the solid, the heat equation is

$$(D^2 - q^2)\,\Theta = 0$$

which solution is

$$\Theta^{\pm} = \Theta_o^c\, chq\bar{z} + \Theta_o^s\, shq\bar{z}$$

In order to reduce the number of integration constants, we use the variable $z\pm$ (introduced in para. I.3) in each solid. Then, the condition $\Theta^{\pm} = 0$ at $z_{\pm} = 0$ involves $\Theta = \Theta_o^{\pm}\, shqz\pm$ where $\Theta_o^{\pm}$ are the unknown integration constants. Elimination of p in equation (I) and (II) involves

$$(D^2 - q^2)\,\omega = q^2\,(R_T T - R_s S) \qquad (\overline{IV})$$

Taking the Laplacian of both members of this equation and eliminating T and S via equations (III) and (IV) leads to an equation in w alone:

$$(D^2 - q^2)^3\,\omega = -q^2\,(R_T - \tfrac{1}{6} R_s)\,\omega \qquad (\underline{\chi})$$

which solution is

$$\omega = \sum_{i=1}^{2} \omega_i^c\, chq_i z + \omega_i^s\, shq_i z$$

and (q_i) i = 1, 2, 3, are the solutions of

$$(q_i^2 - q^2)^3 = -q^2(R_T - R_S/\zeta).$$

The equation for T is

$$(D^2 - q^2)\,T = -\omega$$

which general solution is

$$T = T_o^c\, chqz + T_o^s\, shqz - \sum_{i=1}^{3} \frac{\omega_i^c}{q_i^2 - q^2}\, chq_i z + \frac{\omega_i^s}{q_i^2 - q^2}\, shq_i z$$

In the same manner, S writes

$$S = S_o^s\, shqz + S_o^c\, chqz - 1/\zeta \sum_{i=1}^{3} \frac{\omega_i^c}{q_i^2 - q^2}\, chq_i z + \frac{\omega_i^s}{q_i^2 - q^2}\, shq_i z$$

T and S must satisfy equation ($\overline{X}$) for all z, and so

$$R_S S_0^C = R_T T_0^C$$

$$R_S S_0^S = R_T T_0^S$$

We are left with ten unknown coefficients (w_1^c, w_1^s, Θ_o^t, T_o^c, T_o^s) and the boundary conditions at $z = \pm 1/2$ provide ten equations

$$\omega\vartheta = \partial_z \omega\vartheta = 0$$

$$S = 0$$

$$T = \Theta; \quad \partial_z \Theta = \chi_T \partial_z T$$

So, we have to solve a 10 x 10 determinant to get the critical relation $F_0(R_S, R_T, q) = 0$. In fact, if we choose $h_+ = h_- = h$, the effective boundary conditions seen by the fluid are symmetrical with respect to the plane $z = 0$, and we can seek for even solutions with respect to z. In this case, $w_i^s = 0$ for $i = 1, 2, 3$ and the boundary conditions can be written for $z = \pm 1/2$ only. The resulting determinant is:

$$\begin{vmatrix} 1 & 1 & 1 & 0 & 0 \\ q_1 t_1 & q_2 t_2 & q_2^* t_2^* & 0 & 0 \\ \dfrac{1}{q_1^2 - q^2} & \dfrac{1}{q_2^2 - q^2} & \dfrac{1}{q_2^{*2} - q^2} & R_T & 0 \\ \dfrac{1}{q_1^2 - q^2} & \dfrac{1}{q_2^2 - q^2} & \dfrac{1}{q_2^{*2} - q^2} & R_S/\zeta & -\chi_T T_H \\ \dfrac{q_1 t_1}{q_1^2 - q^2} & \dfrac{q_2 t_2}{q_2^2 - q^2} & \dfrac{q_2^* t_2^*}{q_2^{*2} - q^2} & q\, t_0 \dfrac{R_S}{\zeta} & q \end{vmatrix}$$

where we have used the fact that $q_2^* = q_3$ and defined $t_i = th\, q_i/2$,

$t_0 = th\, q/2$ and $T_H = th\, qh$

Depending on R_T and R_S, q_1 is either real or imaginary but the determinant is always real, providing one single relation

$$F_0(R_S, R_T, q) = 0$$

2) The case $\varphi \neq 0$

The solution in the liquid is the same as before, and the same formal calculation in the solid leads to the solution:

$$W = \sum_{i=1}^{2} W_i \, \text{sh} \, m_i z_{\pm}$$

$$\Theta = \Theta_0 \, \text{sh} \, q z_{\pm} - \chi_T^2 \varphi \sum_{i=1}^{2} \frac{W_i}{m_i^2 - q^2} \, \text{sh} \, m_i z_{\pm}$$

$$\Sigma = \frac{R_T}{R_S} \Theta_0 \, \text{sh} \, q z_{\pm} - \chi_S^2 \frac{\varphi}{\zeta} \sum_{i=1}^{2} \frac{W_i}{m_i^2 - q^2} \, \text{sh} \, m_i z_{\pm}$$

where m_1 and m_2 are solutions of

$$(m^2 - q^2)^2 = - K q^2 \varphi \left[R_S \frac{\chi_S^2}{\zeta} - R_T \chi_T^2 \right]$$

The pressures p and $\pi_{\pm}$ are given by

$$p = (1/q^2) \, D(D^2 - q^2) w$$

$$\pi_{\pm} = - \frac{1}{q^2} \frac{D W_{\pm}}{K}$$

The boundary conditions then lead to a 14 x 14 determinant in the general case ($h_+ \neq h_-$), which can be reduced to 7 x 7 for $h_+ = h_-$.

$$
\begin{vmatrix}
1 & 1 & 1 & 0 & \text{th} m_1 h & \text{th} m_2 h & 0 \\[2mm]
q_1 t_1 & q_2 t_2 & q_2^* t_2^* & 0 & 0 & 0 & 0 \\[2mm]
\dfrac{1}{q_1^2 - q^2} & \dfrac{1}{q_2^2 - q^2} & \dfrac{1}{q_2^{*2} - q^2} & R_{S/\zeta} & \dfrac{\chi_T^2 \, \text{th} m_1 h}{m_1^2 - q^2} & \dfrac{\chi_T^2 \, \text{th} m_2 h}{m_2^2 - q^2} & -\chi_T \chi_S T_H \dfrac{R_S}{\zeta} \\[3mm]
\dfrac{t_1 q_1}{q_1^2 - q^2} & \dfrac{t_2 q_2}{q_2^2 - q^2} & \dfrac{t_2^* q_2^*}{q_2^{*2} - q^2} & q t_0 \dfrac{R_S}{\zeta} & \dfrac{\chi_T m_1}{q^2 - m_1^2} & \dfrac{\chi_T m_2}{q^2 - m_2^2} & q \chi_S \dfrac{R_S}{\zeta} \\[3mm]
\dfrac{1}{q_1^2 - q^2} & \dfrac{1}{q_2^2 - q^2} & \dfrac{1}{q_2^{*2} - q^2} & R_T & \dfrac{\chi_S^2 \, \text{th} m_1 h}{m_1^2 - q^2} & \dfrac{\chi_S^2 \, \text{th} m_2 h}{m_2^2 - q^2} & -\chi_T \chi_S T_H R_T \\[3mm]
\dfrac{q_1 t_1}{q_1^2 - q^2} & \dfrac{q_2 t_2}{q_2^2 - q^2} & \dfrac{q_2^* t_2^*}{q_2^{*2} - q^2} & q t_0 R_T & \dfrac{\chi_S m_1}{q^2 - m_1^2} & \dfrac{\chi_S m_2}{q^2 - m_2^2} & q \chi_T R_T \\[3mm]
q_1 t_1 (q_1^2 - q^2) & q_2 t_2 (q_2^2 - q^2) & q_2^* t_2^* (q_2^{*2} - q^2) & 0 & \dfrac{m_1}{K \varphi} & \dfrac{m_2}{K \varphi} & 0
\end{vmatrix}
$$

Both cases $\varphi = 0$ and $\varphi \neq 0$ have been solved numerically using an IMSL routine computing a complex determinant and the equations $F = 0$ have been solved by Muller's method (Muller, 1956).

III) The Results

1) Influence of the thermal conductivity ratio λ_T in the case $\varphi = 0$.

For $\lambda_T = \infty$ and $R_S = 0$, the critical curve in the plane (R_T, q) has its minimum at $R_T^c = 720$ and $q_c = 0$ (Hurle, Jakeman and Pike, 1967).

Figure 1 shows the shape of the critical curves in the (R_T, q) plane for $\lambda_T = \infty$ and for different values of R_S.
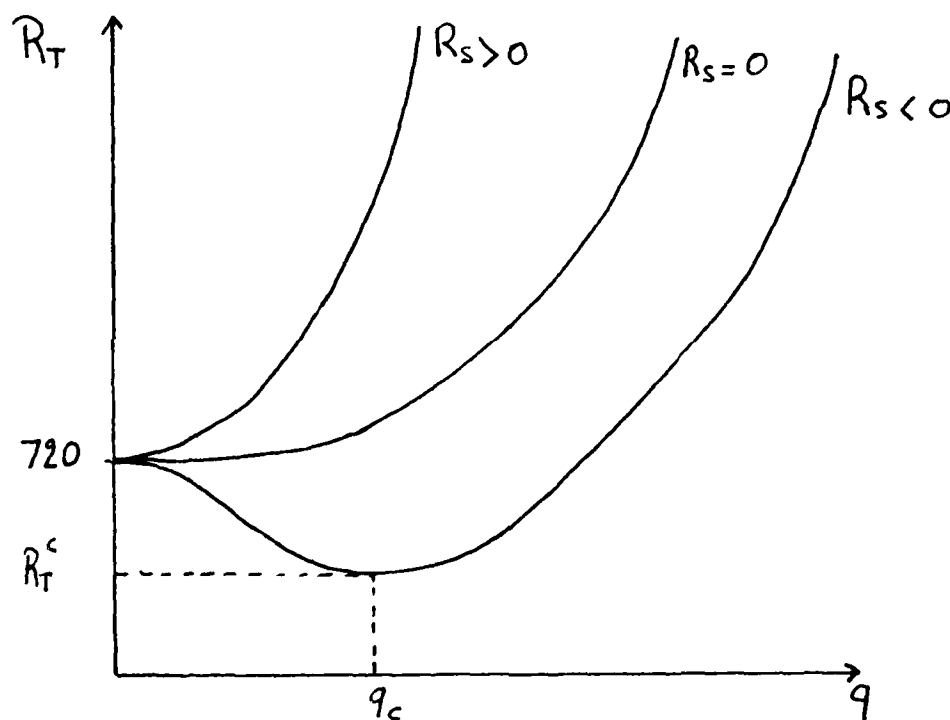
Figure 1

We are mainly interested in the case $R_S < 0$ (destabilizing salt gradient) since for $R_S > 0$ overstability may occur. The most important result is that a destabilizing salt gradient favors a structure with finite wavelength ($q_c \neq 0$) whereas an infinite wavelength is preferred for $R_S > 0$ (as far as no finite amplitude perturbations are concerned).

It is known, since the earliest results for free boundaries (Stern, 1960), that the critical Rayleigh number for the onset of stationary convection is a decreasing function of R_S, but in both rigid-rigid and free-free cases, the critical curve $R_T = f(R_S)$ is a straight line when temperature and salinity are kept fixed on the boundaries. In figure 2, we have plotted the corresponding curves for different values of λ_T which show that this no longer holds for values of $\lambda_T \neq 0$.
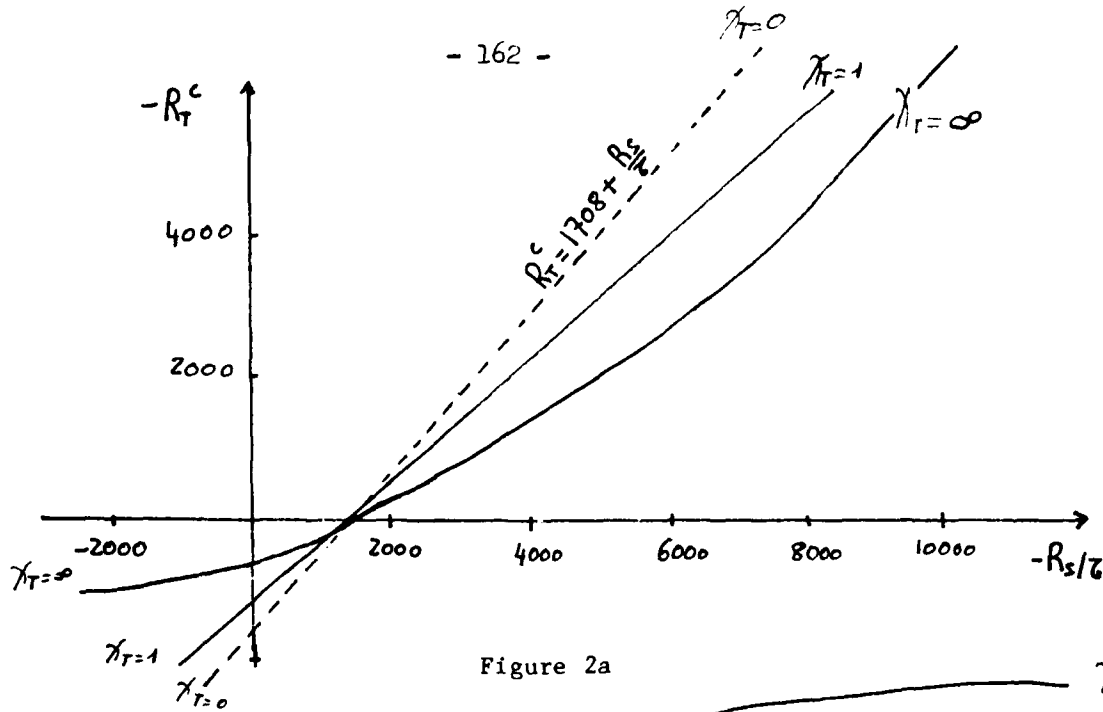
Figure 2a
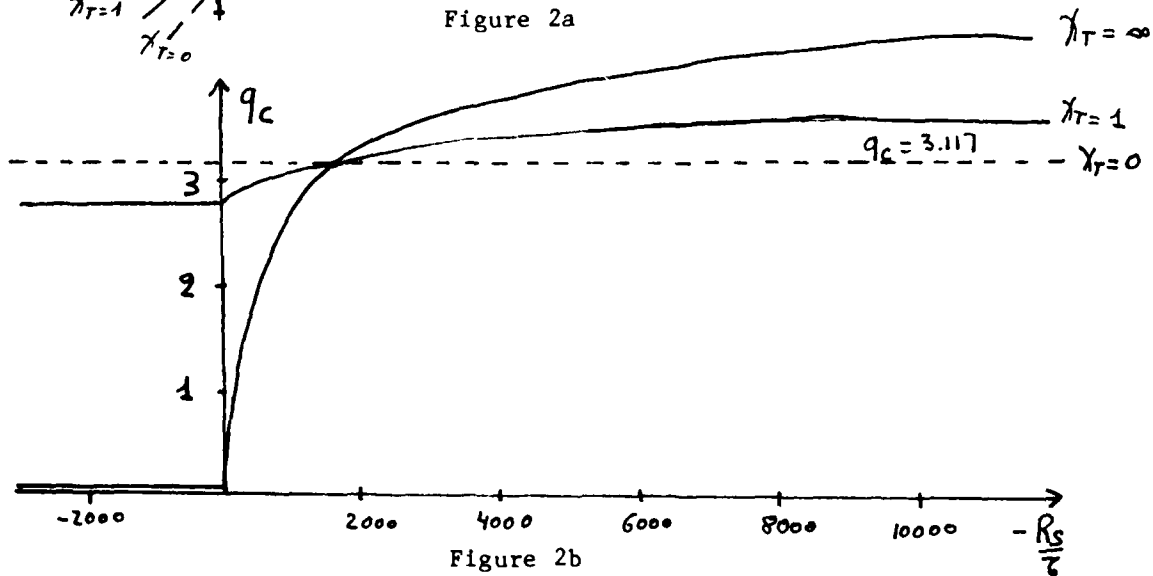
Figure 2b

All the curves cross at the points where $R_T^c = 0$, $q_c = 3.117$, and $R_S/\zeta = -1708$: when no temperature gradient is present, salt plays the role of the temperature gradient in ordinary convection, but the relevant critical parameter is $-R_S/\zeta$ for our definition of R_S, and so takes the usual value 1708. The critical wave number is then $q_c = 3.117$ (Hurle, Jakeman and Pike, 1967).

As expected (Nield, 1967), when $\chi_T = 0$, the critical wave number q_c becomes independent from R_S and takes the value $q_c = 3.117$, and the critical curve in the (R_S, R_T) plane is the straight line $R_T^c = R_S/\zeta + 1708$.

As it has already been shown (Piquemal, 1979) for ordinary convection, the height h of the solid slabs does not have a crucial importance (as long as $h \neq 0$). In fact, for $h = 2$ or $h = \infty$ and $\chi_T \geqslant 10$ no diffe   e can be seen in the critical curves.

2) Influence of the porosity

In order to investigate the case $\varphi \neq 0$, we had to make a choice concerning χ_T, χ_S and K. It seems reasonable to choose $\chi_T = O(1)$ since we are interested in porous media which are bad heat conductors compared to the liquid they contain, and so the isotherms are focused in the fluid. For this reason, we took $\chi_T = 1$. $\overline{\mathscr{X}}_S$ must be an increasing function of φ and we choose the two limits:

$$\overline{\mathscr{X}}_s(o) = 0$$

$$\overline{\mathscr{X}}_s(1) \leqslant \mathscr{X}_s^L$$

Since we only need a reasonable order of magnitude, we choose $\overline{\mathscr{X}}_s(\varphi) = \frac{\varphi}{10} \mathscr{X}_s^L$ so that

$$\chi_S = \frac{10}{\varphi}$$

Darcy's low coefficient was taken to be that of a package of spheres of diameter δ, given by:

$$D = \frac{\delta^2}{\rho_o \nu} \frac{\varphi^{5.5}}{5.6}$$

So, for d = 1 cm and δ = 0.3 cm, we get K = 10^{-3} $\varphi^{5.5}$. This gives us the qualitative behavior of figure 3 for the critical values R_T^c and q_c as a function of φ for different heights h of the solid media.

As can be seen on these figures, no significant effect on R_T^c is predicted as long as $\varphi \leqslant 0.5$. As φ increases, the critical Rayleigh number decreases by less than 20%. This decreasing can be understood as follows: as φ increases from 0 to 1 the characteristic length of the velocity variations is no longer d, but some d' > d. Longer lengthscales being involved, dissipation is reduced and the critical effective temperature difference ΔT_L is a decreasing function of φ. The increasing of the characteristic lengthscale with φ and h is well reflected by the curve $q_c = f(\varphi)$.
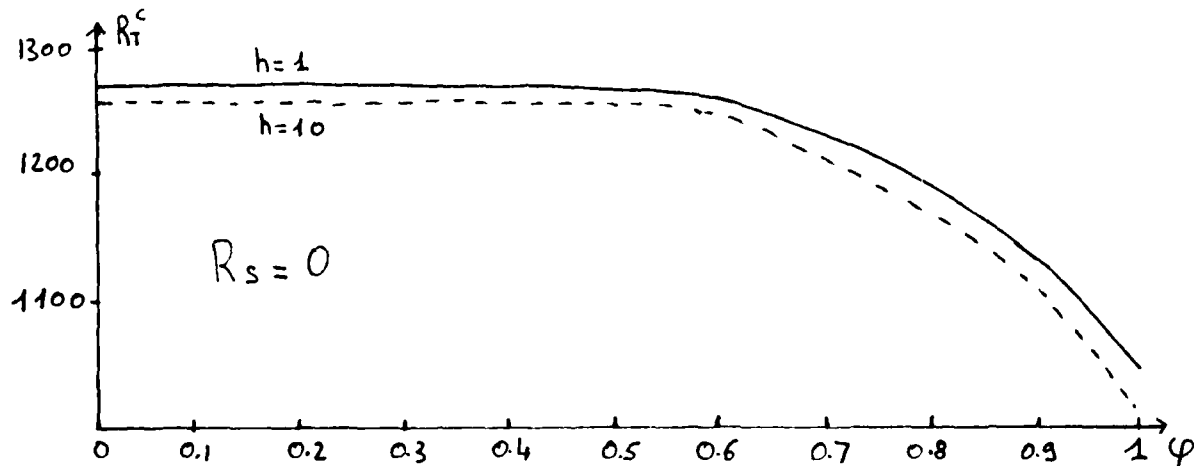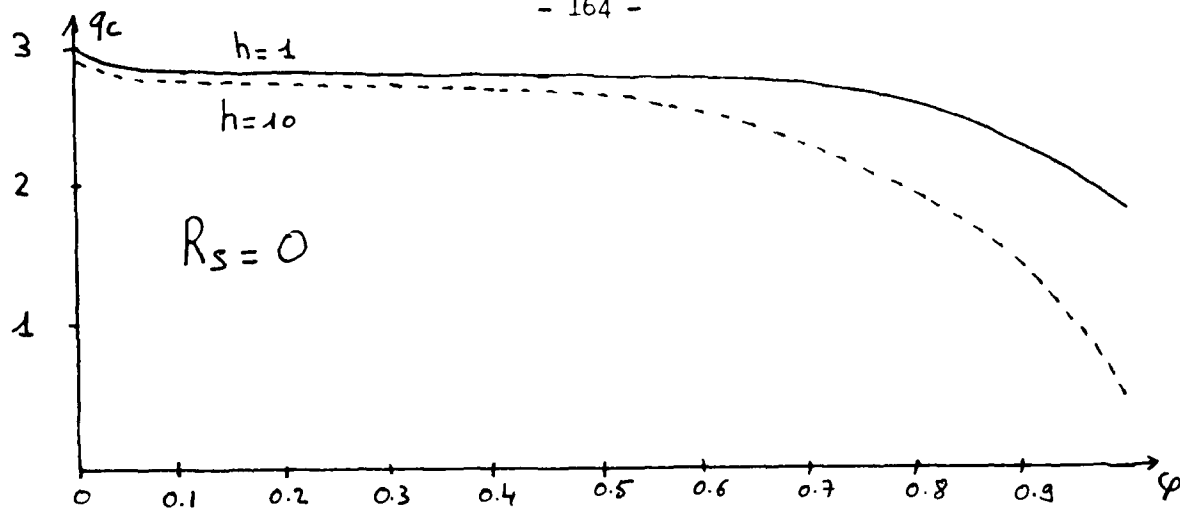

Figure 3a

Figure 3b

When, now, a stabilizing salt gradient is present, the dependence of R_T^c and q_c on φ becomes more important, even for small porosities, as shown in figure 4:
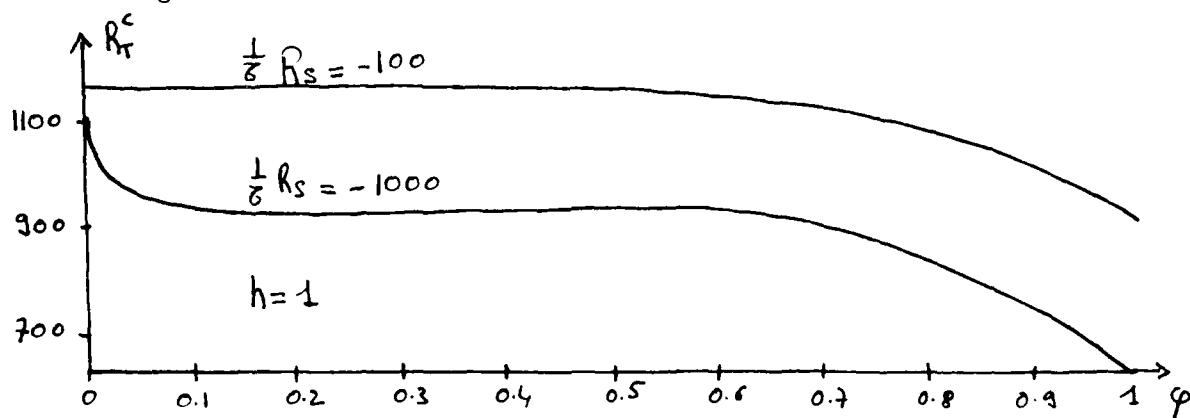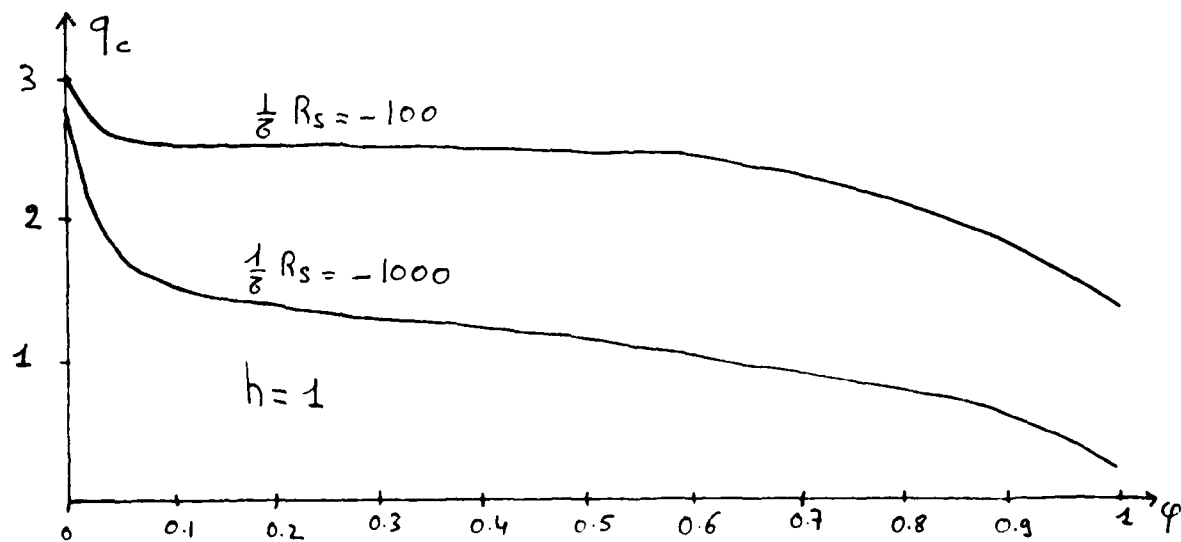

Figure 4a

Figure 4b

As one can see, the critical Rayleigh and wave numbers are significantly affected when the materials are porous so that this effect has to be taken into account in the interpretation of experimental results.

As a conclusion, let us say that both thermal and mechanical boundary conditions play a significant role for the onset of stationary convection driven by thermal and compositional effects. The effect of porosity has been analyzed with model-laws for χ_T, χ_S and Darcy's law coefficient, and so provide merely a qualitative picture of what could happen in real situations.

This work has to be extended to the case of oscillatory instability (for $R_s > 0$), and the above results let us expect at least qualitatively different behaviors from the ideal cases. Of course, an investigation of finite-amplitude effects has to be done since it is known (Veronis, 1965) that the ideal system is unstable to such disturbances for $R_s > 0$.

ACKNOWLEDGEMENTS

REFERENCES

Busse, F.H. and D.D. Joseph, 1972. Journ. of Fluid Mech. 54-3, 521-543.

Chandrasekhar, S., 1961. Hydrodynamic and Hydromagnetic Stability, Oxford: Clarendon Press.

Hurle, D.T.J., E. Jakeman and E.R. Pike, 1967. Proc. Roy. Soc. Lond. A296, 469-475.

Lieber, P. and L. Rintel, 1963. Rept. MD-6, Instt. Engrg. Res., Univ. of Calif., Berkeley.

Muller, D.E., 1956. Math. Tables and Aids to Computation 10, 208-215.

Nield, D.A., 1967. Journ. of Fluid Mech. 29-3, 545-558.

Piquemal, J.M., 1979. These de 3° Cycle, Univ. de Paris VI.

Stern, M.E., 1960. Tellus 12, 172-175.

Veronis, G., 1965. J. Mar. Res. 23, 1-17.

Yih, C.S., 1965. Dynamics of Nonhomogeneous Fluids, New York: MacMillan.

MIXING OF FLUIDS OF DIFFERENT VISCOSITIES:
SALT WATER FINGERS IN GLYCERINE

Bruce J. Bayly

ABSTRACT

A fingering instability has been observed to occur at the interface between a layer of salt water and an underlying layer of glycerine. The instability is investigated by calculating the one-dimensional interdiffusion of the salt water and glycerine, and then considering the local instability of the instantaneous concentration profiles. The diffusion theory is strongly nonlinear, and the requirement of material volume conservation implies the existence of a nonzero velocity field associated with the diffusion processes whose advection of the concentration fields is an important physical effect.

I. INTRODUCTION

IA. The Experiment

Consider a tank containing two deep layers of fluid, one below the other. The lower layer is mostly glycerine, with a small amount of dissolved water, while the upper is water containing a certain amount of dissolved salt ($NaNO_3$ was used in these experiments). The upper layer is less dense than the lower, so that the system is statically stable. With time, however, the fluid in the neighborhood of the interface develops an instability: "fingers" of salt water penetrate down into the glycerine body, while glycerine filaments stream upward and mix efficiently with the overlying salt water.
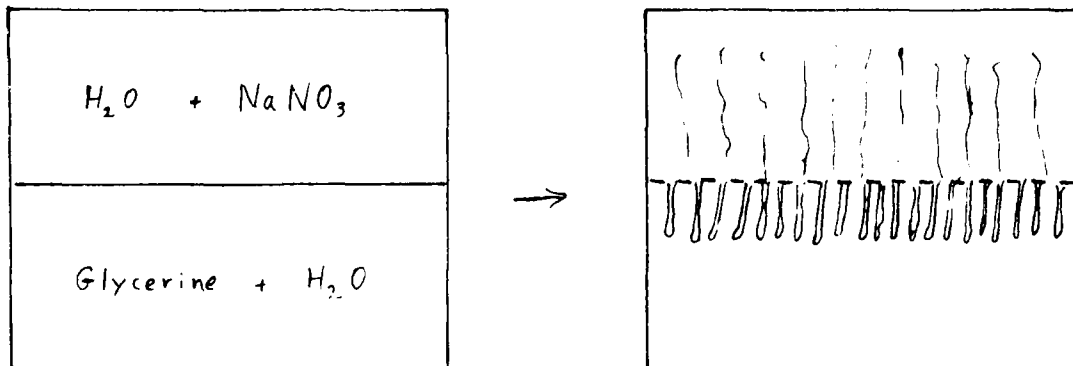
IB. Previous related work

The design of the experiment and the phenomenon observed are strongly reminiscent of investigations of salt fingering in aqueous solutions. The study of Huppert and Manins (1973), on necessary conditions for salt fingering at an interface, is particularly relevant. Huppert and Manins argue that if there is initially a sharp interface between a body of cold fresh water lying under a body of hot salty water, the heat and salt fields will diffuse across the interface. The initial temperature and salinity steps are replaced by smooth gradients, which spread out self-similarly in time (both density fields are functions of the similarity variable $\eta = zt^{-1/2}$). If after some time the instantaneous density profiles satisfy the conditions for the salt-finger instability, it is expected that the instability will indeed occur and proceed on a timescale much more rapid than the diffusion. For such self-similar expanding profiles, the profiles are unstable if

$$\frac{d\rho_s / d\eta}{-d\rho_T / d\eta} > \tau \tag{IB 1}$$

$$\tau = \kappa_s / \kappa_T \qquad \text{=inverse Lewis number}$$

which implies that the initial density contrasts must satisfy

$$\Delta\rho_s / -\Delta\rho_T > \tau^{3/2} \tag{IB 2}$$

This criterion is in excellent agreement with experiments (Huppert and Manins, 1973 and Huppert and Hallworth 1984).

IC. Current Strategy

The success of the Huppert and Manins stability theory for salt fingers suggests that we try a similar approach here. Following Huppert and Manins, we shall consider the problem of the diffusive spreading of the interface separately from the instability of an instantaneous diffusion profile. The instability theory for a density profile is fairly well understood, at least in a local theory assuming approximately linear gradients, although it is not clear a priori whether the first instability to occur will be double-diffusive or Rayleigh-Taylor (i.e. due to a local density inversion) in character. The diffusion of the interface itself is a fairly difficult problem, because the components diffuse at rates that depend very strongly on the local concentrations. Furthermore, it turns out that the strong diffusive fluxes of the components generate a nontrivial velocity field, so that advection of the concentration fields cannot be neglected. Elucidating the nature of this velocity field and its effect on the transport processes is considered to be the major contribution of this investigation, with the stability theory of the diffusing interface viewed as an interesting application.

II. BASIC THEORY

IIA. Diffusion of Small Particles in a Fluid

This section is a review of the derivation of the extended Einstein formula for the diffusion of a species α of small particles suspended in a fluid.

$$\frac{\partial c_\alpha}{\partial t} = \nabla \cdot \left(- \underline{u}\, c_\alpha + \nabla \frac{kT}{6\pi \mu a_\alpha} c_\alpha \right) \qquad \text{(IIA 1)}$$

where

$\underline{u}$ = fluid velocity field
k = Boltzmann's constant
μ = fluid viscosity
c_α = mass concentration of
T = temperature
a_α = effective radius of particle

Equation (IIA 1) reduces to the usual Einstein formula

$$\frac{\partial c_\alpha}{\partial t} = \nabla \cdot \left(- \underline{u}\, c_\alpha + \frac{kT}{6\pi \mu a_\alpha} \nabla c_\alpha \right) \qquad \text{(IIA 2)}$$

in the absence of temperature gradients and concentration-dependent viscosity, or when the concentration variations are very small. Formula (IIA 1) is less well-known than (IIA 2); for this reason, we consider it worthy of a brief discussion.

Consider the motion of a small particle of mass m in a viscous liquid. It will be assumed that viscous hydrodynamics remains valid – in an averaged sense – down to molecular scales, and that the particles do not interact with any long-range forces. Because of the random nature of molecular collisions, the particle executes a highly irregular motion, but "on average", any impulsively started particle velocity $\underline{v}$ decays to the local fluid velocity $\underline{u}$ according to Stokes' law

$$\frac{d}{dt}\, m \langle \underline{v}(t) - \underline{u} \rangle = - 6\pi \mu a_\alpha \langle \underline{v}(t) - \underline{u} \rangle \qquad \text{(IIA 3)}$$

Therefore, the velocity autocorrelation tensor in equilibrium is

$$\left\langle \left(v_i(t+\tau) - u_i \right)\left(v_j(t) - u_j \right) \right\rangle = \frac{kT}{m} \delta_{ij}\, e^{-\frac{6\pi \mu a_\alpha}{m} |\tau|} \qquad \text{(IIA 4)}$$

(This is a special case of the Fluctuation-Dissipation Theorem.)

The particle's displacement from its initial position after time δt is

$$\underline{\xi}(\delta t) = \int_0^{\delta t} dt_1\, \underline{v}(t_1) \qquad \text{(IIA 5)}$$

so its mean displacement is

$$\left\langle \underset{\sim}{\xi}(\delta t) \right\rangle = \underline{u}\,\delta t \qquad \text{(IIA 6)}$$

and the dispersion tensor is

$$\left\langle \left(\xi_i - u_i\delta t\right)\left(\xi_j - u_j\delta t\right) \right\rangle = 2\,\delta t\,\frac{kT}{6\pi\mu a_\alpha}\,\delta_{ij} \qquad \text{(IIA 7)}$$

provided $\quad \delta t \gg \tau_r \doteq \dfrac{m}{6\pi\mu a_\alpha} \quad$ = relaxation time for particle

Now consider the evolution of the density field $c(\underset{\sim}{\alpha}, t)$. At time $t + \delta t$, the density field will have changed slightly due to the random migrations of the particles:

$$c_\alpha(\underset{\sim}{\alpha}\ t+\delta t) = \int d\underset{\sim}{\xi}\ c_\alpha(\underset{\sim}{\alpha}+\underset{\sim}{\xi}, t)\ P\left\{(\underset{\sim}{\alpha}+\underset{\sim}{\xi}, t) \longrightarrow (\underset{\sim}{\alpha}\ t+\delta t)\right\} \qquad \text{(IIA 8)}$$

Taking δt so small that the particle displacements contributing to (IIA 8) are much smaller than the macroscopic scale of variation (but δt still much greater than τ_r), we can approximate the $\alpha-$ dependence of the integrand by the first nontrivial terms of its Taylor expansion:

$$c_\alpha(\underset{\sim}{\alpha}\ t+\delta t) = \int d\underset{\sim}{\xi}\ \left[c_\alpha(\underset{\sim}{\alpha}\ t)\ P\left\{(\underset{\sim}{\alpha}\ t) \rightarrow (\underset{\sim}{\alpha}-\underset{\sim}{\xi}, t+\delta t)\right\}\right]$$

$$+ \xi_i \frac{\partial}{\partial x_i}\left[c_\alpha(\underset{\sim}{\alpha}\ t)\ P\left\{(\underset{\sim}{\alpha}\ t) \rightarrow (\underset{\sim}{\alpha}-\underset{\sim}{\xi}, t+\delta t)\right\}\right] \qquad \text{(IIA 9)}$$

$$+ \frac{1}{2}\xi_i\xi_j \frac{\partial^2}{\partial x_i \partial x_j}\left[c_\alpha(\underset{\sim}{\alpha}\ t)\ P\left\{(\underset{\sim}{\alpha}\ t) \rightarrow (\underset{\sim}{\alpha}-\underset{\sim}{\xi}, t+\delta t)\right\}\right]$$

$$+\ \text{higher order terms}$$

where $\quad P\left\{(\underset{\sim}{\alpha}_1, t_1) \longrightarrow (\underset{\sim}{\alpha}_2\ t_2)\right\}$

is the probability that a particle at $\underset{\sim}{\alpha}_1$ at time t_1 is displaced to $\underset{\sim}{\alpha}_2$ at later time t_2.

Using (IIA 6) and (IIA 7) for $\langle \xi_j \rangle$ and $\langle \xi_i \xi_j \rangle$, we have

$$c_\alpha(\underline{x}, t+\delta t) - c_\alpha(\underline{x}, t) = \frac{\partial}{\partial x_i}\left(-u_i \, \delta t \, c_\alpha\right)$$

$$+ \frac{\partial^2}{\partial x_i \partial x_j}\left(\frac{kT}{6\pi\mu a_\alpha}\, \delta t \, \delta_{ij}\, c_\alpha\right) + O(\delta t^2) \tag{IIA 10}$$

which becomes (IIA 1) in the limit of small δt.

Note that if the temperature field or viscosity field is nonuniform (eg. if the viscosity depends on the concentration of a diffusing component) then cross-diffusive fluxes may be driven by a temperature gradient or a gradient in the concentration of some component which affects the viscosity. Only in the absence of such effects can (IIA 1) be replaced with the original equation (IIA 2). For the interdiffusion of water, salt, and glycerine, the viscosity is a strong function of the glycerine concentration, and it may be that the modification of Einstein's formula represents an important physical effect. Since the correction was only discovered toward the very end of the project, the quantitative conclusions of this report, which are based on the old formula, will be in error. We believe that this work nonetheless captures the essential nature of the diffusive processes, and yields the correct quali- tative description of the physical mechanism of the salt-water-glycerine insta- bility.

IIB. Pure Interdiffusion of Several Substances and Why It is Wrong

In analyzing the diffusive interpenetration of several substances, it is natural to disregard the flux term in (IIA 2) corresponding to advection of concentration by a velocity field, and conclude that the diffusion of species α is described (assuming Einsteinian diffusion) by

$$\frac{\partial c_\alpha}{\partial t} = \nabla \cdot \left(K_\alpha(\{c_\beta\}) \, \nabla c_\alpha \right) \tag{IIB 1}$$

where $K_\alpha(\{c_\beta\}) = kT \Big/ 6\pi\mu(\{c_\beta\}) a_\alpha$

with suitable initial and boundary conditions. The volume fraction occupied by α is directly proportional to the concentration

$$f_\alpha = c_\alpha \, V_\alpha \tag{IIB 2}$$

where the specific volume V_α of species α is constant, to a high degree of experimental accuracy, for the almost incompressible liquids involved here. So

$$\frac{\partial f_\alpha}{\partial t} = \nabla \cdot \left(K_\alpha \, \nabla f_\alpha \right) \tag{IIB 3}$$

But $\sum_\alpha f_\alpha = 1$, therefore summing (IIB 1) over α yields

$$0 = \nabla \cdot \left(\sum_\alpha K_\alpha \, \nabla f_\alpha \right) \tag{IIB 4}$$

which is not true in general for solutions to (IIB 1).

IIC. Interdiffusion with Advection

The paradox in IIB is resolved by restoring the advection flux to the diffusion equation, which then becomes

$$\frac{\partial f_\alpha}{\partial t} = \underline{\nabla} \cdot \left(\mathcal{K}_\alpha \, \underline{\nabla} f_\alpha \; - \; \underline{u} \, f_\alpha \right) \qquad \text{(IIC 1)}$$

($\mathcal{K}_\alpha$ is tacitly a function of $\{f_\beta\}$). Summing again over all species gives

$$0 = \underline{\nabla} \cdot \left(\sum_\alpha \mathcal{K}_\alpha \, \underline{\nabla} f_\alpha \; - \; \underline{u} \right) \qquad \text{(IIC 2)}$$

$$\Rightarrow \quad \underline{u} = \underline{u}_0 \, (\underline{x}, t) \; + \; \sum_\alpha \mathcal{K}_\alpha \underline{\nabla} f_\alpha$$

where $\underline{u}_0$ is some incompressible velocity field. For simple interdiffusion problems, including the one-dimensional interdiffusion of liquids at rest at ∞, $\underline{u}_0$ vanishes, so (IIC 1) becomes

$$\frac{\partial f_\alpha}{\partial t} = \underline{\nabla} \cdot \left(\mathcal{K}_\alpha \, \underline{\nabla} f_\alpha \; - \; f_\alpha \sum_\gamma \mathcal{K}_\gamma \, \nabla f_\gamma \right) \qquad \text{(IIC 3)}$$

The degree of complication of the diffusion problem has now worsened. The inclusion of the advection terms has coupled the diffusion of each component to the gradients of other components, creating nonlinear effective Dufour and Soret fluxes as well as modifying the single component diffusivities. Together with the strongly nonlinear dependence of the diffusivities on composition that occurs with water and glycerine, this new effective cross-diffusion appears to render the problem so complicated as to be virtually inaccessible.

IID. Water-Salt-Glycerine Interdiffusion

For the system of water, salt, and glycerine, the complications of IIC may be relieved somewhat by making some simplifying approximations. Salt has a very small specific volume compared to water or glycerine, so we neglect it, and also assume that the viscosity of the liquid is independent of the salt concentration. Then the volume fractions of water and glycerine are f and $(1 - f)$ respectively, the velocity field is a functional of the water-glycerine field only

$$\underline{u} = \underline{u}_0 \; + \; \left(\mathcal{K}_{H_2O} - \mathcal{K}_{Gly} \right) \underline{\nabla} f \qquad \text{(IID 1)}$$

and the water-glycerine equation becomes independent of the salt field

$$\frac{\partial f}{\partial t} = \underline{\nabla} \cdot \left(\left\{ f \, \mathcal{K}_{Gly}(f) + (1-f) \, \mathcal{K}_{H_2O}(f) \right\} \underline{\nabla} f \right) \qquad \text{(IID 2)}$$

This equation is particularly appealing for two reasons. First, we have recovered an equation of the pure diffusion form, with an effective diffusivity

$$\mathcal{K}_{eff} \, (f) = f \, \mathcal{K}_{Gly}(f) \; + \; (1-f) \, \mathcal{K}_{H_2O}(f) \qquad \text{(IID 3)}$$

Second, it is evident that process of interdiffusion with advection approaches the linear diffusion of water in pure glycerine as $f \to 0$ and the linear diffusion of glycerine into pure water as $f \to 1$. Thus, the one-dimensional diffusion problems are

$$\frac{\partial f}{\partial t} = \frac{\partial}{\partial z}\left(K_{eff}(f)\, \frac{\partial f}{\partial z} \right)$$

$$\frac{\partial c}{\partial t} = \frac{\partial}{\partial z}\left(K_s(f)\frac{\partial c}{\partial z} - wc \right) \qquad\qquad \text{(IID 4)}$$

$$w = \left(K_{H_2O}(f) - K_{GLY}(f) \right)\frac{\partial f}{\partial z}$$

where c is the normalized salt concentration (the physical salt concentration is $(\Delta \rho_s)c$ with $\Delta \rho_s$ being the initial salt density excess in the upper layer.) The local stability of the profile to double-diffusive fingering depends on the effective Lewis number, which is a function of concentration. A direct consequence of the assumption of Einsteinian diffusivities is that the inverse Lewis number

$$\tau_{eff}(f) = K_s(f)/K_{eff}(f) \text{ takes the simple form}$$

$$\tau_{eff}(f) = \left[\frac{f}{\tau_{GLY}} + \frac{(1-f)}{\tau_{H_2O}} \right]^{-1}; \quad \begin{array}{l} \tau_{GLY} = .4 \\ \\ \tau_{H_2O} = 20 \end{array} \quad \text{for } NaNO_3, \qquad \text{(IID 5)}$$

The profile is then unstable to double diffusive fingers if

$$\frac{\partial c}{\partial z} \Big/ \frac{\partial f}{\partial z} > \frac{.26\ g\,cm^{-3}}{\Delta \rho_s}\ \tau_{eff}(f) \qquad\qquad \text{(IID 6)}$$

at some level. The profile will also be unstable to a Rayleigh-Taylor instability if

$$\frac{\partial c}{\partial z} \Big/ \frac{\partial f}{\partial z} > \frac{.26\ g\,cm^{-3}}{\Delta \rho_s} \qquad\qquad \text{(IID 7)}$$

We shall therefore proceed as follows: the diffusive spreading of the initially sharp interface will be calculated as a pair of self-similar profiles for f and c, as functions of the similarity variable

$$\eta = zt^{-1/2} \qquad\qquad \text{(IID 8)}$$

The O.D.E.'s for f and c are

$$-\frac{1}{2}\eta\, f' = \left[K_{eff}(f)\, f' \right]' \qquad\qquad \text{(IID 9a)}$$

$$-\frac{1}{2}\eta\, c' = \left[K_s(f)\, c' - wc \right]' \qquad\qquad \text{(IID 9b)}$$

$$w = \left[K_{H_2O}(f) - K_{GLY}(f) \right] f' \qquad\qquad \text{(IID 9c)}$$

and we use a polynomial approximation to $K_{eff}(f)$:

$$\mathcal{K}_{eff}(f) = .133 + 176.6 \, f^4(1.088^2 - f^2)^2 \qquad (IID \; 10)$$

(in units of $10^{-6} \, cm^2 \, sec^{-1}$. See figure 3)
Then we shall calculate the "stability parameter"

$$Q(\eta) = \left(\frac{dc}{d\eta} \Big/ \frac{df}{d\eta}\right) \Big/ min\left(\tau_{eff}, \; 1\right) \qquad (IID \; 11)$$

and find its maximum

$$Q = Q_{max} \quad at \quad \eta = \eta_0 \; where \; f = f_0 \qquad (II \, D \; 12)$$

The critical salt density in the upper layer of water is then

$$c.s.d. = (\Delta\rho_s)_{crit} = .26/Q_{max} \qquad (II \, D \; 13)$$

and the instability will be double-diffusive or Rayleigh-Taylor depending on whether

$$\tau_{eff}(f_0) < 1 \quad or \quad \tau_{eff}(f_0) > 1 \qquad (II \, D \; 14)$$

respectively.

III. RESULTS

IIIA. Methods of Integrating the O.D.E.'s

The most straightforward way of numerically solving the second order O.D.E.'s for the similarity profiles is to convert them to pairs of first order equations, which are then integrated directly. The values $f = 1$ and $c = 1$ are specified at a large positive value of η together with representations of the slopes of f and c, and the equations are then integrated backwards to a large negative value of η. Some improvement in the numerical behavior is made by introducing the new independent variable ξ defined by

$$\frac{d\eta}{d\xi} = \mathcal{K}_{eff}(f) \qquad (IIIA \; 1)$$

so that (IID 9a) may be converted to the coupled first-order system

$$df/d\xi = exp(u) \qquad (IIIA \; 2a)$$

$$du/d\xi = -\frac{1}{2}\eta \qquad (IIIA \; 2b)$$

which is integrated from $\xi_1 > 0$, to $\xi_2 < 0$. $f = 1$ at $\xi = \xi_1$ is imposed, and we thus obtain a relation between $u(\xi_1)$ and $f(\xi_2)$ The velocity field is simply given by

$$w = \frac{df}{d\xi}\left(\mathcal{K}_{H_2O}(f) - \mathcal{K}_{cly}(f)\right)\Big/\mathcal{K}_{eff}(f) \qquad (IIIA \; 3)$$

The salt advection-diffusion equation is more tricky to integrate, due to the advective flux term. However, it is linear, so we may change variables to

$$S = \log c \qquad\qquad c = \exp(S) \qquad\qquad \text{(IIIA 4)}$$

Then

$$ds/d\xi = \frac{1}{\tau_{eff}(f)}\,(r + w)$$

$$dr/d\xi = \frac{1}{\tau_{eff}(f)}\,(r + w)(r - \tfrac{1}{2}\eta) \qquad\qquad \text{(IIIA 5)}$$

The boundary conditions

$$S \rightarrow 0 \qquad\qquad\qquad \text{(IIIA 6)}$$

and

$$r \downarrow 0 \qquad\qquad \text{as} \quad \xi \rightarrow \infty$$

almost always lead to

$$S \rightarrow -\infty \qquad\qquad \text{as} \quad \xi \rightarrow -\infty$$

so that the B.C. at $-\infty$ on the salt field is automatically satisfied. Solutions to these equations for two different values of $f(-\infty)$ are shown in figures 1a,b and 2a,b.

IIIB. Conclusions

The strong asymmetry of the f profile reflects the nonlinearity of the diffusion process, and the pronounced displacement of the salt curve demonstrates the dramatic effect of the advection of the salt field by the water-glycerine velocity. It is observed that the salt profile has its maximum gradient on the far right of the water-glycerine curve, where the volume fraction of water is very close to 1. This indicates that - since $\tau_{eff}(f)$ is greater than unity in the neighborhood of $f = 1$ - the double diffusive instability might not occur. However, the sheer strength of the salt gradient, together with the weakness of the water-glycerine gradient, suggests that a Rayleigh-Taylor instability may develop from a relatively small initial salt concentration in the upper layer. Plots of the stability parameter $Q(\eta)$ and evaluation of $\tau_{eff}(f_0)$ at the most unstable point support this conclusion (figures 1c, 2c).

Plotting the critical salt density in the upper layer vs. the water volume fraction $f(-\infty)$ in the lower layer shows that the c.s.d. decreases very slowly from 8.7867×10^{-3} as $f(-\infty)$ increases from 0 (figure 4). The resolution of the numerical integration breaks down as $f(-\infty)$ increases beyond 0.6 but it is anticipated that as $f(-\infty)$ approaches 1, the c.s.d. and $(1-f(-\infty))$ will tend toward proportionality

$$\text{c.s.d.} \sim 0.26(1 - f(-\infty)) \qquad\qquad \text{(IIIA 7)}$$

as the system approaches the familiar case of a dilute aqueous solution of salt above a dilute aqueous solution of glycerine.

In comparing these predictions with the observed critical salt density, which is approximately 0.15 , decreasing slowly as $f(-\infty)$ increases from 0., it is seen that there is considerable quantitative disagreement between this theory and experiment. It seems likely that the discrepancy is a consequence of neglecting the non-Einsteinian effects described in IIA , in which case the appropriate modification of this theory would be straightforward. In any case, the qualitative character of the predicted stability criterion is similar to the observations, so that there is reason to believe that this work is a substantial first step toward a quantitatively correct theory.

ACKNOWLEDGEMENTS

REFERENCES

Einstein, A., 1956. Investigations on the Theory of the Brownian Movement, Dover Press. N. Y.

Huppert, H.E. and Manins, P.C., 1973 Limiting Conditions for Salt Fingering at an Interface. Deep Sea Research 20, 315-328.

Huppert, H.E. and Hallworth, M., 1984. To appear in J. Chem. Phys.

ADDITIONAL REFERENCES

Miner, C. S. and Dalton, 1953. Glycerol Reinold, Pres, N.Y.

Pathria, R. K., 1972. Statistical Mechanics, Pergamon Press, Oxford.

Tyrrell, H.J.V., 1961. Diffusion and Heat Flow in Liquids. Butterworth's, London.

FIGURE 1 : Plots of $\dot{f}(\eta)$, $c(\eta)$, $w(\eta)$, $Q(\eta)$ for $f(-\infty) = .34$

$Q_{max} = 30.0$ c.s.d. $= 8.62 \times 10^{-3}$ g cm^{-3}

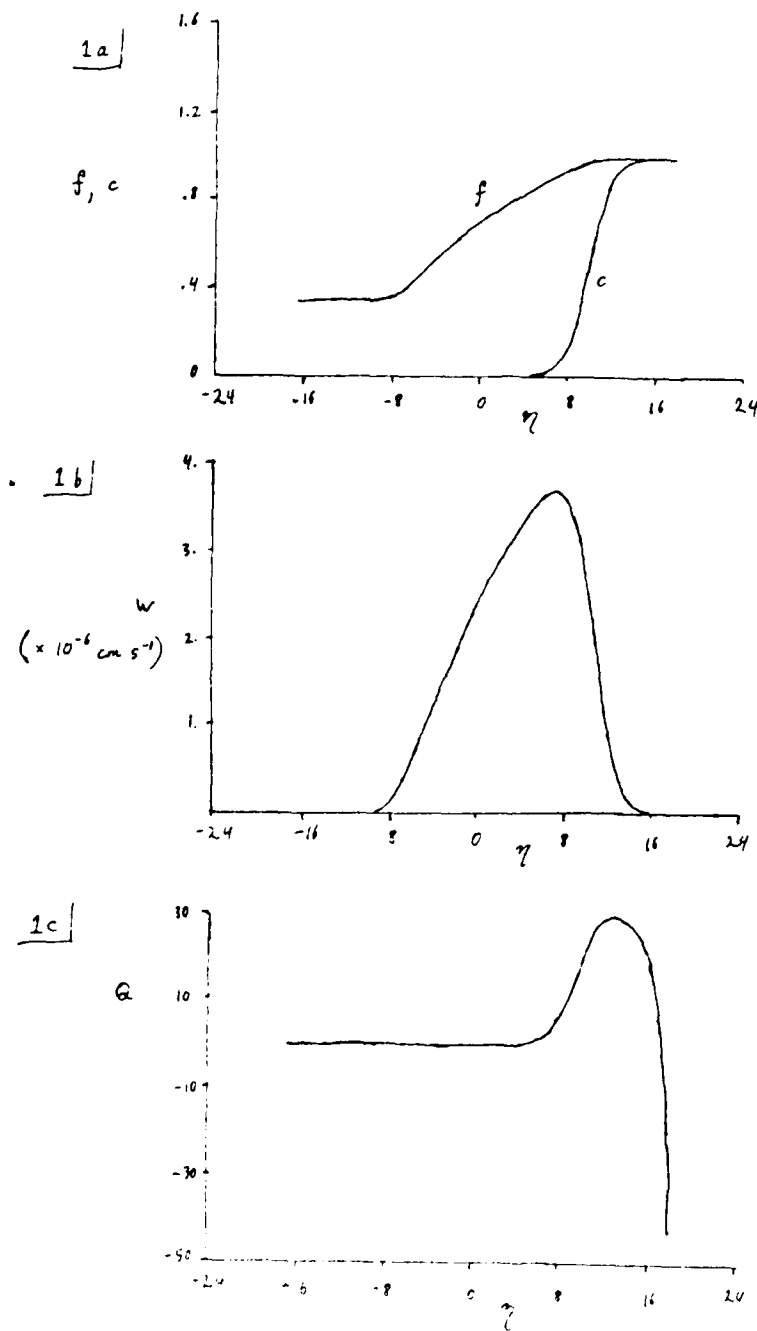$\tau_{eff}(f_0) = 2.3 \implies$ Rayleigh - Taylor instability
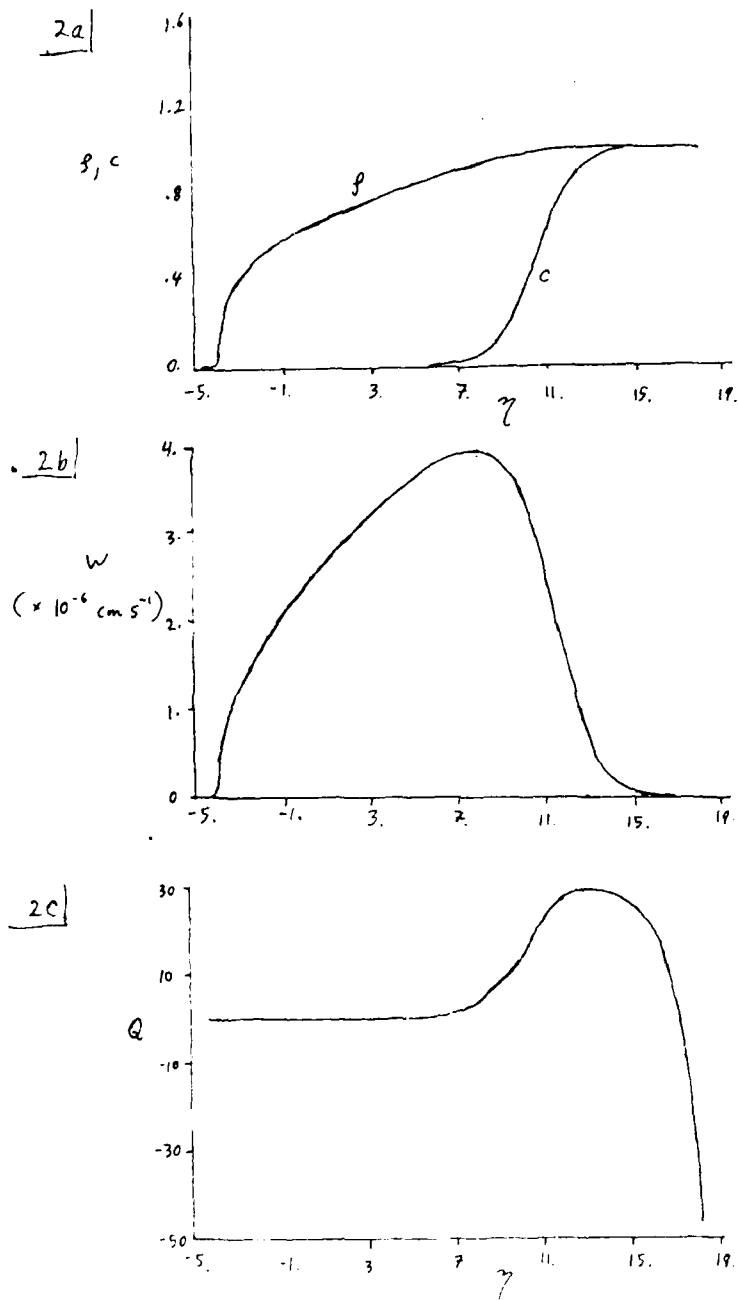
FIGURE 2: Plots of $f(\eta)$, $c(\eta)$, $w(\eta)$, $Q(\eta)$ for $f(-\infty) = 0.0$

$Q_{max} = 29.6$ $c.s.d. = 8.79 \times 10^{-3}$ g cm^{-3}

$T_{eff}(-\infty) = 2.28$ $\Longrightarrow$ Rayleigh Taylor instability
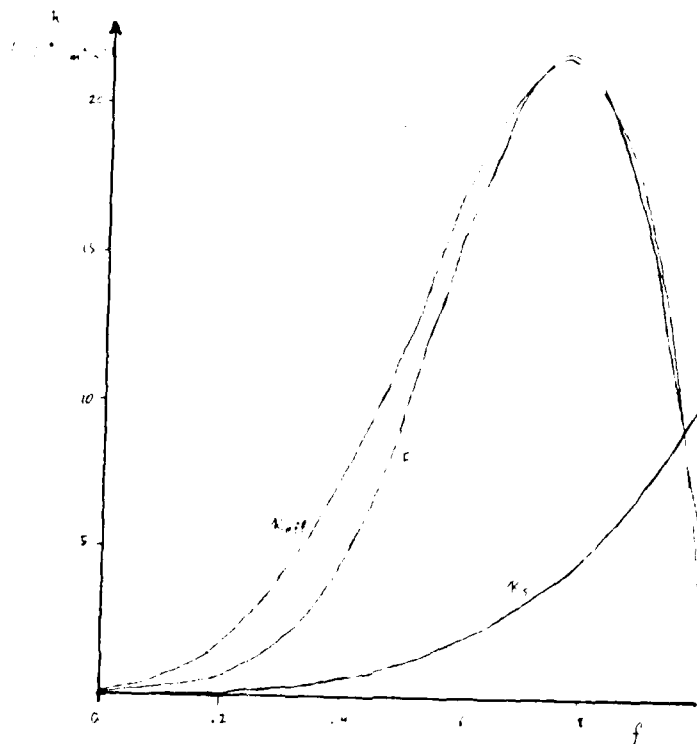
FIGURE 3 : Plots of diffusivities $K_S(f)$ (for $NaNO_3$), $K_{eff}(f)$, and polynomial approximation $F(f)$ to K_{eff}.

$$F(f) = .133 + 176.6 \, f^4 \left(1.088^2 - f^2\right)^2$$

$$K_{eff}(f) = f \, K_{air}(f) + (1-f) \, K_{H_2O}(f)$$

where $\qquad K_{H_2O}(f) \triangleq \dfrac{\mu(0)}{\mu(f)} \, K_{H_2O}(0)$

$\qquad\qquad\quad K_{air}(f) \triangleq \dfrac{\mu(1)}{\mu(f)} \, K_{air}(1)$

Viscosity $\mu(f)$ is tabulated in Miner & Dalton (1953)
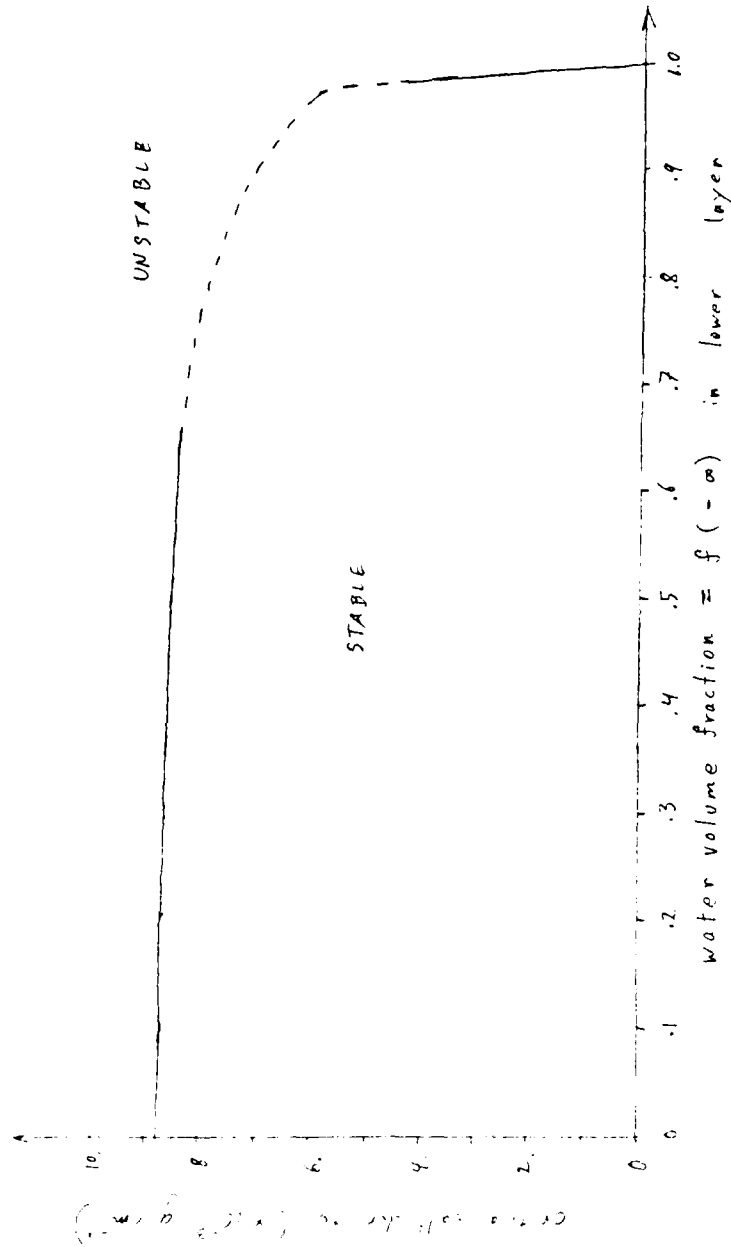
FIGURE 4. Predicted stability diagram for experiment
(Dotted line indicates plausible interpolation between
calculated solid lines)
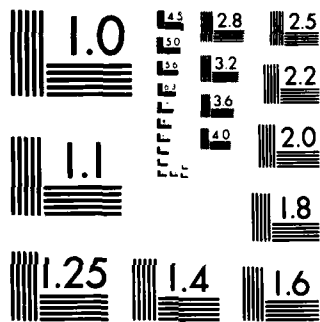
MICROCOPY RESOLUTION TEST CHART
NATIONAL BUREAU OF STANDARDS-1963-A

SALT FINGERS IN A HELE SHAW CELL

John Taylor

Abstract

Several approaches were taken to the investigation of the behaviour of salt fingers in a Hele Shaw cell. The stability of linear temperature (T) and salinity (S) gradients maintained between perfectly conducting boundaries in a vertical Hele Shaw cell was studied. The wavenumber which maximises the growthrate of periodic disturbances in the cell was:

$$\pi k_m = \left(\frac{12 d^2 g \alpha \overline{T}_z}{\nu k_t} \right)^{\frac{1}{2}} \left[\frac{1}{(\tau R_\rho)^{\frac{1}{2}}} - 1 \right]^{\frac{1}{2}}$$

where d is the width of the Hele Shaw cell; $\alpha \overline{T}_z$ the mean T gradient; ν the kinematic viscosity; k_t the molecular diffusivity of T; $\tau = k_s / k_t$ the diffusivity ratio and $R\rho$ is the ratio of gradients ($\alpha \overline{T}_z / \beta \overline{S}_z$). The scale of fingers in a Hele Shaw cell is not limited by the increase of viscous drag between up and downgoing fingers with increasing wavenumber as occurs for fingers remote from rigid boundaries, but by the need for a finger to be large enough not to lose its S anomaly by lateral diffusion.

Using the results from a model of infinitely long fingers in a Hele Shaw cell possible parameters for which fingers could be set up in the laboratory were suggested. The boundary conditions used in these analyses are not easy to realise in the laboratory so the stability of a sharp positive salinity jump with a linear stabilising temperature gradient was analysed. The wavenumber of instabilites which arise from this analysis, at least for the parameters used in the long finger model, is not consistent with the assumption of Hele Shaw flow.

1. Introduction

If a fluid is stratified by two components so that the contribution to the fluid density of the slower diffusing component is increasing upwards some of the potential energy of the unstably distributed component may be released by an array of tall thin conterflowing fluid columns called salt fingers. Fluid motion is possible even though the overall density distribution is hydrostatically stable because of the different molecular diffusivities of the two components. Because the initial interest in this phenomenon was in its oceanographical applications the two components of interest were heat and salt, however, convection can also occur with pairs of solutes; salt and sugar have been used in many laboratory experiments as a convenient analogue for the heat salt system with salt now being the faster diffusing T component. Huppert and Turner (1981) have reviewed salt fingering and related double diffusive phenomena.

In this paper the instability of an initially sharp salinity interface in the presence of a linear stabilising temperature gradient will be considered. To make it possible to treat these property distributions

analytically the analysis is restricted to considering flow in a Hele Shaw cell. Because the stratification is arranged in the salt fingering sense the processes which set the scale of fingers in a Hele Shaw cell are of interest and these will be studied in section 2 by analysing the stability of linear gradients of T and S between horizontal boundaries maintained at constant T and S.

In most experimental investigations of salt fingering fingers which grow from an interface with initially step-like distributions of T and S are studied. Theoretical analysis of this situation has been restricted to finding the condition for marginal stability (Sartory,1969, Huppert and Manins, 1973) which is $R_\rho < \tau^{-3/2}$, where $R_\rho = \alpha \Delta T/\beta \Delta S$ is the ratio of the density step due to T to that due to S. This criterion describes a dynamic instability; no horizontally averaged static instability is necessary for fingers to occur. However for $R_\rho < \tau^{-1/2}$ the solution to the diffusion equation shows that at any time after diffusion is switched on there will be a region which is statically unstable at the interface because of the more rapid diffusion of T compared to S. Thus the initial property profiles adopted for the analysis in this paper could be considered as an approximation to this state although experimentally the situation would be realised with a linear gradient of the T-component and a finite step of the S-component.

One of the major problems of understanding salt finger convection is how the horizontal scale of the cells is selected. The interface stability calculations mentioned above give no information about the scale of the cells since there is no well defined lengthscale in the problem. The linear stability analysis for the thermohaline Benard problem (Stern,1960) shows that the horizontal scale at marginal stability is determined by the plate separation so that the aspect ratio of the convection cells should be one. For supercritical conditions the cell size which maximises the growth rate of instabilities found from this analysis correctly predicts the scale of salt fingers observed in experiments (Linden,1973, Huppert and Manins,1973) even when the experiments are near the marginal state. Experiments have not been conducted which reproduce the conditions of the theoretical Bénard-type problems which have been studied because of the difficulty of maintaining the required constant T and S boundary conditions. However, recent work by Krishnamurti (this volume, page 00) for the inverse diffusive case has shown that the constant salinity boundary condition may be closely approximated in the laboratory. The sharp interface analysis attempts to avoid this problem by dealing with a supercritical initial state so that the scale of the fingers which grow at the interface should be predicted by a linear stability analysis.

There are advantages to experimenting in the Hele shaw cell provided salt fingers governed by Hele Shaw dynamics can be produced. One advantage is that a single finger would be observable in an experiment rather than the horizontally or vertically averaged picture through many fingers which is seen in a conventional experiment. This would make the determination of the finger width simple. Another advantage is the slower evolution time of flows in a Hele Shaw cell. The component of gravitational acceleration driving the flow can be varied by tilting the cell away from the vertical without changing the characteristics of the flow. Piacsek and Toomre (1980) computed a two-dimensional numerical model of ordinary viscous salt fingers growing from a sharp interface into constant property layers which showed that the fingers tended to form bulbous ends which could break off from the main finger. Such interesting finite amplitude features should be

visible in a Hele Shaw cell experiment. Typical experimental parameters which are needed to produce fingers in a laboratory experiment which satisfy the conditions that make a description of the flow in the Hele Shaw approximation valid will be discussed in section 3.

2.The stability of linear gradients of T and S between parrallel boundaries in a Hele Shaw cell.

2.1 Flow in a Hele Shaw cell.

A Hele Shaw cell consists of a layer of fluid contained between two closely spaced plates. For sufficiently small plate spacing or large fluid viscosity the flow of the fluid will be governed by a balance between the applied pressure gradient and viscous drag (Batchelor, 1967). In this limit the mean fluid velocity across the narrow dimension of the cell will be given by:

$$\overline{u} = -\frac{1}{12}\frac{d^2}{\nu}\frac{1}{\rho_0}\frac{dp}{dx} . \tag{1}$$

The flow in a Hele Shaw cell is an exact analogy to flow in a porous medium governed by Darcy's Law with effective permittivity given by $d^2/12$. In (1) d is the plate spacing, ν the kinematic viscosity of the fluid, dp/dx the driving pressure gradient and ρ_0 a reference density. A quantity μ (T^{-1}), the flow resistance, will be defined as $12\nu/d^2$.
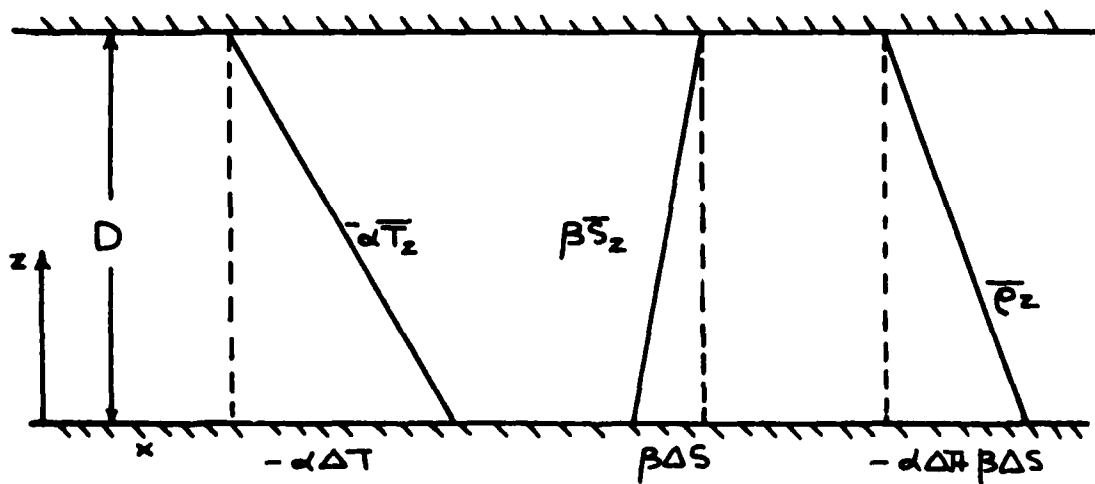

Figure 1. A sketch of the T,S and density distributions for this analysis.

2.2 The stability problem

The easiest geometry to investigate the double diffusive problem in a Hele Shaw cell is that of linear T and S gradients between two semi infinite parrallel boundaries maintained at constant temperature and salinity (fig.1). Nield (1968) has investigated the conditions for the onset of thermohaline convection in a porous medium for both the oscillatory (diffusive) and direct (fingering) modes of convection. He found the marginal stability condition for a range of boundary conditions but did not discuss the wavenumber which maximises the growthrate under supercritical conditions. The analogous problem for ordinary two component convection was first discussed by Stern (1960) and later by Baines and Gill (1969). The problem is discussed here because of the correspondence in the ordinary case between the fastest growing mode from the linear stability analysis and the finger wavenumber observed in experiments. This agreement should carry over to the Hele Shaw problem providing a basis for the discussion of finger physics in the Hele Shaw cell and a comparison with the sharp interface model in section 4.

The linearised equations which describe the behaviour of perturbations to the T and S fields shown on fig.1 within a Hele Shaw cell are:

$$\nabla'^2 w' = R_T T'_{xx} - R_S S'_{xx}$$

$$\left(\frac{\partial}{\partial t'} - \nabla'^2\right) T' = -w'$$

$$\left(\frac{\partial}{\partial t'} - \nabla'^2\right) S' = -w'$$

(2)

where the non-dimensional variables $t'=\kappa_t/D^2$, $(x,z)=(x,z)/D$, $w'=D/\kappa_t w$, $T'=T/\Delta T$, $S'=S/\Delta S$, $\overline{T}_z=\Delta T/D$, $\overline{S}_z=\Delta S/D$, $R_T=g\alpha\overline{T}_z D^2/\mu\kappa_t$, $R_S=g\beta\overline{S}_z D^2/\mu\kappa_t$, $\tau=\kappa_s/\kappa_t$ are used. Given the boundary conditions:

$$w',T',S'=0 \text{ at } z'=0,1$$

solutions to (2) of the form:

$$(w',T',S')=(w_0,T_0,S_0)e^{pt'}\cos\pi kx' \sin\pi nz'$$

are sought. With the substitution of these functions for w',T',S' into (2) and defining $\pi^2(k^2+n^2)=\lambda^2$ a series of algebraic equations (3) are found:

$$\lambda^2 w' = \pi^2 k^2 \left(R_T T' - R_S S'\right)$$

$$\left(p + \lambda^2\right) T' = -w'$$

$$\left(p + \tau\lambda^2\right) S' = -w' .$$

(3)

Eliminating the temperature and salinity perturbations from the momentum equation gives a characteristic equation for p:

$$p^2 + p\left[\lambda^2(\tau+1) + \frac{\pi^2 k^2}{\lambda^2}\left(R_T - R_S\right)\right] + \tau\lambda^4 + \pi^2 k^2\left(R_T\tau - R_S\right) = 0. \quad (4)$$

The marginal stability condition is found by setting p=0 in (4). The most unstable vertical mode will be the n=1 mode. By fixing an R_T value the

minimum horizontal wavenumber for instability is found to be k=1 which then
gives a result for the marginal stability curve:

$$R_T = \frac{R_s}{\tau} - 4\pi^2 .$$

This result, given by Nield (1968), is identical to the marginal stability
criterion for the direct mode in ordinary double diffusive convection
(Baines and Gill,1969) except that the Hele Shaw cell has a much smaller
critical Rayleigh number 39.5 as opposed to 658. This equation may be
rearranged to show the the maximum value of $R\rho$ at which convection will
occur for a given stabilising R_T:

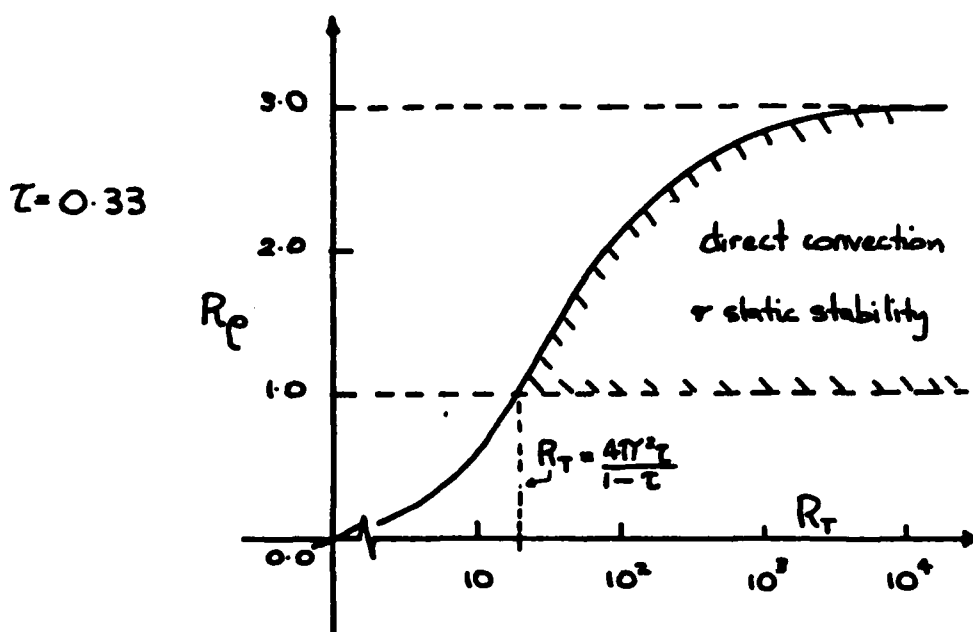$$R_\rho = \frac{R_T}{\tau(4\pi^2 + R_T)} .$$

$\tau = 0.33$

Figure 2. A sketch of the marginal stability curve for the direct mode of
convection.

2.3 The wavenumber which maximises the growth rate

If the diffusivity of T is much larger than S, as is the case for heat salt the growth rate term in the T equation may be neglected and (4) reduces to:

$$p = -\tau \lambda^2 + \frac{\pi^2 k^2 \lambda^2 R_S}{\lambda^4 + R_T \pi^2 k^2} \quad . \tag{5}$$

If the growth rate and wavenumber are now scaled by R_T, $\hat{p} = p/R_T$, $\hat{a}^2 = \pi^2 k^2/R_T$ the dispersion relationship (5) may be written as:

$$\hat{p} = -\tau \left(\hat{a}^2 + \frac{\pi^2}{R_T} \right) + \frac{\hat{a} \left(\hat{a}^2 + \frac{\pi^2}{R_T} \right)}{R_\rho \left[\left(\hat{a}^2 + \frac{\pi^2}{R_T} \right)^2 + \hat{a}^2 \right]} \quad . \tag{6}$$

For large R_T π^2/R_T is neglected in comparison to $\hat{a}^2$ and the wavenumber which maximises the growth rate found by setting $d\hat{p}/d\hat{a}^2 = 0$. The resulting wavenumber is:

$$\hat{a}_m^2 = \frac{1}{(\tau R_\rho)^{\frac{1}{2}}} - 1 \tag{7}$$

or in dimensional terms:

$$\pi k_m = \left(\frac{g \alpha \overline{T}_z}{\mu k_t} \right)^{\frac{1}{2}} \left[\frac{1}{(\tau R_\rho)^{\frac{1}{2}}} - 1 \right]^{\frac{1}{2}} \quad . \tag{8}$$

The largest value of $\hat{a}_m$ will be at $R_\rho = 1$ where $\hat{a}_m^2 = 3$ for $\tau = 0.01$, the value for heat salt and $\hat{a}_m^2 = 1.4$ for $\tau = 0.33$ for salt sugar. To find the maximum growth rate (7) is substituted into (5) with the result:

$$\hat{p}_m = \left(\frac{1}{(R_\rho)^{\frac{1}{2}}} - \tau^{\frac{1}{2}} \right)^2 . \tag{9}$$

The behaviour of the growth rate as a function of wavenumber may be calculated from (6) for a range of values of R_T, R_ρ and τ. The full quadratic expression (4) may also be rescaled to the new variables and the corresponding expression for $\hat{p}$ is given by (10).

$$\hat{p}^2 + \hat{p} \left[\left(\hat{a}^2 + \frac{\pi^2}{R_T} \right) (\tau + 1) + \frac{\hat{a}^2 \left(1 - \frac{1}{R_\rho} \right)}{\hat{a}^2 + \frac{\pi^2}{R_T}} \right] + \tau \left(\hat{a}^2 + \frac{\pi^2}{R_T} \right) + \hat{a}^2 \left(\tau - \frac{1}{R_\rho} \right) = 0 \tag{10}$$
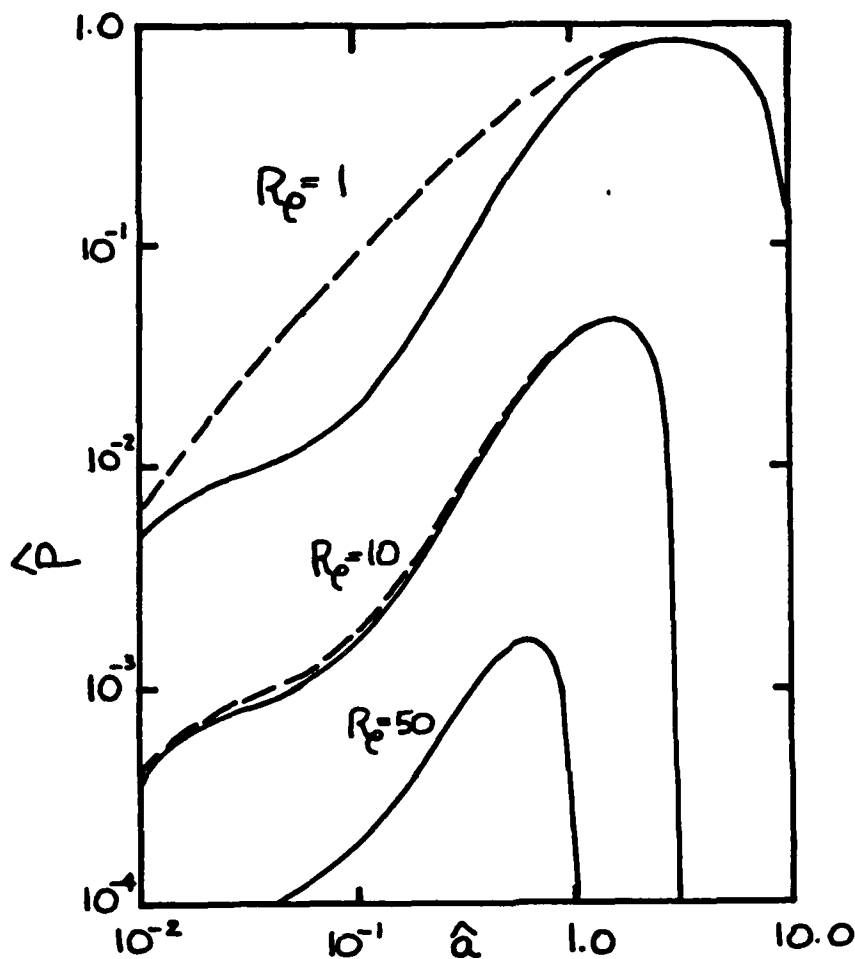
Figure 3. Graph of wavenumber versus growthrate for $\tau=0.01$ $R_T=1.0\times10^3$. Dashed curve is calculated from the full relation (10), solid curve from the approximate relation (6).

2.4 Discussion

Stern (1960) showed that for $\tau\ll1$ and large R_T and R_ρ the maximum growthrate in the normal finger problem occurred for a dimensional wavenumber:

$$\pi k_m \sim \left[\frac{g\alpha\bar{T}_z}{\nu k_t}\right]^{1/4}.$$

In the Hele Shaw cell there is no corresponding limit since if $\tau\to0$, $\hat{a}_m\to\infty$ and $\hat{p}_m\to(R_\rho)^{-1}$. Clearly the process of the wavenumber selection in the two problems must be quite different.

Fig.3 is a plot of the wavenumber versus growthrate for $\tau=0.01$ (corresponding to heat salt fingers) and for $R_T=10^3$. The dashed curve is the solution to the quadratic (10) and the solid curve is the approximate

result given by (6). For wavenumbers just beyond $\hat{a}_m$ the growthrate goes to zero and any perturbation on these scales would be strongly damped. The neglect of the growthrate term is well justified for $\tau=0.01$ although if τ is increased to 0.33 (fig.4) there is an increase in the maximum growthrate and a shift of $\hat{a}_m$ to a lower wavenumber if the full expression is used.
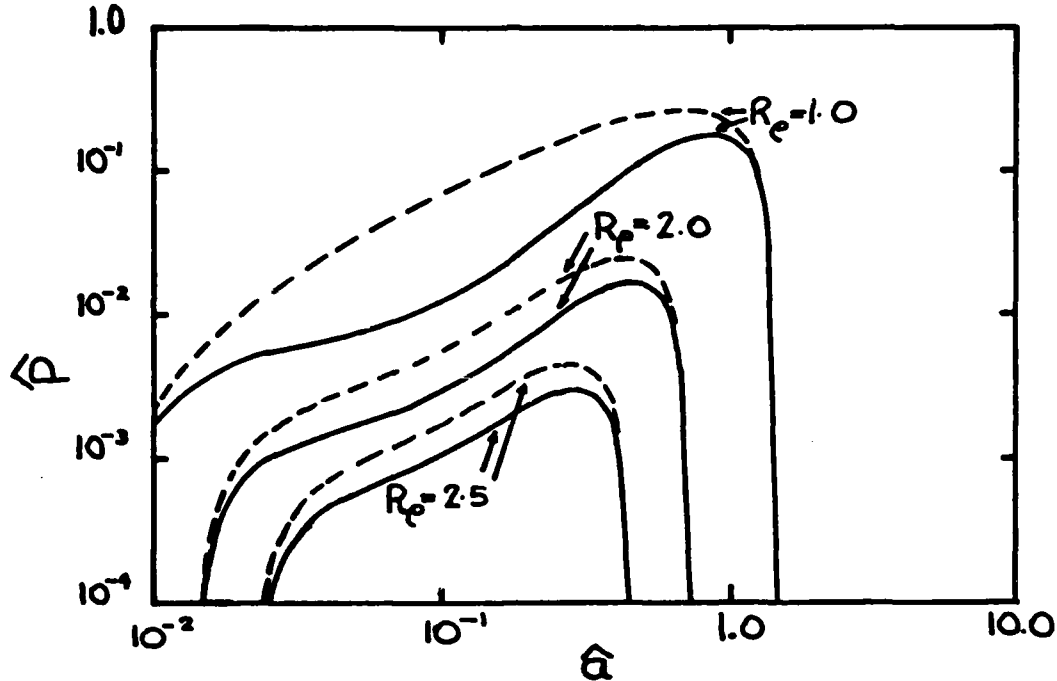

Figure 4. Graph of wavenumber versus growthrate for $\tau=0.33$ $R_T=1.0\times10^3$. Curves are as for fig.3.

The physical reason why long thin cells are the favoured mode of convection for the stratification shown in fig.1 was also first discussed by Stern. In a downward (upward) going finger the temperature excess (deficit) of the finger must be diffused sideways at a sufficiently rapid rate to maintain the finger's negative buoyancy. If the amplitude of the temperature perturbation stays constant a thinner column increases the temperature gradient between adjacent fingers. This increases the lateral heat flux and leads to higher vertical velocites in the fingers. The higher vertical velocities mean that the potential energy of the salt stratification is more efficiently released. However, as the finger becomes thinner shear between adjoining fingers increases, decreasing the efficiency of the energy release. A wavenumber is selected which balances the competing effects of the increasing heat flux and viscous drag.

In a Hele Shaw cell the flow is everywhere strongly damped by viscosity due to the proximity of the sidewalls. In fact for the Hele Shaw desription of the flow to be accurate the finger scale must be such that the shear between fingers be negligible compared to the cross channel shear. It has been shown that if salt diffusion is neglected ($\tau=0$) the growth rate has no maximum value. The slow diffusion of S sets an upper limit to the wavenumber of a disturbance which can grow before lateral diffusion fluxes away the driving S anomaly. At a slightly lower wavenumber

there is a maximum p which defines a balance between the need to rapidly diffuse heat but not to flux away the salinity perturbation.

The problem of realising salt fingers in a Hele Shaw cell is to ensure that the fingers will be limited by the diffusivity of the S component before the motions become three-dimensional, the Hele Shaw approximation breaks down and viscously limited finger form.

3. Experimental Possibilities

As discussed in section 2 the production of salt fingers governed by Hele Shaw dynamics depends on a limiting wavenumber being less than the wavenumber implied by the plate spacing. In this section the well known finite amplitude model of long fingers (Stern, 1975) will be used to calculate the limiting wavenumbers of Hele Shaw fingers for a set of typical laboratory parameters as well as the wavenumbers for viscous fingers in an infinite environment for the same overall parameters.

Under the conditions that there are no vertical variations in the mean or perturbed quantities the non-linear terms in the momentum equations are identically zero and there are simple exact solutions which describe infinitely long couterflowing fluid columns. These solutions have been extensively used (Stern,1975, Schmitt,1979) to describe salt fingers. The solutions are degenerate in the sense that there is a spectrum of finger wavenumbers which satisfy the equations and the amplitudes of the perturbation quantities cannot be determined, however, the analysis predicts a maximum wavenumber beyond which fingers cannot grow.

The equations governing the fingers in a Hele Shaw cell are:

$$\mu w = g(\alpha T - \beta S)$$
$$\left(\frac{\partial}{\partial t} + k_t \frac{\partial}{\partial x^2}\right) T = -w \overline{T}_z$$
$$\left(\frac{\partial}{\partial t} + k_s \frac{\partial}{\partial x^2}\right) S = -w \overline{S}_z .$$

(11)

Periodic solutions in x of the form $(w,T,S)=(w_0,T_0,S_0)e^{pt}\sin(ax)$ are sought which lead to the dispersion relationship:

$$p^2 + p\left[a^2 k_T(1+\tau) + \frac{g\alpha \overline{T}_z}{\mu}\left(1 - \frac{1}{R_e}\right)\right] + a^4 \tau k_T^2 + \frac{g\alpha \overline{T}_z}{\mu} k_T a^2\left(\tau - \frac{1}{R_e}\right) = 0 . \quad (12)$$

The maximum wavenumber permitted occurs when p=0 which gives a finger width, λ', normalised by the transverse plate spacing, d:

$$\lambda' = \frac{\Pi}{d}\left(\frac{g\alpha \overline{T}_z}{\tau \mu k_t}\right)^{-\frac{1}{2}}\left(\frac{1}{R_e} - \tau\right)^{-\frac{1}{2}} . \quad (13)$$

The analogous result for viscous fingers where it is assumed that the Lewis number, ν/κ_t, is large and hence the growth rate term in the momentum

equation may be neglected is:

$$P^2 + P\left[a^2 k_T(1+\tau) + \frac{g\alpha\bar{T}_z}{\nu a^2}\left(1-\frac{1}{R_\rho}\right)\right] + a^4\tau k_T^2 + \frac{k_T g\alpha\bar{T}_z}{\nu}\left(\tau-\frac{1}{R_\rho}\right) = 0. \quad (14)$$

This expression should be valid for salt sugar experiments where the Lewis number is $O(10^3)$ but $\tau=0.33$ and the diffusion of S is not insignificant compared to the diffusion of T. The smallest square finger permitted will have a side of length:

$$\lambda' = \frac{\pi}{\sqrt{2}}d\left(\frac{g\alpha\bar{T}_z}{\nu k_t\tau}\right)^{-\frac{1}{4}}\left(\frac{1}{R_\rho}-\tau\right)^{-\frac{1}{4}}. \quad (15)$$

Equation (13) may be rearranged to express the minimum R_ρ for the smallest allowed fingers to have a width equal to the plate spacing:

$$R_\rho = \left[\tau(1+\pi^2/R_T')\right]^{-1}. \quad (16)$$

where $R_T'=g\alpha\bar{T}_z d^2/\mu\kappa_t$ has the form of a Rayleigh number. For typical laboratory parameters in a salt sugar experiment $\alpha\bar{T}_z=5.0\times10^{-4}$, $d=0.1$cm, $\mu=12\nu/d^2=12s^{-1}$ and fluid properties $\kappa_t=1.48\times10^{-5}$cm^{2}s^{-1}, $\tau=0.33$ $R_T=27.6$ and R_ρ need only be greater than 2.2 for the smallest scale of finger possible to be equal to the plate spacing. Under the same conditions (15) predicts that the maximum viscous finger size would be $\lambda'=0.66$. The fact that a viscously limited finger can be narrower than a diffusively limited finger reflects the stronger constraint on the velocity field in the Hele Shaw cell imposed by the rigid boundaries of the cell.

It seems that the restrictions on the experimental conditions could be eased by increasing the viscosity of the fluid. This is not the case for a two solute experiment since the molecular diffusivity of a solute is almost inversly proportional to the viscosity of the solution. Mullin (1972) suggested the empirical relationship:

$$k\,(cm^2s^{-1}) = \frac{14\times10^{-5}}{\eta^{1.1}V_1^{0.6}}$$

where η is the solution viscosity (poise) and V_1 the molar volume of the solute (cm^3). Thus an increase in μ would leave R_T' virtually unchanged because of the corresponding change in κ_t.

It is of interest to compare the the wavenumber growthrate spectrum of the Hele Shaw fingers with that to be expected for viscous or ordinary fingers. Equation (12) and (14) have been solved for several R_ρ values with the other parameters as given above (fig.5). The curves have similar form except in the limit where $R_\rho=1$ and the overall density stratification is neutrally stable. While the Hele Shaw fingers still have a maximum growthrate at high wavenumbers the growthrate of the viscous fingers becomes very flat over a large range of wavenumbers. If the constraint of side boundaries is removed larger scale overturning seems to be the

preferred mode of convection in this limit.

For the conditions used in calculating fig.5 the growthrates of Hele Shaw fingers are comparable with those of viscous fingers although as commented previously for $R_\rho > 1$ the limiting wavenumber is lower.

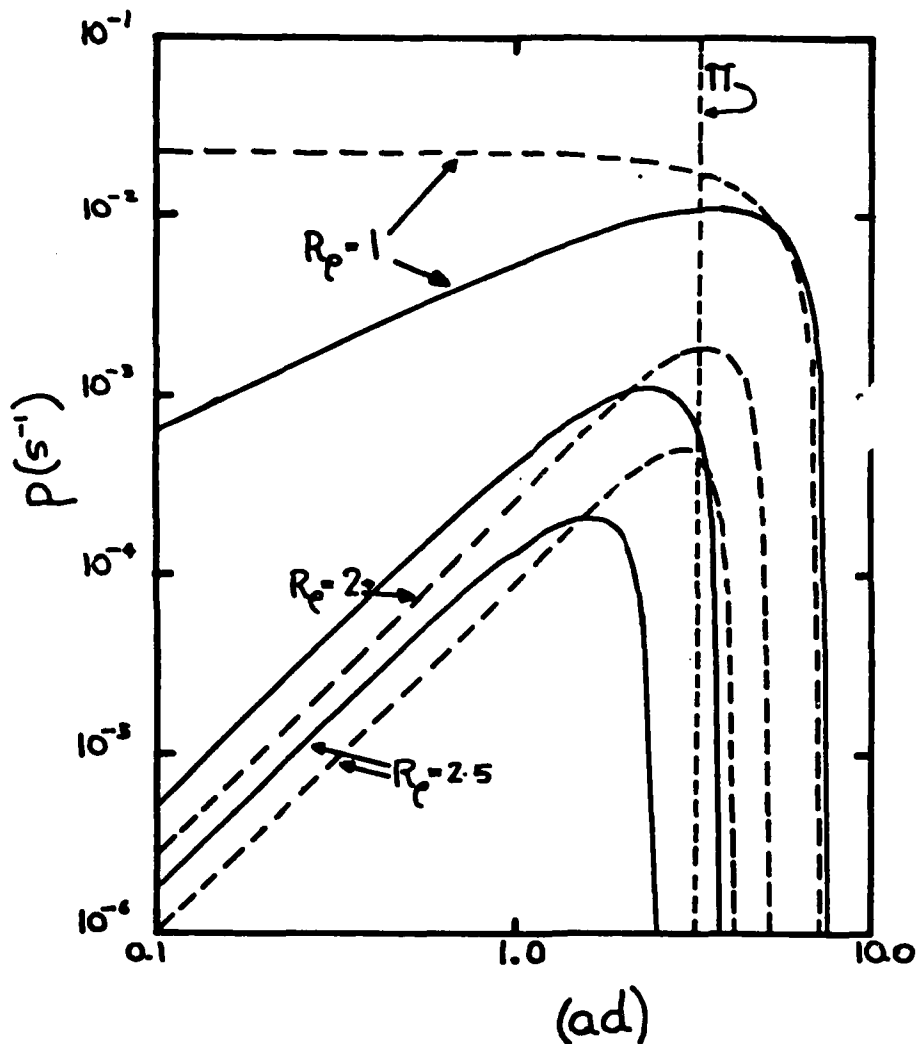Figure 5. Wavenumber growthrate spectra (a) Hele Shaw fingers (solid curves) (b) ordinary fingers (dashed curves). Conditions are as discussed in the text.

4.Linear theory for the evolution of a sharp interface

In the previous sections the possibility of producing salt fingers in a Hele Shaw cell have been investigated . By reworking the usual stability calculations for linear gradients between parrallel plates and the

infinitely long finger model with Hele Shaw dynamics it has been shown that high wavenumber cells limited by the diffusivity of the component with the smaller diffusing will be the favoured mode of convection in a Hele Shaw cell stratified in the finger sense. With reasonable experimental parameters the finger width should be large enough to make the Hele Shaw description of the flow valid. However these analyses have dealt with idealised geometries which are not fully realisable in laboratory experiments. The stability analysis to follow desribes the initial growth of instability from a sharp S interface with a background linear gradient of T. Such an initial system may be realised using a tank with a barrier at mid-depth which is withdrawn to begin the experiment. This kind of geometry has been utilised by Wooding (1969) in his experiments on Saffman-Taylor instability at an interface between two miscible fluids. It will be shown that in one limit $\alpha \bar{T}_z \to 0$, $\kappa_S \to 0$, the analysis predicts the correct behaviour for a Saffman-Taylor instability between immiscible fluids neglecting surface tension effects.

4.1 Stability analysis

The initial property profiles in the system to be analysed are shown on fig.**6**. There is a region of static instability close to the interface but the overall density distribution is stable.
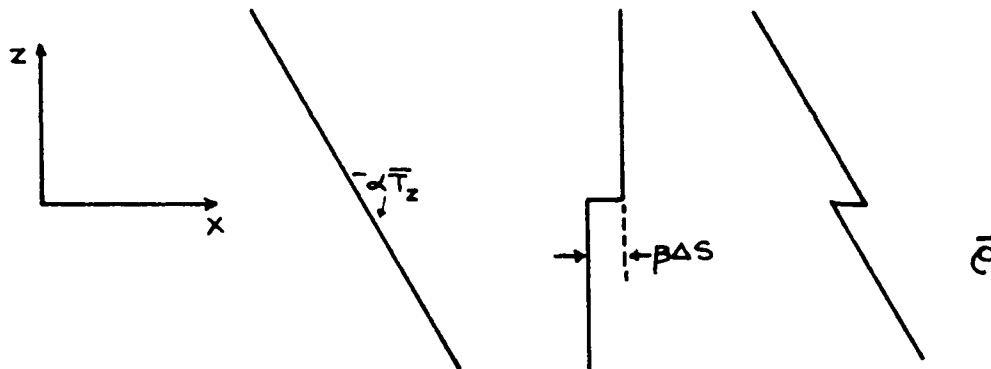
Figure 6. A sketch of the vertical T,S and ρ profiles of the system

Using the Hele Shaw equation (1) the momentum equations for the system become, after subtracting the hydrostatic part of the the pressure field from the z equation:

$$\mu u = -\frac{1}{\rho_o} P_x$$
$$\mu \omega = -\frac{1}{\rho_o} P_z + g\left(\alpha T - \beta S\right) \tag{17}$$

where the density has been written as:

$$\rho(x,z,t) = \rho_o\left(1 - \alpha \bar{T}_z - \alpha T(x,z,t) + \beta \Delta S H(z) + \beta S(x,z,t)\right)$$

and the perturbation quantities are small compared to ρ_o. $H(z)$ is the Heaviside step function. After cross differentiation to remove the pressure from the equations and using the continuity equation $\partial u/\partial x + \partial w/\partial z = 0$ (17) may be reduced to:

$$\mu \nabla^2 \omega = g\alpha T_{xx} - g\beta S_{xx} . \tag{18}$$

The conservation of T and S are described by (19), neglecting the advection of the temperature and salinity perturbations by the velocity field.

$$\frac{\partial T}{\partial t} + \omega \frac{\partial \overline{T_z}}{\partial z} = k_t \nabla^2 T$$

$$\frac{\partial S}{\partial t} + \omega \frac{\partial}{\partial z}(\Delta S H(z)) = k_s \nabla^2 S . \tag{19}$$

A major assumption made in writing the S equation is that the growthrate of any perturbation is fast enough so that the diffusion of the S step is not important. This assumption should be valid if the e-folding time for the fastest growing disturbance is greater than the characteristic time for the diffusion of S over a typical lengthscale of the problem d^2/κ_s. However the neglect of the term $\kappa_s \partial(\Delta S H(z))/\partial z^2$ means that this analysis cannot be used to investigate the marginal stability of the system.

Equations (18) and (19) are non-dimensionalised by substituting in the scaled variables $z'=z/d$, $t'=\kappa_t t/d^2$, $w'=dw/\kappa_t$, $T'=T/T_z d$ and $S'=S/\Delta S$. These substitutions result in the dimensionless equations (20):

$$\nabla'^2 \omega' = R_T' T_{xx} - R_S' S_{xx}$$

$$\left(\frac{\partial}{\partial t'} - \nabla'^2\right) T' = -\omega'$$

$$\left(\frac{\partial}{\partial t'} - \nabla'^2\right) S' = -\omega' \delta(z) . \tag{20}$$

where $R_T'=g\alpha\overline{T}_z d^2/\mu\kappa_t$, $R_S'=g\beta\Delta S d/\mu\kappa_t$ and $\delta(z)$ is the Dirac delta function. The lengthscale d is the spacing of the walls of the Hele Shaw cell and is physically significant because it is the lower limit to the scale of motion permitted before the assumption of two dimensional flow breaks down. The salinity step and plate spacing together define a salinity gradient. As long as the smallest scale of motion is larger than d then the fluid would see the salinity change as a discontinuity and its description as a delta function should be mathematically valid even if it is smeared out over a distance d.

Solutions are sought which are periodic in x and exponentially growing in time so that $\phi=\phi_o e^{pt+ix}$. Substituting for $\phi=(T,S,w)$ into (20) gives a set of equations:

$$\left(-a^2 - \frac{\partial}{\partial z^2}\right)\omega = -R_T T a^2 + R_S S a^2$$

$$\left(-a^2 - \frac{\partial}{\partial z^2}\right)T = -\omega \tag{21}$$

$$\left(p - \tau(-a^2 - \frac{\partial}{\partial z^2})\right)S = -\omega \delta(z) \ .$$

The primes have been dropped from the variables and the growthrate term in the temperature equation neglected. These equations are Fourier transformed in z:

$$\tilde{\phi}(\xi) = \int_{-\infty}^{\infty} \phi e^{i\xi z} dz$$

which results in a set of simultaneous equations in the Fourier transformed variables $\tilde{T}, \tilde{S}, \tilde{W}$:

$$\left(\xi^2 + a^2\right)\tilde{\omega} = R_T \tilde{T} a^2 - R_S \tilde{S} a^2$$

$$\left(\xi^2 + a^2\right)\tilde{T} = -\tilde{\omega}$$

$$p + \tau(\xi^2 + a^2)\tilde{S} = -\omega_o \tag{22}$$

where w_o is the vertical component of the velocity at the interface $w_o = w(x, 0, t)$. Using the temperature and salinity equations the first equation of (22) may be reduced to an equation for the Fourier transform of w:

$$\tilde{\omega} = \frac{\omega_o a^2 R_S (\xi^2 + a^2)}{\left[p + \tau(\xi^2 + a^2)\right]\left[(\xi^2 + a^2) - R_T\right]} \ . \tag{23}$$

The inverse of this transform is given by the integral:

$$\omega = -\frac{1}{2\pi} \int_{-\infty}^{\infty} e^{-i\xi z} d\xi$$

which may be evaluated by summing the residues at the poles of the transform in the complex plane. The result of this inversion is after some manipulation:

$$w = \frac{\omega_o a^2 R_S}{p^2 + a^2 \tau^2 R_T} \left[\frac{-p e^{z(\frac{p}{\tau} + a^2)^{\frac{1}{2}}}}{2(\frac{p}{\tau} + a^2)^{\frac{1}{2}}} + e^{zb} \frac{\left[(pb + ac\tau R_T^{\frac{1}{2}})\cos zc + (pc - ab\tau R_T^{\frac{1}{2}})\sin zc\right]}{(b^2 + c^2)} \right] \tag{24}$$

where: $b = \left(\frac{a^2 + a(a^2 + R_T)^{\frac{1}{2}}}{2}\right)^{\frac{1}{2}}$, $c = \left(\frac{-a^2 + a(a^2 + R_T)^{\frac{1}{2}}}{2}\right)^{\frac{1}{2}}$.

This expression was found by evaluating the residuals in the upper half of the complex plane and describes the velocity for $z \leq 0$. A similar expression for $z \geq 0$ could be found by evaluating the residuals in the lower half of the complex plane, however (24) contains sufficient information to find the dispersion relationship for the system. This was found by evaluating w at $z=0$ (25).

$$\frac{\tau^{\frac{1}{2}} p}{2(p + \tau a^2)^{\frac{1}{2}}} = \frac{p b + a c \tau R_T^{\frac{1}{2}}}{(b^2 + c^2)} - \frac{p^2 + a^2 \tau^2 R_T}{a^2 R_S} . \tag{25}$$

Before proceeding with the analysis its validity in the limit $\alpha \overline{T}_z \to 0$, $\kappa_s \to 0$ may be checked. Because the variables have been scaled by the thermal diffusivity (25) needs to be rewritten in dimensional variables to investigate this limit. The result of this procedure is:

$$p^* = \frac{g}{\mu} \beta \Delta S \, a^* \quad (s^{-1}). \tag{26}$$

This is the correct result for the Saffman-Taylor instability in this limit (Wooding, 1969). The growthrate is directly proportional to the buoyancy jump across the interface and inversly proportional to the effective viscosity. In this limit there is no limiting wavelength to the interfacial instability. If the two fluids are immiscible then surface tension acts to select a wavelength, for miscible fluids molecular diffusivity has the same effect.

Before proceeding (25) is rewritten in terms of the scaled variables $\hat{a}^2 = a^2/R_T$, $\hat{p} = p/R_T$ and $R_\rho = R_T/R_S$. The new expression is:

$$\frac{R_\rho (\hat{p}^2 + \hat{a}^2 \tau^2)}{\hat{a} R_T^{\frac{1}{2}}} = \frac{\hat{p} \left[\frac{\hat{a}^2 + \hat{a}(\hat{a}^2 + 1)^{\frac{1}{2}}}{2} \right]^{\frac{1}{2}} + \hat{a} \tau \left[\frac{-\hat{a}^2 + \hat{a}(\hat{a}^2 + 1)^{\frac{1}{2}}}{2} \right]^{\frac{1}{2}}}{(\hat{a}^2 + 1)^{\frac{1}{2}}}$$
$$- \frac{\hat{a} \hat{p} \tau^{\frac{1}{2}}}{2(\hat{p} + \tau \hat{a}^2)^{\frac{1}{2}}} . \tag{27}$$

Rather than expand this expression to find a polynomial for $\hat{p}$ as a function of $\hat{a}, \tau$, and R_ρ then solving the polynomial to find the growthrate the simpler approach of calculating R_ρ for a spectrum of $\hat{p}$ and $\hat{a}$ values at the conditions described in section 3 was adopted. The results of these calculations are shown on fig.7. Here again there is a limiting wavenumber $\hat{a} = \pi/R_T^{1/2}$. If the scale of the motion permitted by the linear stability analysis exceeds this value then the Hele Shaw cell approximation breaks down and some other type of 3-dimensional flow occurs. As can be seen from fig.7 this condition does not appear to be satisfied for the parameters tested although the analysis does predict a high wavenumber cut off and a wavenumber that maximises the growth rate. The prediction of this analysis is that, in contrast to the ideal geometry studied in section 3, the instabilities which grow on the sharp interface with these conditions could not be described as Hele Shaw salt fingers, at least in the initial stages of evolution described by the linear theory.
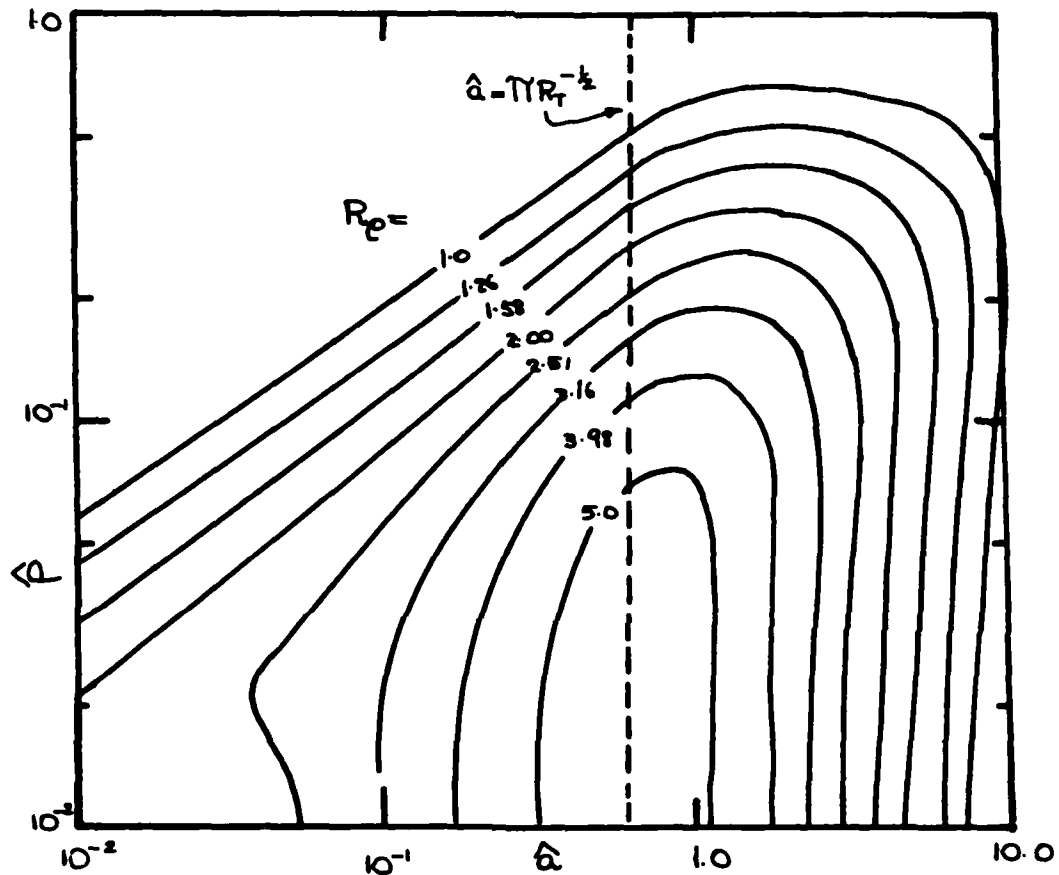
Figure 7. Wavenumber growthrate spectrum calculated from (27). $R_T=27.6$
The maximum wavenumber for which the Hele Shaw approximation is valid
is shown.

5.Conclusion

The possibility of producing salt fingers in a Hele Shaw cell has been
investigated. A linear stability analysis of linear gradients of T and S
maintained between perfectly conducting boundaries showed that under
supercritical conditions high wavenumber cells were favoured. The limiting
wavenumber was determined by the diffusivity of the slower diffusing
component. Using a model of infinitely long fingers it was shown that
fingers which satisfy the correct limits can exist with feasible laboratory
parameters.

It had been hoped that a model set up with supercritical initial
conditions would also show salt-finger like perturbations. With the same
overall physical parameters which were used in the long finger model the

analysis did not support this conclusion. Whether this is a correct physical result or a mathematical problem is not clear. It is hoped to clarify this problem experimentally.

Acknowledgements

I would like to thank George Veronis for his help with the work presented in this report. Thanks also to the staff members and particularly the other Fellows who made the summer such a lively and informative experience.

References

Baines P.G. and A.E. Gill (1969) On thermohaline convection with linear gradients. J.Fluid Mech. 37 289-306

Batchelor G.K. (1967) An introduction to fluid dynamics. Cambridge Univ. Press

Huppert H.E. and P.C. Manins (1973) Limiting conditions for salt fingering at an interface. Deep-Sea Res. 20 315-328

Huppert H.E. and J.S. Turner (1981) Double diffusive convection. J.Fluid Mech 106 299-329

Linden P.F. (1973) On the structure of salt fingers. Deep Sea Res. 20 325-340

Mullin J.W. (1972) Crystallisation. Butterworths pg480

Nield D.A. (1968) Onset of thermohaline convection in a porous medium. Water Resources Res. 4 553-560

Piacsek S.A. and J. Toomre (1980) Non evolution and structure of salt fingers. in Marine Turbulence ed. C.J. Nihoul. Elsevier 193-219

Sartory W.K. (1969) Instability of diffusing fluid layers. Biopolymers 7 252-263

Schmitt R.A. (1979) The growthrate of supercritical salt fingers. Deep-Sea Res. 26A 23-40

Stern M.E. (1960) The 'Salt Fountain' and thermohaline convection. Tellus 12 172-175

Stern M.E. (1975) Ocean circulation physics. Academic Press

Wooding R.A. (1969) Growth of fingers at an unstable diffusing interface in a porous medium or Hele Shaw cell. J.Fluid Mech 39 477-495

ZERO POTENTIAL VORTICITY FLOW ON AN EQUATORIAL β-PLANE

Yoshi-Yuki Hayashi

1. INTRODUCTION

The dynamics of the equatorial region are of great interest to both meteorologists and oceanographers, especially because of the recent El Nino-Southern Oscillation (for instance, Philander, 1983). The usual approach is linear wave theory on an equatorial β-plane, where the familiar Kelvin waves, mixed gravity-Rossby waves and so on play various important roles. Hence, for instance, movement of warm water pool on the equatorial ocean is described, in a linear framework, by combination of those waves. This involves the assumption that distortion of the stratification does not qualitatively alter the properties of the waves.

In the present study, however, we will consider the dynamics of a warm water pool from a different viewpoint, where the pool alters the wave structure completely. The method used here is almost parallel to the theory of coastal fronts (Stern, 1980; Paldor, 1983), where a constant potential vorticity field is assumed and the long wave approximation is employed. In this study, the equator is analogous to the coast. The configuration considered on the equatorial β-plane is shown in figure 1, where a fluid of uniform density flows above an infinite stationary fluid. From the peculiar nature of the equator, if the pool is symmetric then the value of the potential vorticity must be zero. This may also avoid the inertial instability near the equator (cf. Stevens, 1983).

The assumption of zero potential vorticity, combined with the long wave approximation, simplifies the mathematics considerably. However, the results obtained by this simplification are still interesting as an example of the equatorial dynamics in which the variation of currents and static stability (equivalent depth) completely changes the wave structure. In section 2, we will describe basic equations and the current structure. In section 3, linear stability will be discussed for zonally uniform flows with zero potential vorticity. In section 4, nonlinear theory for long waves will be considered and several nonlinear features of the movement of warm water pools will be derived.
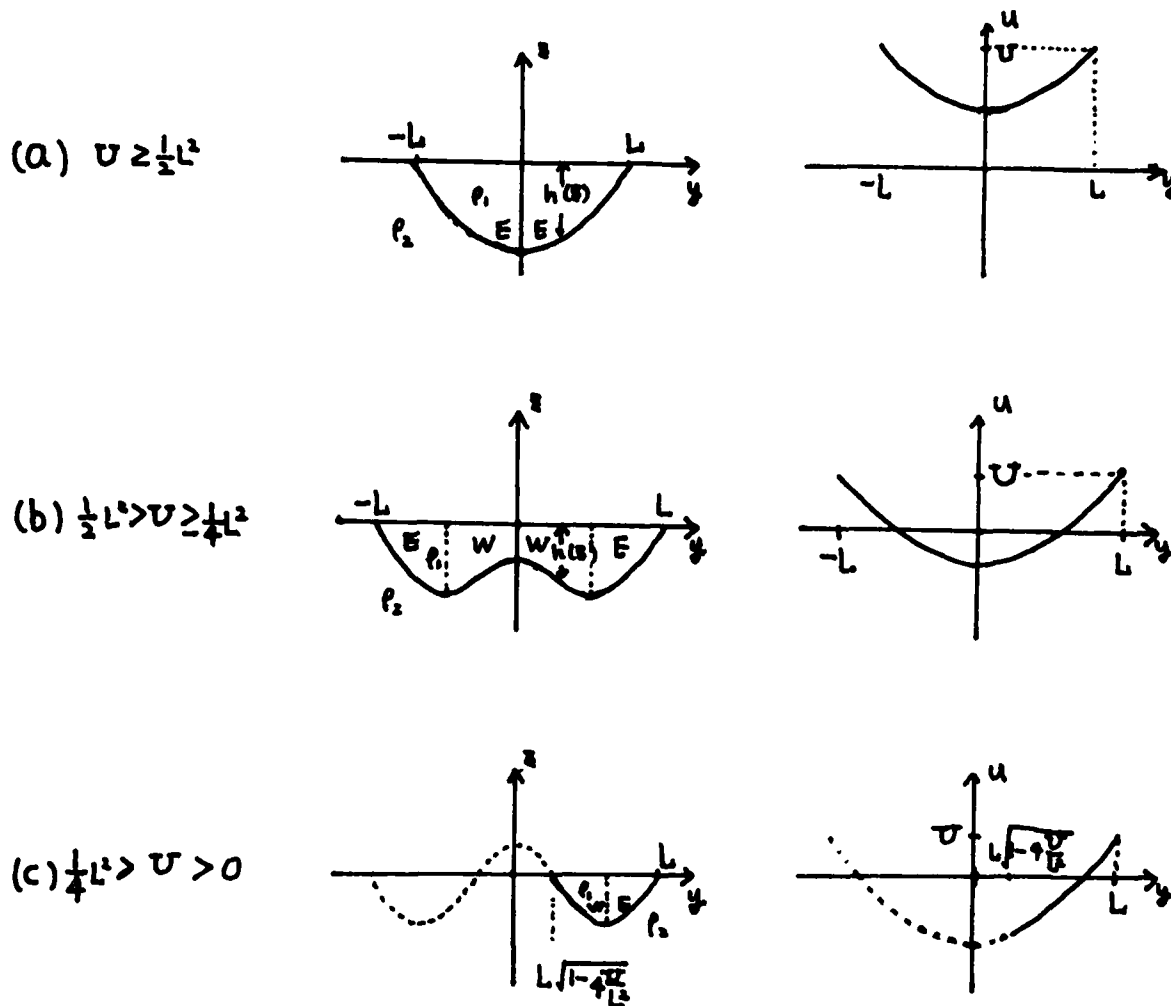
Figure 1: Three cases of warm water pool with zero potential vorticity on an equatorial β-plane: (a) whole region is covered with eastward flow, (b) westward flow exists on the equator, (c) water mass is separated from the equator.

2. BASIC EQUATIONS

The movement of the upper layer is governed by the equatorial shallow water equations:

$$u_t + uu_x + vu_y - yv = -h_x \tag{2.1a}$$

$$v_t + uv_x + vv_y + yu = -h_y \tag{2.1b}$$

$$h_t + (uh)_x + (vh)_y = 0 \tag{2.1c}$$

where u, v are the velocity components in the x (eastward), y (northward) directions respectively, and h is the thickness of the upper layer (figure 1). These quantities have been nondimensionalized by some length unit L*, the reduced gravity $g' = g(\rho_2 - \rho_1)/\rho_2$ and the north-south gradient of the Coriolis parameter, β. The dimensional forms of these quantities are obtained by

$$t^* = \frac{1}{\beta L^*} t \ , \quad \begin{pmatrix} x^* \\ y^* \end{pmatrix} = L^* \begin{pmatrix} x \\ y \end{pmatrix}, \quad \begin{pmatrix} u^* \\ v^* \end{pmatrix} = \beta L^{*2} \begin{pmatrix} u \\ v \end{pmatrix}, \quad h^* = \frac{\beta^2 L^{*4}}{g'} h$$

where * means a dimensional value.

The assumption of zero potential vorticity is:

$$y - u_y + v_x = 0 \tag{2.2}$$

By using this constraint, the momentum equations (2.1a,b) becomes

$$u_t = -(h + 1/2u^2 + 1/2\ v^2)x, \tag{2.3a}$$

$$v_t = -(h + 1/2u^2 + 1/2\ v^2)y. \tag{2.3b}$$

The long wave approximation which simplifies mathematics of zero potential vorticity flow is obtained by rescaling the time and x-directional unit as $(\beta L^*)^{-1} \rightarrow (\beta L^* \epsilon)^{-1}$ and $L^* \rightarrow L^* \epsilon^{-1}$ and also the northward velocity unit as $\beta L^{*2} \rightarrow \beta L^{*2} \epsilon$, where ϵ is a small parameter. Then the lowest order equations reduced from (2.1) are:

$$u_t + uu_x + vu_y - yv = -h_x, \tag{2.4a}$$

$$yu = -h_y, \tag{2.4b}$$

$$h_t + (hu)_x + (hv)_y = 0. \tag{2.4c}$$

The constraint of zero potential vorticity (2.2) becomes

$$y - u_y = 0, \tag{2.5}$$

which means that the zonal velocity should be quadratic in the y-direction;

$$u = 1/2(y^2 - L^2) + U, \tag{2.6}$$

where L is the coordinate of the front of water pool and U is the eastward velocity of the front (see figure 1). U and L are generally functions of x and t. From the expression (2.6) and the geostrophic balance (2.4b), the form of the upper layer in the y direction can be determined as

$$h = -1/8 \ [y^4 + 2(2U - L^2)y^2 + L^4 - 4U]. \tag{2.7}$$

Three typical cases of u and h are shown in figure 1. (a) ($U \gtrsim 1/2L^2$) is the case where no westward flow appears; (b) ($1/2L^2 > V \gtrsim 1/4L^2$) contains westward flow on the equator, and (c) ($1/4L^2 > U > 0$) is the case where a negative thickness appear near the equator which means the above profile is

valid within the region $\sqrt{L-4U} < y < L$ $(or -\sqrt{L-4U} > y > L)$ Note that those profiles of u and h determined from zero potential vorticity are symmetric around the equator.

3. LINEAR STABILITY OF ZERO POTENTIAL ZONAL FLOW

In this section, the linear stability of zero potential zonal flow, whose meridional profile are shown in figure 1, is investigated. The zonally uniform steady solution has been derived previously by Salmon (1982). The basic profiles considered are, from (2.6) and (2.7),

$$\overline{u} = 1/2(y^2 - 1) + \overline{\phi}, \tag{3.1}$$

$$\overline{h} = -1/8 \, [y^4 + 2(2\overline{\phi} - 1) \, y^2 + 1 - 4\overline{\phi} \,]. \tag{3.2}$$

where $-1 \le y \le 1$ when $\overline{\phi} \ge 1/4$, and $\sqrt{1 - 4\overline{\phi}} \le y \le 1$ when $0 < \overline{\phi} < 1/4$. Since the basic state is independent of x, the length unit L* has been chosen such that $\overline{L} = 1$ and $\overline{U}$ was redefined as $\overline{\phi L^2} = \overline{\phi}$, where $(\overline{})$ means the basic value. Griffiths, Killworth and Stern (1983) discusses the analogous f-plane stability problem and it is shown below that their results are obtained by taking the limit $\overline{\phi} \longrightarrow 0$.

When a small perturbation of the form $(u', v', h') = (\hat{u}, \hat{v}, \hat{h}) \, e^{i(x-ct)}$ is imposed on the above basic flow, the momentum and continuity equations (2.1) give the following linearized equations:

$$(\overline{u} - c)\hat{u} = -\hat{h}, \tag{3.3a}$$

$$\epsilon^2 ik(\overline{u} - c)\hat{v} + y\hat{u} = -\hat{h}_y, \tag{3.3b}$$

$$(\overline{u} - c)\hat{h} + h\hat{u} + \frac{1}{ik}(h\hat{v})_y = 0, \tag{3.3c}$$

where ϵ is a small parameter which is set to be zero for a long wave limit. (3.3a) and (3.3b) yield the vorticity equations,

$$(\overline{u} - c) \, (ik\epsilon^2\hat{v} - \hat{u}_y) = 0 \tag{3.4}$$

The solutions for $\overline{u} - c = 0$ are necessary just for the completeness of the eigenfunctions. Physically interesting solutions are obtained from $ik\epsilon^2\hat{v} - \hat{u}_y = 0$, which means that the perturbation vorticity also vanishes. Substituting (3.3a) and (3.4) into (3.3c), an eigenvalue problem is given as,

$$(\overline{h}\hat{u}_y)_y - \epsilon^2 k^2[\overline{h} - (\overline{u} - c)^2]\hat{u} = 0 \tag{3.5}$$

For the case of long wave limit ($\epsilon \ll 1$), the eigenfunctions and the eigenvalues are easily obtained. Since $\hat{u}$ becomes a constant from (3.4), the eigenvalue c is given by integrating (3.5) with the boundary condition $\overline{h} = 0$ at $y = \pm 1$ for $\overline{\phi} \ge 1/4$ or at $y = 1$ and $\sqrt{1 - 4\overline{\phi}}$ for $0 < \overline{\phi} < 1/4$.

$$0 = \hat{u} \int_{-1}^{1} [\overline{h} - (\overline{u} - c)^2] \, dy \qquad \text{for} \qquad \overline{\phi} \ge 1/4, \tag{3.6a}$$

$$0 = \hat{u} \int_{\sqrt{1-4\overline{\phi}}}^{1} [\overline{h} - (\overline{u} - c)^2] \, dy \qquad \text{for } 1/4 > \overline{\phi} > 0. \tag{3.6b}$$

which, with $\bar{h}$ and $\bar{u}$ given by (3.1) and (3.2), yields

$$c_{\pm} = \bar{\phi} - 1/3 \pm \sqrt{-4/45 + 1/3\,\bar{\phi}} \qquad \text{for} \quad \bar{\phi} \gtrsim 1/4, \qquad (3.7a)$$

$$= \frac{1}{1-\sqrt{1-4\bar{\phi}}} \left\{ \frac{1}{3}[\,3\bar{\phi}-1-\sqrt{1-4\bar{\phi}}\,(\bar{\phi}-1)\,] \right.$$
$$\left. \pm \left\{ \frac{8}{45}[\,2\bar{\phi}^3 - 7\bar{\phi}^2 + 6\bar{\phi} - 1 + \sqrt{1-4\bar{\phi}}\,(3\bar{\phi}^2 - 4\bar{\phi} + 1)\,]\right\}^{\frac{1}{2}} \right\} \qquad (3.7b)$$
$$\text{for} \quad 1/4 > \bar{\phi} > 0.$$

(3.7a) indicates that, when $1/4 \lesssim \bar{\phi} < 4/15$, c becomes complex and perturbation is over stable. In the expression (3.7b), the term within the square root can be shown always negative for $0 < \bar{\phi} < 1/4$. Figure 2 shows the real part and the imaginary part of c given by (3.7) as a function of $\bar{\phi}$. When the basic current is separated from the equator, it is always unstable. There remains unstable region when the upper layer is on the equator with sufficiently large westward flow. Or, in other words, if the thickness at the equator is less that 1/120, then that profile is unstable.

For $\bar{\phi} = 0$, (3.7b) gives c = 0, i.e. double roots, which means geometric instability. The limiting case $\bar{\phi} \longrightarrow 0$ can be regarded as the f-plane approximation in the mid latitude where β-effect is neglected. Actually, regarding $\bar{\phi}$ and 1-y is small in the expressions (3.1) and (3.2), they are approximated as,

$$\bar{u} \cong \bar{\phi} - (1 - y), \qquad (3.8a)$$

$$\bar{h} \cong \bar{\phi}(1 - y) - 1/2(1 - y)^2, \qquad (3.8b)$$

which are the profiles studied by Griffiths et al. (1983) and Paldor (1983a,b). Thus, we recover their results in the limit $\bar{\phi} \to 0$.

Griffiths et al. show that the basic state (3.8) is always unstable for short waves. (3.7) shows that β-effect destabilizes long waves.

There is another double root when $\bar{\phi} = 4/15$. For $\bar{\phi} > 4/15$, the flow is stable (neutral) for long waves. However, there remains a possibility that (3.6) is unstable for short waves. For a sufficiently large value of $\bar{\phi}$, the profile of figure 1a can be shown to be stable. Following the method used by Paldor (1983a), we define $\gamma \equiv \gamma_r + i\gamma_i = \bar{\phi} - c$. Multiplying (3.5) by $\hat{u}^*$ and integrating it from -1 to 1, then separating real and imaginary parts,

$$\int_{-1}^{1} dy\, \bar{h}\,|\hat{u}_y|^2 + \epsilon k^2 |\hat{u}|^2 [\,\bar{h} - (\bar{u}-\bar{\phi})^2 - 2(\bar{u}-\bar{\phi})\,\gamma_r - \gamma_r^2 + \gamma_i^2\,] = 0, \qquad (3.9a)$$

$$\gamma_i \int_{-1}^{1} dy\, k^2 |\hat{u}|^2 [(\bar{u}-\bar{\phi}) + \gamma_r] = 0. \qquad (3.9b)$$

If $\gamma_i \neq 0$, then from (3.9b), (3.9a) becomes

$$\int_{-1}^{1} dy\, \bar{h}\,|\hat{u}_y|^2 + \epsilon k^2 |\hat{u}|^2 [\,\bar{h} - (\bar{u}-\bar{\phi})^2 + \gamma_r^2 + \gamma_i^2\,] = 0. \qquad (3.10)$$

By the use of (3.1) and (3.2),

$$\bar{h} - (\bar{u}-\bar{\phi})^2 = \frac{1}{8}(1-y^2)(3y^2 + 4\bar{\phi} - 3), \qquad (3.11)$$

which means that when $\bar{\phi} \geq 3/4$ (3.10) cannot be satisfied. Hence, γ_i is zero for $\bar{\phi} \geq 3/4$.
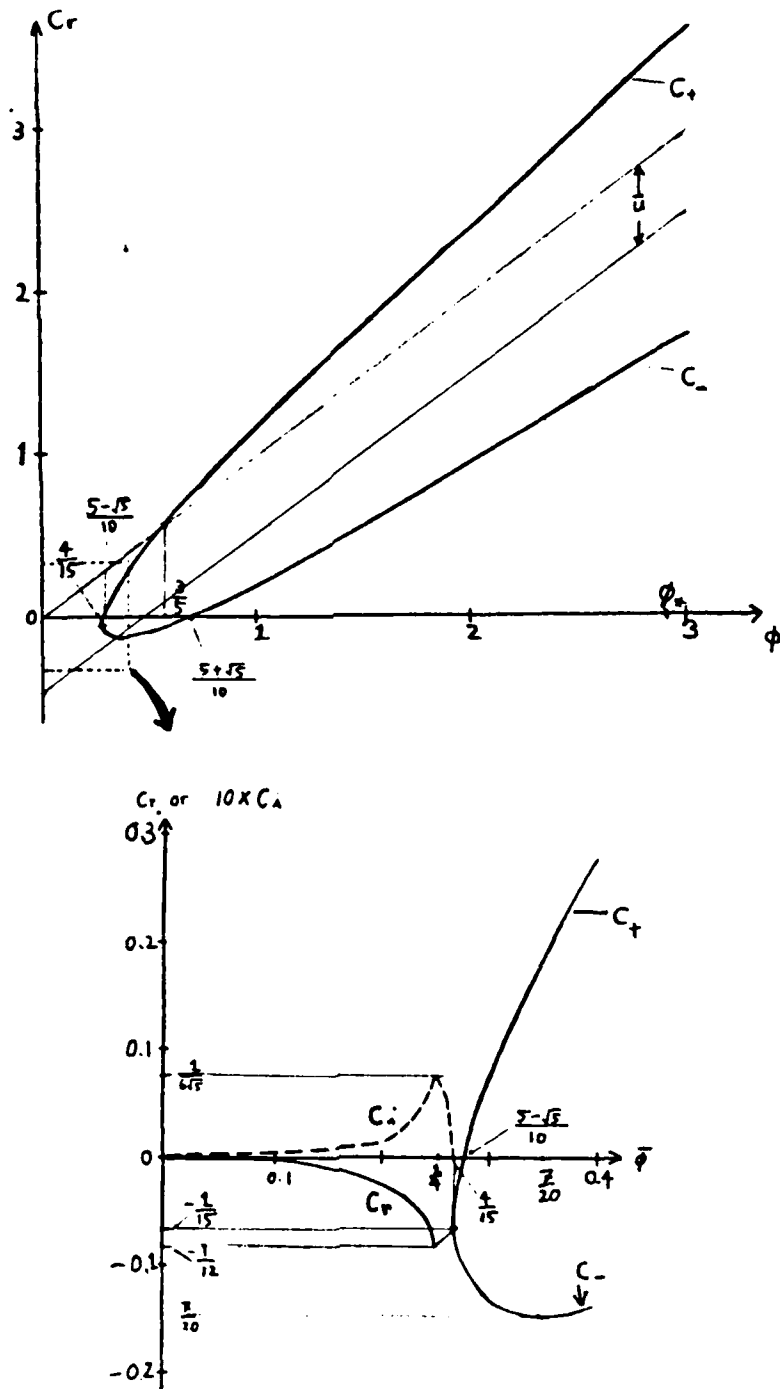
Figure 2: Complex phase speed of disturbance on a zero potential zonal flow at the long wave limit. Thin lines in the upper figure indicate the range of the basic zonal flow $\bar{u}$ which is $\bar{\phi} - 1/2 \sim \bar{\phi}$ for $\bar{\phi} \geq 1/4$ and $-\bar{\phi} \sim \bar{\phi}$ for $\bar{\phi} < 1/4$.

The long wave structures in the stable region are shown schematically in figure 3. Since $\hat{u}$ is constant, the anomaly in thickness, $\hat{h}$, is determined roughly by the sign of $\bar{u} - c$ in (3.3a). It can be seen from figure 2 that

$$\bar{u} - c_+ < 0 \quad \text{for } -1 < y < 1 \qquad \text{when} \qquad \bar{\phi} \gtrsim 3/5,$$

$$\begin{array}{ll} < 0 & |y| < y_* \\ & \text{for} \\ > 0 & 1 \geq |y| > y_* \end{array} \qquad \text{when} \qquad 3/5 > \bar{\phi} > 4/15,$$

$$\bar{u} - c_- > 0 \quad \text{for } -1 < y < 1 \qquad \text{when} \qquad \bar{\phi} > 7/20,$$

$$\begin{array}{ll} < 0 & |y| < y_* \\ & \text{for} \\ > 0 & 1 \geq |y| > y_* \end{array} \qquad \text{when} \qquad 7/20 > \bar{\phi} > 4/15,$$

where y_* is a certain value determined by c. From the functional form of $\bar{u}$ (3.1), $|\bar{u} - c|$ is an increasing (decreasing) function of $|y|$ when $\bar{u} - c > 0$ (< 0). Hence, when $\bar{\phi} > 3/5$, the c_+ solution has a structure similar to the equatorial Kelvin wave which is trapped on the equator, while $\bar{\phi} > 3/20$ c_- solution has the larger amplitude in $\hat{h}$ at the north and south boundary than on the equator. It is "trapped" at the free boundaries. The structure for small $\bar{\phi}$ (but still larger than 4/15) is a mixture of both patterns.

The basic flow given by (3.1) and (3.2) is marginal for barotropic instability according to the usual criterion of quasi-geostrophic flow (Gill, 1982). The necessary condition for shear instability is the existence of inflection point in the velocity profile (Rayleigh's inflection-point theorem). The present basic state does not have an inflection point because it has zero potential vorticity. It is also marginal in inertial instability (Charney, 1973). When the effect of gravity is neglected, the necessary condition is $f(f - u_y) < 0$, where f is the Coriolis parameter. Either criterion, however, is not applicable, because the disturbance is not quasigeostrophic or the effect of gravity (variation of thickness) cannot be neglected.

Shear instability, in which vorticity disturbance plays an important role, is not likely to occur, since the basic state is zero potential vorticity and stretching or shrinking due to the change of thickness does not cause any vorticity anomaly. On the other hand, there may be a possibility of generalizing the criterion of inertial instability. The simple criterion $f(f - u_y) < 0$ does not include the change of angular momentum due to the variation of thickness.

Figure 4d shows the schematic structure of unstable wave for $\bar{\phi} < 1/4$. Since c is complex, there is a phase lag between u' and h'. The configuration is similar to $O(\epsilon)$ correction in long wave expansion (Griffiths, et al., 1982) where undisturbed flow is strictly antisymmetric and undisturbed depth profile is symmetric. The deformation of symmetry due to β- terms has a similar effect to that of short wave disturbance.
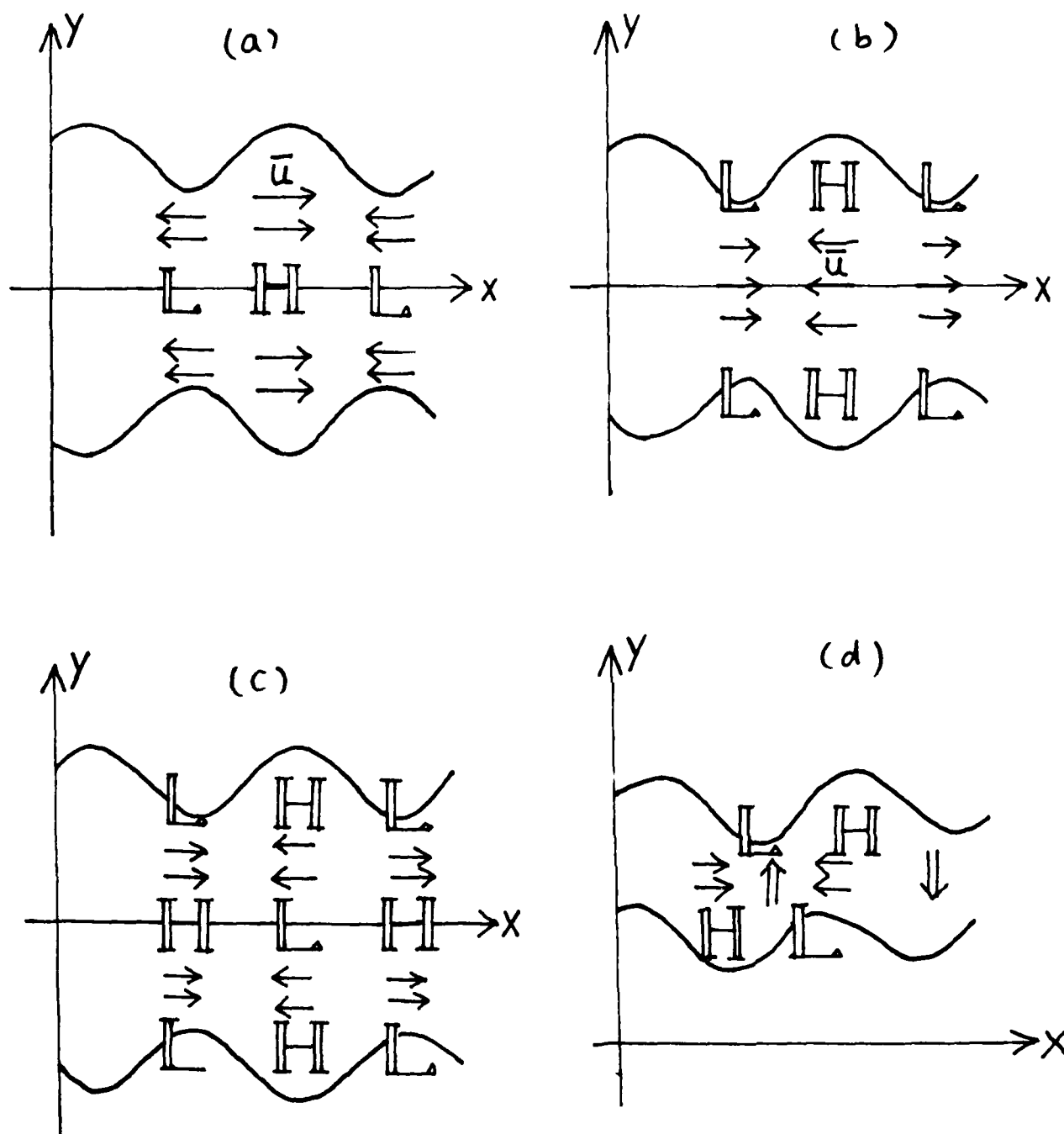
Figure 3: Structures of long waves: (a) c_+ solution with $\bar{\phi} > 3/5$, (b) c_- solution with $\bar{\phi} > 7/20$, (c) c_+ solutions with $3/5 > \bar{\phi} > 4/15$ or c_- solution with $4/15 < \bar{\phi} < 3/20$, (d) unstable solution for $\bar{\phi} < 1/4$.
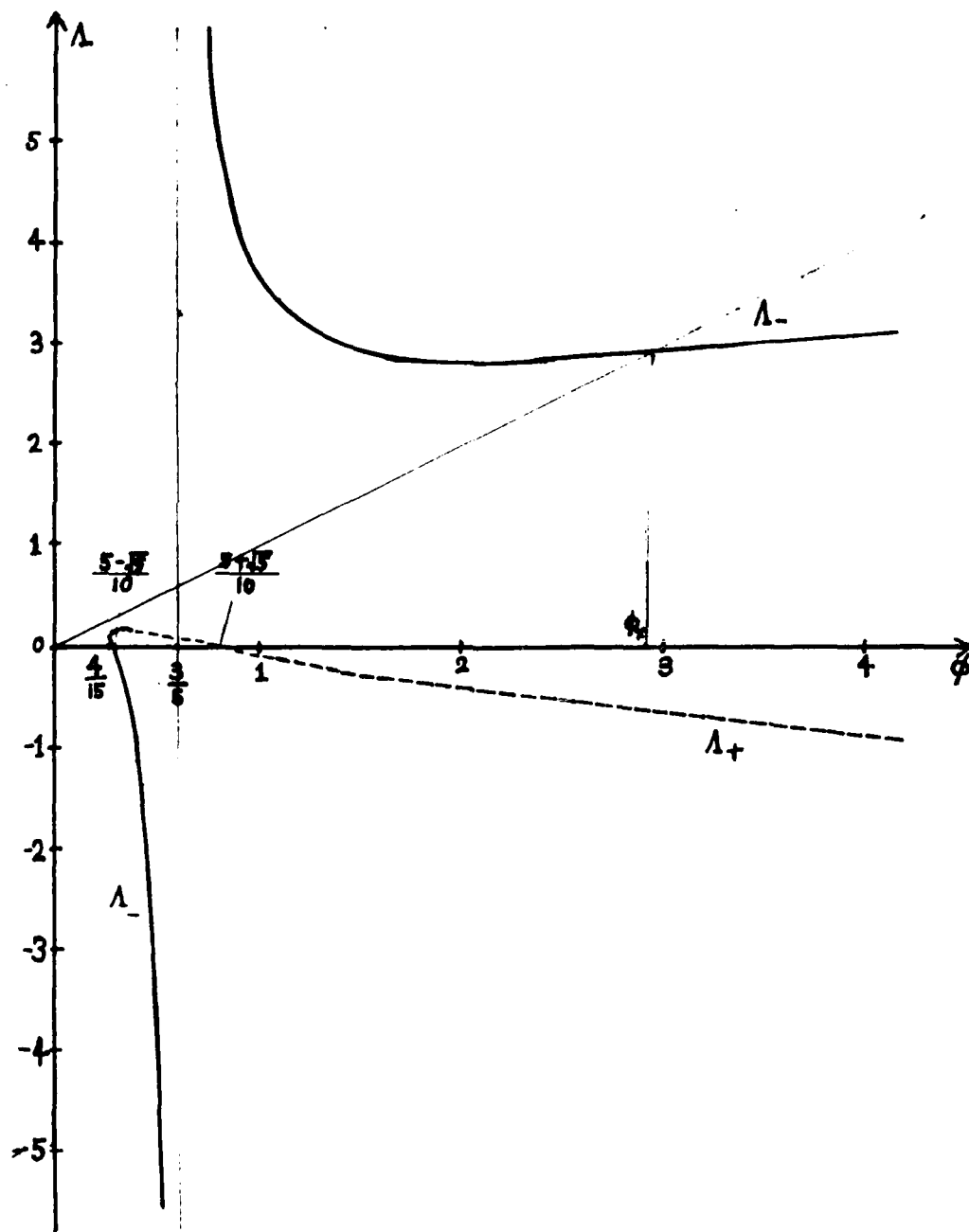
Figure 4: Plot of the function $\Lambda_{\pm}(\phi)$.

4. NONLINEAR WAVE PROPAGATION

In this section we will consider the nonlinear motion of equatorial water masses with zero potential vorticity within the framework of the long wave approximation. Following the method of Stern (1980) and Stern et al. (1982), we will derive the equations for $U(x,t)$ and $L(x,t)$ in (2.6) and (2.7). Since, as mentioned in section 2, the long wave approximation determines the y-dependence of zero potential vorticity flow completely, it remains to determine the integral constants U and L. From the discussion of the previous section we will deal with the profile $U > 4/15L^2$ where the zonally uniform solution is neutral to long wave disturbances. In the range $4/15L^2 < U < 3/4L^2$ there may be unstable short wave disturbances, but for the moment we ignore this possibility.

From the y-momentum equation (2.3b), the Bernoulli function is:

$$h + \tfrac{1}{2}(u^2 + v^2) = - \int_L^y v_t \, dy + \tfrac{1}{2}(U^2 + V^2)$$

$$= - \partial_t \int_L^y v \, dy - L_t V + \tfrac{1}{2}(U^2 + V^2), \qquad (4.1)$$

where $V \equiv v|_u = L_t + UL_x$. From the vorticity constraint (2.2), the x gradient of Bernoulli function becomes

$$(h + \tfrac{1}{2}u^2 + \tfrac{1}{2}v^2)_x = -\partial_t \int_L^y (u_y - y) \, dy + V_t L_x - V_x L_t + \tfrac{1}{2}(U^2 + V^2)_x$$

$$= - u_t + U_t - \tfrac{1}{2}(L^2)_t + V_t L_x - V_x L_t + \tfrac{1}{2}(U^2 + V^2)_x \quad (4.2)$$

substituting (4.2) into x-momentum equation (2.3a)[*],

$$U_t + UU_x - LL_t = -V_t L_x + L_t V_x - 1/2(V^2)_x \qquad (4.3)$$

The right hand side of (4.3) is neglected when long wave approximation is made (V is one order smaller quantity). The lowest order equation for this approximation is

$$U_t + UU_x - LL_t = 0 \qquad (4.4)$$

Another equation for U and L is derived from mass conservation (2.4c). Substituting the expressions (2.6) and (2.7) for u and h into (2.4c) and integrating with y from -1 to 1, we have

$$2 \left(-\tfrac{1}{15}L^5 + \tfrac{1}{3}UL^3 \right)_t + 2 \left(\tfrac{1}{35}L^7 - \tfrac{1}{5}UL^5 + \tfrac{1}{3}U^2L^3 \right)_x = 0. \qquad (4.5)$$

It is essential to have explicit solutions of u and h to obtain (4.5) and it is easy with the long wave approximations. Note the net transport is given by the term within the second parentheses which is positive when

$$U/L^2 > 3/10(1 + \sqrt{1/21})$$

and negative when

$$1/4 < U/L^2 < 3/10(1 + \sqrt{1/21}).$$

---

[*] (4.3) can be derived without using the constraint of zero potential vorticity.

For the later convenience, we define $M \equiv L^2$ and $\phi \equiv U/L^2 = U/M$. Equations (4.4) and (4.5) become

$$U_t + M\phi \, U_x - \tfrac{1}{2} M_t = 0, \tag{4.6a}$$

$$-\tfrac{1}{3} U_t + (\tfrac{1}{5} - \tfrac{2}{3}\phi) M U_x + (\tfrac{1}{6} - \tfrac{1}{2}\phi) M_t + (-\tfrac{1}{10} + \tfrac{1}{2}\phi - \tfrac{1}{2}\phi^2) M M_x = 0. \tag{4.6b}$$

Then, for a given initial condition of the warm water pool $U = U(x,o)$ and $L = L(x,o)$, its time development can be calculated from (4.6) so long as the long wave approximation is valid. It is useful to consider Riemann invariants of (4.6) to understand the nonlinear features of this system (Whitham, 1974). Since (4.6a,b) are quasi-linear first order equations, an appropriate linear combination gives the equations of the Riemann invariant which is constant on a characteristic:

$$(\partial_t + r_\pm \partial_x) R_\pm (U, M) = 0, \tag{4.7}$$

where $r_\pm$ are the characteristic speeds given by

$$r_\pm = M(\phi - \tfrac{1}{3} \pm \sqrt{-\tfrac{4}{45} + \tfrac{1}{3}\phi}), \tag{4.8}$$

and $R_\pm$ are the Riemann invariants given by the differential equation

$$\left(\frac{dU}{dM}\right)_\pm = \frac{3 - 10\phi \pm 15\phi\sqrt{-\tfrac{9}{45} + \tfrac{1}{3}\phi}}{6 - 10\phi} \equiv \Lambda_\pm(\phi). \tag{4.9}$$

The characteristic speeds are exactly the same as the phase speeds derived in section 3 (figure 2) except for the factor M which is set to be 1 in the linear stability arguments. The values of $\Lambda_\pm(\phi)$ are plotted in figure 4 and several curves $R_+(U,M) = 0$ are shown in figure 5. The gross features of the curves are qualitatively similar to those obtained by Stern (1980), where coastal fronts on an f-plane are considered. Since the equator plays a role as a coast because of the symmetry of both hemispheres, the similar results are almost expected.

It is informative to consider the development of warm water whose initial condition is strictly on a certain Riemann invariant. (This is the case of a simple wave.) Let $R_1(U,M) = 0$ (1 is either + or -) at $t = 0$. Then, from (4.7),
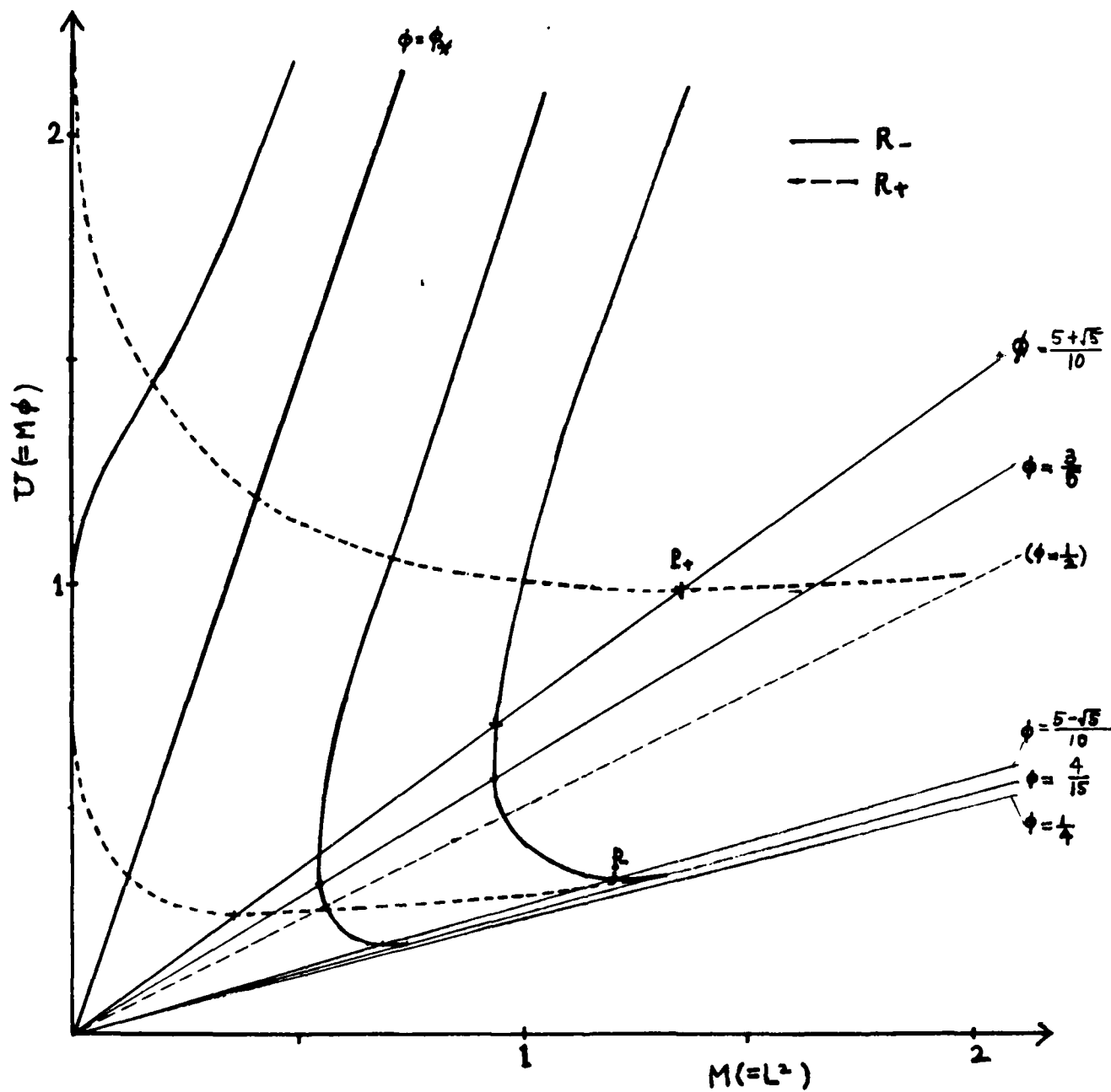
$$(\partial_t + r_1 \partial_x) R_1(U, M) = 0, \tag{4.10}$$

Figure 5: Several lines of Riemann invariants $R_\pm(U,M) = 0$.

which means that $R_1(U,M) = 0$ is satisfied at subsequent times. There is a functional relation $U = U(M)$, which yields, from the other equation of (4.7),

$$(R_{2,v} U_M + R_{1M}) (\partial_t + r_2 \partial_x) M = 0,$$

i.e.

$$\begin{cases} (\partial_t + r_2 \partial_x) M = 0, \\ (\partial_t + r_2 \partial_x) U = 0, \end{cases} \tag{4.11}$$

where 2 means the other one of + or -. M and U remain constant along the other characteristic lines. The shape of warm pool propagates at the speed r_2, (figure 6). Note that the values of U and M are bounded by the ranges given by initial condition because they are conserved along $dx/dt = r_2$. They remain on the segment of Riemann invariant curve determined at $t = 0$. From (4.6a) and (4.9), r_2 is given by

$$r_2 = \frac{U \Lambda_1}{\Lambda_1 - \frac{1}{2}}. \tag{4.12}$$
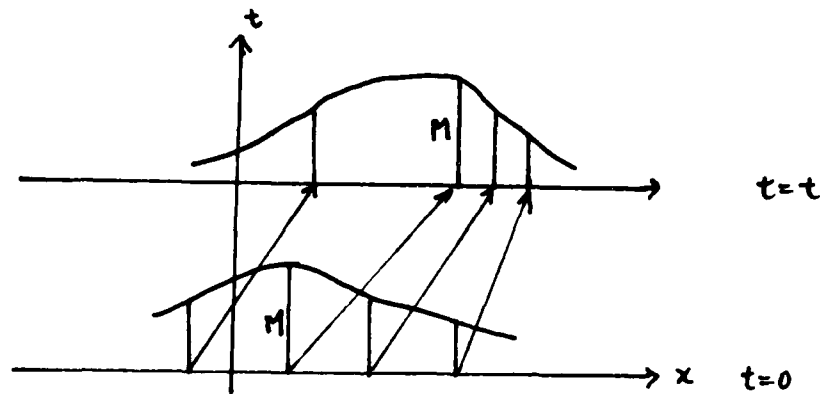

Figure 6: Characteristic lines and time evolution of wave patterns.

Particular values of Λ, ϕ, r are summarized in Table 1, from which qualitative arguments about the behavior of simple waves can be made.

TABLE 1

R_1	ϕ	Λ_1	r_2^*
R_-	$\phi \to \infty$	$\Lambda_- \to \frac{1}{2\sqrt{3}}\sqrt{\phi}$	$r^* \to \phi$
	$\phi > \phi_*$	$\Lambda_- > 0 \ (\Lambda_- - \phi < 0)$	$r_+^* > 0, \ r_{+,\phi}^* > 0$
	$\phi = \phi_* = 2.7071$	$\Lambda_- = \phi_*$	—————
	$\phi_* > \phi > \frac{3}{5}$	$\Lambda_- > 0$	$r_+^* > 0$
	$\phi = \frac{3}{5}$	$\begin{array}{c} \Lambda_- = +\infty \\ \hline \Lambda_- = -\infty \end{array}$ $(\Lambda - \phi > 0)$	$r_+^* = \frac{3}{5} \quad r_{+,\phi}^* > 0$
	$\frac{3}{5} > \phi > \frac{5-\sqrt{5}}{10}$	$\Lambda_- < 0$	$r_+^* > 0$
	$\phi = \frac{5-\sqrt{5}}{10}$	$\Lambda_- = 0$ $(\Lambda - \phi < 0)$	$r_+^* = 0$
	$\frac{5-\sqrt{5}}{10} > \phi > \frac{4}{15}$	$\Lambda_- > 0$	$r_+^* < 0$
R_+	$\phi \to \infty$	$\Lambda_+ \to -\frac{1}{2\sqrt{3}}\sqrt{\phi}$	$r_-^* \to \phi$
	$\phi > \frac{5+\sqrt{5}}{10}$	$\Lambda_+ < 0$	$r_-^* > 0$
	$\phi = \frac{5+\sqrt{5}}{10}$	$\Lambda_+ = 0$	$r_-^* = 0$
	$\frac{5+\sqrt{5}}{10} > \phi > \frac{4}{15}$	$\Lambda_+ > 0$	$r_-^* < 0$

The condition for the occurrence of wave steepening, and breakdown of long wave theory, is given by

$$\partial_x r_2 < 0 \qquad (4.13)$$

From the expression of r (4.8), (4.13) becomes

$$[r_2^* + r_{2,\phi}^* (\Lambda_1 - \phi)] M_x < 0 \qquad (4.14)$$

where $r^*(\phi) \equiv r/M$. Figure 7 shows particular structures for which (4.14) is easily evaluated.

Figure 7a is the case where the Riemann invariant of the single wave is the straight line shown in figure 5, that is $R_-(U,M) = U - \phi_* M$. ϕ_* is the solution of $\Lambda_-(\phi) = \phi$. There is no solution like that for the other kind of Riemann invariant. For this wave (4.14) becomes simply

$$r_+^* (\phi_*) M_x < 0. \qquad (4.15)$$

Since $r_+^* > 0$ in the neighborhood of $\phi = \phi_*$, wave steepening occurs to the east of the maximum value of M. It is shown later that steepening can be balanced with the shortwave dispersion in a certain case.

Figure 7b is the case where the maximum value of M is on the line $\phi = \frac{5+\sqrt{5}}{10}$ for R_+ (say, P_+ in figure 5) or $\phi = \frac{5-\sqrt{5}}{10}$ for R_- (say, P_- in figure 5). Figure 2 shows $r_- = 0$ on these points $P_\pm$, which means the position of the maximum value of M does not move. Figure 4 indicates $\Lambda_\pm = 0$ on $P_\pm$ so that (4.14) becomes

$$- \phi \, r_{2,\phi}^* \, M_x < 0 \qquad (4.16)$$

As seen from figure 2, $r_{2,\phi}^*$ in the neighborhood of $P_\pm$, the condition for wave steepening becomes $M_x > 0$, that is, steepening occurs to the west of the maximum value of M. This situation corresponds to the "blocking wave" discussed by Stern (1980). However, in the present case (see figure 7), $M = M_{max}$ does not block the net transport. (It is positive for $\phi = (5+\sqrt{5})/10$ and negative for $\phi = (5-\sqrt{5})/10$.

(a) $R_- = U - \phi^* M$
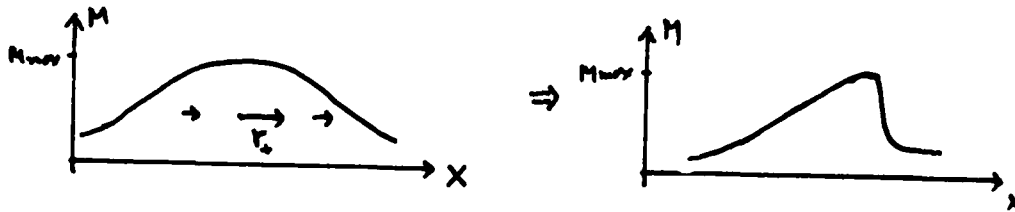
(b) $\Lambda_\pm = 0 \left(\phi = \dfrac{5 \pm \sqrt{5}}{10} \text{ at } M = M_{MAX} \right)$
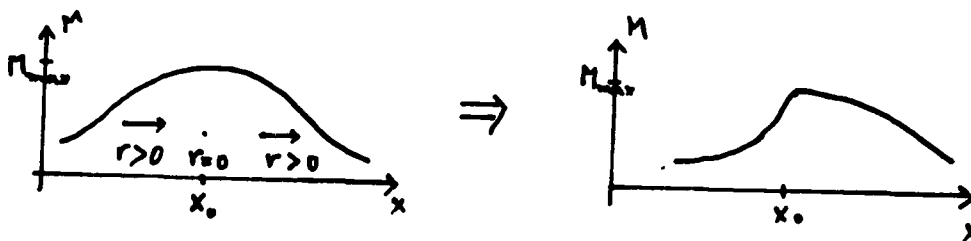
Figure 7: Steepening of particular waves.

As for bore waves and edge waves (Stern, 1980), figures 2, 3 and 4 have similar properties to those of his results. The wave front is considered as a limit where $M \rightarrow 0$ and $\phi \rightarrow \infty$ keeping the value of $U = M\phi$ finite. The propagating speed of the wave front becomes $r_\pm = U$ by this limiting. Since

$$r_\pm^* + r_{\pm,\phi}^* (\Lambda_\mp - \phi) \longrightarrow \pm \frac{1}{2\sqrt{3}} \sqrt{\phi} \qquad \text{as } \phi \rightarrow \infty , \qquad (4.17)$$

the bore wave corresponds to the R- front and the edge wave corresponds to the R_+ front as shown in figure 8.

(a) R_- (bore front)
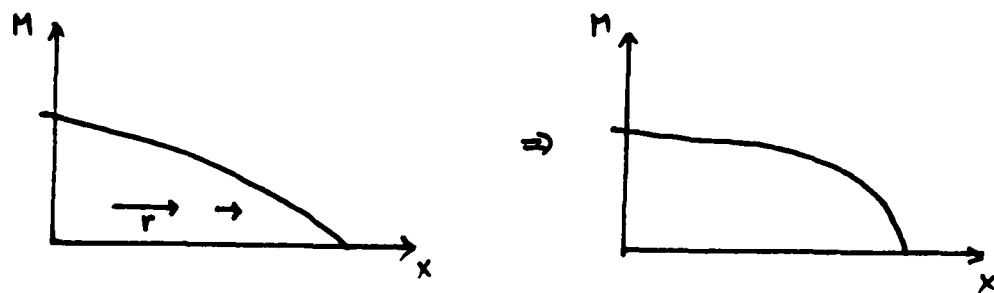
(b) R_+ (edge front)

Figure 8: Wave fronts for + solutions and - solutions.

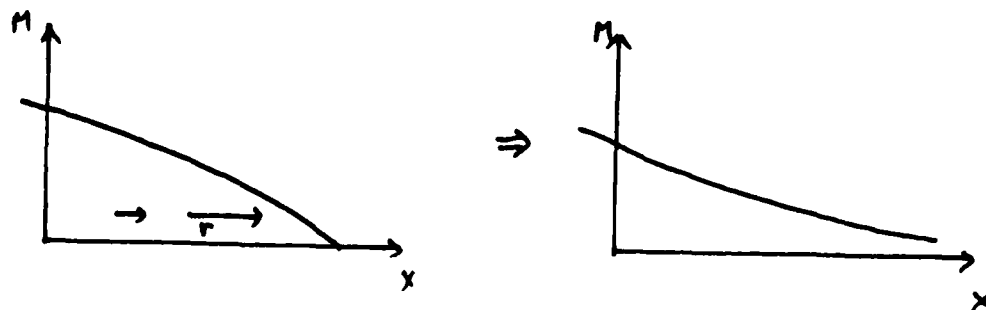It is possible to obtain a short wave correction for simple waves. Assume, to the first order in the long wave limit, U and M are on a Riemann invariant $R_1(U,M) = 0$. Since the time development of U and M are given by (4.11) to this order, the right hand side of (4.10) is calculated iteratively by (4.11) and the functional relation $R_1(U,M) = 0$. The result is

$$U_t + U U_x - \tfrac{1}{2} M_t = \tfrac{1}{8}(\phi - r_2^*)[-2\Lambda_1 + 3 r_2^* + \phi + 4 r_{2,\phi}^*(\Lambda_1 - \phi)](M_x)^3$$

$$- \tfrac{1}{4}(\phi - r_2^*)^2 M M_x M_{xx},$$

(4.18)

Since

$$U_t + U U_x - \tfrac{1}{2} M_t = (\Lambda_1 - \tfrac{1}{2})(\partial_t + r_2^* M \partial_x) M,$$

(4.16) can be written as

$$(\partial_t + r_2^* M \partial_x) M = \tfrac{1}{8} \frac{\phi - r_2^*}{(\Lambda_1 - \tfrac{1}{2})}(-2\Lambda_1 + 3 r_2^* + \phi + 4 r_{2,\phi}^*(\Lambda_1 - \phi)](M_x)^3$$

$$- \tfrac{1}{4}\frac{(\phi - r_2^*)^2}{(\Lambda_1 - \tfrac{1}{2})} M M_x M_{xx}.$$

(4.19)

Hence, for a certain parameter range, the right hand side of (4.19) may balance the steepening caused by the advection due to $r_2^* M$.

Actually, for a simple case where the Riemann invariant is the straight line of figure 5

$$R_-(U, M) = U - \phi_* M$$

(4.20)

on which

$$\left| \begin{array}{l} \Lambda_-(\phi) = \phi_* \quad (\text{constant}), \\[2mm] r_+^*(\phi) = \dfrac{\phi_* \Lambda_-}{\Lambda_- - \tfrac{1}{2}} = \dfrac{\phi_*^2}{\phi_* - \tfrac{1}{2}}. \end{array} \right.$$

(4.21)

(4.19) becomes, for this Riemann invariant,

$$M_t + r_+^* M M_x = -A M_x^3 - B M M_x M_{xx}$$

(4.22)

where

$$\begin{aligned} r_+^* &= 3.507, \\ A &= 0.2394, \\ B &= 0.03796. \end{aligned}$$

A travelling wave solution can be obtained by substituting $\partial_t \to -c\,\partial_x$. Rescaling M, ∂_x and ∂_t by

$$\left| \begin{array}{l} M \propto A^{1/3} r_+^{*-1}, \\[2mm] \partial_x \propto A^{-1/3} r_+^*, \\[2mm] \partial_t \propto A^{-2/3} r_+^*, \end{array} \right.$$

(4.23)

so, (4.22) becomes

$$(M - C) M_x = -M_x^3 - B/A\, M M_x M_{xx}$$

(4.24)

where $B/A = 6.31$.

The first integral of (4.24) is

$$M = M_0 \tag{4.25a}$$

or

$$M'^2 - \alpha M^{-2A/B} + 2A/2A+B \, M = C \tag{4.25b}$$

where M_0 and α are integral constants. Although the solutions of (4.25b) can be classified in three types according to $\alpha \gtrless 0$ (figure 9), the relevant solution of (4.24) which is appropriate to the present assumption is $\alpha < 0$ case with small maximum M'.

$\cdot \alpha = 0$

$$M = \frac{2A+B}{2A} C - 4\left(\frac{2A}{2A+B}\right)^2 (x-x_0)^2$$
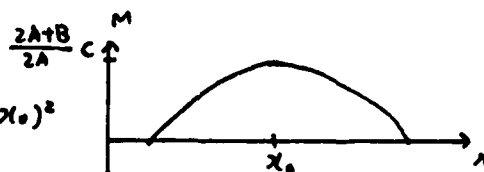
$\cdot \alpha > 0$

$$M'^2 + \left(\frac{2A}{2A+B} M - \alpha M^{-\frac{2A}{B}}\right) = C$$
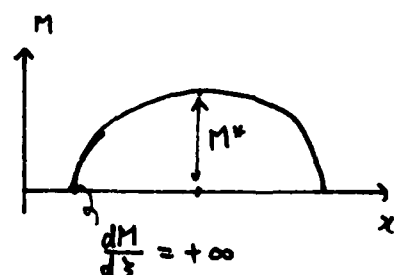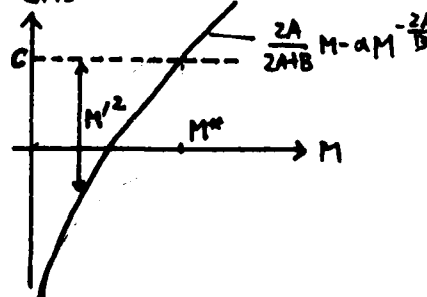
$\cdot \alpha < 0$

$$M'^2 + \left(\frac{2A}{2A+B} M - \alpha M^{-\frac{2A}{B}}\right) = C$$
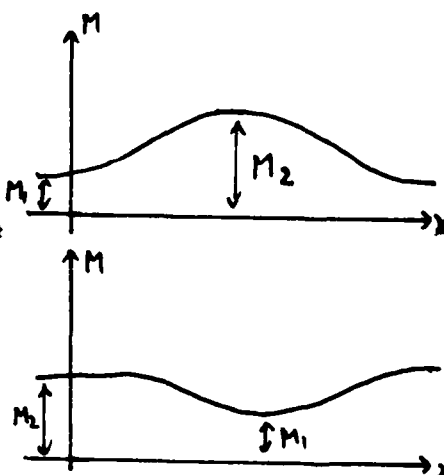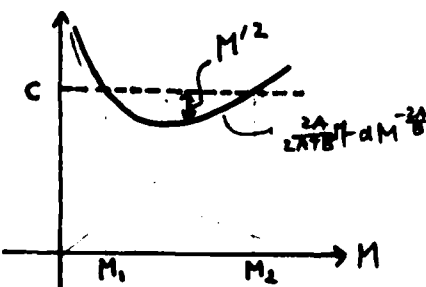
Figure 9: Classification of solutions of (4.25b). For $\alpha = 0$, M becomes quadratic in x. For $\alpha \neq 0$, M' is determined by "potential" 2A/2A+B M $- \alpha M^{-2A/B}$ with given "energy" c. Schematic shapes for M are drawn in the right figures of each case. For $\alpha < 0$, it is possible to connect "outer solution" M' = 0 (4.25a).

Since the equation (4.24) was derived under the assumption that U and M are to the first order on a Riemann invariant, the wave solution must propagate at the corresponding characteristic speed which is M by the scaling (4.23). This means M should be near c (M is almost uniform). Hence, this is the travelling wave solution of a small amplitude disturbance on the zonal current of the type shown in figure 1a.

5. SUMMARY

Several behaviors of zero potential vorticity flow on an equatorial β plane were considered by using long wave approximation.

The linear stability analysis of zonal basic flow (figure 1) revealed the unstable region for long waves. It was shown that, when the flow is separated from the equator ($U < 1/4L^2$), it is always unstable because of β-effect. The limiting case $U/L^2 \rightarrow 0$, which corresponds to f-plane approximation, causes vanishing imaginary part of c and coincides with the results of former investigators. For the parameter region $U \gtrsim 1/4L^2$, there also exists an unstable region for long waves, that is, $4/15 > U/L^2 > 1/4$. The basic flow in this region has a strong westward flow and a shallow thickness on the equator. For the parameter range $U/L^2 \gtrsim 3/4$, it was shown that the basic zonal flow is stable for any linear disturbances. There remains a possibility of short wave instability for the basic state with $3/4 > U/L^2 \gtrsim 4/15$.

Nonlinear theory employing the Riemann invariants and the characteristic speeds were also considered. The behaviors of simple waves, which consist of only a single Riemann invariant, were confirmed to be almost similar to those of coastal zero potential vorticity flow discussed by Stern (1980). Occurrence of wave steepening was qualitatively shown for idealistic cases. Solutions corresponding to bore and wedge fronts also exist. It was indicated that the next order correction of the long wave limit can be carried out along the characteristic line of the Riemann invariant obtained as a first order solution. For the particular Riemann invariant $R_- = U - \phi_* M$, the correction terms suppress the wavebreaking due to the steepening.

The nonlinear theory considered here was restricted to the behavior of simple waves. An interesting problem to be solved next may be a time development of warm water pool, which is not composed of a single Riemann invariant.

REFERENCES

Charney, J.G., 1973. Planetary fluid dynamics. Dynamic Meteorology, P. Morel, Ed., D. Reidel.

Gill, A.E., 1982. Atmosphere-Ocean Dynamics. Academic Press.

Griffiths, R.W., P.D. Killworth and M.E. Stern, 1982. Ageostrophic instability of ocean currents. J. Fluid Mech., 117, 343-377.

Killworth, P.D. and M.E. Stern, 1982. Instabilities on density-driven boundary currents and fronts. Gephys. Astrophys. Fluid Dynamics, 22, 1-28.

Paldor, N., 1983a. Stability and stable modes of coastal fronts. Geophys. Astrophys. Fluid Dynamics, 27, 217-228.

_____, 1983b. Weakly nonlinear frontal waves. Woods Hole Oceanog. Inst. Tech. Rept. WHOI-83-41, 245-256.

Philander, S.G.H., 1983. El Nino Southern Oscillation phenomena. Nature, 302, 245-301.

Salmon, R., 1982. The shape of the main thermocline. J. Phys Oceanogr., 12, 1458 - 1479.

Stern, M.E., 1980. Geostrophic fronts, bores, breaking and blocking waves. J. Fluid Mech., 99, 687-703.

_____, J.A. Whitehead and B.-L. Mua, 1982. The intrusion of a density current along the coast of a rotating fluid. J. Fluid Mech., 123, 237-265.

Stevens, D.E., 1983. On symmetric stability and instability of zonal mean flows near the equator. J. Atmos Sci., 40, 882-893.

FINITE AMPLITUDE DOUBLE-DIFFUSIVE CONVECTION
CAUSED BY COUPLED MOLECULAR DIFFUSION

Ross C. Kerr

ABSTRACT

This study examines the effect on a double-diffusive system of the combination of both finite amplitude convection and significant coupled molecular diffusion. Using a minimum Fourier series representation of the pertubation fields, we find that steady finite amplitude convection can exist for nonzero values of the cross diffusion coefficients. We show that the effect of these coefficients becomes significant when their magnitude is comparable to the conventional diffusion coefficients. We also show that finite amplitude convection can occur in a fluid where both property gradients are stabilizing for relatively small and negative values of these cross-diffusion coefficients.

1. Introduction

The phenomenon of double-diffusive convection in a fluid layer, where two scalar fields (such as heat and salinity concentration) affect the density distribution in a fluid, has become increasingly important and widely studied in recent years. Linearized stability theory (Baines and Gill, 1969) shows that the first occurrence of instability can take the form of oscillations rather than direct convection if the component with the smaller diffusivity is stably stratified, provided that R_s (a dimensionless measure of the stratification) is sufficiently large. Finite amplitude convection was examined by Veronis (1965). He showed that when oscillatory convection was possible there was always an unstable branch of steady solutions bifurcating from the static state at larger values of R (a measure of the destabilizing gradient of the component with the larger diffusivities). He then used a truncated Fourier series representation of the solutions to obtain a guide to the finite-amplitude behavior of the steady solution branch. The results of his minimal modal expansion suggested that steady motion at finite amplitude could occur at values of R much less than that predicted by linearized theory. Subsequent studies by Veronis (1968) and Huppert and Moore (1976) showed, however, that this result is only valid if the ratio of diffusivities (τ) is very small and R_s is large.

Recently, McDougall (1983) has extended the linear stability analysis of double-diffusive convection by including two cross-diffusion flux terms. He showed that, with a sufficiently large coupled diffusion effect, that either the finger or diffusive modes of double-diffusive convection may occur even when both components make the fluid's density gradient statically stable. His analysis ignored, however, the possibility that stable finite amplitude diffusive convection might occur in this system. As a first step towards the understanding of finite amplitude effects in this system, we examine the effect of cross diffusion on the minimal representation study of Veronis (1965).

2. Formulation of the Problem

Following McDougall (1983), we consider a layer of fluid of depth d, confined between two horizontal boundaries which maintain a contrast in fluid properties between the boundaries of ΔT and ΔS. We consider both T and S

to be solute concentrations and that positive ΔT and ΔS imply that the concentrations are greater at the lower boundary. We consider only two-dimensional instabilities from a rest state which has uniform T and S gradients between the plates. The equations for the conservation of T and S are

$$\frac{\partial T}{\partial t} + \underset{\sim}{U} \cdot \nabla T = D_{11} \nabla^2 T + D_{12} \nabla^2 S \tag{1}$$

$$\frac{\partial S}{\partial t} + \underset{\sim}{U} \cdot \nabla S = D_{22} \nabla^2 S + D_{21} \nabla^2 T , \tag{2}$$

where D_{12} and D_{21} are the two cross-diffusion terms and U is the two-dimensional velocity vector. We assume that T diffuses more rapidly than S, so that $D_{11} > D_{22}$. The Navier-Stokes equation for momentum conservation is

$$\frac{\partial U}{\partial t} + \underset{\sim}{U} \cdot \nabla \underset{\sim}{U} = -\frac{1}{\rho_0} \nabla p + \underset{\sim}{g} \frac{\rho}{\rho_0} + \nu \nabla^2 \underset{\sim}{U} . \tag{3}$$

Here $\underset{\sim}{g}$ is the acceleration due to gravity, ρ_0 is the reference density and ρ is the fluid density, given by

$$\rho = \rho_0 \left(1 + \alpha T + \beta S \right) . \tag{4}$$

Taking a horizontal coordinate x and vertical coordinate z (defined positive upwards), we define a stream function ψ by

$$\underset{\sim}{U} = \left(\frac{\partial \psi}{\partial z} , -\frac{\partial \psi}{\partial x} \right) . \tag{5}$$

We also introduce nondimensional variables so that deviations of T and S from the linear vertical gradients ($-\Delta T/d$ and $-\Delta S/d$) are normalized by ΔT and ΔS respectively and the timescale is $d^2 D_{11}^{-1}$. Equations (1), (2) and (3) can then be expressed in dimensionless (dashed) variables:

$$\left(\frac{\partial}{\partial t'} - \nabla^2 \right) T' - (DUFOUR) \frac{R_s}{R} \nabla^2 S' + \frac{\partial \psi'}{\partial x'} = \mathcal{J}(\psi', T') \tag{6}$$

$$\left(\frac{\partial}{\partial t'} - \tau \nabla^2 \right) S' - (SORET) \frac{R}{R_s} \nabla^2 T' + \frac{\partial \psi'}{\partial x'} = \mathcal{J}(\psi', S') \tag{7}$$

$$\left(\frac{1}{\sigma} \frac{\partial}{\partial t'} - \nabla^2 \right) \nabla^2 \psi' = R \frac{\partial T'}{\partial x'} + R_s \frac{\partial S'}{\partial x'} + \frac{1}{\sigma} \mathcal{J}(\psi', \nabla^2 \psi') \tag{8}$$

where the Jacobian is defined by $\mathcal{J}(f, g) = \left[\frac{\partial f}{\partial x} \frac{\partial g}{\partial z} - \frac{\partial f}{\partial z} \frac{\partial g}{\partial x} \right]$, and $\tau = D_{22}/D_{11}$, $\sigma = \nu/D_{11}$, $DUFOUR = D_{12}\alpha/D_{11}\beta$, $SORET = D_{21}\beta/D_{11}\alpha$, $R = g\alpha\Delta T d^3/\nu D_{11}$ and $R_s = \frac{g\beta\Delta S d^3}{\nu D_{11}}$.

We choose stress-free boundary conductions so that

$$\psi' = \frac{\partial^2 \psi'}{\partial z'^2} = T' = S' = 0 \qquad at \ z' = 0, 1. \qquad (9)$$

3. Finite Amplitude Solution using a Minimal Representation

In order to examine the finite amplitude solution to equations (6) to (8) subject to the boundary conditions (9) we expand the variables in a Fourier series and adopt the minimal representation of Veronis (1965):

$$\psi' = \pi^{-2}\alpha^{-1} A_1(t') \sin \pi \alpha x' \sin \pi z'$$

$$T' = \pi^{-2}\alpha^{-1} \left[A_2(t') \sin 2\pi z' + A_3(t') \cos \pi \alpha x' \sin \pi z' \right]$$

$$S' = \pi^{-2}\alpha^{-1} \left[A_4(t') \sin 2\pi z' + A_5(t') \cos \pi \alpha x' \sin \pi z' \right]. \qquad (10)$$

The equations that determine the A_i are derived by substituting the set (10) into equations (6) to (8):

$$\dot{A}_1 = -\sigma \pi^2 (\alpha^2 + 1) A_1 + \frac{\sigma \alpha}{\pi(\alpha^2 + 1)} (R A_3 + R_s A_5)$$

$$\dot{A}_2 = -4\pi^2 \left[A_2 + DUFOUR \frac{R_s}{R} A_4 \right] + \frac{A_1 A_3}{2}$$

$$\dot{A}_3 = -\pi^2 (\alpha^2 + 1) \left[A_3 + DUFOUR \frac{R_s}{R} A_5 \right] - \pi\alpha A_1 - A_1 A_2 \qquad (11)$$

$$\dot{A}_4 = -4\pi^2 \left[\tau A_4 + SORET \frac{R}{R_s} A_2 \right] + \frac{A_1 A_5}{2}$$

$$\dot{A}_5 = -\pi^2 (\alpha^2 + 1) \left[\tau A_5 + SORET \frac{R}{R_s} A_3 \right] - \pi\alpha A_1 - A_1 A_4$$

These equations (with no cross-diffusion terms and R negative) were intergrated numerically by Veronis (1965). He observed that the system has a finite amplitude steady state solution which can exist for values of -R much less than the value required for linear oscillatory instability. After verifying these observations using a third-order accurate numerical scheme (with $\tau = 1/80$, $R_s = 10^3$ and a timestep $\Delta t < 10^{-4}$) I examined the effect on the system of varying SORET and DUFOUR. The main conclusion of this study was that finite amplitude steady state solutions of (11) were found to exist for some values of R, whatever the values of SORET and DUFOUR. In particular, solutions exist for positive values of R if either SORET or DUFOUR is sufficiently negative.

The steady solutions can be found by setting the left-hand sides of equations (11) equal to zero:

$$A_2 = \frac{A_1 A_3}{8\pi^2} - (DUFOUR)\frac{R_s}{R} A_4$$

$$A_3 = \frac{-\pi\alpha A_1 \left[1 + DUFOUR\frac{R_c}{R} - \frac{(\alpha^2+1)^2 A_1^2}{8\alpha^2 R}\frac{DUFOUR}{DET}\right]}{\pi^2(\alpha^2+1)(1-DUFOUR) + \frac{A_1^2}{8\pi^2}\frac{(D + DUFOUR)}{DET}}$$

$$A_4 = \frac{A_1}{8\pi^2}\left[\frac{A_5 - A_3 (SORET)R/R_s}{DET}\right] \tag{12}$$

$$A_5 = \frac{-RA_3}{R_s} + \frac{\pi^3(\alpha^2+1)^2}{\alpha R_s} A_1$$

where we define $R_c = \pi^4(\alpha^2+1)^3\alpha^{-2}$ and $DET = \tau - (DUFOUR)(SORET)$. The amplitude A_1 is given by an equation which can be simplified by defining $A = A_1^2/[8\pi(\alpha^2+1)]$, $R_s^* = R_s/R_c$ and $R^* = R/R_c$:

$$A^2 + A\left[(1+\tau^2+ 2\, DUFOUR\, SORET) + R^*(1 + SORET) + R_s^*(1 + \right.$$

$$\left. DUFOUR\right] + DET\left[DET + R^*(\tau - SORET) + R_s^*(1 - DUFOUR)\right] = 0. \tag{13}$$

For finite amplitude solutions to exist, we require the two roots of (13) to be positive, so that the coefficient of A in (13) must be negative and the constant term must be positive. If the magnitudes of both R^* and R^*_s are large, these conditions are satisfied if DET > 0 (see Appendix) and

$$\tau R^*\left[\tau^{-1} + \frac{\beta D_{21}}{\alpha D_{22}}\right] + R_s^*\left[\tau + \frac{\alpha D_{12}}{\beta D_{11}}\right] < 0 \qquad ,(|R^*|, |R_s^*| \gg 1). \tag{14}$$

4. Comparison of the Results with those of McDougall (1983)

Equation (14) can be compared with the conditions found from the linear stability theory of McDougall (1983) (equations (24) and (25)) for the onset

both oscillatory 'diffusive' instabilities

$$\tau \, R^{*}\left(\frac{\sigma+1}{\tau} + \frac{\beta D_{21}}{\alpha D_{22}}\right) + R_{s}^{*}\left(\tau + \sigma + \frac{\alpha D_{12}}{\beta D_{11}}\right) < 0 \,, \quad \left(|R^{*}|, |R_{s}^{*}| \gg 1\right), \quad (15)$$

and monotonic 'finger' instabilities

$$\tau \, R^{*}\left(1 - \frac{\beta D_{21}}{\alpha D_{22}}\right) + R_{s}^{*}\left(1 - \frac{\alpha D_{12}}{\beta D_{11}}\right) < 0 \,, \quad \left(|R^{*}|, |R_{s}^{*}| \gg 1\right). \quad (16)$$

In the case of both T and S stably stratified, equation (14) shows that finite amplitude diffusive instability requires

$$\frac{\beta D_{21}}{\alpha D_{22}} < -\tau^{-1} \quad \text{or} \quad \frac{\alpha D_{12}}{\beta D_{11}} < -\tau \,. \quad (17)$$

This result can be compared with the conditions required from (15) for the infinitesimal oscillatory 'diffusive' instability

$$\frac{\beta D_{21}}{\alpha D_{22}} < -\left(\frac{\sigma+1}{\tau}\right) \quad \text{or} \quad \frac{\alpha D_{12}}{\beta D_{11}} < -\tau-\sigma \,. \quad (18)$$

Conditions (17) are always less restrictive than condition (18). The negative sign of both quantities reflects the fact that a stable gradient of one property must induce a larger unstable gradient of the other property in order to produce finite amplitude convection. One way of viewing the conditions (17) is to consider what happens if convection is able to completely mix up the fluid so that at some point in time, T, S and U are zero. As the gradients of T and S reestablish themselves due to diffusion from the perfectly conducting boundaries, the equation for the diffusion of density can be found by combining equation (4) with equations (1) and (2) (where U = 0):

$$\frac{1}{\rho_{c}}\frac{\partial \rho}{\partial t} = \left(\alpha D_{11} + \beta D_{21}\right)\nabla^{2}T + \left(\alpha D_{12} + \beta D_{22}\right)\nabla^{2}S \,. \quad (19)$$

This equation can potentially correspond to the negative diffusion of density (and hence to instability and further convection), if either of the bracketed coefficients on the right of (19) are negative, i.e. if conditions (17) are satisfied.

The stability boundaries implied by equations (14), (15) and (16) may be compared by plotting them for fixed R^{*}/R_{s}^{*}, subject to the static stability constraint $R^{*} + R_{s}^{*} > 0$. We see immediately that the three stability boundaries are parallel lines through the points $(1, 1)$, $(-\tau, -\tau^{-1})$ and $(-(\sigma+\tau), -(\sigma+1)/\tau)$. These are shown in figure 1. Figure 1(a) has stable distributions and T and S and the slope of the stability boundaries is negative. Figure 1(b) has $R^{*} > 0$ and $R_{s}^{*} < 0$, the distribution of properties that is normally conducive to fingers, and the slope of the boundaries is between 0 and τ^{-1}. Figure 1(c) has $R^{*} < 0$ and $R_{s}^{*} > 0$, the distribution of properties that is normally conducive to the diffusive instability, and the slope of the stability boundaries is greater

(a)
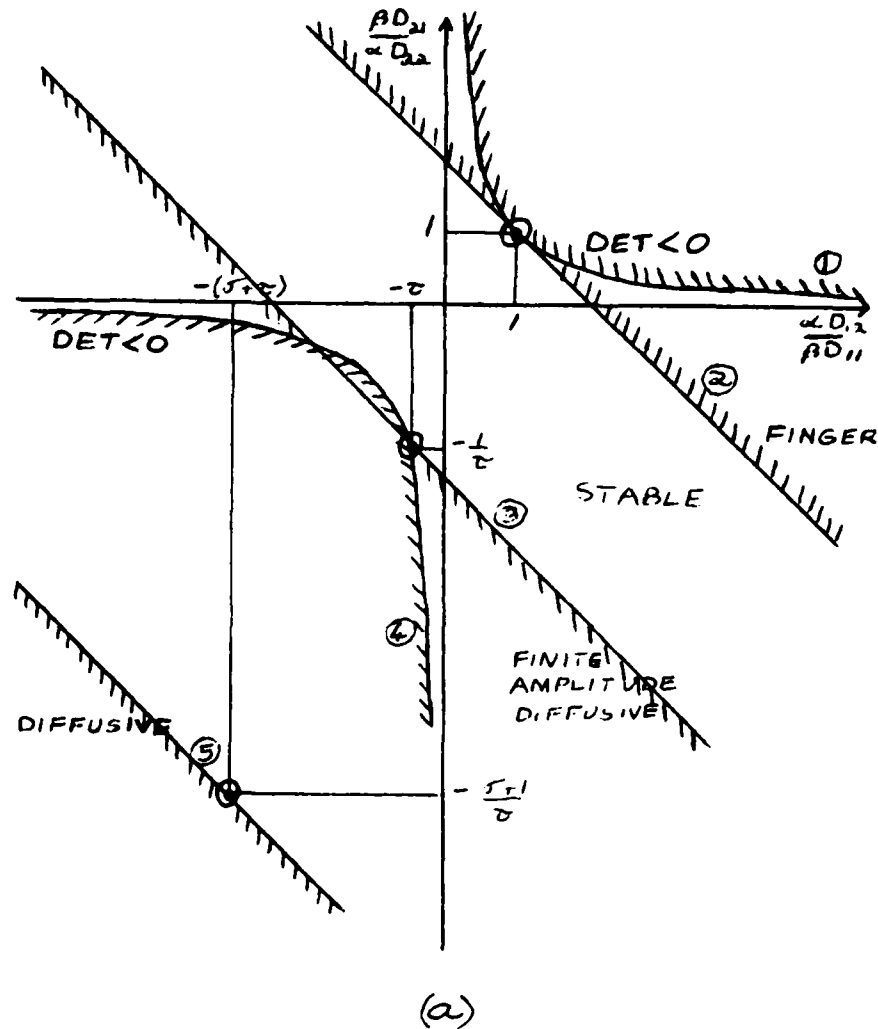
Figure 1. A sketch of the stability boundaries as a function of $\beta D_{21}/\alpha D_{22}$ and $\alpha D_{12}/\beta D_{11}$ for different ranges of R and R_S. (a) has R > 0 and R_S > 0 (i.e. both components stably distributed); (b) has R > 0 and R_S < 0 (i.e. an apparently "finger" property distribution); (c) has R < 0 and R_S > 0 (i.e. on apparently "diffusive" property distribution). The boundaries (2) and (5) are the respective linear stability boundaries found by McDougall (1983) for the finger and oscillatory diffusive instability. Boundaries (1) and (4) are the instability boundaries given by the condition DET < 0 (see the Appendix). Boundary (3) is the instability boundary for finite amplitude diffusive convection using the minimal representation (equation (14)). The slope of parallel boundaries (2), (3) and (5) is equal to $R_S/\tau R$.

FIGURE 1 (b) and (c)

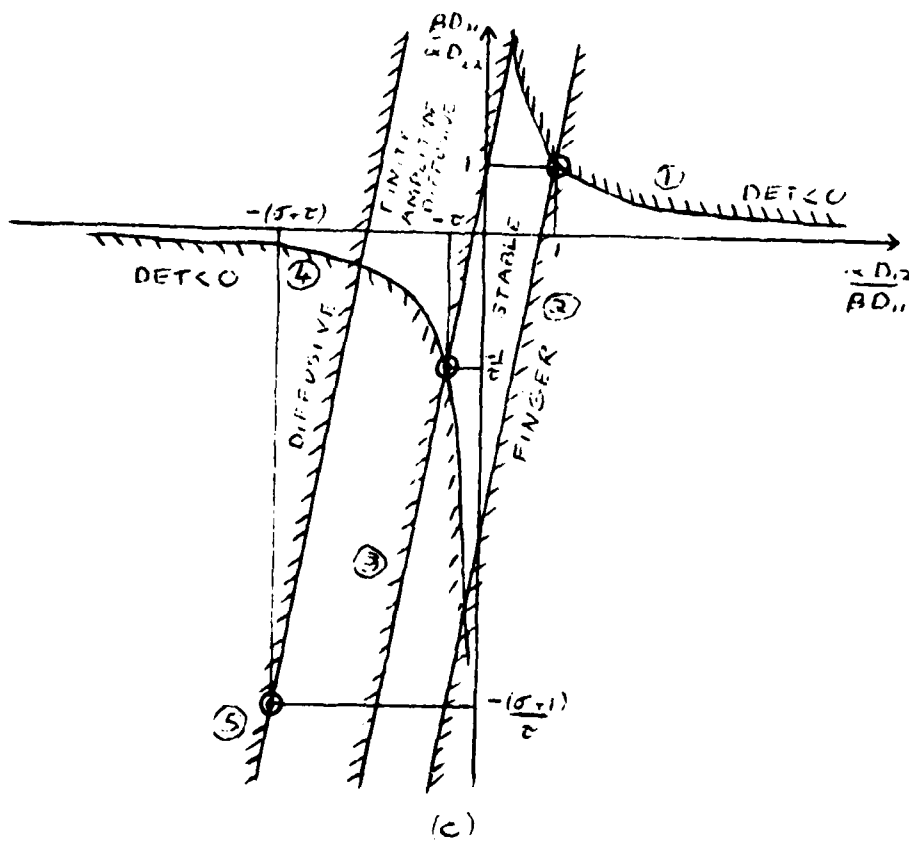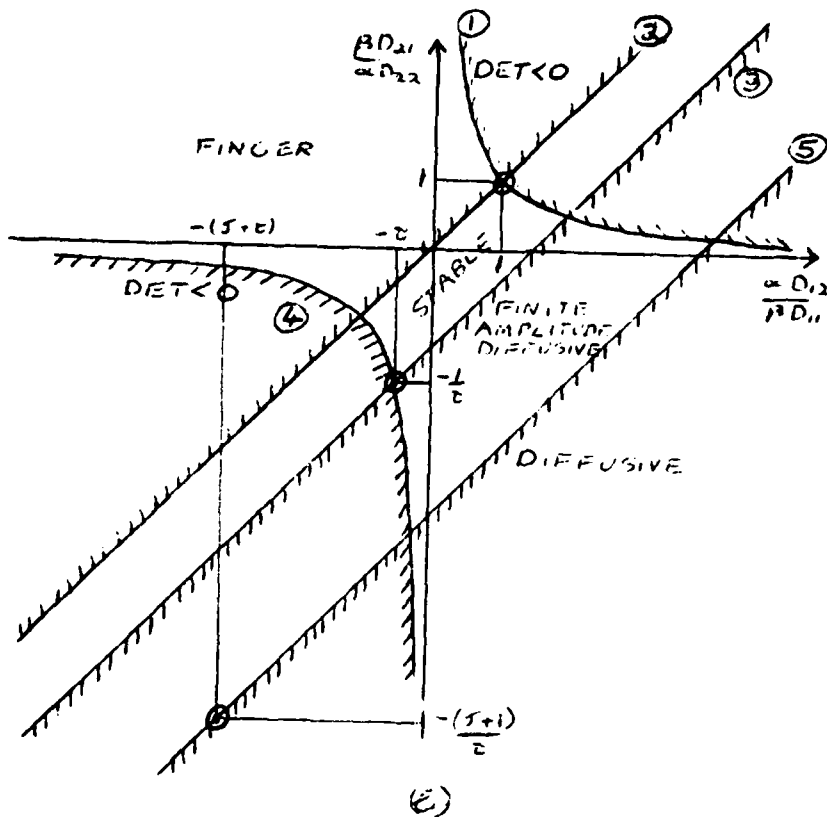than τ^{-1}. These stability boundaries show that the two types of double-diffusive instability never occur together. In addition, these show that the region of finite amplitude diffusive instability always encloses the region of infinitesimal oscillatory diffusive instability. In addition, the stability diagrams in figure 1 have curves plotted corresponding to the limiting condition found in the Appendix for the fluid to be spontaneously unstable to the diffusive separation of T and S:

$$DET = 0 \qquad \left(\omega \cdot \left(\frac{\beta D_{21}}{\alpha D_{12}} \cdot \frac{\alpha D_{12}}{\beta D_{11}} \right) = 1 \right). \qquad (20)$$

These curves serve to further reduce the range of stable values of the cross-diffusion coefficients.

5. Comparison of the Results with Veronis (1965)

In this section, we discuss the individual effect of the two cross-diffusion terms on the finite amplitude results of Veronis (1965). This comparison can be emphasized by considering the flux of T through the fluid, which can be expressed in terms of a Nusselt number:

$$Nu_T \equiv \frac{-D_{11} \left. \frac{\partial T}{\partial z} \right|_{z=0}}{D_{11} \Delta T / d} \qquad (21)$$

when DUFOUR = 0,

$$Nu_T = 1 + 2[1 + 8\pi^4 (\alpha^2 + 1)/A_1^2]^{-1} \qquad (22)$$

(That is, when DUFOUR = 0, the flux of T is due solely to conduction and convection and $1 \leqslant Nu_T \leqslant 3$). In figure 2(a), Nu_T is plotted against log $(-R/R_s)$ for $R < 0$, $\tau = 1/80$, $R_s \gtrsim 10^8$, and various values of the parameter SORET. In the calculations shown in figure 2 , we have chosen $\alpha^2 = 1/2$, which is the most unstable wavenumber for both linear and finite amplitude double-diffusive convection (Veronis 1965, 1968) and for linear double-diffusive convection with coupled diffusion (McDougall 1983). We note however, that we have not proved that it is the most unstable wavenumber for finite amplitude convection with arbitrary values of R, R_s, τ , SORET and DUFOUR. Of the two solution branches, only the upper one corresponding to $Nu_T \approx 3$ is stable. The figure demonstrates equation (14), which can be rearranged in this case to give

$$(-R^*)_{critical} > R^*_s/(1 + SORET) \qquad , (R^* \text{ and } R^*_s \gg 1). \qquad (23)$$

Hence, if SORET > 0, the critical Rayleigh number is lowered while if SORET < 0, it is increased. If SORET < -1, convection can occur for stable gradients of R^* and R^*_s, as is indicated in figure 2(b).

When only SORET = 0, the DUFOUR effect enables a flux of T to be produced even when the temperature contrast ΔT across the fluid is zero. Hence, as $R^* \to 0$ when DUFOUR $\neq 0$, $|Nu_T| \to \infty$. We therefore define a dimensionless T flux

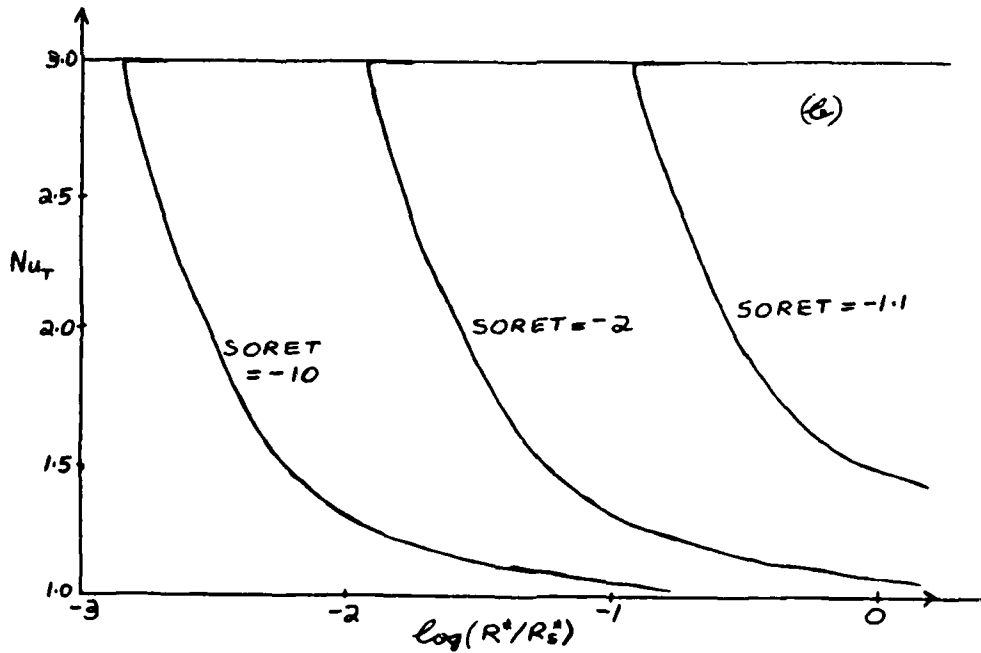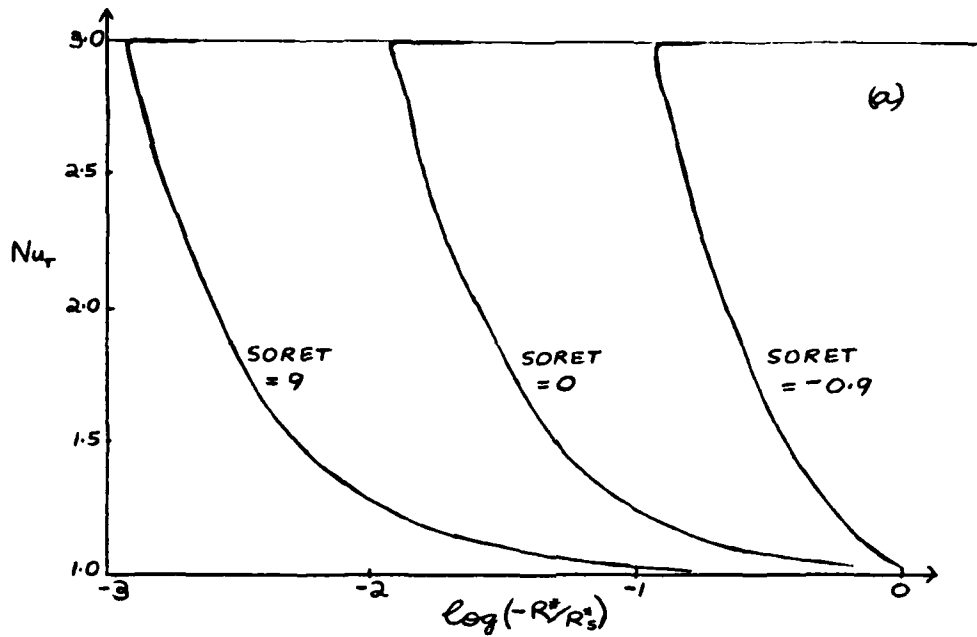$$H_T = \frac{-R^*}{R^*_s} Nu_T \qquad (24)$$

Figure 2. Plots of the Nusselt number Nu_T versus R^*/R_s^* for various values of the SORET coefficient, for $R_s^* \gg 1$, $\tau = 1/80$, and DUFOUR = 0. In (a), SORET > -1 and R < 0, which in (b), SORET > -1 and R > 0. In both cases, only the unstable finite amplitude is clearly visible as the stable finite amplitude branch has $Nu_T \approx 3$.

which will remain finite as $R^* \rightarrow 0$. Calculations of H_T illustrate that when $R^* < 0$ and $R_s^* \gg 1$,

$$(-R)\text{critical} = R_s^*(\tau + \text{DUFOUR}) \tag{25}$$

Hence when $\text{DUFOUR} < -\tau$, the system is unstable to all destabilizing T gradients and will be unstable unless a large enough stabilizing T gradient is applied.

6. Conclusions

The main conclusions of this study are the following:

(A) Steady finite amplitude diffusive convection can occur for nonzero values of the cross-diffusion coefficients.

(B) When a minimal representation of the convecting system is studied, we find that cross-diffusion effects are significant when the magnitude of these coefficients is comparable with the usual diffusion coefficients. In particular, if $\text{SORET} < -1$ or $\text{DUFOUR} < -\tau$, finite amplitude convection may occur when both initial property gradients are stabilizing. We also note that such large cross-diffusion coefficients have been observed by Cussler and Lightfoot (1965) in the combination polystyrene-toluene-cyclohexane.

(C) The minimal representation results are only an approximate solution to the equations (6) and (8) which is likely to be particularly inaccurate for small τ. The logical extension of this study is to examine the steady solution of these equations when the full Fourier series representations of ψ', T' and S' is used (as was done in the case without cross-diffusion by Veronis (1968). A study of the time-dependent equations, analogous to that of Huppert and Moore (1976), is also possible. However, such studies are probably only justified for particular systems where all the diffusion coefficients are known and where the possibility of finite amplitude diffusive instability is suspected.

REFERENCES

Baines, P. G. and A. E. Gill, 1969. On thermohaline convection with linear gradients. J. Fluid Mech. 37, 289-306.

Cussler, E. L. and E. N. Lightfoot, 1965. Multicomponent diffusion involving high polymers. I. Diffusion of monodisperse polystyrene in mixed solvents. J. Phys. Chem. 69, 1135-1144.

Huppert, H. E. and D. R. Moore, 1976. Nonlinear double-diffusive convection. J. Fluid Mech. 78, 821-854.

McDougall, T. J., 1983. Double-diffusive convection caused by coupled molecular diffusion. J. Fluid Mech. 126, 379-39 .

Veronis, G., 1965. On finite amplitude instability in thermohaline convection. J. Mar. Res. 23, 1-17.

Veronis, G., 1968. Effect of a stabilizing gradient of solute on thermal convection. J. Fluid Mech. 34, 315-336.

APPENDIX - THE SIGN OF DET

Consider an infinite volume of stationary fluid where T and S are initially uniform. In this fluid, the time evolution of infinitesimal disturbances is given by the equations

$$\frac{\partial T}{\partial t} = D_{11} \nabla^2 T + D_{12} \nabla^2 S$$

$$\frac{\partial S}{\partial t} = D_{22} \nabla^2 S + D_{21} \nabla^2 T \quad , \tag{A1}$$

In order to examine the stability of this system to arbitrary linear disturbances, let

$$T = T_0 \exp\left(i(lx + my + nz) + \sigma t\right)$$
$$S = S_0 \exp\left(i(lx + my + nz) + \sigma t\right). \tag{A2}$$

Substitution of (A2) into (A1) gives the equations

$$\sigma T_0 = -k^2 (D_{11} T_0 + D_{12} S_0)$$

$$\sigma S_0 = -k^2 (D_{22} S_0 + D_{21} T_0), \tag{A3}$$

where $k^2 = l^2 + m^2 + n^2$. Combining equations (A3) gives the equation

$$\left(\frac{\sigma}{k^2}\right)^2 + \frac{\sigma}{k^2}(D_{11} + D_{22}) + (D_{11} D_{22} - D_{12} D_{21}) = 0 \quad , \tag{A4}$$

We therefore see that both roots of this equation for σ are negative (corresponding to the decay of infinitesimal disturbances) if DET = $D_{11}D_{22} - D_{12}D_{21} > 0$. If DET < 0, we have the apparently unphysical result that the fluid is unstable to infinitesimal disturbance, resulting in the build-up of infinite concentrations of T and S throughout the fluid (note that $|\sigma| \propto k^2$, so that the fastest growing disturbances are infinitely close to each other.

HEATING A SALT GRADIENT FROM A SIDEWALL
Oliver S. Kerr

1. Introduction

In lecture 2 it was noted that the formation of horizontal layers is often found in double-diffusive processes. These layers can be formed, for example, by heating a salt gradient from below or from the effects of a side wall.

Side walls can generate horizontal interleaving in two ways. If the side wall is not vertical then the no flux condition at the wall prohibits horizontal isopycnals from existing which leads to motions up and down the wall. These motions lead to the formation of layers (Linden and Weber, 1977). The other way is for a temperature and/or salt concentration to be created at the wall which will drive motions that will lead to the formation of layers. It is this second care that we will be looking at here.

The case of laterally heating a salt gradient in a vertical slot has been investigated theoretically and experimentally by Thorpe Hutt and Soulsby (1969) and Hart (1971). In these cases it was assumed that a linear temperature profile had been established between the two walls before any horizontal convective rolls were set up. In this paper we will look at the case of a semi-infinite body of water, and so there is no steady temperature profile. This case has been investigated experimentally by Chen, Briggs and Wirtz (1971) or a fixed temperature difference between the wall and the fluid, and by Narusawa and Suzakawa (1981) for a constant heat flux. We will only look at the case of a constant temperature difference.

2. Basic Flow
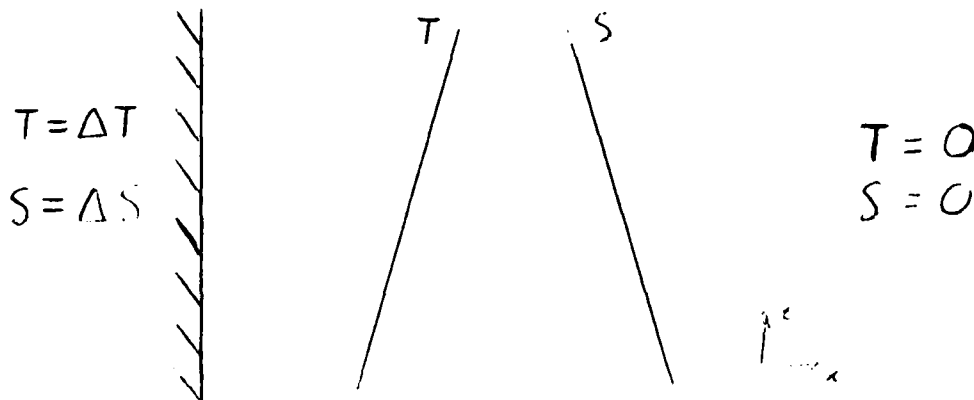
First we will look at the case of a semi-infinite body of fluid bounded by a rigid wall at x = 0. We will always take the vertical salt and temperature gradients to be linear. This removes any explicit z dependence from the governing equations and so we will be able to work for solution which has no z dependence. If the fluid only has a temperature gradient causing the stratification and it is then heated, then a steady uniform boundary layer solution exists. This steady thermal boundary layer has a balance between the temperature diffusing away from the wall and the fluid rising into a warmer environment, so reducing the heat perturbation from the local level.

We can look for a similar solution with two components causing the stratification. The governing Boussinesq will then be

$$C = g(\alpha T - \beta S) + \nu \frac{\partial^2}{\partial x^2} w$$

$$w \bar{T}_z = K_T \frac{\partial^2}{\partial x^2} T$$

$$w \bar{S}_z = K_s \frac{\partial^2}{\partial x^2} S$$

$$\rho = \rho_\cdot (1 - \alpha T + \beta S)$$

The boundary conditions are

at	$x = 0$	$w = 0$	$T = \triangle T$	$S = \triangle S$
as	$x \rightarrow \infty$	$w \rightarrow 0$	$T \rightarrow 0$	$S \rightarrow 0$

These have solutions

$$T = T \cos Mx \exp(-Mx)$$
$$S = S \cos Mx \exp(-Mx)$$
$$W = A \sin Mx \exp(-Mx)$$

where

$$M^+ = \frac{g}{4\nu} \left(\frac{\alpha \bar{T}_z}{K_T} - \frac{\beta \bar{S}_z}{K_s} \right)$$

This requires that $K_T \triangle T M^2 = T_z A$ and $K_S \triangle S M^2 = S_z A$.

The steady boundary layer solution will only exist when the vertical velocity is at the correct rate to counteract the increasing thickness of the layer due to diffusion in both components simultaneously. In general this will not happen and so we must look for an unsteady motion.

Instead of looking at the full problem with both components contributing to the vertical stratification we will look at the case where the density gradient in the resting fluid is due entirely to a vertical salt gradient. This salinity gradient will then have its side wall's temperature raised at time $t = 0$. This simplification has been made for two reasons:

1) This configuration matches the experiments that have been done.

2) It leads to some simplification in the mathematics as the temperature equation decouples.

The governing equations are now

$$\frac{\partial w}{\partial t} = g(\alpha T - \beta S) + \nu \frac{\partial^2 w}{\partial x^2}$$

$$\frac{\partial T}{\partial t} = K_T \frac{\partial^2}{\partial x^2} T$$

$$\frac{\partial S}{\partial t} + w \bar{S}_z = K_s \frac{\partial^2}{\partial x^2} S$$

The boundary conditions are:

when $t = 0$ $w = 0$ $T = 0$ $S = 0$ for all x

for $t > 0$ $w = 0$ $T = \Delta T$ $S = 0$ at $x = 0$

                                        $w \to 0$ $T \to 0$ $S \to 0$ as $x \to \infty$

This gives the solution to the temperature to be

$$T = \Delta \, erfc \left(\frac{x}{2\sqrt{K_T t}} \right)$$

The boundary condition at $x = 0$ for the salt is not very realistic; however, it makes the mathematics simpler. The effect of a more realistic boundary condition at $x = 0$ (for example, either taking $S = \Delta S$ or $\frac{\partial S}{\partial x} = 0$) will be discussed later.

Taking Laplace transforms with respect to time we get

$$p \hat{w} = g(\alpha \hat{T} - \beta \hat{S}) + \nu \frac{d^2}{dx^2} \hat{w}$$

$$p \hat{T} = K_T \frac{d^2}{dx^2} \hat{T}$$

$$p \hat{S} + \hat{w} \bar{S}_z = K_S \frac{d^2}{dx^2} \hat{S}$$

with $\hat{w} = 0$ $\hat{T} = \dfrac{\Delta T}{p}$ $\hat{S} = 0$ when $x = 0$

          $\hat{w} \to 0$ $\hat{T} \to 0$ $\hat{S} \to 0$ as $x \to \infty$

This gives the equations for $\hat{w}$ and $\hat{S}$ of the form

$$\left(p - K_T \frac{d^2}{dx^2} \right) \left[\left(p - K_S \frac{d^2}{dx^2} \right) \left(p - \nu \frac{d^2}{dx^2} \right) + N^2 \right] \begin{pmatrix} \hat{w} \\ \hat{S} \end{pmatrix} = \begin{pmatrix} 0 \\ 0 \end{pmatrix}$$

where N is the buoyancy frequency given by

$$N^2 = -g\beta \bar{S}_z$$

These give the solutions for $\hat{w}$ and $\hat{S}$

$$\hat{w} = \frac{g\lambda\Delta T(1-\tau)}{(p^2(1-\sigma)(1-\tau)+N^2)} \exp\left(-\sqrt{\frac{p}{\kappa_\tau}}\,x\right)$$

$$+ g\lambda\Delta T\left[-\frac{(1-\tau)}{2(p^2(1-\sigma)(1-\tau)+N^2)} - \frac{p^2(\tau-\sigma)(1-\tau)+2\tau N^2}{2p(p^2(1-\sigma)(1-\tau)+N^2)(p^2(\sigma-\tau)^2-4\sigma\tau N^2)^{\frac{1}{2}}}\right]\exp(-k_1 x)$$

$$+ g\lambda\Delta T\left[-\frac{(1-\tau)}{2(p^2(1-\sigma)(1-\tau)+N^2)} + \frac{p^2(\tau-\sigma)(1-\tau)+2\tau N^2}{2p\,p^2(1-\sigma)(1-\tau)+N^2)(p^2(\sigma-\tau)^2-4\sigma\tau N^2)^{\frac{1}{2}}}\right]\exp(-k_2 x)$$

$$\hat{S} = \frac{\lambda\Delta T N^2}{\beta}\left\{\frac{\exp\left(-\sqrt{\frac{p}{\kappa_\tau}}\,x\right)}{(p^2(1-\sigma)(1-\tau)+N^2)}\right.$$

$$+\left[-\frac{1}{2p(p^2(1-\sigma)(1-\tau)+N^2)} + \frac{(\sigma+\tau-2\sigma\tau)}{2(p^2(1-\sigma)(1-\tau)+N^2)(p^2(\sigma-\tau)^2-4\sigma\tau N^2)^{\frac{1}{2}}}\right]\exp(-k_1 x)$$

$$+\left[-\frac{1}{2p(p^2(1-\sigma)(1-\tau)+N^2)} - \frac{(\sigma+\tau-2\sigma\tau)}{2(p^2(1-\sigma)(1-\tau)+N^2)(p^2(\sigma-\tau)^2-4\sigma\tau N^2)^{\frac{1}{2}}}\right]\exp(-k_2 x)\left.\right\}$$

The Prandtl number $\qquad \sigma = \frac{\nu}{\kappa_\tau}$, $\quad 0 < \sigma < \infty$

Diffusivity ratio $\qquad \tau = \frac{\kappa_s}{\kappa_\tau}$, $\quad 0 < \tau < 1$

and

$$k_1^2 = \frac{p(\sigma+\tau) + \sqrt{p^2(\sigma-\tau)^2 - 4\sigma\tau N^2}}{2\sigma\tau\kappa_\tau}$$

$$k_2^2 = \frac{p(\sigma+\tau) - \sqrt{p^2(\sigma-\tau)^2 - 4\sigma\tau N^2}}{2\sigma\tau\kappa_\tau}$$

We will assume that we are dealing with heat and salt in water, and so $\sigma > 1$.

These Laplace transforms cannot be inverted explicitly. However, their small and large time behavior can be found (see Appendix).

For small time the leading order asymptotic behavior is

$$T = \Delta T \, \mathrm{erfc}\left(\frac{x}{2\sqrt{K_T t}}\right)$$

$$W \approx \frac{g\alpha\Delta T}{\sigma - 1} \, 4t \left[i^2\mathrm{erfc}\left(\frac{x}{2\sqrt{\nu t}}\right) - i^2\mathrm{erfc}\left(\frac{x}{2\sqrt{K_T t}}\right) \right]$$

$$S \approx S_z \frac{g\alpha\Delta T}{\sigma - 1} \, 16t^2 \left[i^4\mathrm{erfc}\left(\frac{x}{2\sqrt{K_T t}}\right) \frac{}{(\sigma-1)(1-\tau)} - \frac{\sigma \, i^4\mathrm{erfc}\left(\frac{x}{2\sqrt{\nu t}}\right)}{(\sigma-\tau)(\sigma-1)} - \frac{\tau_c \, i^4\mathrm{erfc}\left(\frac{x}{2\sqrt{K_s t}}\right)}{(\sigma-\tau)(1-\tau)} \right]$$

For large time the leading order asymptotic behavior is

$$T = \Delta T \, \mathrm{erfc}\left(\frac{x}{2\sqrt{K_T t}}\right)$$

$$W \approx \frac{g\alpha\Delta T (1-\tau)}{2 N^2} \frac{x}{\sqrt{K_T \pi t^3}} \, \exp\left[-\frac{x^2}{4K_T t}\right]$$

$$+ \frac{g\alpha\Delta T}{N} \sqrt{\frac{K_s}{\nu}} \, \exp\left(-Mx\right) \sin(Mx)$$

$$- \frac{2g\alpha\Delta T}{N^2(\sigma+\tau)} \frac{x \cos(Nt)}{\sqrt{2\pi(\nu+K_s)t^3}} \exp\left[-\frac{x^2}{2(\nu+K_s)t}\right]$$

$$S \approx \frac{\alpha\Delta T}{\beta} \, \mathrm{erfc}\left(\frac{x}{2\sqrt{K_T t}}\right)$$

$$- \frac{\alpha\Delta T}{\beta} \, \exp\left(-Mx\right) \cos(Mx)$$

$$- \frac{2\alpha\Delta T}{\beta N}\frac{x \sin(Nt)}{(\sigma+\tau)\sqrt{2\pi(\nu+K_s)t^3}} \exp\left[-\frac{x^2}{2(\nu+K_s)t}\right]$$

where
$$M^4 = \frac{N^2}{4K_s\nu}$$

The large time solutions have three parts. The first part has the same length scale as the thermal diffusion. This represents the upwelling of the water so that the negative buoyancy of the saltier water balances the positive buoyancy of the temperature.

The first term in the salt equation has a mismatch at x = 0. The upwelling water tries to impose a salt boundary condition of $S = \frac{\alpha \Delta T}{\beta}$ at x = 0 as opposed to the actual condition of S = 0. The second term is the salt boundary layer that you would get if you applied a salt difference $\Delta S = -\frac{\alpha \Delta T}{\beta}$ to the salt gradient, without any temperature effects (see beginning of this section). Thus this term is the matching of the salt boundary condition to the thermal layer.

The last term is a decaying oscillation at the buoyancy frequency that results from the initial disturbance.

If we had a different salt boundary condition at x = 0 then some of these results would be changed. If we had the condition that $S = \Delta S$ at x = 0, then, since the problem is linear, this is equivalent to superimposing the motion due to adding salt to a salt gradient on the above solution. This alters the salt boundary layer terms and also the buoyancy frequency terms. If we had a no flux condition on the salt ($\frac{\partial S}{\partial x} = 0$ at x = 0) then we would have a decaying salt boundary layer (dying off as $t^{-1/2}$) and an altered buoyancy frequency term. Neither of these alterations to the salt boundary condition has any effect on the thermal terms.

3. Stability Analysis

When a salt gradient is heated sufficiently strongly from the side in experiments, the fluid develops long thin horizontal layers that grow from the wall into the interior of the fluid (Chen, Briggs and Wirtz, 1971). In this section we will look at the stability of the results from the previous section to small perturbations.

To make any progress analytically we will have to make several assumptions:

(1) Since the instabilities have a small growth rate compared to the buoyancy frequency, these oscillations have no effect on the motions over a longer time scale.

2) The instabilities are driven by the region of the fluid with the horizontal temperature and salinity gradients and are not affected by the salt boundary layer. Hence the salt boundary terms will be neglected. For this to be true we would want the length scale of the thermal layer to be much larger than the length scale of the salt boundary layer, i.e.

$$M^{-1} \ll 2\sqrt{K_T t}$$

For typical experiments (c.f. Chen et al, 1971) this would give

$$(1 \text{ sec})^{1/2} \ll t^{1/2}$$

Since the time for the onset of the formation of the interleaving layers is usually measured in minutes when the system is marginally unstable this condition is usually satisfied.

(3) We will assume that the thermal boundary layer is quasi-static. This means that the form of the temperature profile is assumed fixed and is not affected by diffusion.

(4) The small vertical velocity associated with the thermal layer can be ignored.

With these assumptions the linearized equations of motion for a small perturbation are:

$$\frac{\partial}{\partial t} \nabla^2 \psi = g\left(\alpha \frac{\partial T}{\partial x} - \beta \frac{\partial S}{\partial x}\right) + \nu \nabla^4 \psi$$

$$\frac{\partial}{\partial t} T - \frac{\partial \psi}{\partial z}\frac{\partial \bar{T}}{\partial x} = K_T \nabla^2 T$$

$$\frac{\partial}{\partial t} S - \frac{\partial \psi}{\partial z}\frac{\partial \bar{S}}{\partial x} + \frac{\partial \psi}{\partial x}\frac{\partial \bar{S}}{\partial z} = K_S \nabla^2 S$$

where ψ is the stream function for the perturbation and

$$\bar{T} = \Delta \bar{T} f\left(\frac{x}{L}\right)$$

$$\bar{S} = \alpha \frac{\Delta \bar{T}}{\beta} f\left(\frac{x}{L}\right) + z \bar{S}_z$$

$$f(x^*) = erfc\left(\frac{x^*}{2}\right) \qquad L = \sqrt{K_T t} \quad \text{(assumed constant)}$$

(5) For large vertical density gradients the observed motions are very thin and horizontal. In the diffusion terms the $\frac{\partial^2}{\partial z^2}$ part will dominate the $\frac{\partial^2}{\partial x^2}$ term, hence we will assume

$$\nabla^2 \approx \frac{\partial^2}{\partial z^2}$$

The order of the system and so we are only left with the one boundary condition at x = 0 that the wall is a streamline (ψ = 0 when x = 0).

Having made all these assumptions we will look for a marginally stable mode, ie. one with zero growth rate ($\frac{\partial}{\partial t} \equiv 0$). This gives us the following equations:

$$0 = g\left(\alpha \frac{\partial \bar{T}}{\partial x} - \beta \frac{\partial S}{\partial x}\right) + \nu \frac{\partial^4}{\partial z^4} \psi$$

$$-\frac{\partial \psi}{\partial z}\frac{\partial \bar{T}}{\partial x} = K_T \frac{\partial^2}{\partial z^2} T$$

$$-\frac{\partial \psi}{\partial z}\frac{\partial \bar{S}}{\partial x} + \frac{\partial \psi}{\partial x}\frac{\partial \bar{S}}{\partial z} = K_S \frac{\partial^2}{\partial z^2} S$$

If we now nondimensionalize the variables with respect to the following quantities

$$T \text{ with respect to } \Delta T$$

$$S \text{ with respect to } \frac{\alpha \Delta T}{\beta}$$

$$x \text{ with respect to } l$$

$$z \text{ with respect to } (1-c)\frac{\alpha \Delta T}{(-\beta S_z)}$$

$$\psi \text{ with respect to } K, \frac{l}{h}$$

The vertical distance is nondimensionalized with respect to $-(1-c)\frac{\alpha \Delta T}{\beta S_z}$ since $-\frac{\alpha \Delta T}{\beta S_z}$ is the height to which a fluid element heated by an amount ΔT would have to rise in order to be in an environment of the same density. The $(1-c)$ factor is for simplification of the resulting equation.

We will look for a solution that is periodic in the vertical direction so

$$\psi(x,z) = \phi(x)\, e^{imz}, \text{ etc.}$$

This gives an equation for ϕ

$$0 = \phi'' + im(\phi f')' - Pm^6\phi$$

with

$$\phi(0) = \phi(\infty) = 0$$

and

$$P = \frac{l^2 K \nu (-g\beta S_z)^5}{(1-c)^6 (g\alpha\Delta T)^6}$$

This equation can be applied to a simple case that has been treated theoretically before (Thorpe, Hutt and Soulsby, 1969 and Hart, 1971) when the vertical salt gradient tends to infinity. If we consider an infinite slot with walls at x = 0 and x = 1 (i.e. ∞ = 1), and a linear temperature profile (i.e. $f=1-x$) then we get the problem

$$0 = \phi'' - im\phi' - Pm^6\phi$$

$$\text{with} \quad \phi(0) = \phi(1) = 0$$

This is analogous to the approach taken in Linden and Weber, 1977 where they assumed the streamfunction vanished at the outside edge of the region of perturbed salt and temperature, and that the compositional gradients are linear across this layer.

This has a solution of the form

$$\phi = A e^{iax} + B e^{ibx}$$

where

$$a = \frac{m + \sqrt{m^2 - 4m^6 P}}{2}$$

$$b = \frac{m - \sqrt{m^2 - 4m^6 P}}{2}$$

Applying the boundary condition at x = 0 gives

$$A = -B$$

and at x = 1 gives

$$e^{ia} = e^{ib}$$
$$\Rightarrow a = b + 2n\pi$$

and so

$$P = \frac{m^2 - 4n^2\pi^2}{4m^6}$$

The graph of P plotted against m looks like:
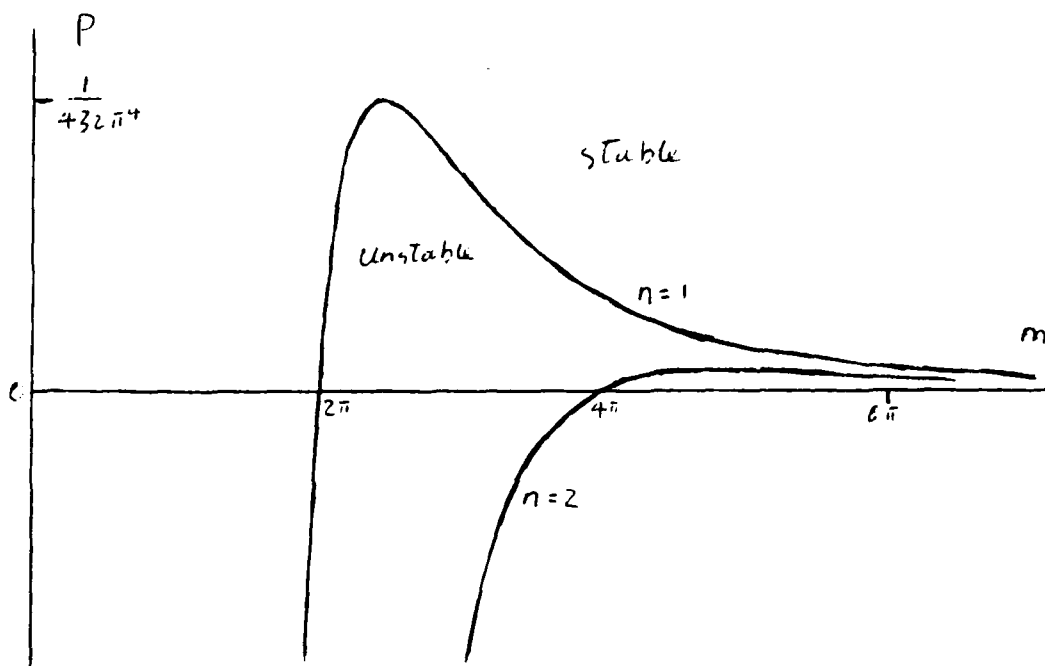
Since P decreases as the temperature difference increases the region of instability lies below the line, and the point where the system is marginally stable is the maximum of the P curve. This point occurs when n = 1 at the following values of m and P

$$m = \sqrt{6}\,\pi \quad \text{and} \quad P = \frac{1}{432\,\pi^4}$$

When these are expressed in terms of the thermal and saline Rayleigh numbers used in Hart (1971) this gives the result derived there that

$$(\tau^{-1} - 1)\ Ra = 5.90\ (-R_S)^{5/6}$$

and

$$k = 1.30\ (-R_S)^{1/6}$$

where the thermal Rayleigh number $Ra = \dfrac{g \lambda \Delta T\, l^3}{K_T\, \nu}$

saline Rayleigh number $R_s = \dfrac{g \beta \bar{S_z}\, L^4}{K_s\, \nu}$

and k is the vertical wave number nondimensionalized with respect to l.

4. Conclusions

This equation reproduces the results obtained by Thorpe, Hutt and Soulsby (1969) and Hart (1971) for the case of strong salt gradient in a finite slot. However, problems were encountered when trying to apply this equation to a seim-infinite region by integrating the equation for ϕ using $f = erfc\ (\frac{x}{2})$. It was found to be hard to satisfy both the boundary condition at infinity and at zero simultaneously. The reason for this is not known at the moment, but we hope to be able to overcome them soon.

REFERENCES

Chen, C. F., D. G. Briggs and R. A. Wirtz, 1971. Stability of thermal convection in a salinity gradient due to lateral heating. Int. J. Heat Mass Transfer, 14, 57-65.

Hart, J. E., 1971. On sideways diffusive instability. J. Fluid Mech., 49, 279-288.

Linden, P. F. and J. E. Weber, 1977. The formation of layers in a double-diffusive system with a sloping boundary. J. Fluid Mech., 81, 757-773.

Narusawa, U. and Y. Suzukawa, 1981. Experimental study of double-diffusive cellular convection due to a uniform lateral heat flux. J. Fluid Mech., 113, 387-405.

Thorpe, S. A., P. K. Hutt and R. Soulsby, 1969 The effects of horizontal gradients on thermohaline convection. J. Fluid Mech., 38, 375-400.

APPENDIX

To invert the Laplace transforms $\hat{w}$ and $\hat{S}$ we use the Bromwich integral

$$W(x,t) = \frac{1}{2\pi i} \int_{c-i\infty}^{c+i\infty} e^{pt}\, \hat{w}(x,p)\, dp$$

where c is chosen so that the contour lies to the right of any singularities or cuts of $\hat{w}$ in the complex plane.

The Laplace transform of w is

$$\hat{w} = g\alpha\Delta T \left\{ \frac{(1-\tau)}{p^2(1-c)(1-\tau)+N^2} \exp\left(-\sqrt{\frac{p}{k_1}}\,x\right)\right.$$

$$+\left[-\frac{(1-\tau)}{2(p^2(1-c)(1-\tau)+N^2)} - \frac{p^2(\tau-c)(1-\tau)+2\tau N^2}{2p(p^2(1-c)(1-\tau)+N^2)(p^2(c-\tau)^2-4c\tau N^2)^{\frac{1}{2}}}\right]\exp(-k_1 x)$$

$$+\left[-\frac{(1-\tau)}{2(p^2(1-c)(1-\tau)+N^2)} + \frac{p^2(\tau-c)(1-\tau)+2\tau N^2}{2p(p^2(1-c)(1-\tau)+N^2)(p^2(c-\tau)^2-4c\tau N^2)^{\frac{1}{2}}}\right]\exp(-k_2 x)\right\}$$

Below is a diagram with the cuts and singularities of the w in the complex plane.
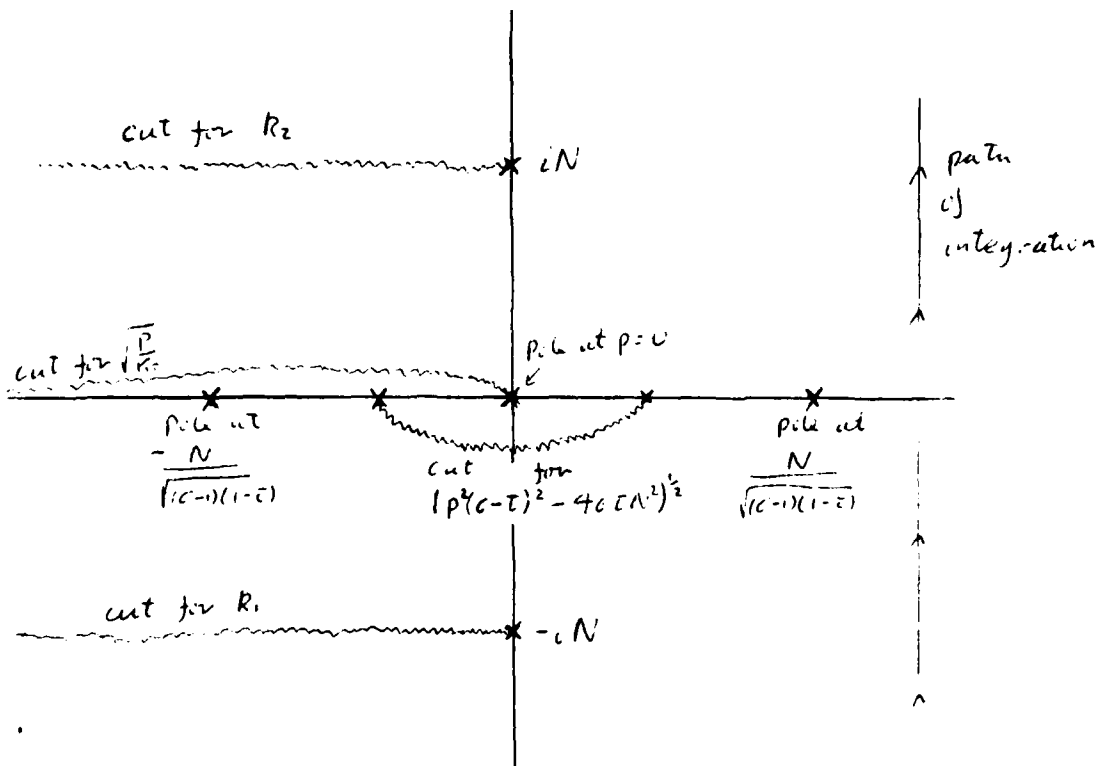
This contour can be deformed to
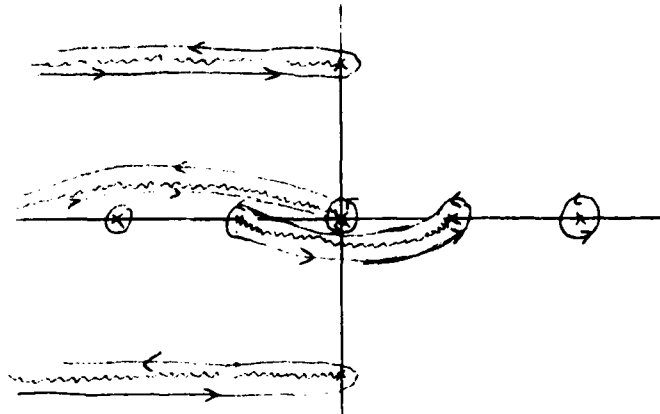
The residue at the pole at $p = \dfrac{N}{\sqrt{(\tau-1)(1-\tau)}}$ is zero and so this part of the contour makes no contribution to w. Also the contribution from the part of the contour encircling the cut between $\mp \dfrac{2N\sqrt{\sigma\tau}}{(\sigma-\tau)}$ is also zero. This is to be expected since the behavior of w at large time is dominated by the parts of the contour with the largest real part. If any part of the contour in the right hand half plane made any contribution then w will grow exponentially. The parts of the contour in the right hand plane are only there because of the presence of the stabalizing salt gradient and it would be unexpected if the addition of a stabalizing effect would change the system from algebraic growth to exponential growth.

For the large time asymptotics the results will be dominated by the contributions from the parts of the contours rounding the poles and cuts on the imaginary axis. The leading order terms are found by expanding the parts of w that do not contain x as a power series in p (or $p \pm iN$) and ignoring all but the leading order term in p. The remaining part is then inverted by consulting any table of Laplace transforms.

For example to find contribution near $p = 0$

$$\hat{w} \sim \frac{g_x \Delta\tau (1-\tau)}{N^2} \exp\left(-\sqrt{\frac{p}{\kappa_\tau}}\, x\right)$$

$$+ g_x \Delta\tau\left[-\frac{g_x \Delta\tau(1-\tau)}{2N^2} - \frac{\tau N^2}{p(-4\sigma\tau N^2)^{\frac{1}{2}}}\right] \exp(-k_1 x)$$

$$+ g_x \Delta\tau\left[-\frac{g_x \Delta\tau(1-\tau)}{2N^2} + \frac{\tau N^2}{p(-4\sigma\tau N^2)^{\frac{1}{2}}}\right] \exp(k'_1 x)$$

$k'_1 = k_1$ evaluated at $p = 0$. Note this is complex.

The first term in $\hat{w}$ has a cut because of the square root sign in the exponential term. So its leading order behavior is the inverse of

$$\frac{g_x \Delta\tau (1-\tau)}{N^2} \exp\left(-\sqrt{\frac{p}{\kappa_\tau}}\, x\right)$$

This gives the thermal response. If the cut between $\frac{2\sqrt{\pi} N}{\tau(\tau-i)}$ is deformed away from the origin then the first terms in the $exp(-k_1 x)$ and $exp(-k_2 x)$ terms are both analytic at the origin and so make no contribution to the integral. The second terms consist of a p^{-1} term times an analytic function and so the contributions will just be the residues evaluated at $p = 0$. This gives the salt boundary layer contribution. The cuts at $p = \pm iN$ are treated in a similar manner giving the asymptotic behavior for large time for the oscillatory part of the solution.

For small time the behavior is dominated by large values of p and a similar procedure but expanding in powers of p^{-1} yields the small time asymptotics.

PARTICULATE DISPERSAL IN A TIME-DEPENDENT FLOW
Leonard A. Smith

1. INTRODUCTION

Questions concerning the suspension and fall out of negatively buoyant particles are of central importance in several fields of current research. They arise in a wide range of phenomena including precipitation formation and the lifetime of volcanic aerosols in the atmosphere, suspension of plankton in the sea and geophysical processes such as the suspension of growing crystals in a convecting magma chamber. As an initial step toward understanding such phenomena, we examine the motion of particles in a simple laminar flow which is periodic in time. Stommel (1949) developed the theory for the case of steady rolls. Experimental investigations of a similar steady flow field have been performed by Tooby et. al. (1977). Aref (1984) has modeled the stirring of a tank of fluid by point vortices. This paper outlines the analytic treatment of the time-dependent case to third order and presents the results of numerical experiments over a wide range of conditions. In addition to regions of retention and simple fallout, regions of chaotic particle motions, including some in which the particle slowly migrates downward through a series of cells, are observed. Initial observations concerning the stabilization of particles which would fall out of the steady mean flow are discussed.

The dynamical system representing particle motion is of interest in its own right. It is a two-dimensional Hamiltonian system, periodic in both space and time, so the phase space of the system is three-dimensional and of finite volume, and therefore may be easily visualized. Two-dimensional Poincare sections of phase space reveal regions in which particle motion is described by either a simple torus, a twisted torus (islands), the breakup of islands into chaotic regions, sheets which act as barriers to particle motion and the breakdown of these sheets into islands and then chaotic regions. Which behavior a particle will display depends on its initial position and the strength and frequency of the oscillations. Hamiltonian chaos is most commonly observed in three-dimensional systems. In this system, the role of the third degree of freedom is played by the explicit time dependence of the Hamiltonian.

2. STEADY BACKGROUND FLOW

The suspension of negatively buoyant particles in horizontal fluid rolls is easily observed in the laboratory. The standard apparatus consists of a cylindrical tank filled with a high viscosity fluid and mounted with its axis horizontal. As the cylinder is rotated about its axis, the fluid quickly (~ 10 seconds) reaches solid body rotation. Small spheres placed in the ascending flow are observed to follow nearly circular orbits about the particle stagnation point, where the fluid velocity is equal to the negative of the particle settling velocity. In addition to the negatively buoyant particles, several small, almost spherical air bubbles (positively buoyant) were observed to execute similar motion in the descending fluid on the opposite side of the tank. A detailed investigation of this system has been performed by Tooby, Wick and Isaacs (1977), using a tank 15 cm. in diameter, with test particles of radius between 0.8 mm. and 3.0 mm. and rotational periods in the range 5.0 to 40.0 seconds. They find that particle orbits generally have periods slightly greater than that of the fluid. On longer time scales the

orbits evolve, the radius changing by a factor of two in 30 to 100 fluid
oscillations. The density and diameter of the test particle determine whether
its orbit grows or contracts. This instability is due to inertial effects and
_he influences of the walls on finite diameter test particles. Particle-
particle interactions are also observed to produce large perturbations in
particle motions (Whitehead, private communication). In the cases of precipi-
tation formation and magma crystal growth, the properties of a single particle
change influencing the particle's motion, which in turn feeds back upon the
particle's growth. None of these complicating effects are considered here.

The effect of steady convective rolls on the motion of a small, slowly
sinking body was first investigated by Stommel (1949). This work was stimu-
lated by the observation that the yield of the plankton tows taken along the
direction of the wind, and therefore parallel to the axis of wind-induced fluid
rolls, were much more variable than those from tows taken perpendicular to the
wind. Stommel considered a particle slowly sinking through fluid rolls with a
stream function.

$$\Psi_F(x,y) = A \sin x \sin y \qquad (2.1)$$

where the subscript F denotes the fluid, x is measured in the horizontal
direction and y in the vertical. The streamlines of this flow are shown in
figure 1. The velocity of the particle is that of the fluid plus a settling
velocity, v_s, in the negative y direction. Specifically,

$$\frac{dx}{dt} = \dot{x} = \frac{\partial \Psi_F}{\partial y} \qquad = A \sin x \cos y$$

$$\frac{dy}{dt} = \dot{y} = -\frac{\partial \Psi_F}{\partial x} - v_s \qquad = -A \cos x \sin y - v_s \qquad (2.2)$$

Thus the particle motion has a stream function

$$\Psi_\rho(x,y) = A \sin x \sin y + v_s x \qquad (2.3)$$

Particle trajectories may be classified by the ratio of the settling velocity
to a measure of the maximum fluid velocity:

$$s = \frac{v_s}{A} \qquad (2.4)$$

In the case $s = 0$ the particles are neutrally buoyant and follow the stream-
lines of the fluid. For $s > 1$ (or $s < -1$), all particles fall (rise) through
the cells, horizontally displaced away from the region of maximum fluid up-
flow. This displacement results from sinking (rising) particles having mini-
mum vertical velocity in regions of maximum upward (downward) fluid velocity.
This increases their residence time in the area, and hence their horizontal
displacement from the background flow.

For an intermediate value, $-1 <= s <= 1$ there exists a region of
retention in which particles will execute closed orbits, and therefore, remain
suspended in the cell. Streamlines of particle motion for several values of s
are shown in figure 2. The boundary of the region of retention is delineated
by the largest closed orbit within the cell. Along this boundary the particle
stream function has the same value it takes along the cell border. This may
be seen in figure 2. In the steady case, this is the orbit of a particle
which rises (sinks) infinitesimally close to the upward (downward) flow at the
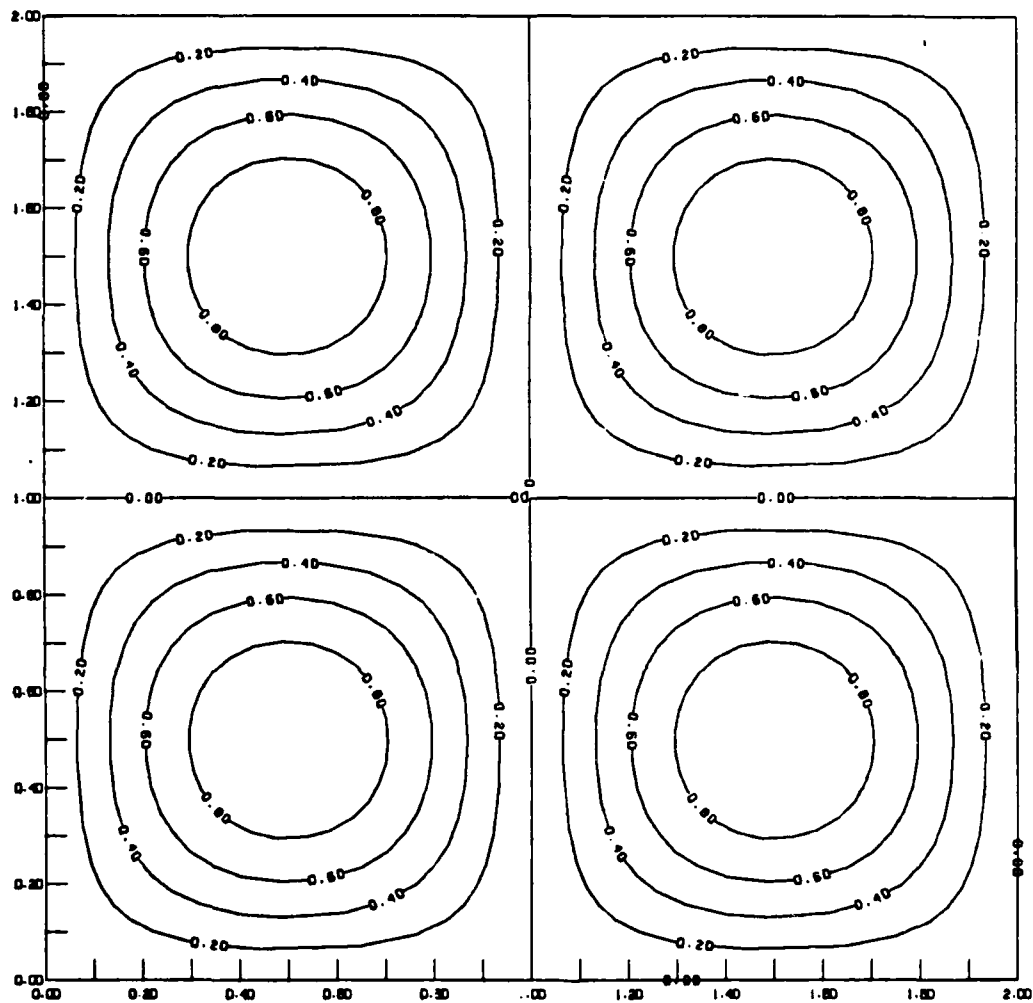
Figure 1

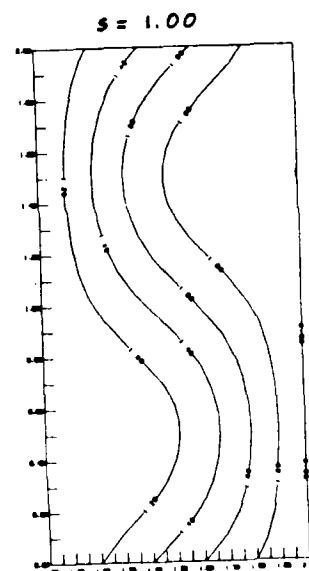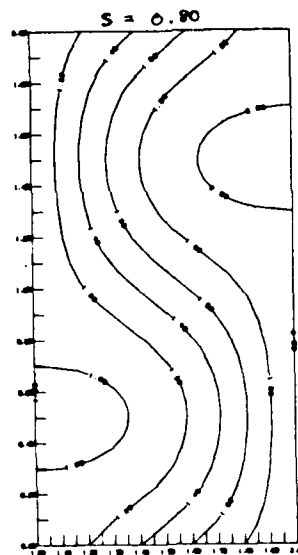Streamlines of the background flow field described by
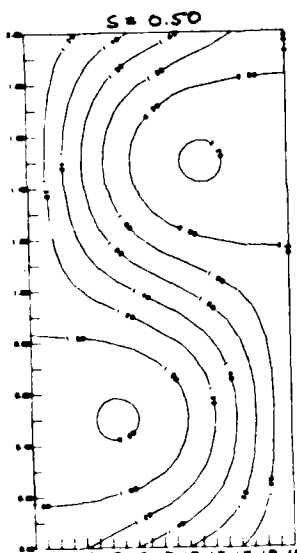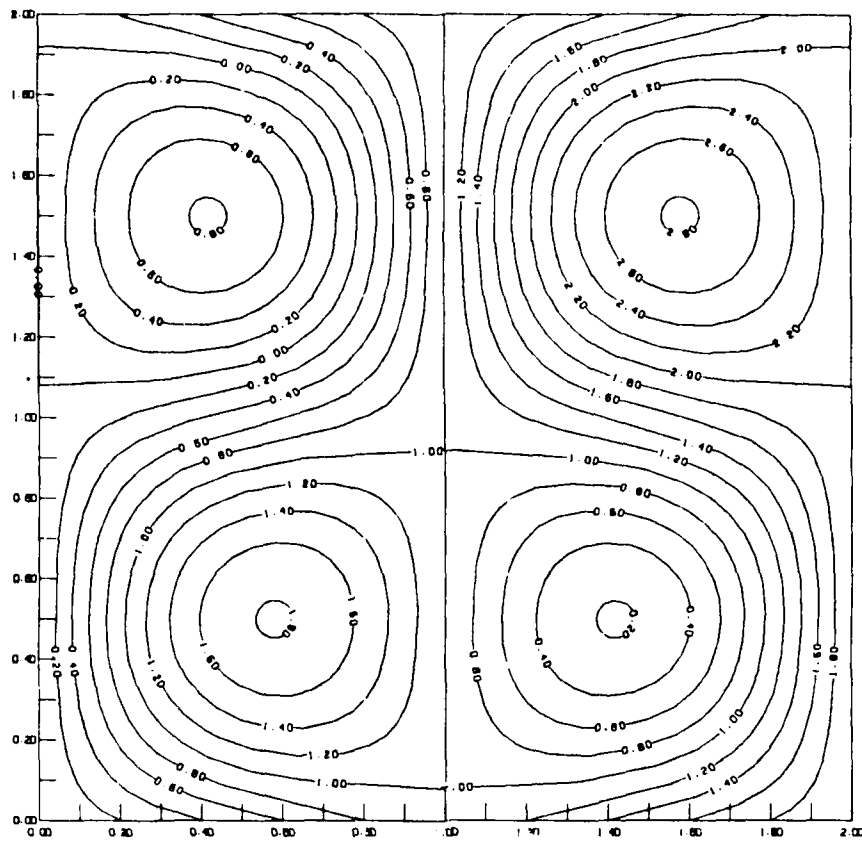equation 2.1 .

Figure 2

Particle streamlines for several values of s. Contours of Ψ_p/v_s are plotted so that verticle cell boundaries are integer contours.

cell boundary. The large variations in yield distinguish tows which sample a region of retention from those which are taken in relatively plankton-free region between them. Tows perpendicular to the rolls sample both the plankton-dense and plankton-free regions.

For the remainder of this paper, we restrict the discussion to negatively buoyant particles in a cell in which the fluid motion is counter-clockwise. All results apply to positively buoyant particles and clockwise cells with the appropriate reversal of signs. Speicifically, we will consider particles initially within the cell with fluid stagnation point at ($x = \frac{3\pi}{2}$, $y = \frac{3\pi}{2}$) This cell is the upper right quarter of figure 1. Let us denote the stagnation point of the particle motion by x_s. At this point the fluid velocity is directed upward and equal to the settling velocity of the particle in magnitude ($x_s = \sin^{-1}(s)$). For a given value of s, the orbit of a retained particle may be uniquely identified by the location of its right most crossing of a line of zero horizontal velocity ($y = n\pi$, n = 0,1,...). The value of x at this point is denoted x_r. In steady flows, paths of particles with different initial positions do not cross unless they follow the same streamline.

The following observations of the motion of particles in steady flows were made with the numerical model described in section 4. Consider particles located within a region at retention. Figure 3 shows the period of the particle orbit as a function of x_r for several values of s. Near the fluid stagnation point, x_F, the fluid and s = 0 particles are in solid body rotation with period P = 2π. The period increases with increasing x_r, becoming infinite for a particle on an ascending cell boundary. For a given value of s, particles near the particle stagnation point have the minimum x_r and lowest period orbits. As s increases, the period of these tightest orbits ($x_r \sim x_s$) also increases. All particles with $x_r > x_s$ are retained.

The increase of the minimum period with s may be understood as follows. To simplify the algebra, shift the coordinate origin to the fluid stagnation point and let A = 1. The stream function is then

$$\psi_p (x,y) = \cos x \cos y + v_s x \qquad (2.5)$$

Near the particle stagnation point ($x_s = \sin^{-1}(v)$, y = 0) the particle motion may be described by the first terms of a Taylor series

$$\dot{x}(x,y) = \dot{x}(x_s,y_s) + (x-x_s)\frac{\partial \dot{x}}{\partial x}\Big|_{x_s,y_s} + (y-y_s)\frac{\partial \dot{x}}{\partial y}\Big|_{x_s,y_s} \qquad (2.6)$$

$$\dot{y}(x,y) = \dot{y}(x_s,y_s) + (x-x_s)\frac{\partial \dot{y}}{\partial x}\Big|_{x_s,y_s} + (y-y_s)\frac{\partial \dot{y}}{\partial y}\Big|_{x_s,y_s}$$

or

$$\tilde{\dot{x}} = -\kappa y \qquad (2.7)$$

$$\tilde{\dot{y}} = \kappa x$$
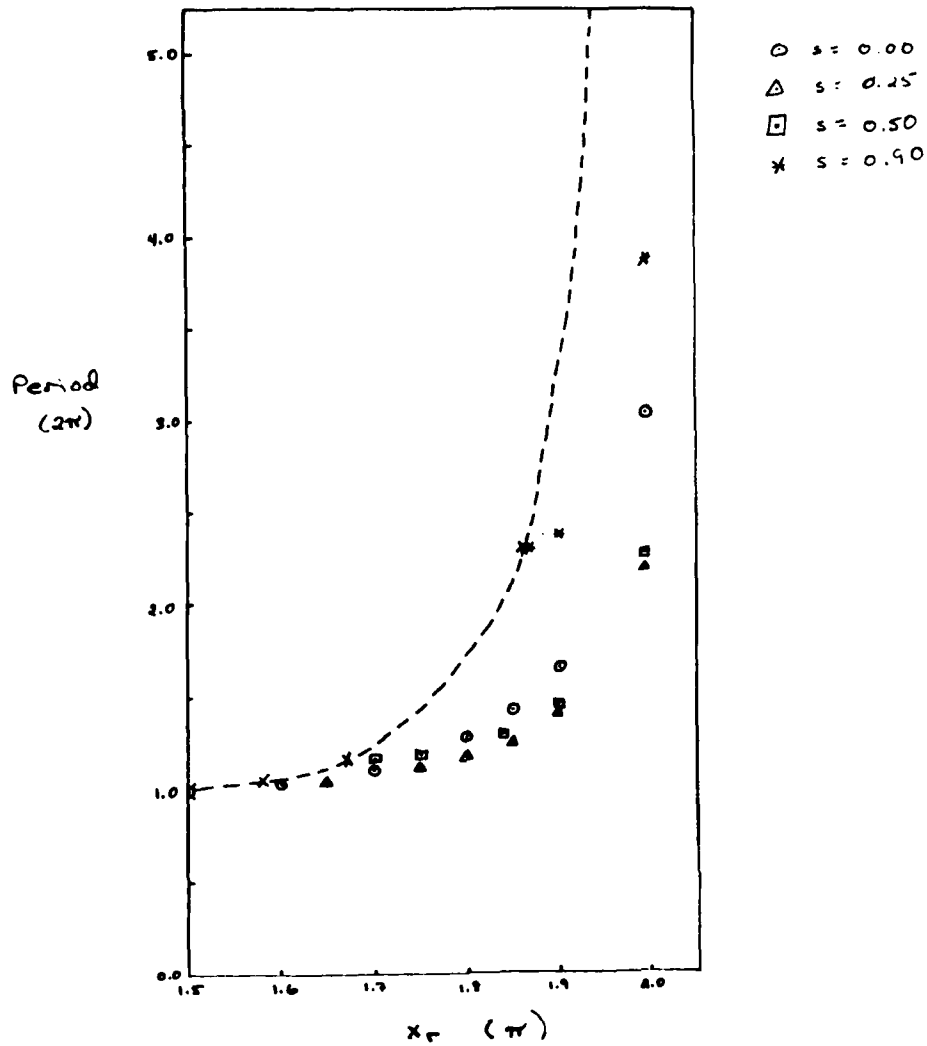
Figure 3. The period of retained particle orbits as a function
of x for s = 0.0, 0.25, 0.5 and 0.9.

where

$$\tilde{x} = x - x_s$$
$$\tilde{y} = y - y_s$$
$$\kappa = \cos(x_s) \qquad\qquad (2.8)$$

Thus particles near the particle stagnation point are in solid body rotation
with period

$$P = \frac{2\pi}{\kappa} \qquad\qquad (2.9)$$

This is the dashed line in figure 3. The cross marks along this line mark the
location of the stagnation points for the numerical results shown in the
figure.

3) PERIODIC BACKGROUND FLOW

To investigate the effects of allowing the background flow to vary in a periodic manner, redefine A as

$$A(t) = 1 + \varepsilon \cos(\omega \alpha t) \tag{3.1}$$

where ε is the magnitude and ω the frequency of the oscillations of the fluid flow. The parameter α is used to separate time scales in the slowly varying case. With the coordinate origin at the fluid stagnation point, the stream function is now

$$\psi_p(x,y,t) = A(t) \cos x \cos y + v_s x \tag{3.2}$$

Two cases are considered analytically: first where the fluctuations about the mean flow are small ($\varepsilon \ll 1$, $\alpha = 1$); and second, where oscillations in the flow occur on a time scale long relative to that of orbital periods ($\omega \alpha \ll 1$). In both cases, the expansions assume small x and y as measured from the relevant stagnation point.

Case A)   Small Oscillations ($\varepsilon \ll 1$)

Consider small oscillations about the mean flow ($\varepsilon \ll 1$; $\alpha = 1$). Expanding the particle velocity field in x and y and retaining only linear terms yields

$$\begin{aligned}
\mathring{x} &= -A(t)\, y \\
\mathring{y} &= A(t)\, x - v_s
\end{aligned} \tag{3.3}$$

or

$$\begin{aligned}
x_T &= -y \\
y_T &= x - v_s (1 - \varepsilon \cos \omega T) + O(\varepsilon^2)
\end{aligned} \tag{3.4}$$

where a new time T has been defined such that

$$\begin{aligned}
\frac{\partial}{\partial T} &= \frac{1}{A(t)} \frac{\partial}{\partial t} \\
T(t) &= t + \varepsilon \left(\frac{1}{\omega} \sin \omega t \right)
\end{aligned} \tag{3.5}$$

Note that $|T - t| \leq \frac{\varepsilon}{\omega}$ for all t. Solving for x(T), y(T) yields

$$\begin{aligned}
x(T) &= \alpha_0 \sin(T + \phi_0) + v_s - \varepsilon \left(v_s \frac{\cos \omega T}{(1-\omega^2)} \right) \\
y(T) &= -\alpha_0 \cos(T + \phi_0) - \varepsilon \frac{v_s \omega}{(1-\omega^2)} \sin \omega T
\end{aligned} \tag{3.6}$$

where α_0 and ϕ_0 depend on the initial position of the particle. For $\omega = 0$ the motion is that of solid body rotation. For small ω, the particle makes order ε oscillations about the circular path centered on the particle stagnation point. This motion is observed in the numerical simulation. Figure 4a is a representative trace of particle motion.

Case B) Slow Oscillations ($\alpha \ll 1$)

In this case we reduce the third-order problem to one of elliptic integrals by suitable transformations. Specifically, we first transform from coordinates relative to the fluid stagnation point to an origin located on the particle stagnation point while rescaling time as in the small oscillation case. This transformation removes the constant terms in the velocity equations but introduces quadratic terms. These quadratic terms are then removed by an additional transformation so that the lowest order nonlinear terms are cubic. The resulting equations are solved for $(\dot{x})^2$ and the solution presented in terms of elliptic functions.

Recalling the initial equations

$$\dot{x} = -A(t) \cos x \, \sin y$$
$$\dot{y} = A(t) \sin x \, \cos y - v_s$$
$$A(t) = 1 + \varepsilon \cos(\omega \alpha t)$$

(3.7)

first remove the constant term with the transformation

$$\xi = x - x_o$$
$$\eta = y$$
$$\gamma = \alpha t$$

(3.8)

where

$$v = \frac{v_s}{A} \quad , \qquad x_o = \sin^{-1} v$$
$$\kappa = \cos x_o$$

(3.9)

to obtain

$$\xi_t = -\kappa \eta + v \xi \eta + \frac{\kappa}{2} \xi^2 \eta + \frac{\kappa}{6} \eta^3$$
$$\eta_t = \kappa \xi - \frac{v}{2}(\xi^2 + \eta^2) - \frac{\kappa}{6} \xi^3 - \frac{\kappa}{2} \xi \eta^2$$

(3.10)

which, upon rescaling, becomes

$$x_T = -y + \mathcal{S}(x,y)$$
$$y_T = x + g(x,y)$$

(3.11)

where

$$\mathcal{S}(x,y) = \frac{v}{\kappa} xy$$
$$g(x,y) = -\frac{v}{2\kappa}(x^2 + y^2)$$

(3.12)

The desired form is

$$\dot{\zeta} = -\eta + \mathcal{F}(\zeta, \eta)$$
$$\dot{\eta} = \zeta + \mathcal{D}(\zeta, \eta) \tag{3.13}$$

where the lowest order terms in $\mathcal{F}$ and $\mathcal{D}$ are cubic. Define $\phi(\zeta, \eta)$ and $\psi(\zeta, \eta)$ such that

$$x = \zeta + \phi(\zeta, \eta)$$
$$y = \eta + \psi(\zeta, \eta) \tag{3.14}$$

From equations (3.11) and (3.14)

$$\frac{d}{dt}\begin{pmatrix} x \\ y \end{pmatrix} = \begin{pmatrix} 0 & -1 \\ 1 & 0 \end{pmatrix} \begin{pmatrix} x \\ y \end{pmatrix} + \begin{pmatrix} f \\ g \end{pmatrix}$$

$$= \begin{pmatrix} \dot{\zeta} \\ \dot{\eta} \end{pmatrix} + \begin{pmatrix} \phi_\zeta & \phi_\eta \\ \psi_\zeta & \psi_\eta \end{pmatrix} \begin{pmatrix} \dot{\zeta} \\ \dot{\eta} \end{pmatrix} \tag{3.15}$$

$$\begin{pmatrix} 0 & -1 \\ 1 & 0 \end{pmatrix} \begin{pmatrix} \zeta + \phi \\ \eta + \psi \end{pmatrix} + \begin{pmatrix} f \\ g \end{pmatrix} = \begin{pmatrix} \dot{\zeta} \\ \dot{\eta} \end{pmatrix} + \begin{pmatrix} \phi_\zeta & \phi_\eta \\ \psi_\zeta & \psi_\eta \end{pmatrix} \begin{pmatrix} \dot{\zeta} \\ \dot{\eta} \end{pmatrix} \tag{3.16}$$

and the requirement

$$\begin{pmatrix} \dot{\zeta} \\ \dot{\eta} \end{pmatrix} = \begin{pmatrix} 0 & -1 \\ 1 & 0 \end{pmatrix} \begin{pmatrix} \zeta \\ \eta \end{pmatrix} + \begin{pmatrix} \mathcal{F} \\ \mathcal{D} \end{pmatrix} \tag{3.17}$$

Expansion of $\phi(\zeta, \eta)$ and $\psi(\zeta, \eta)$ in Taylor series

$$\phi(\zeta, \eta) = A_1 \zeta^2 + B_1 \zeta\eta + C_1 \eta^2 + \phi_3(\zeta, \eta) + \cdots$$
$$= \phi_2(\zeta, \eta) + \phi_3(\zeta, \eta) + \cdots \tag{3.18}$$
$$\psi(\zeta, \eta) = \psi_2(\zeta, \eta) + \psi_3(\zeta, \eta) + \cdots$$

and substitution into equation (3.15) yields, for ϕ_2 and ψ_2

$$-\eta\phi_\zeta + \zeta\phi_\eta + \psi - \zeta = 0$$
$$-\eta\psi_\zeta + \zeta\psi_\eta - \phi - g = 0 \tag{3.19}$$

Determining the quadratic parts of $f(x,y)$ and $g(x,y)$ in terms of ζ and η and solving the above equations for ϕ_2 and ψ_2 yields

$$\phi_2(\zeta,\eta) = \frac{v}{6}\zeta^2 + \frac{5v}{6}\eta^2$$

$$\psi_2(\zeta,\eta) = -\frac{2v}{6}\zeta\eta \tag{3.20}$$

With equation (3.20) and the rescaling

$$x = \beta\zeta \qquad y = \beta\eta \qquad \beta = \left(\frac{6}{v}\right)^{1/2} \tag{3.21}$$

equations (3.17) become

$$\dot{x} = -y - x^2 y + 5y^3$$

$$\dot{y} = x - 3xy^2 - x^3 \tag{3.22}$$

Eliminating y yields

$$\ddot{x} = -x + 10 x (\dot{x})^2 \tag{3.23}$$

or

$$(\dot{x})^2 = A e^{10x^2} + \frac{1}{10} \tag{3.24}$$

Expanding the exponential and solving the truncated system as an elliptic integral yields (Abramowitz and Stegan (1964))

$$x = \frac{b}{50A} sc\left(t, \frac{a^2 - b^2}{a^2}\right) \tag{3.25}$$

where

$$a^2 = \frac{1}{10}\left(1 + (-(1 + \tfrac{1}{5A}))^{1/2}\right)$$

$$b^2 = \frac{1}{10}\left(1 - (-(1 + \tfrac{1}{5A}))^{1/2}\right) \tag{3.26}$$

and sc is a Jacobian elliptic function. The process must now be repeated allowing the constants of this case to become functions of the slow time, τ .

4) NUMERICAL EXPERIMENTS

In order to explore particle motion outside those areas accessible to analytic investigation, a numerical model of the tank was constructed. The model evolves the particle position given the fluid flow field of equation (2.1) with A(t) as in equation (3.1). We simulate the region $0 <= x <= 2$; $0 <= y <= 2$ with periodic boundary conditions. Any particle passing through the bottom (x,0) is reintroduced at the top (x,2π). A particle which passes through the bottom boundary is said to "fall out" of the cell, as opposed to a "retained" particle which does not cross a horizontal cell boundary. The horizontal motion of the particles is strictly that of the fluid, thus contours of zero horizontal fluid velocity, such as the lines

$y = n \mathcal{W}$, $n = 0,1,2,\ldots$, are barriers which the particles cannot cross. None were observed to do so. As noted above, all particles were initially placed in the counter-clockwise cell which is centered at $(1.5 \mathcal{W}, 1.5 \mathcal{W})$.

Observations with a steady fluid flow were noted in Section 2 above. When the flow becomes periodic, there is a qualitative change in the regions of retention. In the steady case, negatively buoyant particles arbitrarily near an upflowing branch are retained, completing closed orbits. This is apparent in the lower part of figure 2a where the retention regions of two horizontally adjacent cells appear to merge across the cell boundary, In periodic flow, each region of retention is separated from the cell boundary by a finite band. Particles initially in this band will often remain in the cell for many revolutions, but will fall out. The physical explanation of the phenomenon is straightforward. For small ε , a particle oscillates about its equilibrium path. As long as these excursions are completely within the region of retention, the particle will remain in the cell. A particle which oscillates to a point outside the retention region may remain in the cell for a time, depending on where in the cell it is when it crosses the boundary. Eventually, most such particles will cross the boundary near the bottom of their trajectories and fall out of the cell. It is conceivable that, for certain initial positions, a resonance between the fluid oscillations and the particle orbital motions occurs which tends to stabilize the particle. While the stabilization of particles in regions which are unstable in the mean flow has not been observed, some particles tracing orbits which do not lie entirely within the retention region for the steady flow corresponding to $A = (1 - \varepsilon)$, are retained for the entire observation period (1000 fluid periods) and appear stable.

Consider the paths of particles near the region of retention which, after some time in the initial cell, fall out. When these paths are strobed, chaotic motion is observed. A particle well within the region of retention will remain in the cell for the entire observation period (over 5000 fluid periods), while a particle far outside the region will fall through the cell with an average residence time of approximately one period. A particle in this intermediate region falls out of the original cell, usually passing quickly through several cells before being reentrained. The residence time averaged over a chaotic fall through 500 cells is typically 15 periods per cell. Figure 9 is a histogram of the frequency of various residence times. It is clear that these particles take much longer to fall through a series of rolls than would be predicted from the steady case.

Examples of these motions are shown in figure 10. Particles well within the region of retention display two distinct classes of motion. In the first, a generalization of oscillations about the mean path, the particle moves within the bounds of the two orbits for the steady flow with $A = (1 + \varepsilon)$ and $A = (1 - \varepsilon)$. The particle track fills in a two-dimensional cross-section of a donut, oscillating back and forth along a path which does not close on itself (figures 4 and 5). When the position of the particle is recorded once per cycle of the background fluid flow, the resulting graph is a cross-section (an x,y plot at given phase) of the three-dimensional phase space of the system. Figure 4b is the motion of the particle shown in figure 4a strobed in this way. By strobing at different phases it is seen that the particle winds about on a torus in phase space. Since a single point in phase space defines the future evolution of the system, the particles located within closed curves on Poincare sections are trapped there.
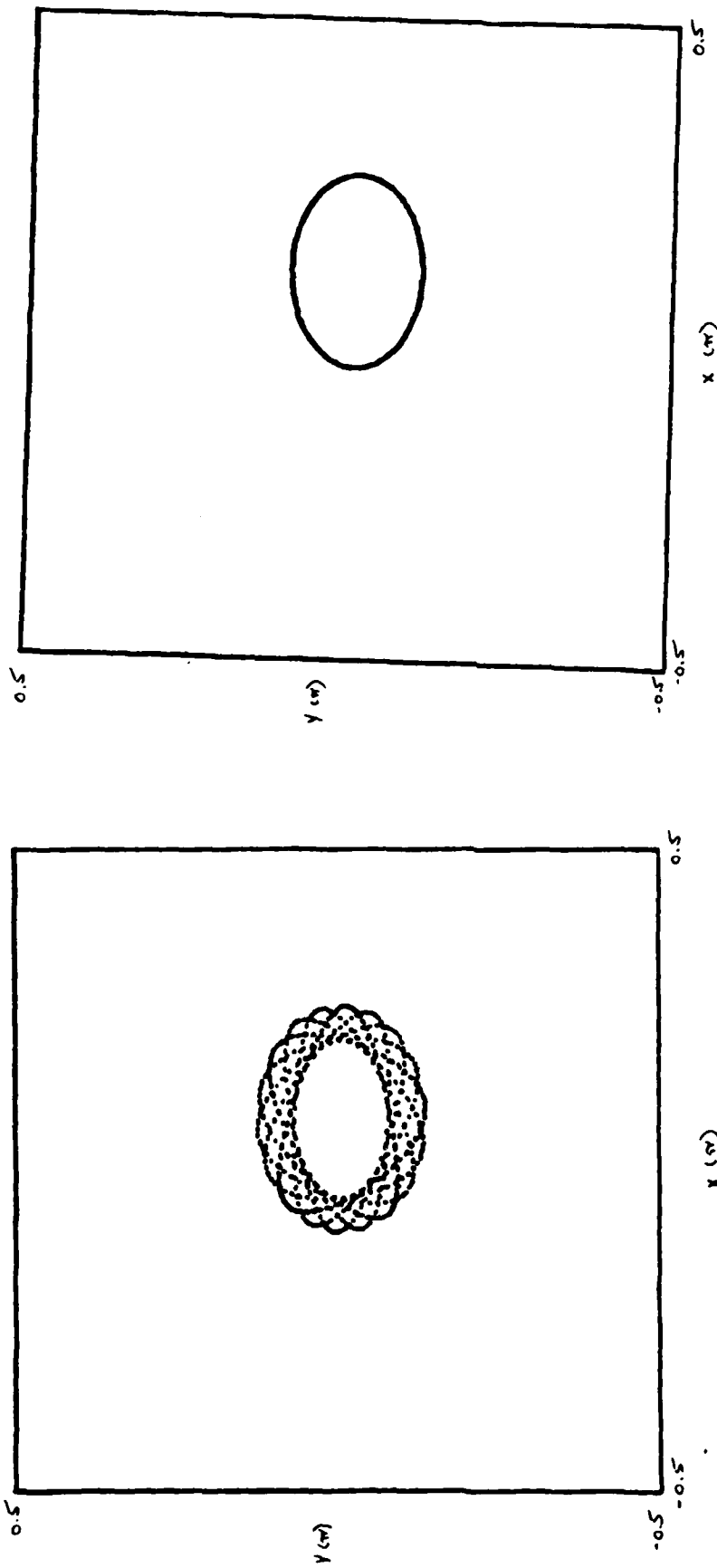
Figure 4

Solution for small amplitude oscillations. Here X0 = 0.10;
Y0 = 0.10 (see equation 2.2); V_s = 0.25; ε = 0.5; P = 4.0;
(A) Particle track with T_{max} = 100.
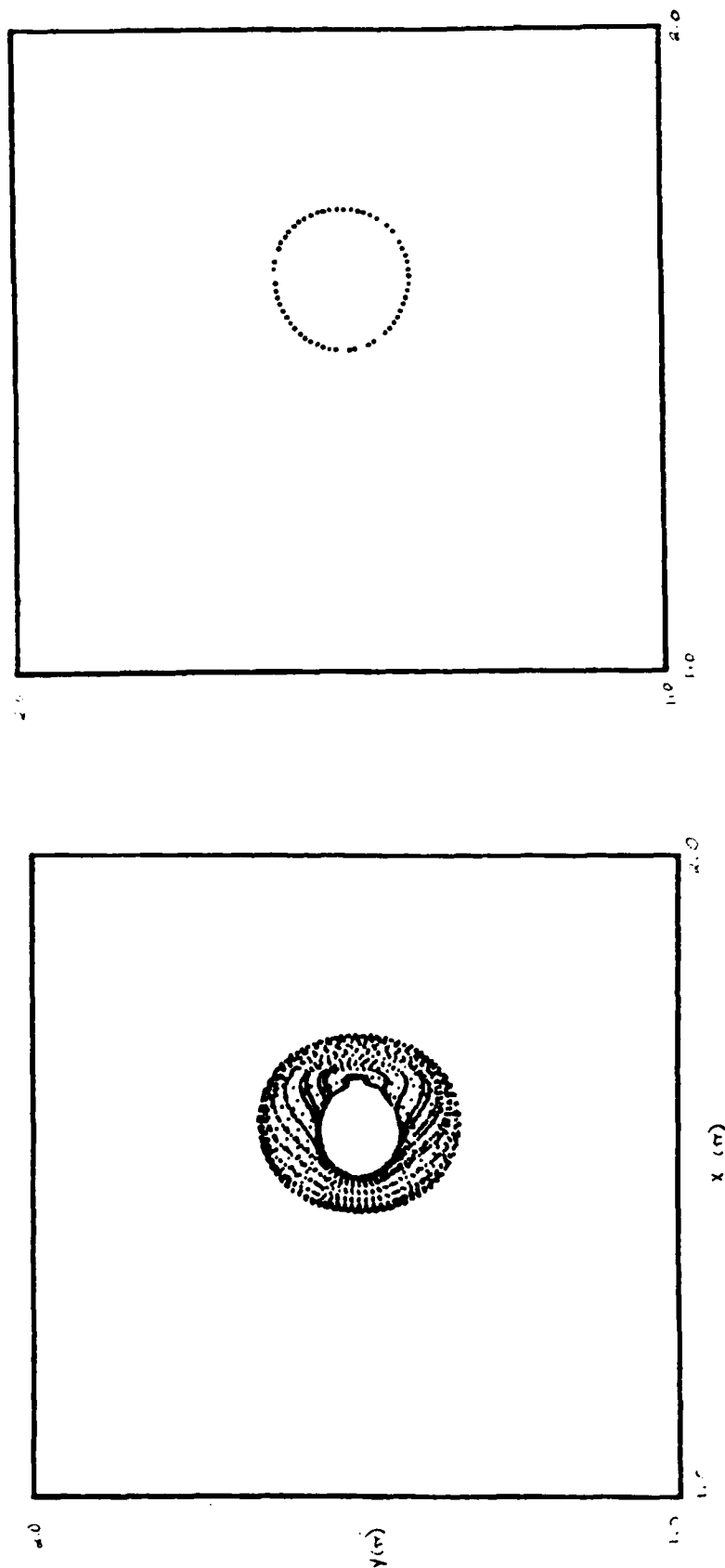(B) Strobed particle motion with T_{max}= 4000.

Figure 5

Model particle trajectory with X0 = 1.50; Y0 = 1.50;
V_s = 0.25; ε = 0.50; P = 4.40. (A) Particle
track with T_{max} = 250. (B) Strobed particle motion
with T_{max} = 2500.

x (σ)

y (σ)

A second behavior is observed when the particle completes an integral number of revolutions about the stagnation point in an integral number of fluid oscillations. During each revolution about x_s, the particle follows one of several distinct pathways. Which path is executed depends on the phase of the flow as the particle crosses the x axis from below ($x > x_s$). An example of this type of motion is shown in figure 6. The clear regions shown remain clear, with the particle being restricted to and slowly filling the outlined region. In this example two revolutions about the stagnation point, one along each branch, occur in three cycles of the background fluid flow. We shall call this completion of the motion (several revolutions until the crossing of the x axis occurs at approximately the same position and phase) a particle orbit. In this case the particle orbital period is three times the fluid flow period.

When this motion is strobed at the fluid flow frequency, islands are observed (figure 7). Particle motion on these islands is stable for all times observed. The particle visits every island in turn, slowly delineating each. Poincare sections taken at different phases are shown in figure 8. The islands slowly deform and rotate in the direction of particle motion until, one full fluid period later, particles initially on island 1 (2,3) have taken positions on island 3 (1,2). Recalling that these figures are cross-sections of a three-dimensional phase space, it is seen that this motion takes place on a torus which is stretched and twisted, closing on itself in three fluid periods. Particle paths wind around on this torus.

Particles initially just inside or outside the island ring (relative to the particle stagnation point) wind abut a single torus. Particles within the boundaries of an island wind about a similarly twisted torus always bounded by the outer torus (coaxially). Particles initially located between the islands at the same distance from the stagnation point are observed to display chaotic motion contained by the tori which bound the island ring.

The strobed paths for a variety of initial positions are shown in figure 10. Counting from the left, the first particle (1.1 π , 1.5 π) falls through the cell, oscillating about the strobed path shown. This line presents a barrier which other particles do not cross - hence the open region in the lower left-hand side of the figure. This open area is occupied by the mirror particles of those plotted. As the initial position of the point is moved to the right along y = 1.5 π , this curve breaks up into islands, which in turn becomes part of the chaotic sea shown in the figure. Particles initially in this area are found to become trapped in a cell for many revolutions and then fall (drifting) through the cell (often several) before becoming reentrained. Embedded in this chaotic sea are regions avoided by the falling particle. The largest of such areas is the region of retention containing the particle stag- nation point. Islands are observed in this and several other of the barren regions where the particle motion is such that they are stabilized against fall out by the oscillations. An example of this behavior is the particle whose motion produces the "ears" in figure 10. Here the period of the particle motion is such that the maximum of the fluid flow occurs twice in each revolution - once at the top of the trajectory and once at the bottom. Particles following these trajectories travel outside the region of retention for a steady flow with A = (1-ϵ). The three islands located within the retention region ("eyes" and "mouth") are the same islands shown in figure 7. Also shown are one enclosed and one encompassing torus.

Figure 7

Particle path of figure 6 stobed at the frequency of the
fluid oscillations. T_{max} = 1000.
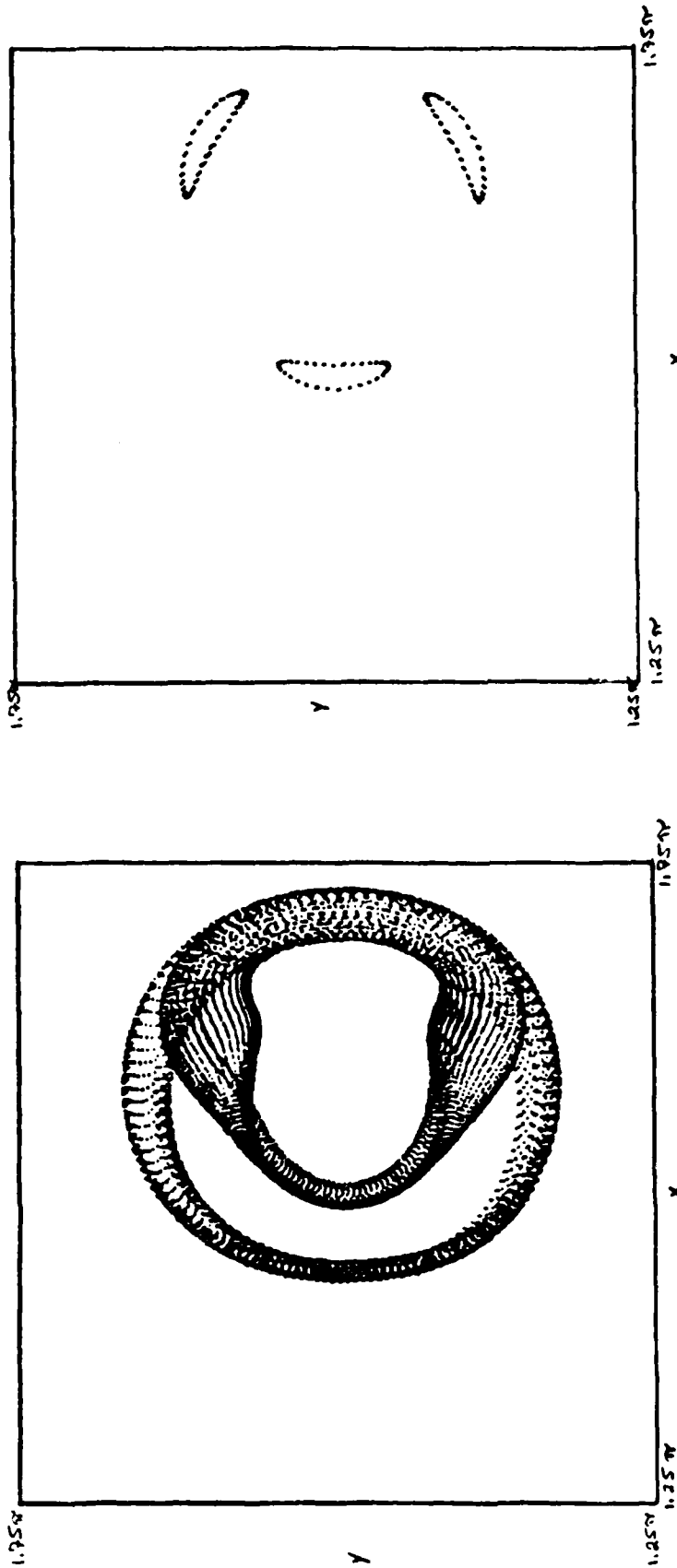
Figure 6

Particle trajectory charactoristic of islands. In this
case X0 = 1.50; Y0 = 1.50; V = 0.25; ε = 0.50; P = 4.50 .
Note that this figure is an enlargement of the cell.
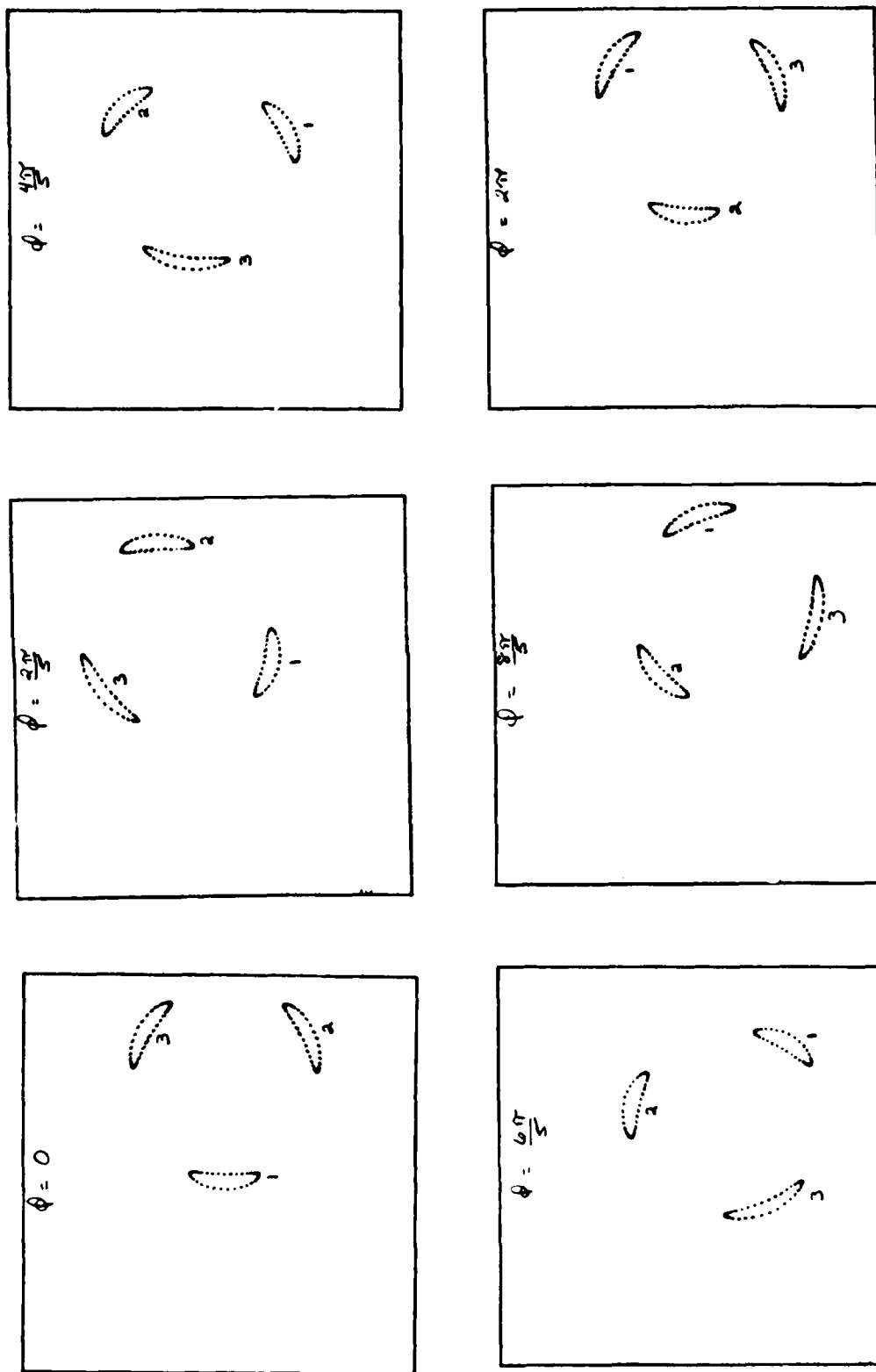
Figure 8

Location of the islands of figure 7 at various phases of
the fluid flow. The region shown in each box above is the
same as shown in figure 6.
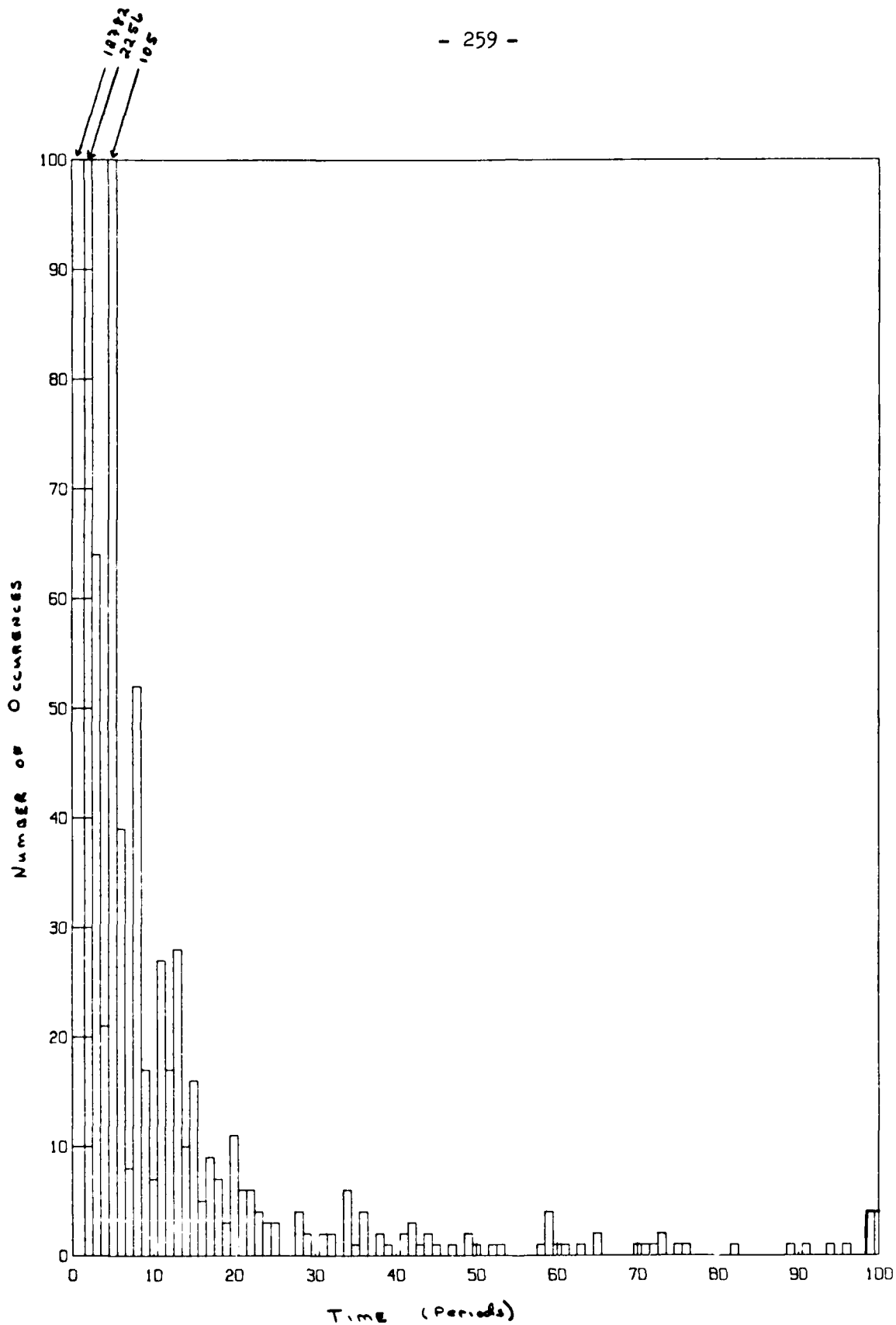
Figure 9

A sample histogram showing the relative frequency of
various residence times for particles in the fallout
region. Maximum time observed = 100 periods.
$V_s = 0.25$; $\mathcal{E} = 0.50$; $P = 4.50$.
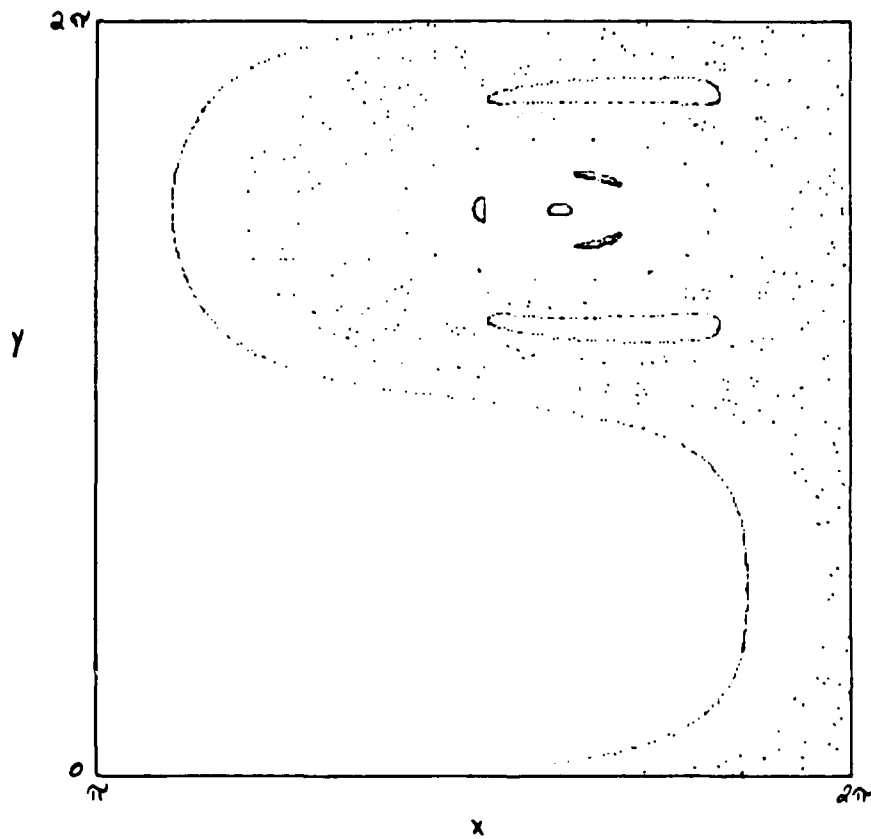
Figure 10

Strobed motions of six particles with V_s = 0.25 ;
ϵ = 0.50 ; P = 4.50 .

Whether particles outside the mean region of retention can be stabilized by the fluid oscillations is a question which deserves further investigation. Here we briefly note some initial observations with regard to the effect of increasing the magnitude of the flow oscillations on the retention of particles in marginally stable regions. Figure 11 shows the region of the upper ear in figure 10 for several values of ε. At small ε, a stable orbit is observed. As ε increases this torus breaks up into islands and then disintegrates altogether, the particles falling through the cell after only a few revolutions. As ε is increased further, the region again begins to stabilize - particles still fall through, however they spend a great deal of time in these quasi-stable regions between vertical drops.

At very large values of ε a different type of behavior is observed. Figure 12 displays the strobed trajectories for particles with the same initial positions as those in figure 10, with $\varepsilon = 8.0$. For $\varepsilon > 1$, the flow reverses direction. Quasistable particle motion is observed to be centered about the stagnation point of the fluid. A large portion of the cell is subject to chaotic particle motions. The three island ring and fuzzy inner and outer elliptical paths are observed to be slowly evolving outward. The evolution of the islands is much slower than that of either of the simple tori. It would be interesting to observe how (if) the particles within the island ring escape. Although their orbits are evolving outward, the inner particles in figure 10 are still in the initial cell after over 500 periods of the fluid flow.

The motion at large ε is qualitatively different from that of small ε (see figure 13). Quasistable regions in this flow have been found where the particle revolution period is slightly less than half the fluid period. Such a particle, initially near the top of its orbit will be swept around by the strong flow, again to near the top of the cell, as the flow weakens it will sink down toward the cell center and then be swept around in the opposite direction sense by the second half cycle of the fluid flow. Often the radius of the particle from the stagnation point will increase until the particle falls out, however some initial conditions particles have been observed to be carried up above their initial points and then dropped back near their original position (and phase). In this manner the particle is retained in the cell for a very long time ($t > t$ max observations = 500 fluid periods).

5) CONCLUDING REMARKS

The motion of slowly sinking particles in a simple time dependent flow has been examined. It is found that this system is quite rich, displaying a surprising variety of particle motions. In addition to bounded chaotic motions, particles falling through the cells chaotically are often entrained and retained for significant periods of time, so that the sedimentation rate in this case varies substantially from the case of steady rolls. Investigations of the effects of both small and large fluid oscillations reveal that retained particles are more stable than might be expected.

The model may be extended to consider inertial effects. These will not necessarily be destabilizing, especially in the case of large fluid oscillations. Inclusion of Brownian motion would allow migration across vertical cell boundaries, as well as into and out of regions of retention, with interesting effects on the mean sedimentation rate. More applied problems,

$\mathcal{E} = 0.40$

$\mathcal{E} = 0.45$

$\mathcal{E} = 0.475$
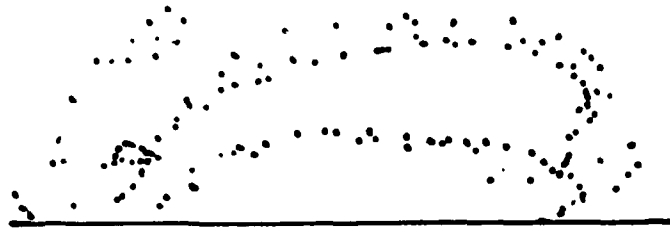
$\mathcal{E} = 0.50$
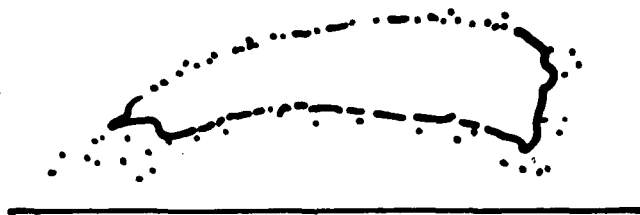
Figure 11

Relative stability of the ear region of figure 10 for several values of $\mathcal{E}$.
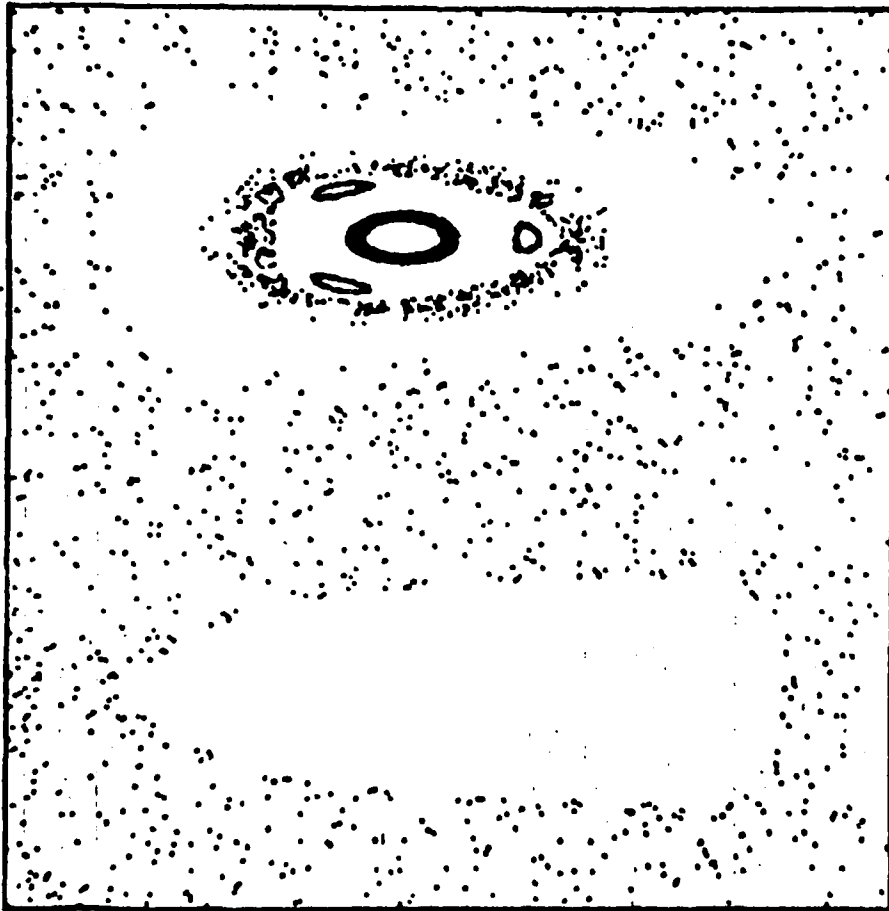
Figure 12

Strobed motions of six particles with $V_S = 0.25$;
$\varepsilon = 0.50$; $P = 8.00$.
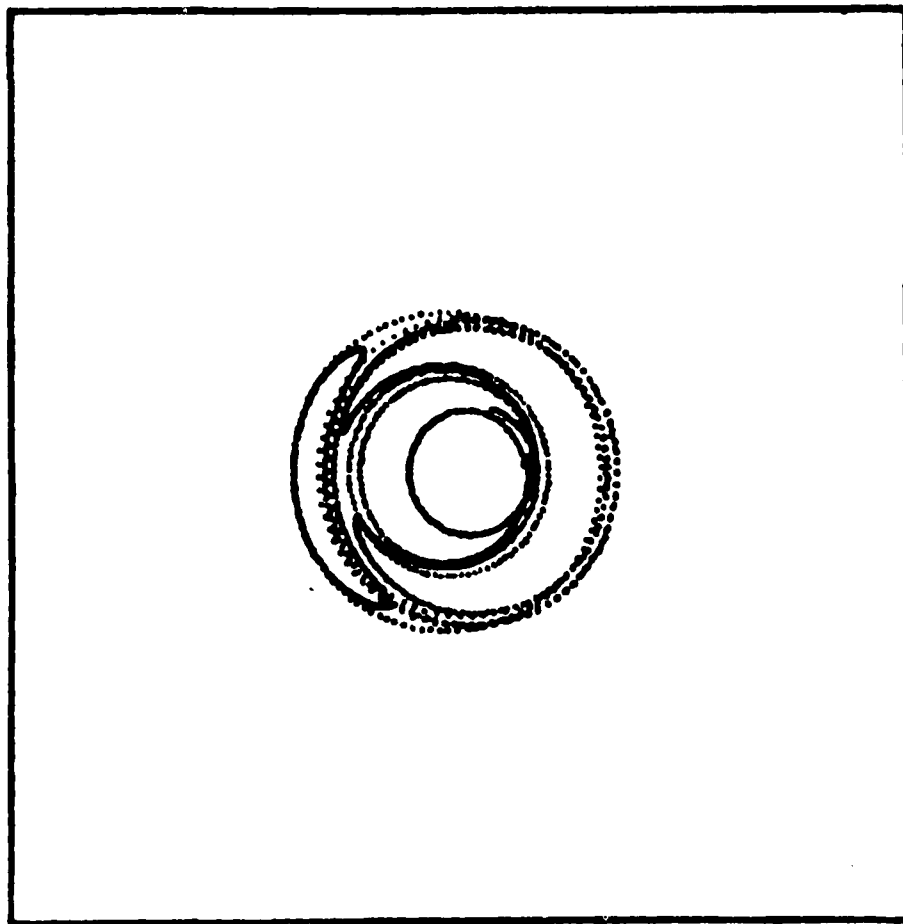
Figure 13

Particle track with $\varepsilon = 8.0$; $V_s = 0.25$; $P = 4.50$.

such as precipitation and magma crystal growth may be approached by including a growth parameter which is a function of location and time. In all, this type of model provides a foothold into many topics of current interest.

REFERENCES

Abramowitz, M. and L. Stegun, 1964. Handbook of Mathematical Functions. U. S. Government Printing Office, Washington, D. C.

Aref, H., 1984. Stirring by chaotic advection. J. Fluid Mech., 143, 1.

Stommel, H., 1949. Trajectories of small bodies sinking slowly through convection cells. J. Mar. Res., 8, 24.

Tooby, P., G. Wick and J. Isaacs, 1977. The motion of a small sphere in a rotating velocity field. J. Geophys. Res., 82, 2096.

THE LINEAR INSTABILITY OF CONTINUOUS HETON BAND CLOUDS

Lorenzo M. Polvani

Consider a fluid consisting of two homogeneous layers of equal equi-
librium heights; the upper layer contains a point vortex; the lower layer con-
tains a point vortex of equal and opposite strength; unless the two vortices
are directly above one another, the pair will move in a straight line perpen-
dicular to its axis. Such a pair of vortices has been named "Heton" by Hogg
and Stommel (1984a) since it has the important property of transferring heat;
a Heton is said to be hot (cold) if the vortex in the upper layer is anti-
cyclonic (cyclonic) in which case, via the thermal wind relation, the inter-
face between the two layers is lowered (raised).

Hogg and Stommel (1984b) have investigated several interesting inter-
actions between Hetons. The explosive behavior of a band cloud of Heton point
vortices is the one which we are going to discuss in this work.

A cloud of regularly spaced, untilted Hetons (i.e. with the upper and
lower vortices lying directly above one another) occupy the lower half plane
($y \leq 0$) as illustrated in Figure 1.

fig. 1
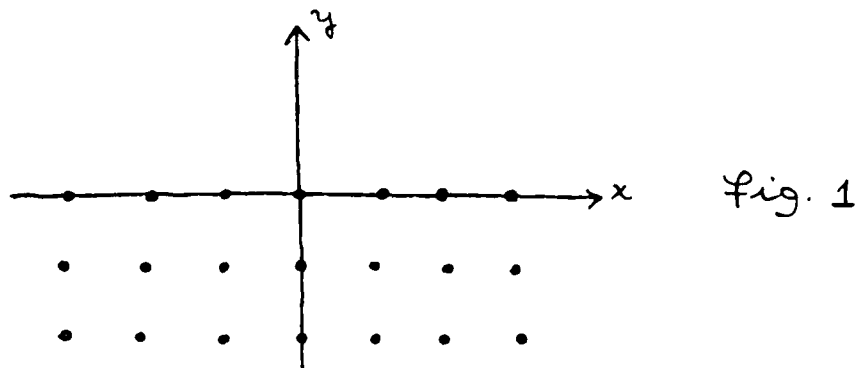
If the Hetons are spaced far enough from one another the cloud is
unstable since the Hetons at the edge of the cloud are split by the baroclinic
shear flow produced by the Hetons in the interior of the cloud, and as they
split they are self-propelled to $y > 0$. However, an explosion will not occur
in the case where neighboring Hetons are very close; indeed in such a case the
top vortex of the split Hetons at the edge of the cloud will be affected more
by its neighbor's bottom vortex than by its own, and this will have the effect
of restoring the Hetons to their original positions (Hogg and Stommel, 1984b).

The purpose of this work is to investigate the stability of a Heton
band cloud from a somewhat complementary point of view. Instead of con-
sidering a large number of Heton point vortices, we study the stability of a
band cloud in which the vorticity is spread uniformly throughout the cloud.
We will first do the inviscid problem and then add dissipation and see what
effect it has on the stability of the system.

1. The Linear Stability of an Inviscid Heton Band Cloud.

Our model for the Heton band cloud is a fluid made up of two homogeneous layers of equal equilibrium depths occupying the region $-L_c \leq y \leq \infty$ with the following vorticity distribution: in the region $-L_c \leq y \leq 0$ (the cloud) the upper layer has uniform potential vorticity Q and the lower layer has uniform potential vorticity $-Q$; in the region $0 \leq y$ the potential vorticity is zero in both layers. This situation, illustrated in Figure 2, simulates a uniform Heton band cloud confined in the region $-L_c \leq y \leq 0$.
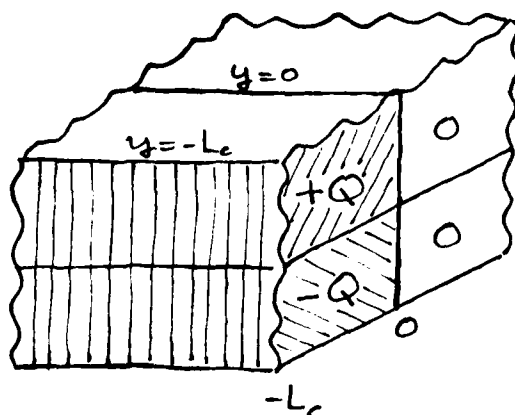
fig. 2

It is convenient to use the width of the cloud L_c as the length scale. Then the inviscid, quasigeostrophic potential vorticity equation for the two-layer system can be written (Pedlosky, 1979) in nondimensional form

$$\frac{\partial}{\partial t} q_n + J(\psi_n, q_n) = 0 \qquad n = 1, 2 \qquad (1)$$

where

$$q_n = \nabla^2 \psi_n + (-1)^n F (\psi_1 - \psi_2)$$

The only parameter appearing is F, and it is defined by

$$F = (L_c/L_D)^2$$

where L_D is the radius of deformation. Note that since lengths have been scaled with L_c, the nondimensional cloud width is 1.

The first thing we wish to determine is the basic velocity field associated with the distribution of potential vorticity illustrated in Figure 2.

We need to solve the following system:

$$\begin{cases} q_1 = \nabla^2 \Psi_1 - F(\Psi_1 - \Psi_2) = +Q \qquad -1 \le y < 0 \\ \qquad\qquad\qquad\qquad\qquad = 0 \qquad\qquad y > 0 \\ \\ q_2 = \nabla^2 \Psi_2 - F(\Psi_2 - \Psi_1) = -Q \qquad -1 \le y < 0 \\ \qquad\qquad\qquad\qquad\qquad = 0 \qquad\qquad y > 0 \end{cases}$$

together with the requirement that Ψ_1 and Ψ_2 be continuous at $y = 0$, to insure continuity of the interface between the two layers. It is easy to show that the above system requires

$$\nabla^2 (\Psi_1 + \Psi_2) = 0 \qquad\qquad \text{for all } y.$$

Since we wish to consider a purely baroclinic cloud we simply choose

$$\Psi_1 = -\Psi_2 \qquad\qquad \text{for all } y.$$

Then we only need to solve the problem in one layer, say the upper layer:

$$\begin{cases} \nabla^2 \Psi_1 - 2F \Psi_1 = 0 \qquad y > 0 \\ \nabla^2 \Psi_1 - 2F \Psi_1 = Q \qquad -1 \le y < 0 \end{cases}$$

The solution which is continuous at $y = 0$, bounded as $y \rightarrow \infty$ and whose derivative is continuous at $y = 0$ is

$$\begin{cases} \Psi_1 = -\dfrac{Q}{4F} e^{-\sqrt{2F}\, y} \qquad\qquad y > 0 \\ \\ \qquad = +\dfrac{Q}{4F} e^{+\sqrt{2F}\, y} - \dfrac{Q}{2F} \qquad -1 \le y < 0 \\ \\ \Psi_2 = -\Psi_1 \qquad\qquad\qquad \text{for all } y. \end{cases}$$

From this we can now calculate the velocities and the shears induced by the Heton cloud.

$$
\begin{cases}
U_1 = -\dfrac{\partial}{\partial y}\,\Psi_1 = -\dfrac{Q}{2\sqrt{2F}}\,e^{-\sqrt{2F}\,y} & y > 0 \\[2em]
\qquad\qquad = -\dfrac{Q}{2\sqrt{2F}}\,e^{+\sqrt{2F}\,y} & -1 \le y < 0 \\[2em]
\qquad U_2 = -U_1 & \text{for all } y.
\end{cases}
$$

$$
\begin{cases}
\dfrac{\partial}{\partial y}\,U_1 \bigg|_{y=0^+} = \dfrac{Q}{2} \\[2em]
\dfrac{\partial}{\partial y}\,U_1 \bigg|_{y=0^-} = -\dfrac{Q}{2} \\[2em]
\dfrac{\partial}{\partial y}\,U_2 = -\dfrac{\partial}{\partial y}\,U_1 & \text{for all } y
\end{cases}
$$

The important thing to note is that while U_1 and U_2 are continuous at $y = 0$ the horizontal velocity shear is not.
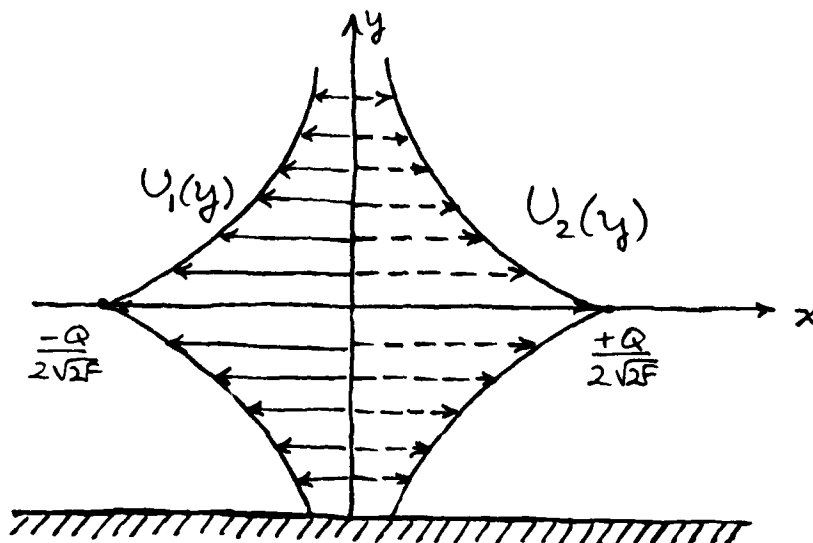
fig. 3

The basic velocity profile induced by the Heton band cloud is illustrated in Figure 3. At this stage nothing happens since the potential vorticity is spread uniformly throughout the cloud; the system is steady.

To test the stability of the cloud, we must now introduce a perturbation on its boundary in order to create some nonuniformity in the vorticity distribution. As is customary we write

$$\psi_n(x,y,t) = \Psi_n(y) + \phi_n(x,y,t) \qquad n = 1,2$$

where ϕ_n are the perturbations. The equations satisfied by the ϕ_n are easily found from (1):

$$\begin{cases} \nabla^2\phi_1 + F(\phi_2 - \phi_1) = 0 \\ \nabla^2\phi_2 + F(\phi_1 - \phi_2) = 0 \end{cases}$$

together with the boundary conditions

$$\begin{cases} [\phi_n] = 0 & \text{at } y = 0 \\ \left[\left(\frac{\partial}{\partial t} + U_n\frac{\partial}{\partial x}\right)\frac{\partial}{\partial y}\phi_n - \frac{\partial}{\partial y}U_n\frac{\partial}{\partial x}\phi_n\right] = 0 & \text{at } y = 0 \\ \frac{\partial}{\partial x}\phi_n = 0 & \text{at } y = -1 \\ \phi_n \quad \text{bounded as } y \to +\infty \end{cases}$$

where we have used the notation

$$[f] = \lim_{\varepsilon \to 0}\left(f(y+\varepsilon) - f(y-\varepsilon)\right)$$

The first condition follows from the requirement that the boundary of the Heton cloud be continuous. The second is a linearization of the continuity of pressure at y = 0. The third is due to the existence of a solid boundary at y = -1.

If one tries solutions of the form

$$\phi_n = \varphi_n e^{ik(x-ct)}$$

one finds that

$$\varphi_1 = A e^{-ky} + B e^{-ly}$$
$$\varphi_2 = A e^{-ky} - B e^{-ly}$$
$$\left.\right\} \quad y > 0$$

(11)

$$\varphi_1 = A \frac{\sinh k(y+1)}{\sinh k} + B \frac{\sinh l(y+1)}{\sinh l}$$
$$\varphi_2 = A \frac{\sinh k(y+1)}{\sinh k} - B \frac{\sinh l(y+1)}{\sinh l}$$
$$\left.\right\} \quad -1 \le y < 0$$

provided A and B satisfy

$$A\left[(c+U_0)k(1+\coth k)-Q\right] + B\left[(c+U_0)l(1+\coth l)-Q\right] = 0$$

$$A\left[(c-U_0)k(1+\coth k)+Q\right] + B\left[(-c+U_0)l(1+\coth l)-Q\right] = 0$$

where

$$U_0 = -U_1(y=0) = U_2(y=0) = \frac{Q}{2\sqrt{2F}} \quad \text{and} \quad l^2 = k^2 + 2F$$

The dispersion relation for c is obtained by requiring that a nontrivial
solution for A and B exist; this gives

$$c^2 = \frac{Q^2}{2F} \frac{\left[\sqrt{2F} - \frac{1}{2}k(1+\coth k)\right]\left[\sqrt{2F} - \frac{1}{2}l(1+\coth l)\right]}{k(1+\coth k)\,l(1+\coth l)}$$
(111)

The second bracket in the numerator is always negative since

$$\sqrt{2F} < \sqrt{2F+k^2} \ \frac{1}{2}\left(1+\coth\sqrt{2F+k^2}\right) \qquad \text{for all k.}$$

The condition for instability is then given by the first bracket alone. The
Heton cloud will be unstable when F exceeds the critical value F_c given by

$$F_c = \frac{1}{8}k^2(1+\coth k)^2$$

The domain of instability is illustrated in Figure 4.

FIG. 4
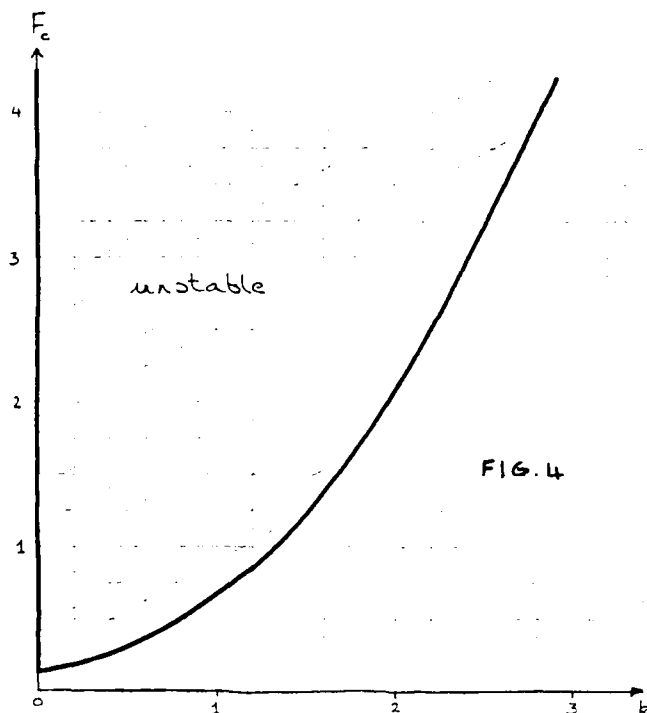
Two interesting limiting cases can be considered: $k \ll 1$ and $k \gg 1$. Since *we have scaled lengths with the width of the cloud band* L_c

$$k = 2\pi \frac{L_c}{\lambda}$$

where λ is the dimensional wavelength of the perturbation. In the respective asymptotic limits the instability condition becomes:

$$L_D < 2\sqrt{2} \, L_c \qquad \text{for} \qquad \lambda \gg L_c$$

and

$$L_D < \frac{1}{\sqrt{2}\,\pi} \lambda \qquad \text{for} \qquad \lambda \ll L_c$$

Therefore instability requires that, apart from some O(1) factors, the radius of deformation of the two-layer model be smaller than the lesser of L_c and λ.

From the dispersion relation (iii) it follows that for an unstable growing wave the real part of c is identically zero: unstable waves are stationary.

Finally, one can easily show that for the marginally stable wave B = 0 in (11). This means that the velocity field induced by the marginal wave is totally barotropic, which in turn implies that the wave is extracting no energy from the basic flow.

2. The Linear Stability of a Heton Band Cloud in the Presence of Dissipation.

In order to investigate the effect of dissipation on the growth of a perturbation on the boundary of a Heton band cloud it is helpful to consider a situation which the basic fields ψ_n induced by the cloud are time independent. We can, for this purpose, assume the presence of a source of potential vorticity which supplies as much vorticity as is dissipated by friction, so as to maintain the basic distribution of potential vorticity time independent and identical to the one shown in Figure 2.

The usual way to represent dissipation in a two-layer model is to introduce a term of the form $-n\nabla^2\psi_n$ on the righthand side of (1); such a term represents Ekman layers of equal strength located at the top and bottom of the cloud (friction at the interface between the upper and lower layers can be neglected). The presence of a term proportional to $\nabla^2\psi_n$ would, however, make the differential equation for the perturbation potential vorticity impossible to solve analytically. In order to make the problem more tractable we have therefore chosen to represent dissipation by a term $-\alpha q_n$ on the righthand side of (1). With this choice the dispersion relation becomes:

$$\left(c + i\,\alpha/k\right)^2 = \frac{Q^2}{2F}\; \frac{\left[\sqrt{2F} - \frac{1}{2}k(1+\coth k)\right]\left[\sqrt{2F} - \frac{1}{2}\ell(1+\coth \ell)\right]}{k(1+\coth k)\,\ell(1+\coth \ell)}$$

$$\ell^2 = k^2 + 2F$$

The second bracket in the numerator is always negative. When

$$F < \frac{1}{8} k^2 (1+\coth k)^2$$

the righthand side is positive and upon taking the square root one gets

$$c = \pm \frac{Q}{\sqrt{2F}}\left\{ \frac{\left[\sqrt{2F} - \frac{1}{2}k(1+\coth k)\right]\left[\sqrt{2F} - \frac{\ell}{2}(1+\coth \ell)\right]}{k(1+\coth k)\,\ell(1+\coth \ell)}\right\}^{1/2} - i\,\frac{\alpha}{k}$$

For all k, the perturbation is damped by the dissipation and no growth is possible. Alternatively when

$$F > \frac{1}{8} k^2 (1+\coth k)^2$$

the dispersion relation becomes

$$c = -\frac{i\alpha}{k} \pm i\frac{Q}{\sqrt{2F}} \left\{ \frac{\left[\sqrt{2F} - \frac{1}{2}k(1+\coth k)\right]\left[\frac{1}{2}l(1+\coth l) - \sqrt{2F}\right]}{k(1+\coth k)\, l(1+\coth l)} \right\}^{1/2}$$

The curve of marginal stability, which must lie above the inviscid curve $F_c = \frac{k^2}{8}(1+\coth k)^2$, is then given by

$$\frac{\alpha^2}{k^2} = \frac{Q^2}{2F_c} \frac{\left[\sqrt{2F_c} - \frac{k}{2}(1+\coth k)\right]\left[\frac{l}{2}(1+\coth l) - \sqrt{2F_c}\right]}{k(1+\coth k)\, l(1+\coth l)} \qquad\text{(iv)}$$

$$l^2 = k^2 + 2F_c$$

In order to solve this equation for F_c as a function of k we have found it useful to rewrite it as follows:

$$\frac{\alpha^2}{Q^2} = M(x, R) \qquad\text{(v)}$$

where $k \equiv \sqrt{2F_c}\, x$ and $R \equiv \sqrt{2F_c}$ and

$$M(x,R) = \frac{x\left[1 - x\left(\frac{1+\coth xR}{2}\right)\right]\left[\sqrt{1+x^2}\left(\frac{1+\coth R\sqrt{1+x^2}}{2}\right) - 1\right]}{\sqrt{1+x^2}\,(1+\coth xR)\,(1+\coth R\sqrt{1+x^2})}$$

This choice of variable is suggested by the limiting case $R \to \infty$; in such a case the hyperbolic cotangents disappear and $M(x, \infty)$ takes the simple form

$$M_\infty(x) \sim \frac{x(1-x)\left[\sqrt{1+x^2} - 1\right]}{4\sqrt{1+x^2}}$$

$$\sim \frac{1}{4} x(1-x)\left(1 - \frac{1}{\sqrt{1+x^2}}\right)$$

FIG. 5
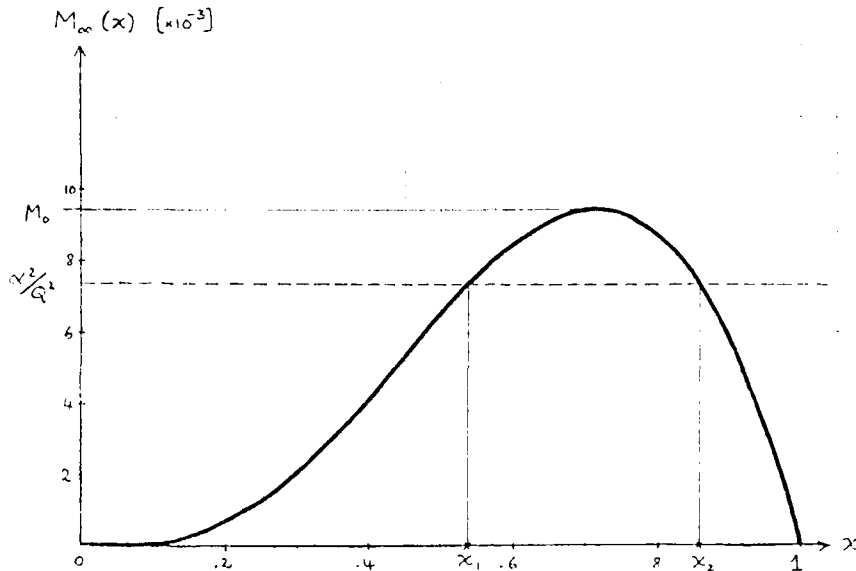
On Figure 5 we have plotted the curve $y = M_\infty(x)$ together with the horizontal line $y = \alpha^2/Q^2$. The solution of (v) are the points where the two curves intersect.

The first thing to notice is that for $\alpha^2/Q^2 > M_o$ no solution exists; this implies that when dissipation exceeds some maximum value all perturbations will be damped. If, alternatively, the dissipation is not too strong then, in the limit of large R (i.e. of large E), the marginal curve is made up of two branches corresponding to the two solutions of

$$\frac{\alpha^2}{Q^2} = \frac{1}{4} x(1-x)\left(1 - \frac{1}{\sqrt{1+x^2}}\right)$$

Both of these branches are parabolas given by

$$F_c \approx \frac{k^2}{2x_i} \qquad i = 1,2 \qquad \text{for} \quad F_c \gg 1$$

In order to understand the behavior of $F_c(k)$ for small values of F_c, we must next examine the shape of $M(x,R)$ vs x for values of $R \gg 1$. In Figure 6 are illustrated several curves of $M(x,R)$ vs x for different values of R.
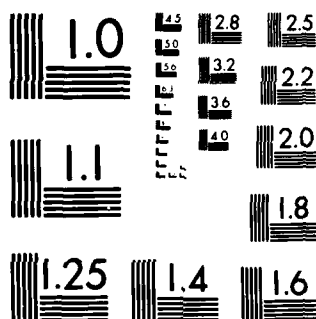
MICROCOPY RESOLUTION TEST CHART

NATIONAL BUREAU OF STANDARDS-1963-A

FIG. 6
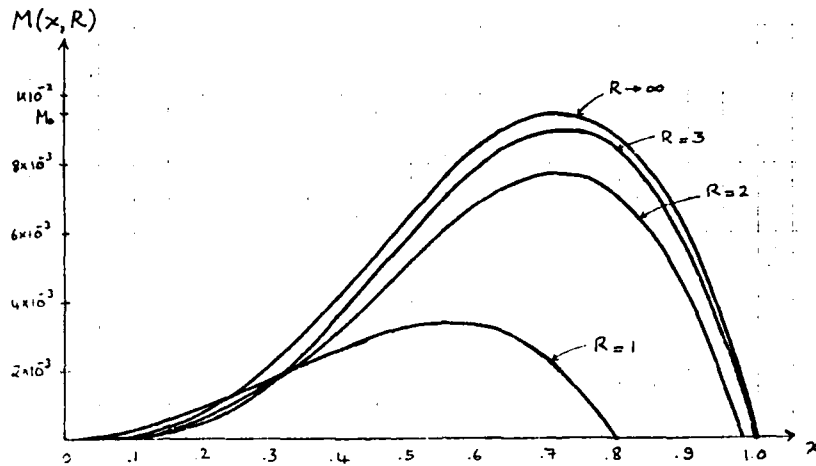
For R = 1/2 the curve collapses to the point 0 (for R < 1/2 $M(x,R)$ becomes negative for all x); as R is increased the curve approaches continuously its asymptotic shape $M_\infty(x)$. From this it is easy to obtain a qualitative picture of the marginal curve $F_c(k)$. For a given $\alpha^2/Q^2 < M_\infty$ the curve consists of two branches which, as shown above, are parabolas for large values of F_c. As F_c is decreased two distinct solutions to (v) exist until they collapse into a single one, for the value of F_c such that the maximum of M equals α^2/Q^2 ; for F_c less than this value no solution exists.

We have calculated numerical solutions of (iv) for a number of values of α^2/Q^2 ; they are plotted in Figure 7.

FIG. 7
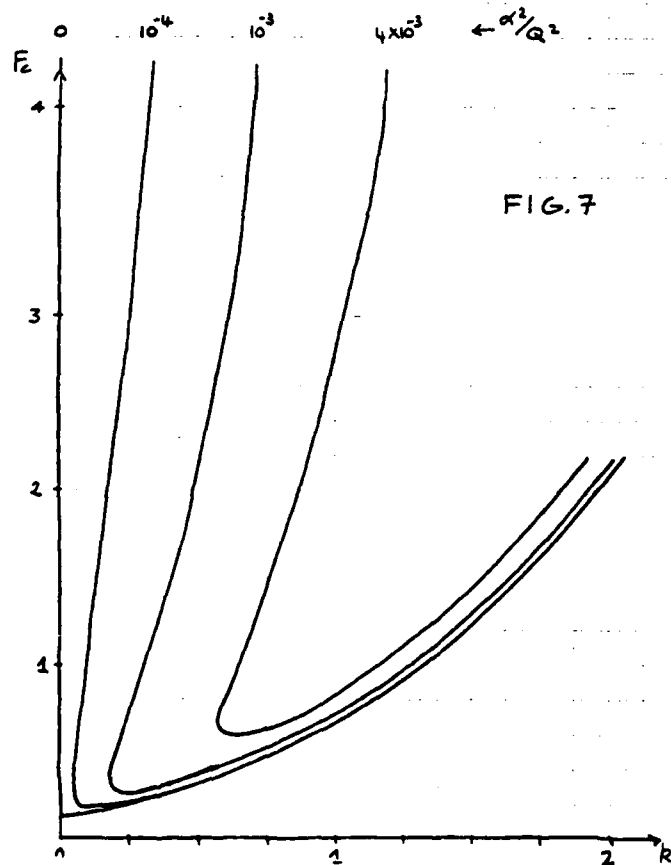
The domain of instability is the region enclosed by the curve $F_c(k)$.

We have already shown that when α^2/Q^2 exceeds the maximum value $M_0 \sim .0095$ the domain of instability disappears. Since Q is the potential vorticity associated with the unperturbed basic state, we can think of 1/Q as the time scale associated with the vorticity of the Heton band cloud (t_Q); similarly $1/\alpha$ would be the time scale of the dissipation (t_d). Then $(\alpha^2/Q^2)^{-1/2} \sim t_d/t_q$ can be thought of as a kind of Reynolds number. With this in mind we can restate the above conclusion as follows: for this system instability will not occur unless the Reynolds number exceeds a value of approximately 10.

Finally, we point out that for the dissipative band cloud the velocity field induced by the marginally stable perturbation is not purely barotropic as in the inviscid case. The reason for this is that the marginal wave, neither growing nor decaying, must extract energy from the basic state in order to maintain itself against dissipation.

3. Discussion

It is of interest to compare these results with the linear stability analysis of the Phillips (1954) two-layer baroclinic model, which is somewhat complementary to the band cloud problem. In Phillips model the gradient of potential vorticity is constant in each layer, while in the band cloud it is zero everywhere except at the cloud boundary where it is infinite. In other words, in the former case the potential vorticity gradient is spread uniformly through each layer of the fluid while in the latter it is all concentrated in an infinitesimally narrow region. The inviscid marginal stability curve for Phillips model is qualitatively identical to the one in Figure 4; the effect of dissipation is to stabilize the very long waves (i.e. make $F_c \rightarrow \infty$ as $k \rightarrow 0$), while the short waves are essentially unaffected.

In the presence of dissipation, three important differences between the band cloud and Phillips model should be pointed out. First, given a certain value of the dissipation it is always possible in Phillips model to find an F and a k which make the system unstable; this is, however, not true for the band cloud when dissipation becomes too large. Second, for a given dissipation and a given wavenumber one can always find F large enough for Phillips model to become unstable; on the other hand, for a given dissipation it is always possible to find a wavenumber for which the band cloud is stable, no matter how large F is. Third, the viscous marginal curve $F_c(k)$ in Phillips model is a single-valued function of k, but this is not true for the band cloud. The reason why $F_c(k)$ becomes multivalued in the case of the band cloud model is that the basic velocity profile of the unperturbed cloud is an exponential function of F ($U(y) \propto \exp(\pm\sqrt{2F}\, y)$); this implies that for a given dissipation and a given wavenumber it is always possible to make F large enough so that the given wavelength appears long compared to the scale on which U(y) varies.

REFERENCES

Hogg, N. and H. Stommel, 1984a. The Heton, an elementary interaction between discreet baroclinic geostrophic vortices, and its implications concerning eddy heat-flow. Submitted to Proc. Nat. Acad. of Sci.

Hogg, N. and H. Stommel, 1984b. What Hetons tell us about the general circulation. (Submitted).

Pedlosky, J., 1979. Geophysical Fluid Dynamics. Springer-Verlag, 624 pp.

Phillips, N. A., 1954. Energy transformations and meridional circulations associated with simple baroclinic waves in a two level, guasi-geostrophic model. Tellus, 6: 273-286.

DOCUMENT LIBRARY

August 3, 1984

DISTRIBUTION LIST FOR TECHNICAL REPORT EXCHANGE

Institute of Marine Sciences Library
University of Alaska
O'Neill Building
905 Koyukuk Ave. North
Fairbanks, AK

Attn: Stella Sanchez-Wade
Documents Section
Scripps Institution of Oceanography
Library, Mail Code C-075C
La Jolla, CA 92093

Hancock Library of Biology & Oceanography
Alan Hancock Laboratory
University of Southern California
Los Angeles, CA 90007

Gifts & Exchanges
Library
Bedford Institute of Oceanography
P.O. Box 1006
Dartmouth, NS, B2Y 4A2, CANADA

Office of the International
  Ice Patrol
c/o Coast Guard R&D Center
Avery Point
Groton, CT 06340

Library
Physical Oceanographic Laboratory
Nova University
8000 N. Ocean Drive
Dania, FL 33304

NOAA/EDIS Miami Library Center
4301 Rickenbacker Causeway
Miami, FL 33149

Library
Skidaway Institute of Oceanography
P.O. Box 13687
Savannah, GA 31406

Institute of Geophysics
University of Hawaii
Library Room 252
2525 Correa Road
Honolulu, HI 96822

Library
Chesapeake Bay Institute
4800 Atwell Road
Shady Side, MD 20876

MIT Libraries
Serial Journal Room 14E-210
Cambridge, MA 02139

Director, Ralph M. Parsons Laboratory
Room 48-311
MIT
Cambridge, MA 02139

Marine Resources Information Center
Bldg. E38-320
MIT
Cambridge, MA 02139

Library
Lamont-Doherty Geological Observatory
Colombia University
Palisades, NY 10964

Library
Serials Department
Oregon State University
Corvallis, OR 97331

Pell Marine Science Library
University of Rhode Island
Narragansett Bay Campus
Narragansett, RI 02882

Working Collection
Texas A&M University
Dept. of Oceanography
College Station, TX 77843

Library
Virginia Institute of Marine Science
Gloucester Point, VA 23062

Fisheries-Oceanography Library
151 Oceanography Teaching Bldg.
University of Washington
Seattle, WA 98195

Library
R.S.M.A.S.
University of Miami
4600 Rickenbacker Causeway
Miami, FL 33149

REPORT DOCUMENTATION PAGE	1. REPORT NO. WHOI-84-44	2. AD-A149386	3. Recipient's Accession No.

4. Title and Subtitle	5. Report Date
Summer Study Program in Geophysical Fluid Dynamics, The Woods Hole Oceanographic Institution, Dynamic Differentiation	
	6.

7. Author(s)	8. Performing Organization Rept. No.
Willem V. R. Malkus, Director and Florence K. Mellor, Editor	WHOI-84-44

9. Performing Organization Name and Address	10. Project/Task/Work Unit No.
Woods Hole Oceanographic Institution Woods Hole, Massachusetts 02543	11. Contract(C) or Grant(G) No. (C) N00014-82-G-0079 (G) MSC-82-00450

12. Sponsoring Organization Name and Address Office of Naval Research; National Science Foundation. Partial support from Center for Analysis of Marine Systems which is supported by The Exxon Foundation, Mobil Foundation, Inc., The Ambrose Monell Foundation; the Atlantic Richfield Foundation & by an anonymous donor.	13. Type of Report & Period Covered Technical
	14.

16. Abstract (Limit: 200 words)

The lectures by Herbert Huppert, recorded in the first section of this report, served to introduce the novel topic of Geological Fluid Mechanics which was the principal theme of the twenty-sixth summer program in Geophysical Fluid Dynamics at the Woods Hole Oceanographic Institution. Geological Fluid Mechanics has been the responsible process for the formation and modification of most of the geological objects studied today. The dynamics of fluid mixtures in magma chambers, the changing fluid boundary conditions and composition during selective crystallization of parts of the melt, and the separation of fluid fractions of different density and viscosity all represent areas in which quantitative theories are curently being tested. However, equally many areas, including convection mechanisms in the Earth's core and quantitative predictions for upper mantle motion, resist simplistic modeling. The abstracts of seminars by invited speakers address many challenging issues raised by this new field of study.

The following pages also contain abstracts of a symposium by geophysicists on observed fluid-like geological phenomena co-sponsored by the Center for Analysis of Marine Systems at W.H.O.I.

The Fellowship lectures which make up the final section of the report reflect the interests of the Principal Lecturer more than at any time in the recent past. Five of these involve double-diffusive processes in one way or another. These reports are to be treated as unpublished manuscripts. Readers desiring to quote from the material should seek the permission of the author. As in past years, these reports are often reworked for publication or are incorporated into doctoral theses.

17. Document Analysis a. Descriptors

1. Geophysical Fluid Dynamics
2. Geological Fluid Dynamics
3. Double-diffusive processes

b. Identifiers/Open-Ended Terms

c. COSATI Field/Group

18. Availability Statement	19. Security Class (This Report) UNCLASSIFIED	21. No. of Pages 288
Approved for publication; distribution unlimited.	20. Security Class (This Page)	22. Price

END

FILMED

2-85

DTIC